POWER CONVERTERS
FOR
RENEWABLE ENERGY APPLICATIONS

Teză destinată obţinerii
titlului ştiinţific de doctor inginer
la
Universitatea Politehnica Timişoara
în domeniul INGINERIE ELECTRICĂ
de către

Ing. Emil Guran

Conducător ştiinţific: Prof.univ.dr.ing Nicolae Muntean
Referenţi ştiinţifici: Prof.univ.dr.ing Mircea Rădulescu
                           Prof.univ.dr.ing. Loránd Szabó
                           Prof.univ.dr.ing. Lucian Nicolae Tutelea

Ziua susţinerii tezei: 24 aprilie 2015

Copyright © Editura Politehnica – Timişoara, 2015

Acknowledgements

This thesis is the result of teamwork and this is why I first want to express my gratitude to the person who managed this team, a person who showed me a lot of patience, trust and competent guidance, my supervisor Professor Nicolae Muntean.

Lecturer Octavian Cornea has offered me a lot of support during this study, being a friend, work colleague and mentor in the same time. I want to thank him for this.

I want to express my gratitude to Professor Gheorghe Daniel Andreescu for his unconditioned help regarding the stability analyses and the professionalism she showed me every time we met.

I wish to thank the referents, Professor Mircea Rădulescu, Professor Loránd Szabó from Technical University of Cluj and Professor Lucian Tutelea from Politehnica University of Timisoara, for their observations and relevant suggestions.

I also want to mention here eng. Dan Hulea and all my friends and colleagues who helped me in different ways to face this period. I thank them and I hope that our friendship will continue to keep us close.

Last but not the least, I want to thank to my family for the moral support and to my fiancée and future wife Veronica Barbu for her unlimited support, patience and understanding during this period.

Timişoara, April 2015   Emil Guran

Abstract,
        The smart grid applications have a considerable development nowadays. Being complex systems they integrate relative simple and robust elements in order to be profitable and stable on long term.
        This work presents a research in the field of bidirectional DC-DC and DC-AC power converters, looking for topologies suitable for DC or AC busses interfaces. Two converters are presented in this thesis, a bidirectional DC-DC converter whose topology was found in literature but it was never studied in detail and novel topology of DC-AC Flyback inverter.
        A full analysis and simulation design for both the bidirectional DC-DC converter with large voltage conversion ratio and for the flyback inverter are presented.
        Stability studies are made for the two converters in order to verify their behaviour during perturbations, using the state-space average and the PWM switch model methods. Using the AC response, two compensation functions were developed in order to improve the systems stabilities. The new compensated systems are presented and analyzed.
        The stability analysis results are integrated in simulation models. The simulation results for voltages and currents through the circuit elements are given here. Their shapes and values highlights the well operation for the both DC-DC and DC-AC converters.
        A prototype for the bidirectional hybrid DC-DC converter with large conversion ratio was designed. The experimental results are compared with the simulation results highlighting that the BHDC operation is stable and it can be used in a microgrid application.
        A prototyping procedure is initiated for the flyback inverter.

Table of Contents

The Thesis Objectives

After a preliminary research and a fair debate, the thesis objectives were established. Well divided, this study follows to:

➢ realize an overview of the renewable and unconventional sources of energy highlighting their residential versions;
➢ make a review of bidirectional DC-DC converters used in microgrid applications;
➢ make a review of high efficiencies DC-AC inverters used in microgrids;
➢ propose a DC-DC converter topology intended to be used in an intended microgrid;
➢ study analytically and reveal through digital simulation the proposed topology;
➢ perform stability studies in order to verify the converter behavior and develop compensation functions to improve the stability;
➢ build the prototype of the proposed converter and obtain experimental results in order to confirm the simulation results;
➢ propose a DC-AC topology of an inverter intended to be used in microgrids;
➢ study analytically and reveal through digital simulation the proposed topology;
➢ perform stability studies in order to verify the converter behavior and develop compensation functions to improve the stability;
➢ realize a synthesis of the experimental results obtained, highlighting the stability and good operation of the proposed topologies;

After the objectives accomplishment, the goal is the integration of the proposed converters in a microgrid application.

The Thesis Outline

This thesis presents a synthesis of DC-DC and DC-AC converters designed to be used in microgrids and proposes two different original topologies to be analyzed in detail.

➢ The first chapter offers an introduction about the importance of smart microgrids nowadays, highlighting the special features of these systems and why they are considered a response to the energy production problems on long term. Their main components like green energy sources and storage systems are presented here. These components are described offering an overview regarding their functionality depending on the environment, their functional constraints and capabilities. All these requirements are related to the microgrid applications.

➢ The second chapter contains a review of bidirectional DC-DC power converters from literature, which are close related to renewable energy applications. The chapter continues with the presentation of a bidirectional transformerless DC-DC converter with a high voltage conversion ratio topology. A full analytical study and digital simulations of this topology were realized in order to determine the converter behavior. The equations of the currents through the main components are given here and they are verified by simulation. A detailed stability analysis is realized using two stability analysis procedures- steady-state average and PWM switch model. Using the stability analysis results, a compensation function is added to the system and integrated as a phase boost circuit to the prototype in order to improve the system stability. The operating principles are presented analytically and verified through simulation. All the obtained results lead to a prototype construction for the proposed DC-DC topology. Information about the design is given here. The chapter ends with experimental and simulation results that confirm the system well operation and stability in harsh conditions.

➢ The third chapter presents a list of high efficiency inverters from the literature and it continues with the proposal of two novel topologies of flyback inverters, but only one will be analyzed in detail. An analytic study is presented in order to describe the operating principles. A stability analysis is realized and following the results a compensation function is given here. Using the information obtained during the analytical study and stability analysis, a spice model is realized. The simulation results confirm a good operation of the flyback inverter and a stable behavior after the compensation function integration. A design procedure is presented for the proposed inverter based on the system constraints.

➢ In the fourth chapter is presented a part of an intended microgrid emulator which represent the experimental platform were the BHDC and the HBFAC are going to be integrated. Details about the equipment and the experimental setup are given here.

➢ The fifth chapter consists of conclusions regarding the analyzed power converters. The personal contributions of the author are also presented here. It ends with some details about future research purposes and applications where these converters are intended to be used.

NOMENCLATURE

ABBREVIATIONS

AC	Alternating Current
BCM	Boundary current mode
BHDC	Bidirectional Hybrid DC-DC converter
CCM	Continuous current mode
CP	Power Regulation
DC	Direct Current
DCM	Discontinuous current mode
EV	Electrical Vehicle
HEV	Hybrid Electrical Vehicle
HBFAC	Hybrid Bidirectional Inverter
H_R	Compensation function
HF Tr	High frequency transformer
LC	Inductive-capacitive
RMS	Root mean square
S	Transistor with antiparallel diode
SCC	Switching capacitor cell
SiC	Silicon Carbide
SSA	State-Space Averaging
PV	Photovoltaic Panels
PWMSM	Pulse Width Modulation Switch Model
THD	Total Harmonic Distortion
UPS	Uninterruptible Power Supplies
ZVS	Zero voltage switching

SYMBOLS

A_1, A_2..., B_1, B_2..., ...	State and output matrices	-
C_1, C_2 ...	Capacitors	F
C_i, C_o ...	Filter capacitors	F
D	Duty cycle	-
$\tilde{d}$	Small signal variations of the duty cycle	-
D_1, D_2 ...	Diodes	-
E	Energy	J
f	Switching frequency	Hz
f_{max}	Maximum switching frequency	Hz
I_c, I_{ci} I_{c0}	Currents through the capacitors	A
I_{Dmin}	Minimum current through a diode	A
$I_{L1limmax}$, $I_{L2limmax}$ ...	Maximum current through L_1 and L_2 in BCM	A
I_{L1max}, I_{L2max} ...	Maximum current through inductors	A

I_{L1med}, I_{L2med} ...	Mean current through inductors	A
I_{L1min}, I_{L2min} ...	Minimum current through inductors	A
I_{peak}	Peak Current	A
$I_{S1limmax}, I_{S2limmax}$	Maximum current through transistors in BCM	A
I_{S1max}, I_{S2max} ...	Maximum current through transistors	A
I_{S1min}, I_{S2min} ...	Minimum current through transistors	A
I_{valley}	Valley Current	A
k	Transformation ratio of the flyback transformer	
L	Inductance	H
L_1, L_2 ...	Inductors	H
N_1, N_2	Primary and secondary windings turns	-
P	Power	W
P_1, P_2 ...	Poles	-
P_{1max}, P_{2max} ...	Maximum rated powers	W
R	Resistive load	Ω
r_{L1}, r_{L2} ...	Equivalent resistance for L_1 and L_2	Ω
r_{C0}, r_{C1}, r_{C2}	Equivalent resistance for C_0, C_1 and C_2	Ω
S_1, S_2 ...	Transistors	
V_1, V_2 ...	Input/output voltages	V
V_{c1}, V_{c2} ...	Voltage drop across the capacitors C_1 and C_2	V
V_c	Voltage drop across the capacitor cell	V
V_{cp}	Output voltage	V
V_{in}	Input voltage	V
V_{out}	Output voltage	V
$\tilde{v}_{out}$	Small variations of output variables	-
V^*_C	Reference voltage over the capacitor	V
V_{S1}, V_{S2} ...	Voltage drop over the transistors	V
t_{on}, t_{off}	Switching periods	s
T_s	Switching period	s
x_1, x_2 ...	State variables for currents and voltages	-
$\dot{x}_1, \dot{x}_2$ ...	Time derivatives of the state variables x_1, x_2 ...	-
$\tilde{x}$	Small variations of state variables	-
$\dot{\tilde{x}}$	Averaged small variations of state variables	-
Z_1, Z_2 ...	Zeros	-
ΔI	Current Variation	A
ΔV	Voltage Variation	V

LIST OF FIGURES AND TABLES

List of tables

1. INTRODUCTION

In a modern society, the presence of the electric energy is highly needed and even mandatory sometimes, thinking to hospitals or other similar fields. Used in industry or for improving the human quality of life, the electricity is used at such a level that forces the actual researchers to leave behind the traditional fossil fuels based energy sources, seeking to create and develop a wide variety of unconventional energy sources, able to compensate the relative irreversible consumption of these fuels, which are limited. Still, all these new and existing energy sources need to be integrated in efficient systems in order to collect their energy and supply the consumers with it, following to obtain low production and distribution costs with very small losses.

Starting from these hypotheses, relative small systems develop every day. Widely known as smart grids, they are better versions of the traditional centralized electricity system. They become more and more popular mostly because they integrate a variety of energy sources, managing their energy flow and they are able to provide electric energy to a wide range of loads and storage systems. They do not depend by a large distribution system and may be successfully implemented islanded in remote or hard to reach areas. Because of their special features, they can be connected to the existing centralized distribution system, valuing this way the excess of energy or obtain extra energy if the loads need it.

Nowadays the market offers many solutions for smart grids at different scales. Besides the energy sources and storage systems, the number of the existent topologies of power converters that may be integrated in these new systems is very high and continues to grow. Because of the continuous improvement of the active power elements, the rated efficiencies of some traditional converters have been improved and some of them even surpassed other effective newer converters. The microprocessors became cheap and in the same time more powerful facilitating better control strategies. These important changes create a new direction in power electronics. Old and new topologies are "reinvented" or combined in order to obtain better hybrid converters with higher efficiencies, able to be integrated in complex smart grids, mostly because of their adaptability to special conditions [1.1, 1.2].

1.1. Energy: Past-Present-Future

The conversion of energy in electricity has determined a big change to the humanity. The number of inventions grew very fast and today we are able to use the electric energy in almost all the existing fields. On the other hand, this progress has caused an important damage to the environment. Almost all the traditional energy sources depend on fossil fuels, which are relative limited and run low due to the inefficient exploitation. Another major problem they raise is related to the resulted pollution. The nuclear energy is also an important alternative as an energy source. Unfortunately, it becomes very dangerous in unexpected critical conditions. The resulted waste represents a big risk for the environment and life in general by being radioactive, not biodegradable and hard to be stored in safe conditions for a

long time. The concerns regarding the traditional and nuclear energy sources have appeared relatively late and only after 1980's the trend of renewable energy was considered a mandatory solution on long term for all the electrical loads. Happily, at this moment, there are many engineering departments whose main activity is to find and design integrated unconventional energy systems. Based on the keep growing need of energy, lots of futuristic ideas came alive. So, the **wind power** is collected with different types of wind turbines. The **solar energy** is used for an easy generation of electric and thermal energy. The **power of waves and water** in general is the main energy for the hydro-electrical power plants. The **geothermal energy** is used by steam turbines or air conditioning. Another green power source is based on **bio fuels** and more and more alternatives are found every day. For a better efficiency all these energy sources are supposed to be integrated in smart grids, depending by environment and applications [1.3].

At this moment, the renewable energy sources are able to cover less than 25% of the global energy consumption and most of the existing countries continues to use the main traditional energy sources. The efficiencies of the main electrical machines and power converters have increased up to 99%, but even so, the energy need is at a very high level and this need continues to grow. This low level of green energy consumption increases the researchers devotion to reduce and even eliminate the traditional power sources and replace them with new unpolluting renewable energy sources in the next forty years. This trend raises a high motivation for scientists to continue their research and more and more costumers see it as a good investment on long term, since the price of energy will grow [1.4].

The graph presented in fig.1.1 shows the stats of the world wide used energy, the first one represent the percent of traditional unrenewable energy, and the second one shows the percent of how the "green energy" consumption in 2013 [1.5, 1.6, 1.7].
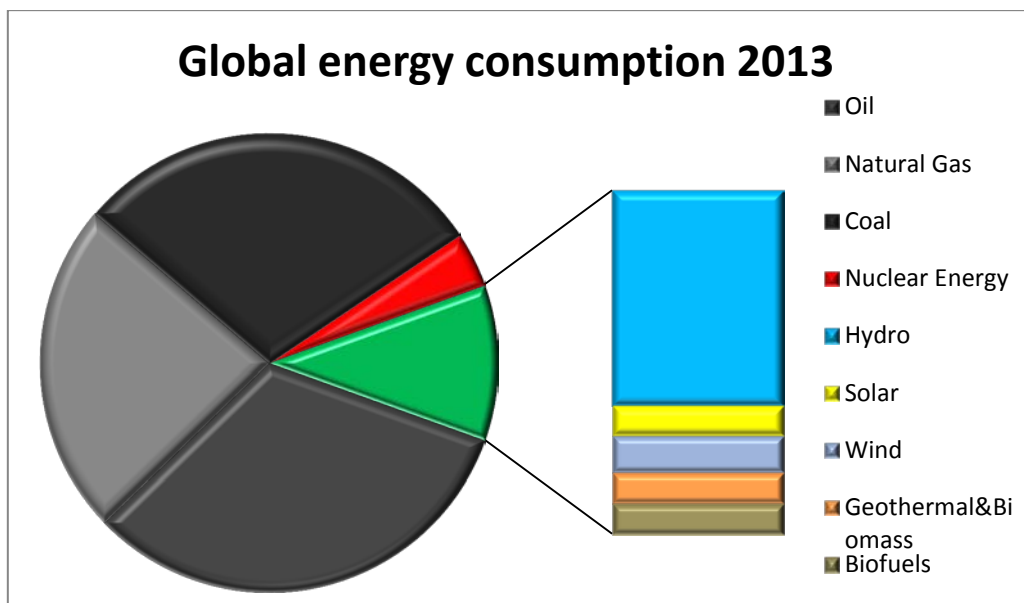
Fig.1.1. Global energy repartition

Energy demand worldwide continues to increase due to the transformation of the industry and people life style. Traditional energy sources like fossil fuels are vanishing and their high pollution character became a real problem by having a big contribution to the greenhouse effect. All these facts force us to have an innovative view regarding the future of energy.

The renewable energy sources were and they still are used in different ways by being integrated in various applications. Solar and geothermal energy are used for heating and even mechanical applications for example. The wind and water energy were also used in mechanical applications and the humanity used all these sources with their special characteristics in simple ways in order to improve the life comfort. The development of the electricity and its transportation has guided these sources, first to distributed generation units of electrical power and after a while in wide electric power distribution systems [1.3].

Nowadays the trends are reversed and many times people are looking for islanded systems where all solar, wind, water, even geothermal energy and biomass are used together. Renewable energy can provide all the energy services available from conventional energy sources: heating, cooling or electricity and it has the big advantage of being a naturally infinite resource. These systems can provide energy to remote areas without the need for expensive energy distribution systems. It is worth noting and it is not always necessary to convert the renewable energy into electricity. Solar and geothermal water heating or wind applications are good examples of systems that can work very well without involving electricity at all. However, the major contribution that renewable energies will have in supplying people's need will be in electrical form, because the energy can be converted much easier and supplied to several applications, which can involve many traditional and new generation electric loads [1.8, 1.9].

The literature offers a variety of topologies and patents for both DC-DC and DC-AC power converters with special features that make possible their integration in these complex systems.

The basis of this thesis is close related to the general scientific research regarding smart microgrids. This thesis presents two different converters. The first is a transformerless bidirectional DC-DC converter with a high conversion ratio and a low number of active elements. The second converter is a flyback inverter with low number of elements and galvanic isolation whose hybrid operation makes it original and feasible for specific applications. The goal of this study is to highlight their originality and show if they represent feasible solutions for smart microgrids or similar systems. The project planning has begun with a special attention directed to an intended microgrid and only after it has been determined the requirementsand constraints the needed converters were searched and designed.

In conclusion, the main goal of this thesis was to find new converters structures intended to be used in microgrids. These converters had to be able to satisfy the requirements of the proposed microgrid and to be adaptable to different conditions and applications. The presented topologies are studied in detail for the first time in order to obtain analytical and digital simulation information. The theoretical results are confirmed in the end by the experimental results for the bidirectional converter and through simulation for the flyback inverter.

In the following is presented the actual trend of the distribution of energy related to smart grids with their special features, which may introduce the DC voltage as the primary voltage for electric load, or even dual DC and AC voltage busses [1.10, 1.11].

1.2. Smart Microgrids

The development of electric distribution systems has begun islanded and close related with different energy sources like steam turbines or hydro-turbines. It started with DC applications and it was spread mostly on limited areas. After the discovery and progress of AC generation, the transport of energy became much easier and efficient. Its evolution made possible a very large expansion of the electric distribution systems, many of them being used even nowadays. The transportation of energy at high AC voltages offered the possibility of connecting large energy sources located at long distances and supply with electrical energy many industrial and non-industrial consumers. The traditional energy sources were and they still are based on fossil fuels and partially on hydro jams. The nuclear energy became also an important energy source after 1950's. Once with the growing need of energy, the fossil fuels reserves have decreased, making the price of the electric energy to grow. The environment has been damaged by the pollution and it raises big problems nowadays through many natural disasters due to the global warming [1.12].

Starting from these facts, the development of the unconventional energy sources and their use is mandatory. The price of this undertaking is very high, but it is understandable and unavoidable. The predictions for the next forty years are not very optimistic mostly because fossil fuels reserves are supposed to end, before getting an alternative solution for the energy demand. A goal of the last decades was to improve the efficiency of the main electrical loads in order to decrease the consumed energy. The results can be seen in today's electrical machines, lighting and power electronic devices where the efficiency grew up to 99% and the engineers continue to develop new devices with smaller losses and better features. In the same time, they struggle to discover new energy sources and improve as much as they can the old ones. Advancing with these objectives, it is clear that the old distribution systems are outdated and they have to be re-technologized in order to decrease the resulting losses from the relative poor management. The transportation of the energy, even at high voltages, continues to raise problems related to the losses and costs. This is the point where the smart grids appear and try to solve all the related issues. It offers a great management of the energy distribution between multiple energy sources, which are supposed to be unconventional [1.13, 1.14, 1.15].

When the microgrids grow to larger grids, the management of the energy becomes a serious problem. In order to reduce the losses/costs and offer in the same time full functionality, the entire grid is analyzed up to each electrical load. During this process, most of the equipment is categorized depending on their energy demand and operating periods during the day or even larger time intervals. When this classification is done, a much better design of the system can be done. The actual prices of the green energy sources are very high, but if the dimensioning is accurate, the initial costs are much lower and this is because a smart management can equilibrate the energy consumption. Processes like home heating, air conditioning, electrical cars charging, water extraction and heating, can be controlled in smart grids. This management of the high consuming loads is based on the complementary operating times and provides an intelligent use of the energy where the human comfort is assured full time with lower costs [1.16, 1.17, 1.18].

The smart grid systems trends are to eliminate as much as possible the unnecessary losses, collect energy from any sources and all these with small costs, fig.1.2.
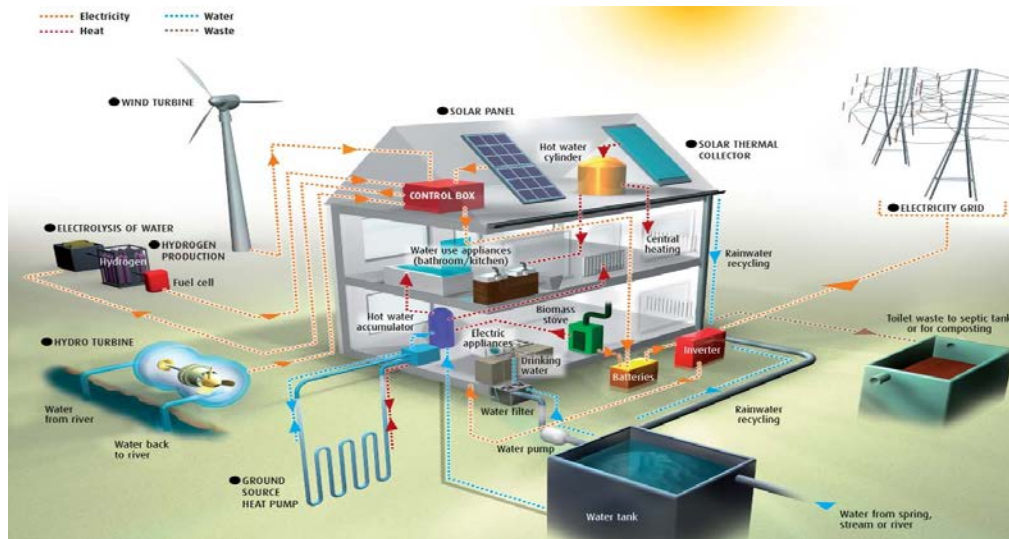
Fig.1.2. Energy independent house

In order to obtain reasonable prices, all the integrated parts are designed to be multitasking. The energy collected is used primary for the main intended use and secondary for various tasks in order not to be lost. These systems integrate multiple DC and AC busses, which are interfaced each other. Their parameters are close related to the standard loads and can be connected directly to them. The storage systems represent a serious drawback and many times these smart grid systems require a diesel generator and/or connection to a centralized electric grid. Since the batteries are very expensive, with a limited lifetime, a connection between the smart grids and hybrid-electrical vehicles is made. The rechargeable batteries of the vehicle are used for an extra storage capacity when the owners are home. Currently the price for complex smart grids is high and the investment payback time is long. Thinking to the fact that their maintenance is expensive too we get another minus. Still the environment crisis is pushing us to adopt this attitude and many governmental organizations support these interchange programs of the traditional fossil fuels and nuclear-based energy sources [1.18, 1.19, 1.20, 1.21].

Each smart grid is unique depending by the application and possibilities, but the main idea of this concept is always the same. In the following subchapters are presented some of the most common elements and some actual trends about how they are or may be integrated in micro grids.

1.3. Renewable energy sources

The Sun provides a high amount of energy and it can be considered unlimited. At this moment, this energy is harnessed in different forms. Its warmth is

used for heating domestic hot water installations and it also helps in air conditioning systems. Going back to the production of electrical energy, the sun represents an important energy source. Neglecting its major disadvantage of being discontinued during the day and night cycle and having a variable power during the seasons and metrological conditions, we are able to collect solar energy in many forms. Unconventional storage systems were designed and the research continues.

The most popular electrical solar energy sources are related to the **photovoltaic panels**. They have a lower efficiency and they have to be integrated in special systems in order to track their maximum power point.

In fig.1.3 are presented different types of photovoltaic panels that are usually used in residential applications or even PV plants.

Polycrystalline   Monocrystalline   Hybrid   AllBlack
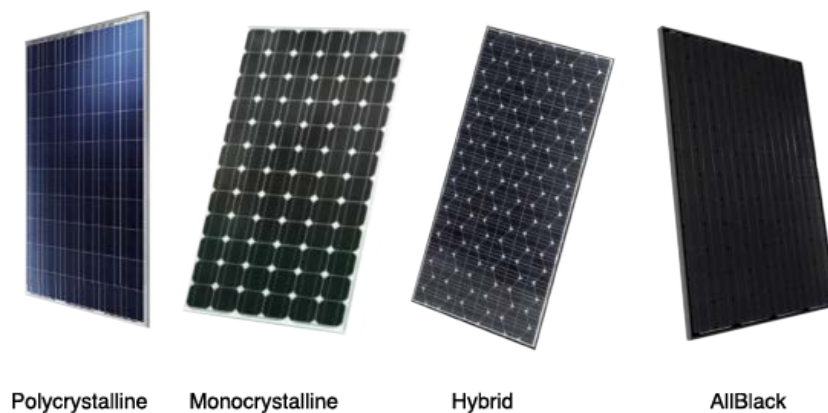
Fig.1.3. Types of photovoltaic panels

The polycrystalline panels are the most widespread, because their efficiencies reported to the costs are the highest. The monocrystalline panels have the best performances. Unfortunately the production costs are higher and because of that many times they are left aside for the other types of panels. The hybrid panels, widely known as amorphous, have a special frame and production costs are lower. Unfortunately they have a lower efficiency and their use is preferred in well-known conditions. The last common type of photovoltaic panels is represented by the Black Backed Panels. They also have a special construction and their costs go higher even if their efficiency is average. Mostly wanted for their better look, they have serious problems because of the higher heating. A relative new unconventional photovoltaic source is realized using a new special ink and a printer able to print it on different supports, which act like photovoltaic cells. With lower efficiencies and costs, they have a big advantage of being flexible, offering an easier way to be mounted anywhere [1.22, 1.23].

Since the Black-Backed Panels are typical for customized applications only and they are preferred particularly for their design, in Table 1.1 only the other three types of common photovoltaic panels are treated, highlighting their specifications [1.24].

Table 1.1. Photovoltaic panels specifications.

	Monocrystalline	Polycrystalline	Hybrid/Amorphous
Typical efficiency	15-20%	13-16%	6-8%
Best efficiency	26-28%	20-22%	13-15%
Area/1kWp	6-9m^2	6-10m^2	12-20m^2
Warranty	25 years	25 years	15-25 years
Costs(Euro/W)	0.65€/W	0.55€/W	0.60€/W
Temp. obs.	High temperatures causes 10-15% additional losses	High temperatures causes 15-25% additional losses	High temperatures don't affect much their performance
Additional details	They are most widely used but the production costs are high	Less silicon waste in their production process.	The production materials are less harmful for environment

Another way to collect the energy from the Sun is to concentrate and transform its heat in mechanical work. The most common two ways to do this are close related to thermodynamics. The sunrises are concentrated using mirrors and focused to one point where the temperatures can rise up to thousands of degrees. These temperatures are used in **solar steam turbines** or in **Stirling applications**. An electric generator is needed each time.

In fig.1.4 a solar concentrator and a steam turbine application are presented. Worldwide, many power plants of this kind can be found. The rated power can range from several kilowatts up to hundreds of megawatts. These systems are very expensive and most of the time their final costs are not representative, being one of a kind project. Still, residential versions can be realized. The rated efficiencies of these systems are around 30-40%, but they can be increased to 80% or even more if secondary circuits are realized [1.25].

Fig.1.4. Solar steam turbine and concentrator

In fig.1.5 a Stirling engine and the related sunrises concentrator are shown. The difference compared to the previous application is related to the operating temperature, which in this case is higher than 550 degrees Celsius. The maximum rated power of the actual Stirling engines goes up to 60 kW. The costs also depend by the application. The efficiencies rise over 95% for rated powers of about 10 kW [1.26].
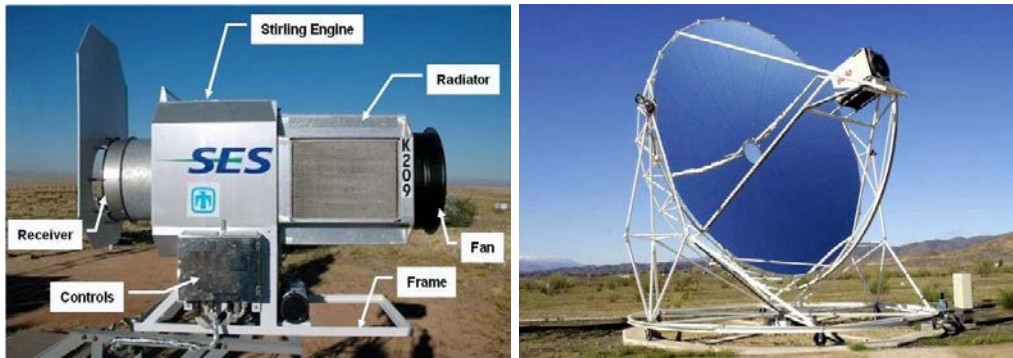
Fig.1.5. Stirling engine and sunrises concentrator

Around the world, there are many places where because of the landform, pressure or differences of the temperature, permanent air currents appear. In these places, large power plants of **wind turbines** are built day by day. With rated powers up to hundreds of megawatts, these systems offer a real solution for high power applications. Besides the large wind turbines, there are interesting designs of residential versions able to collect energy from the wind almost everywhere [1.27, 1.28]. Some of them are presented in fig.1.6.

Fig.1.6. Residential Wind Turbines

The **energy of water** is collected nowadays in many ways. Large artificial dams exist everywhere in the world along the rivers. They convert the mechanical work produced by the water force in electricity, resulting impressive amounts of electric power. At high level, the hydro energy comes also from the **waves**, **tidal power** and **ocean currents**. There are also many residential applications to obtain energy from small rivers and creeks, fig.1.7, [1.29, 1.30, 1.31].

Fig.1.7. Residential Hydro Turbines

The **geothermal energy** refers to different categories of thermal energy that can be collected from the Earth crust. The most common applications use this energy for air conditioning. In order to obtain electrical energy higher temperatures are needed and the pipes with refrigerant have to be buried at great depths, process which is very difficult and expensive. Because of this, most of the time they only represent a feasible solution if there is a volcanic activity, fig.1.8, [1.31, 1.32].
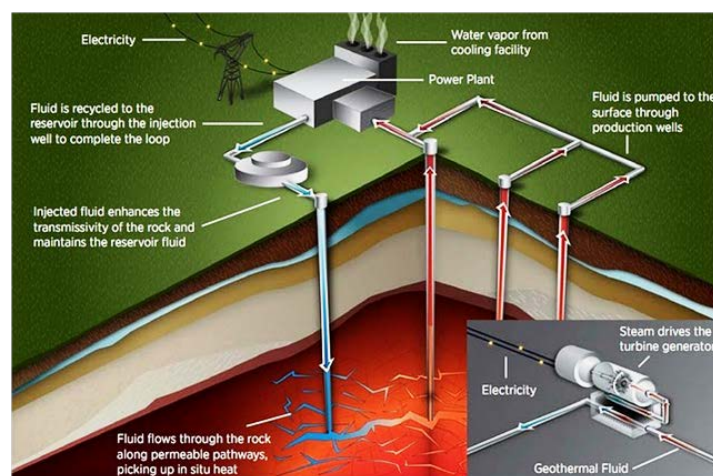
Fig.1.8. Geothermal energy collection process

The energy collected from **biomass, waste and hydrogen** represent a significant part of the global unconventional energy. They can be used to produce electricity or heat in special power plants. The rated power of these thermal centrals can vary on large scale, depending by the application. Practically the biomass or hydrogen can substitute the fossil fuels in applications of hundreds and even tens of megawatts. In residential applications, biofuels are used in diesel engines-electric generators to produce electricity up to tens of kilowatts and in small thermal centrals [1.33, 1.34, 1.35].

1.4. Energy storage technologies

The biggest disadvantage of the unconventional energy sources used in residential applications is the fact that their operation depends many times by the environment. Because of this, all the proposed smart grids must have different storage and backup systems. The storage systems are very useful when the amount of collected energy is bigger than the need and the excess is kept for the moments when more energy is needed or the collected energy is lower. The back-up systems have a relative similar role, because they maintain the most important systems in use during emergencies.

The most common storage systems are the **rechargeable batteries.** Based on the electrochemical reactions which are electrically reversible, these storage batteries represent the most practical solution in relative low power applications, up to tens or even hundreds of kilowatts. Several combinations of chemicals are used for their fabrication, but the most usual are the lead-acid and the lithium ion ones. They have two important disadvantages. The first one is that in some cases they need maintenance and even if not, their lifetimes are limited to about 500-2000 of complete charge-discharge cycles. The second disadvantage is related to the time of the charging cycle. The rechargeable batteries are charged usually with a current of about 10% of its rated capacity and this process takes hours [1.36, 1.37].

When unconventional energy sources are used, due to environmental variations, many times the energy has big fluctuations and these batteries cannot collect it completely. In their support come **ultra-capacitors.** With a rated capacitance starting from tens of Farads, these passive components are able to store energy no matter of its fluctuations. Their lifetime and costs are high and they are usually used in combination with the traditional rechargeable batteries in automotive and smart grid applications [1.38, 1.39]. In fig.1.9 are presented a high capacity Li-Ion Battery, an ultra-capacitor and a flywheel.

Fig.1.9. Li-Ion Battery, ultra-capacitor and flywheel

The **hydraulic accumulator** permits to storage the extra energy as compressed air. There are applications of hundreds of megawatts where the compressed air is stored in large caverns and reused blended with natural gas to drive gas turbines to generate electricity when more power is needed [1.40].

Another energy storage system, mechanical this time, is the **flywheel energy storage**. It is suitable for residential applications, when the rated power do

not exceed hundreds of kilowatts. These flywheels are connected to electrical machines working in both motor and generator modes accelerating on extra power peaks and producing energy otherwise [1.41, 1.42].

Thermal inertia of the objects and substances is also used for the energy storage, mostly for small residential applications [1.43].

The last solution for storing energy is the **pumped-storage hydroelectricity**. Because of the costs and complexity, this method is suitable only for high power applications. The feasibility of these projects is strictly related to the environment opportunities [1.44, 1.45, 1.46].

1.5. Conclusion

This chapter offers an introduction into the smart microgrids theory, a relatively new field in which the following proposed DC-DC and DC-AC converters are intended to be used.

The smart microgrid systems might be a long-term partial solution for the limited traditional energy reserves. By collecting energy from various renewable energy sources, they are able to eliminate the problems and costs involved by the conventional centralized distribution systems. Depending by application, they can supply with energy different loads at different parameters directly in DC or AC modes, avoiding this way the use of additional DC-DC or DC-AC converters. Since the energy storage problem is far from being solved, these systems offer the possibility of using various and ingenious storage systems in order to offer a continuous operation. Their "smart" feature permits the intelligent management of the collected energy, the way it is stored and also the loads supply in order to use the energy more effective.

References

[1.1]   H.F.Sennholz. (2006, Apr. 3). The third industrial revolution [Online]. Available: http://mises.org/library/third-industrial-revolution.

[1.2]   Ipakchi, A.; Albuyeh, F., "Grid of the future," Power and Energy Magazine, IEEE , vol.7, no.2, pp.52,62, March-April 2009.

[1.3]   Bull, S.R., "Renewable energy today and tomorrow," Proceedings of the IEEE , vol.89, no.8, pp.1216,1226, Aug 2001.

[1.4]   Liserre, M.; Sauter, T.; Hung, J.Y., "Future Energy Systems: Integrating Renewable Energy Sources into the Smart Power Grid Through Industrial Electronics," Industrial Electronics Magazine, IEEE , vol.4, no.1, pp.18,37, March 2010.

[1.5]   B. Bose, "GLOBAL ENERGY SCENARIO AND IMPACT OF POWER ELECTRONICS IN 21ST. CENTURY," IEEE Transactions on Industrial Electronics, vol. 60, no. 7, p. 2638-2651, July 2013.

[1.6]   "Renewables 2013 - Global Status Report" 2013 [Online]. Available: http://www.ren21.net/ren21activities/globalstatusreport.aspx.

[1.7]   "Renewables 2014 - Global Status Report" 2014 [Online]. Available: http://www.ren21.net/ren21activities/globalstatusreport.aspx.

[1.8]   Carrasco, J.M.; Franquelo, L.G.; Bialasiewicz, J.T.; Galvan, E.; Guisado, R.C.P.; Prats, Ma.A.M.; Leon, J.I.; Moreno-Alfonso, N., "Power-Electronic Systems for the Grid Integration of Renewable Energy Sources: A Survey", IEEE Transactions on Industrial Electronics, vol.53, no.4, pp.1002,1016, June 2006.

[1.9]   Atwa, Y.M.; El-Saadany, E.F.; Salama, M.M.A.; Seethapathy, R., "Optimal Renewable Resources Mix for Distribution System Energy Loss Minimization", IEEE Transactions on Power Systems, vol.25, no.1, pp.360,370, Feb. 2010.

[1.10] Kurohane, K.; Senjyu, T.; Yona, A.; Urasaki, N.; Goya, T.; Funabashi, T., "A Hybrid Smart AC/DC Power System", IEEE Transactions on Smart Grid, vol.1, no.2, pp.199,204, Sept. 2010.

[1.11] F. Blaabjerg, Youngheng Yang and Ke Ma, "Power electronics - key technology for renewable energy systems – status and future", 3rd International Conference on Electric Power and Energy Conversion Systems (EPECS), Yildiz Technical University, Istanbul, Tyrkey, October 2004, pp. 1-6.

[1.12] Hatziargyriou, N.; Asano, H.; Iravani, R.; Marnay, C., "Microgrids," Power and Energy Magazine, IEEE , vol.5, no.4, pp.78,94, July-Aug. 2007.

[1.13] Cecati, C.; Mokryani, Geev; Piccolo, A.; Siano, P., "An overview on the smart grid concept," IECON 2010 - 36th Annual Conference on IEEE Industrial Electronics Society , vol., no., pp.3322,3327, 7-10 Nov. 2010.

[1.14] Vandoorn, T.L.; Vasquez, J.C.; De Kooning, J.; Guerrero, J.M.; Vandevelde, L., "Microgrids: Hierarchical Control and an Overview of the Control and Reserve Management Strategies," Industrial Electronics Magazine, IEEE , vol.7, no.4, pp.42,55, Dec. 2013.

[1.15] Keyhani, A.: Design of Smart Grid Renewable Energy Systems. Wiley, New Jersey, (2011).

[1.16] Boroyevich, D.; Cvetkovic, I.; Dong Dong; Burgos, R.; Fei Wang; Lee, F., "Future electronic power distribution systems a contemplative view," 12th International Conference on Optimization of Electrical and Electronic Equipment (OPTIM), 2010, vol., no., pp.1369,1380, 20-22 May 2010 (2011).

[1.17] Strzelecki, R. and Benysek, G. (authors). "*Power Electronics in Smart Electrical Energy Networks*". London: Springer-Verlag LTD, 2008.

[1.18] R.H. Lasseter, A. Akhil, C. Marnay, J. Stephens, J. Dagle, R. Guttromson, A. Meliopoulous, R. Yinger, and J. Eto. "Integration of Distributed Energy Resources: The CERTS MicroGrid Concept," April 2002 [Online]. Available: http://certs.lbl.gov/certs-der.html.

[1.19] Cvetkovic, I.; Thacker, T.; Dong Dong; Francis, G.; Podosinov, V.; Boroyevich, D.; Wang, F.; Burgos, R.; Skutt, G.; Lesko, J., "Future home uninterruptible renewable energy system with vehicle-to-grid technology," Energy Conversion Congress and Exposition, 2009. ECCE 2009. IEEE , vol., no., pp.2675,2681, 20-24 Sept. 2009.

[1.20] Chengzong Pang; Aravinthan, V.; Xiaoyun Wang, "Electric vehicles as configurable distributed energy storage in the smart grid," Power Systems Conference (PSC), 2014 Clemson University , vol., no., pp.1,5, 11-14 March 2014.

[1.21] Battistelli, C., "Generalized microgrid-to-smart grid interface models for vehicle-to-grid," Innovative Smart Grid Technologies (ISGT), 2013 IEEE PES, vol., no., pp.1,6, 24-27 Feb. 2013.

[1.22] Hren, R.,″ *Understanding PV Module Specifications*″, Home Power, November 2011 [Online]. Available: http://www.homepower.com/articles/solar-electricity/equipment-products/understanding-pv-module-specifications?v=print

[1.23] TheSolarPlanner.com, "*PV Module Specs and Features*", 2012 [Online]. Available: http://www.thesolarplanner.com/pv_panel_features.html

[1.24] Maehlum, M.A., "Solar Cell Comparison Chart – Mono-, Polycrystalline and Thin Film", September 2013 [Online]. Available: http:/energyinformative.org/solar-cell-comparison-chart-mono-polycrystalline-thin-film/.

[1.25] Wikipedia contributors, "*Concentrated solar power*", March 2015 [Online]. Available:http://en.wikipedia.org/w/index.php?title=Concentrated_solar_power&oldid=650703622

[1.26] Solar Cell Central, "*Concentrated Solar Power (CSP)*", 2011 [Online]. Available: http://solarcellcentral.com/csp_page.html

[1.27] ENERGY.GOV, "Small Wind Electric Systems", 2012 [Online]. Available: http://energy.gov/energysaver/articles/small-wind-electric-systems.

[1.28] Wind Hybrid Power Generation, ″*Wind Turbine Home*″, 2015 [Online]. Available: http://windhybridpowergeneration.blogspot.ro/2015/02/wind-turbine-home.html.

[1.29] Davies, S., Engineering and Technology Magazine, "*Small hydro delivers local benefits*", 2011 [Online]. Available:http://eandt.theiet.org/magazine/2011/01/small-hydro.cfm.

[1.30] Small Hydro International Gateway, "*Small Scale Hydropower*", [Online]. Available: http://www.small-hydro.com/About/small-scale-hydrpower.aspx

[1.31] Wijesinghe, A.; Loi Lei Lai, "Small hydro power plant analysis and development", 4th International Conference on Electric Utility Deregulation and Restructuring and Power Technologies (DRPT), 2011, vol., no., pp.25,30-, 6-9 July 2011.

[1.32] Hammons, T.J., "Geothermal power generation worldwide," Power Tech Conference Proceedings, 2003 IEEE Bologna , vol.1, no., pp.8 pp. Vol.1,, 23-26 June 2003.

[1.33] Tahersima, F.; Stoustrup, J.; Meybodi, S.A.; Rasmussen, H., "Contribution of domestic heating systems to smart grid control", 50th IEEE Conference on Decision and Control and European Control Conference (CDC-ECC), 2011, vol., no., pp.3677,3681, 12-15 Dec. 2011.

[1.34] Barroso, L.A.; Rudnick, H.; Sensfuss, F.; Linares, P., "The Green Effect," Power and Energy Magazine, IEEE , vol.8, no.5, pp.22,35, Sept.-Oct. 2010.

[1.35] Rahman, S., "Green power: what is it and where can we find it?," Power and Energy Magazine, IEEE , vol.1, no.1, pp.30,37, Jan/Feb 2003.

[1.36] Ribeiro, P.F.; Johnson, B.K.; Crow, M.L.; Arsoy, A.; Liu, Y., "Energy storage systems for advanced power applications," Proceedings of the IEEE , vol.89, no.12, pp.1744,1756, Dec 2001

[1.37] Vazquez, S.; Lukic, S.M.; Galvan, E.; Franquelo, L.G.; Carrasco, J.M., "Energy Storage Systems for Transport and Grid Applications", IEEE Transactions on Industrial Electronics, vol.57, no.12, pp.3881,3895, Dec. 2010

[1.38] Miller, J.M., "Energy storage technology markets and application's: ultracapacitors in combination with lithium-ion," Power Electronics, 2007. ICPE '07 , vol., no., pp.16,22, 22-26 Oct. 2007

[1.39] Khaligh, A.; Zhihao Li, "Battery, Ultracapacitor, Fuel Cell, and Hybrid Energy Storage Systems for Electric, Hybrid Electric, Fuel Cell, and Plug-In Hybrid Electric Vehicles: State of the Art," Vehicular Technology, IEEE Transactions on , vol.59, no.6, pp.2806,2814, July 2010.

[1.40] EI-Ayoubi, A.; Moubayed, N., "Economic study on batteries and hydraulic energy storage for a lebanese hybdrid Wind/PV system", International Conference and Exposition on Electrical and Power Engineering (EPE), 2012, vol., no., pp.972,977, 25-27 Oct. 2012

[1.41] Bitterly, J.G., "Flywheel technology: past, present, and 21st century projections," Aerospace and Electronic Systems Magazine, IEEE , vol.13, no.8, pp.13,16, Aug 1998.

[1.42] Hall, C.D., "High speed flywheels for integrated energy storage and attitude control," American Control Conference, 1997. Proceedings of the 1997 , vol.3, no., pp.1894,1898 vol.3, 4-6 Jun 1997.

[1.43] Cabeza, L.F.; Sole, C.; Castell, A.; Oro, E.; Gil, A., "Review of Solar Thermal Storage Techniques and Associated Heat Transfer Technologies," Proceedings of the IEEE , vol.100, no.2, pp.525,538, Feb. 2012.

[1.44] Ning Lu; Chow, J.H.; Desrochers, A.A., "Pumped-storage hydro-turbine bidding strategies in a competitive electricity market", IEEE Transactions on Power Systems, vol.19, no.2, pp.834,841, May 2004

[1.45] Whittingham, M.S., "History, Evolution, and Future Status of Energy Storage," Proceedings of the IEEE , vol.100, no.Special Centennial Issue, pp.1518,1534, May 13 2012.

[1.46] Ellis, M.W.; von Spakovsky, M.R.; Nelson, D.J., "Fuel cell systems: efficient, flexible energy conversion for the 21st century," Proceedings of the IEEE , vol.89, no.12, pp.1808,1818, Dec 2001.

2. BIDIRECTIONAL DC-DC POWER CONVERTER WITH LARGE VOLTAGE CONVERSION RATIO

Smart grids integrate in their systems different DC busses. Their importance leads to interesting topologies of DC-DC converters used to interface these busses and realize complete operational and stable systems. Highly needed for some applications because of its features, this thesis presents a bidirectional converter, which offers great results in both its operating modes. It can be used as a step-up converter being capable to boost for more than 10 times the input voltage and as a step-down converter lowering the input voltage with the same large ratio. Because of its bidirectional feature and the relative high efficiency, this converter is analyzed and adapted for a specific microgrid application, as an interface between two DC voltage busses.

The higher conversion ratio between the input and output voltages is obtained by using two switching capacitor cells in the main circuit and three transistors. The switching control strategy of the semiconductors permits to choose the current flow direction for the converter (step-up/down) depending on how is needed by the application.

Considering the main characteristics listed above, this converter goal is to make the connection between the main DC voltage line which transports the energy at 400 V DC and a storage system of batteries able to sustain the entire system during critical situations. The safety system needs to be filled with energy at 50 V DC and a current of about 40 A. In critical situations, it can supply the entire system for about 2-3 hours at the same voltage but with a higher current.

This chapter begins with a review of bidirectional DC-DC converters used in automotive and smart grid applications and it continues with the study of the converter. In order to show this converter possibilities and limitations, its power stage circuit is presented in detail and analyzed. A stability analysis is realized using two different methods. Using the obtained data, digital simulation models are designed for testing them. All the established information is merged for the construction of a prototype for the converter. The experimental results validate the analytical and digital simulation results.

2.1. Bidirectional DC-DC Converters

Usually microgrids integrate various DC busses, because it is much simpler to interface them and obtain a complete functional and stable operation. Also, because these systems are small enough to have no distribution losses problems, they can have some additional outputs with various values of the DC voltages, specially created for some DC loads.

These DC converters have to be simple and adaptable to special conditions like large conversion ratios, electromagnetic compatibility, environment and others. They also have to be cheap and offer high efficiencies. Another special and very convenient feature is the bidirectional characteristic, because in smart grids especially, the energy transfer flow is many times random between the sources, loads and storage systems.

In the next sections, some bidirectional converters are presented, highlighting their advantages and features. They also represent an introduction to bidirectional hybrid converter that will be studied in detail.

➢ Buck-Boost Bidirectional DC-DC Converter

This converter is very popular in literature, mostly because it is realized using two traditional DC-DC converters. It uses a step-up converter to raise the voltage value from the left source up to the value of the right voltage source. In this operation mode, the current is injected in the higher voltage source which supplies the loads or it is connected to an inverter and injects the energy directly in the grid. In the opposite operation mode, it uses a traditional step-down converter to decrease the voltage between the two sources. Working in this mode, it transfers the energy between a higher DC bus or a rectified voltage from the grid, to a lower DC bus which may be a battery stack. The construction is reflected in its operation because each converter works separately depending on the sense of the energy flow. The power stage schematic is presented in fig.2.1 [2.1].
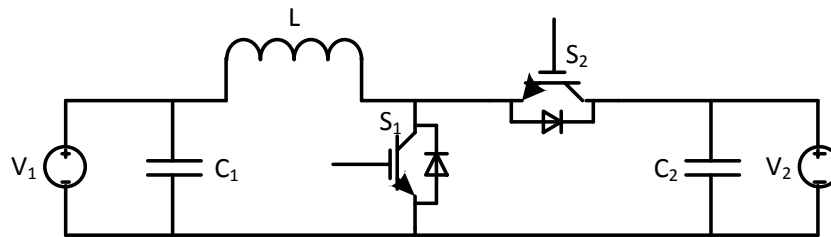
Fig.2.1.Buck-Boost Bidirectional DC-DC Converter

The efficiency of this converter is high due to the low number of active and passive components. Combining a buck and a boost DC converter means that the bidirectional converter uses two different duty cycles D_1 for S_1 and D_2 for S_2 for each switch depending by the operation mode, presented in fig.2.2.

$$V_1 = D_2 \cdot V_2 \qquad \text{for step-down mode} \qquad (2.1)$$

$$V_2 = V_1/(1-D_1) \qquad \text{for step-up mode} \qquad (2.2)$$
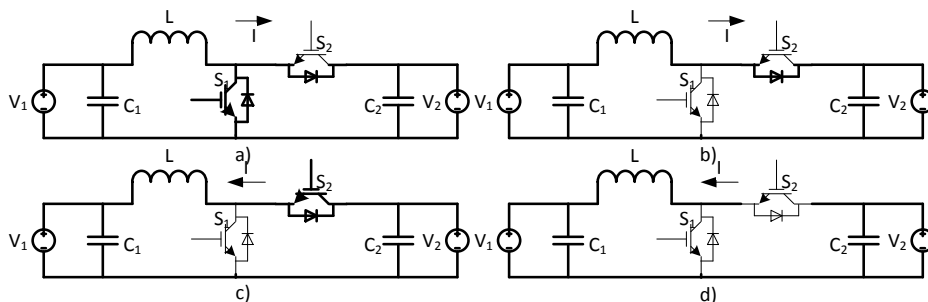
Fig.2.2.Converter a, b) boost operation mode c, d) buck operation mode

Due to the semiconductors limitations and the power stage structure, the voltage-conversion ratio is narrow and it is not suitable for high ratio voltage

conversion applications. With its simple structure, the rated efficiencies can go over 96% if high quality semiconductors are used [2.2, 2.3].

➤ Synchronous Bidirectional DC-DC Converter

Another popular topology of bidirectional DC-DC Converter is the one presented in fig.2.3. It is used in many hybrid or complete electrical vehicles (HEV/EV) and rechargeable power supply unit applications where the power flow is needed in both directions. Its name came from the fact that the two active elements switch synchronous but in opposition. This bidirectional converter is derived from the conventional buck-boost converter with the diode replaced with a transistor. The antiparallel diodes of the semiconductors and the filter capacitors added in parallel with the voltage sources facilitate the bidirectional power flow [2.4, 2.5].
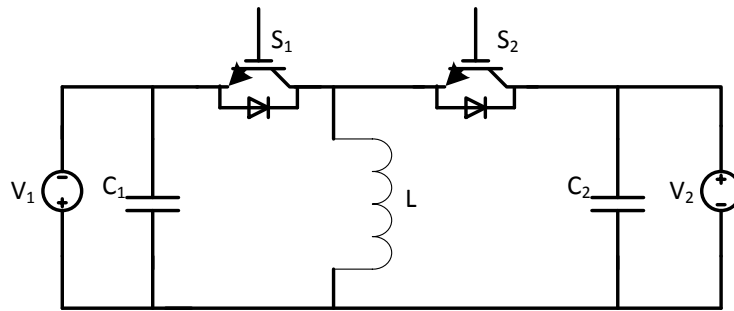
Fig.2.3. Bidirectional Synchronous DC-DC Converter

The relations between the two voltage sources depend by the duty cycle and are given by the following equations, where V_2 is greater than V_1:

$$V_2 = -\frac{D_1}{1-D_1} V_1 \quad \text{for step-up mode} \tag{2.3}$$

$$V_1 = -\frac{D_2}{1-D_2} V_2 \quad \text{for step-down mode} \tag{2.4}$$

The switching states of the synchronous converter are presented in fig.2.4.
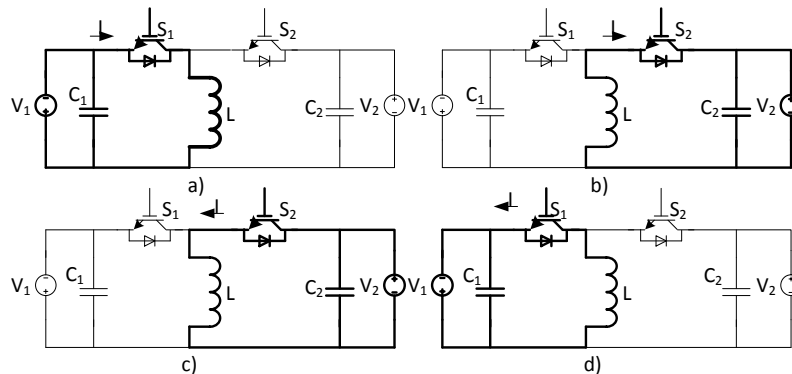
Fig.2.4.Converter operation in boost mode a), b) and in buck mode: c) and d)

This converter needs only one switching control for both semiconductors. It has a low number of components and reaches high efficiencies over 96%. With SiC new generation transistors, the rated efficiency can be even higher [2.6].

> **Dual half-bridge bidirectional DC-DC converter**

The converter presented in fig.2.5 is a high efficiency dual-half-bridge bidirectional DC-DC Converter. With special features like zero-voltage-switching (ZVS) the losses on the active components decrease [2.7, 2.8].
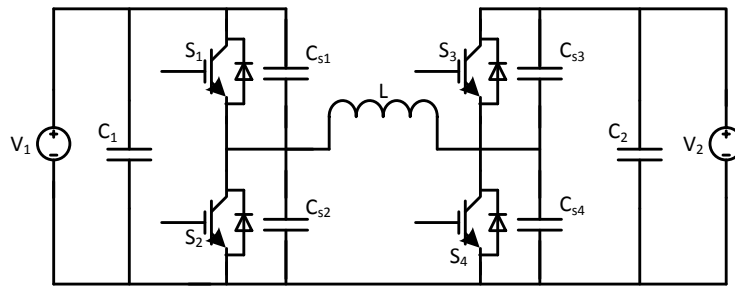
Fig.2.5. Dual half-bridge bidirectional DC-DC converter

The additional capacitors C_{s1}, C_{s2}, C_{s3} and C_{s4} serve for the ZVS feature. It has a mirrored architecture, so with an adaptive control it can be used in various applications and conditions.

The relation between V_1 and V_2 is given by the way how S_1, S_2 and S_3, respectively S_4 are switched, always in opposition (S_1 with S_2 and S_3 with S_4). In fig.2.6 are represented the equivalent circuits during the switching states, considering V_1 lower than V_2 and the energy flowing from V_1 to V_2.
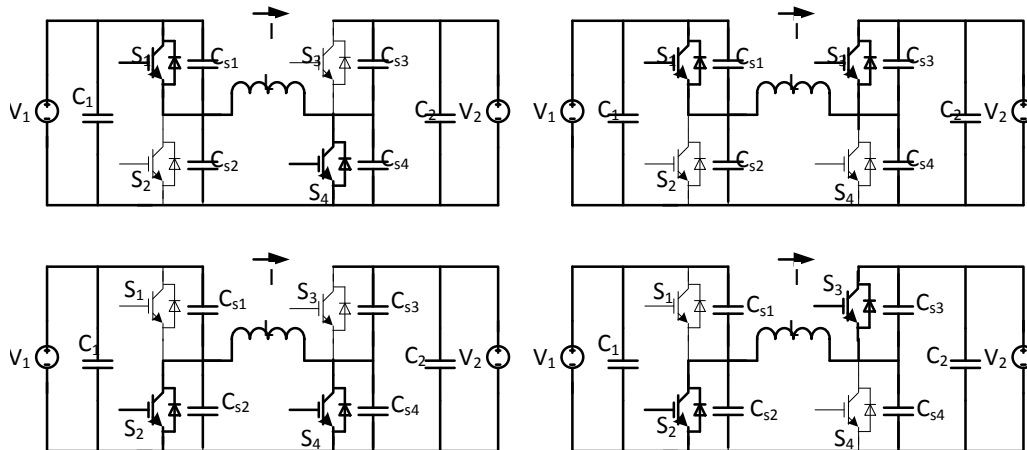
Fig.2.6.Equivalent circuits during switching states a), b), c) and d) in step-up mode

When the energy flows in the opposite direction, the equivalent circuits are the same during switching, but with different duty cycles.

This converter integrates a greater number of components and this increases the costs. Still, this topology is a feasible option considering its robustness, adaptability to various conditions and applications, and most important its high efficiency using the new generation of semiconductors with low losses. This topology rated efficiency is between 90% and 98% in specific conditions for both step-up and step-down modes [2.9].

➢ Bidirectional DC-DC soft-witching converter

The converter presented in fig.2.7 is used in stand-alone photovoltaic systems and in similar smart grid applications. With a bidirectional flow of energy, this converter can be integrated between different DC busses when various storage systems and DC loads are put together. Since the S_1 and S_2 semiconductors switch at low voltage, it results lower losses in both step-up and step-down operation modes [2.10, 2.11].
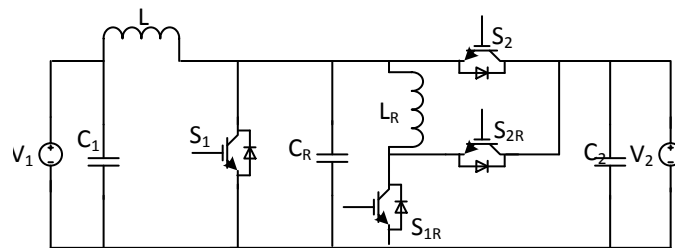
Fig.2.7. Bidirectional DC-DC soft-switching converter

The power stage circuit depends by the two transistors S_1 and S_2, the other two S_{1R} and S_{2R}, are used together with the LC circuit realized by L_R and C_R in order to obtain the soft-switching feature. The auxiliary switch S_{2R} is connected on the high voltage side, while the auxiliary switch S_{2R} is connected on the lower voltage side. This way, the resonant circuit injects the stored energy back in the circuit at specific times, triggered by the S_{1R} and S_{2R} switch. The switching states of the circuit are the same when the converter operates in step-down mode, but their succession is different. Current sense is imposed in the control strategy and then the proper switching sequence is automatically selected.

In fig.2.8 are presented the switching states of the converter in succession sequence for the operation in step-up mode.

The rated efficiency for this converter can go up to 97% and even higher for high efficiency semiconductors when the converter operates in step-up mode and 1-2% lower when operates in step-down mode [2.11].
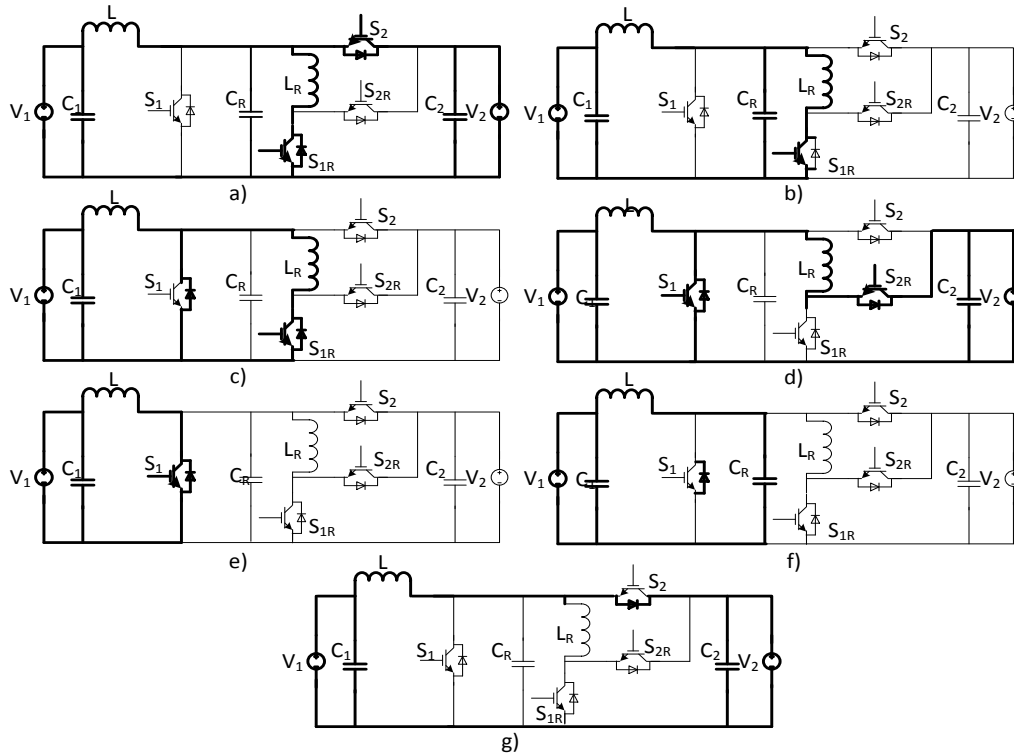
Fig.2.8.Equivalent circuits during switching states a), b), c), d), e), f) and g) in step-up mode

> ➢ **Bidirectional non-isolated DC-DC Converter with large conversion ratio**

The next bidirectional converter has a simple circuit structure. The control strategy can be easily implemented and it allows a significant losses reduction. This topology offers a larger conversion ratio in both step-up and step-down operation modes. It can go up to 200% in step-up mode and down to 50% in step-down related to the conventional bidirectional converters. In fig.2.9 the power stage circuit is presented [2.12 - 2.14].
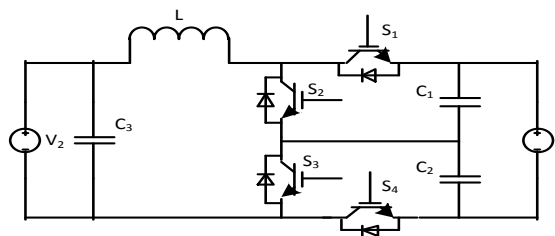
Fig.2.9. Bidirectional non-isolated DC-DC with large conversion ratio

The relations between V_1 and V_2 are given in (2.5) and (2.6) [2.12].

$$V_2 = \frac{2}{1-D_1} V_1 \qquad \text{for step-up mode} \qquad (2.5)$$

$$V_1 = \frac{D_2}{2} V_2 \qquad \text{for step-down mode} \qquad (2.6)$$

The switching states of the circuit are presented in fig.2.10.
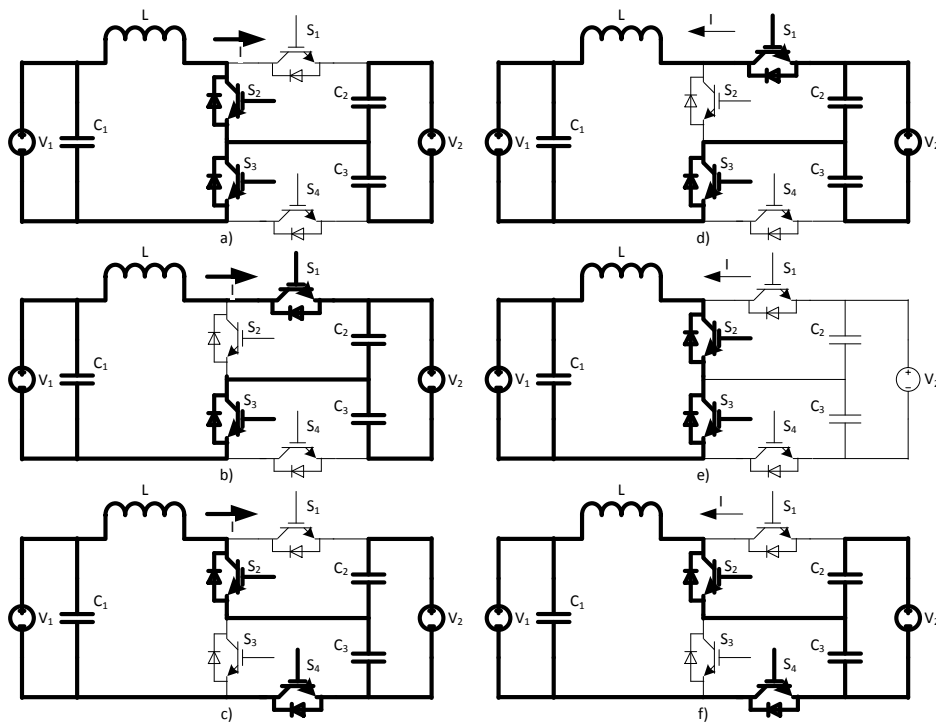
Fig.2.10. Switching states for step-up mode a), b), c) and for step-down mode d), e) and f)

Using high performance semiconductors, this converter offers efficiencies over 98-99%. It has a low number of components and offers a larger conversion ratio than the conventional bidirectional converters. It is adaptive to various automotive and microgrid applications and allows different strategies of control for the switches in order to improve its efficiency. An example of its adaptability is the integration of this topology in a hybrid inverter used in microgrid applications as interface between a high voltage DC bus and AC loads. It is used in the step-down operation mode and the output voltage waveform on the filter capacitor is a rectified sinusoid, which is passed through an H-bridge inverter. The bidirectional feature is used here too because the filter capacitor has to be charged and discharged during each period of the AC voltage. This converter can be used in step-up mode too in similar applications following the same principle. An application where this converter is used in a hybrid inverter is given in [2.15]. The rated efficiency for this inverter is above 99% in special conditions and using high performance transistors [2.16-2.23].

In the following are presented a few bidirectional DC-DC converters with galvanic isolation designed to be used in automotive and microgrids applications with references to our work. When a microgrid offers the possibility of injecting energy into the centralized grid the galvanic isolation is most of the time mandatory. High efficiency bidirectional DC-DC converters with galvanic isolation are needed at different stages in microgrid systems and many topologies can be found in literature. Since the conversion is realized at high frequency the additional losses introduced by the transformer are lower. [2.17-2.24].

> **Bidirectional Flyback DC-DC Converter**

A bidirectional flyback DC-DC converter with very low number of components is presented in fig.2.11. It uses the secondary and primary windings of the flyback transformer as inductors on both opposite circuits. The two switches can be controlled using a single switching control but alternately with sufficient dead time.
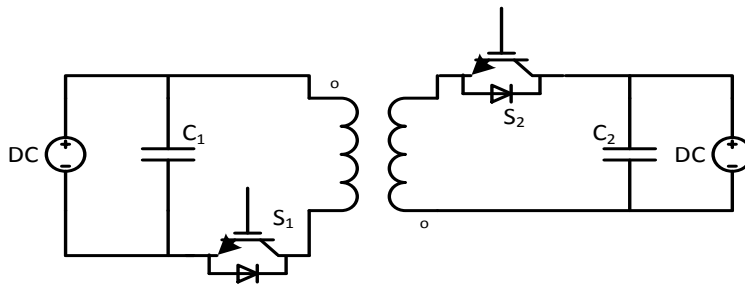
Fig.2.11. Bidirectional Flyback DC-DC Converter

This converter has two states and the relation between the lower and the higher voltage depends by the duty cycle and the conversion ratio of the flyback transformer. The transfer of energy is current controlled and is mandatory that the transformer is well designed, and the control strategy sets the energy flow direction. In fig.2.12 are shown the states of the flyback converter, which are the same for both step-up and step-down operation mode [2.25].
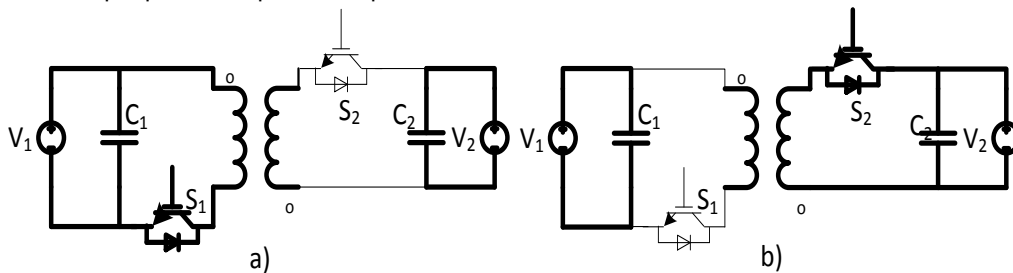
Fig.2.12. Bidirectional Flyback DC-DC Converter Switching States a) and b)

This topology has the advantage of being adaptable to various conditions and requirements. Its simple structure is used in hybrid topologies of DC-DC converters with small modifications and even in hybrid DC-AC converters [2.26, 2.27].

A major problem related to this converter is the snubber circuits necessity on the both sides of the transformer in order to decrease the voltage peaks on the transistors during switching. In order to obtain high efficiencies, resonant snubbers are needed and high performance transistors have to be used.

➢ **Bidirectional voltage and current fed full-bridge converter**

The voltage and current fed full-bridge bidirectional DC-DC converter is presented in fig.2.13.
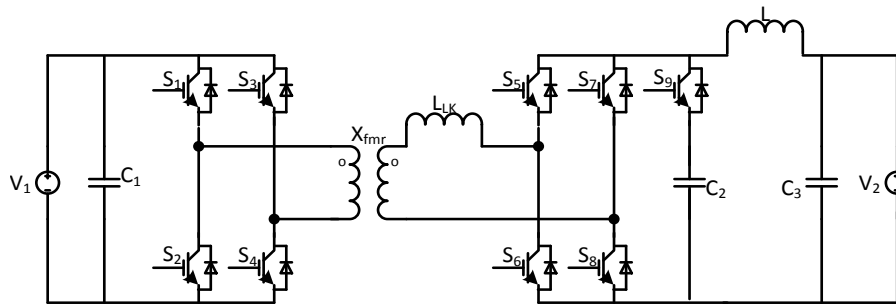
Fig.2.13. Bidirectional voltage and current fed full-bridge DC-DC Converter

The topology offers a wide range of conversion ratios given by the high frequency transformer and it is feasible for high rated power applications. The full-bridge S_1-S_4 is voltage fed on the high voltage side, V_1. On the low voltage side, V_2, the second full-bridge S_5-S_8 is current fed. An additional active clamp circuit is introduced in the low voltage side in order to reduce the stress on the semiconductors. Depending on how are fed the bridges, various configurations with half-bridges and resonant circuits are developed based on this topology [2.28 - 2.30].

➢ **Bidirectional series resonant converter with clamped capacitor voltage**

In fig.2.14 is presented the power stage circuit of a bidirectional series resonant DC-DC converter with clamped capacitor voltage.
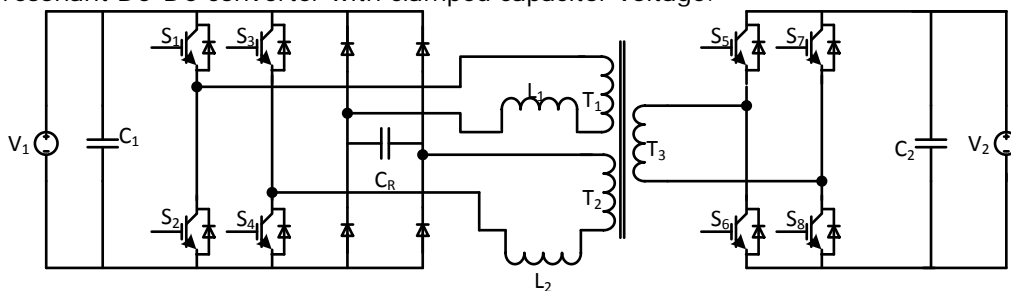
Fig.2.14. Bidirectional series resonant converter with clamped capacitor voltage

The resonant circuit added to the primary windings of the circuit is meant to reduce the current stress in the secondary side, when the transfer of energy is realized at high voltages. This converter is a feasible solution for relative high power microgrid applications where lower voltage DC busses exist on the lower voltage side and much greater voltage DC busses have to be interfaced [2.31-2.34].

The rated efficiency for a bidirectional series resonant DC-DC converter with clamped capacitor voltage is close to 98% for specific conditions and a rated power of 35 kW [2.30].

2.2. Bidirectional DC-DC Converter with Large Conversion Ratio

2.2.1. Analytical Study for step-down operation

The proposed converter is a bidirectional hybrid DC-DC (**BHDC**) topology, which realizes the conversion of energy with at high voltage ratio. In the following, two analytical studies are presented. They are important for understanding how the energy flows through the converter in each direction. They also help to determine the equations and parameters of the currents and voltages on the active and passive components. The hybrid converter, presented in fig.2.15 consists of a simple boost converter followed by a switching capacitor cell (**SCC**), which allows a bi-directional current flow by adding S_1 and S_2 switches with their antiparallel to D_1 and D_2. The left side of it is characterized by a lower voltage and high currents, the energy being normally supplied by or stored in several batteries connected in series, while the right side is connected to a high voltage (400 V-600 V) microgrid DC bus. The operating modes presented in detail below, depends on the action of the switching capacitor cell [2.35].
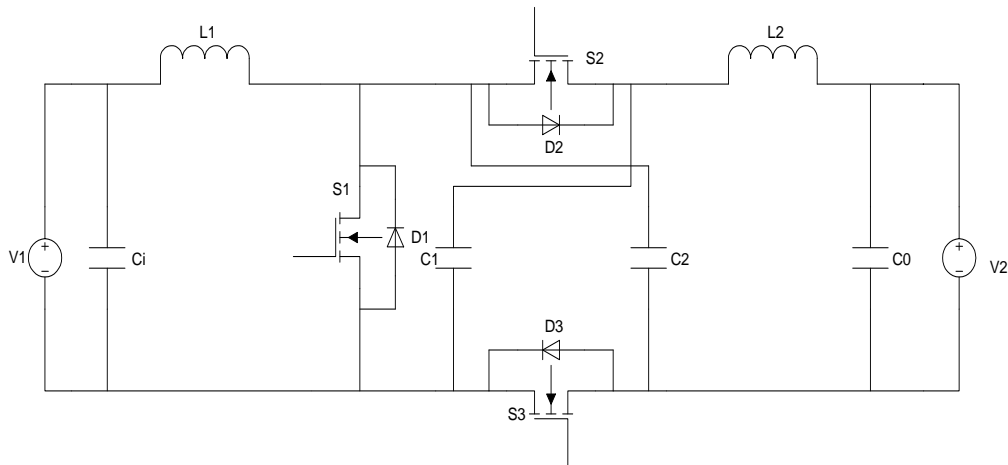
Fig.2.15. Hybrid Bidirectional DC-DC Converter Topology

> ## Continuous current mode analysis (CCM) of BHDC

Considering the converter acting as a battery charger, its operation can be compared with the one of a classical buck converter but with a higher step-down conversion ratio given by the SCC. The switching circuits of the converter during t_{on} and t_{off} are presented in fig.3.2.a) and b), highlighting the current flow for each state of the transistors. During t_{on} the two identical capacitors of the SCC are charged in series while during t_{off} they are discharged in parallel through L_1 inductor, injecting energy in the lower DC voltage bus.

a)

b)
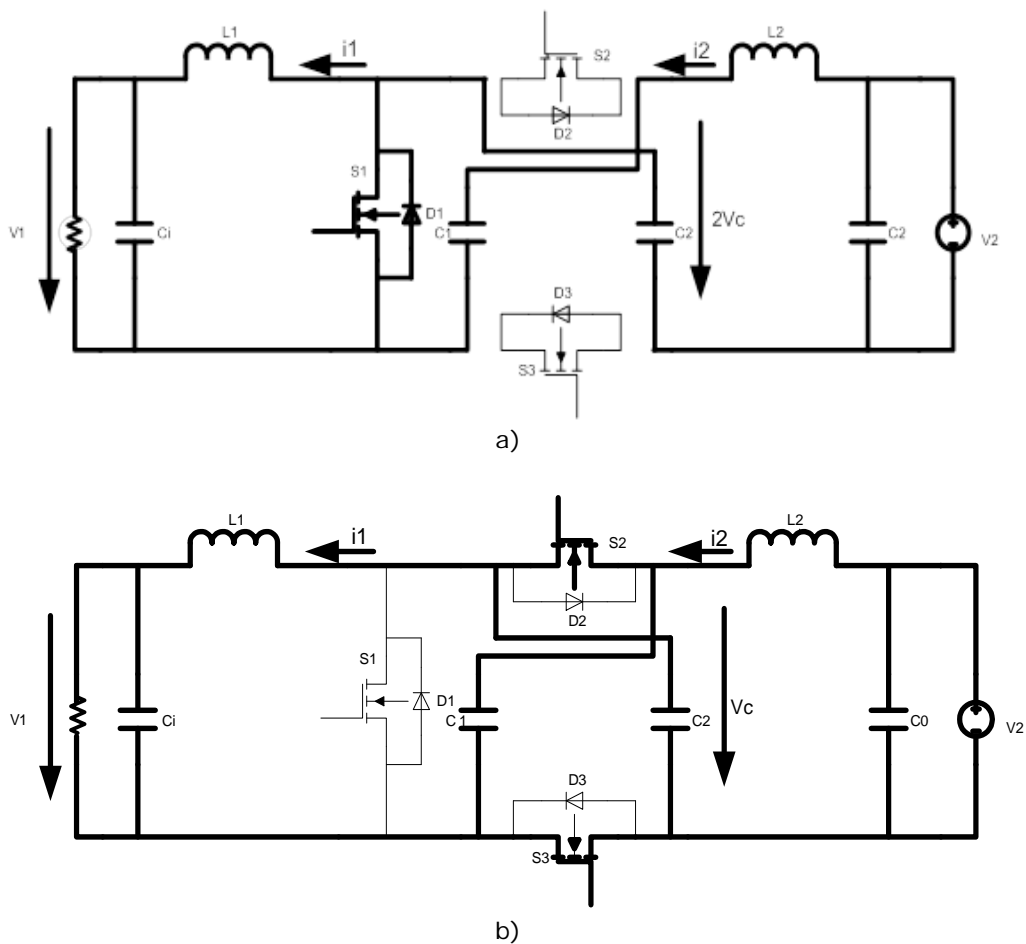
Fig.2.16. Equivalent circuit: a) t_{on}, b) t_{off};

A single command signal is used. It is applied directly to S_1 and inverted to S_2 and S_3. Since S_1 is doubled by the antiparallel diode D_1, in step down mode its control can be inhibited.

Considering the input and output voltages constant (C_i and C_O are sufficiently large to assume zero voltage ripples), the following equations arise during a switching period:

$$[(1-D) \cdot (V_2 - V_C) + D \cdot (V_2 - 2 \cdot V_C)] = 0 \ (t_{on}) \tag{2.7}$$

$$[(1-D) \cdot (V_C - V_1) + D \cdot (-V_1)] = 0 \ (t_{off}) \tag{2.8}$$

The relation between V_1 and V_2 is obtained by solving the system of equations (2.7) and (2.8) and it is given in (2.9):

$$V_1 = \frac{1-D}{1+D} \cdot V_2 \tag{2.9}$$

In the equations above:

V_1 – is the output voltage;
V_2 – is the input voltage;
V_C – is the voltage drop across the capacitors C_1 and C_2;
D – is the duty cycle $D = \frac{t_{on}}{T_s}$, considered for S_1.

Another form of (2.9), which highlights the relation between the duty cycle and the two voltages is:

$$D = \frac{V_2 - V_1}{V_2 + V_1} \tag{2.10}$$

The voltage drop across capacitors C_1 and C_2 related to the input voltage, respectively to the output voltage results also from (2.7) and (2.8):

$$V_C = \frac{1}{1+D} \cdot V_2 \tag{2.11}$$

$$V_C = \frac{1}{1-D} \cdot V_1 \tag{2.12}$$

The switching signal of S_1 is given opposition (1-D) for S_2 and S_3. Depending by the operation mode, step-down or step-up, the switching control can be inhibited for S_1 or for $S_{2,3}$, once at a time, and the current flow is managed by the additional antiparallel diodes of the transistors. Like it was said above, in step-down mode, the switching command for S_1 can be inhibited and only S_2 and S_3 switch with a duty cycle of 1-D. The current through the SCC is close related to the currents through the L_1 and L_2 inductors. The main waveforms of the voltages and currents through the converter components, when working as a step-down converter, are presented in fig.2.17.
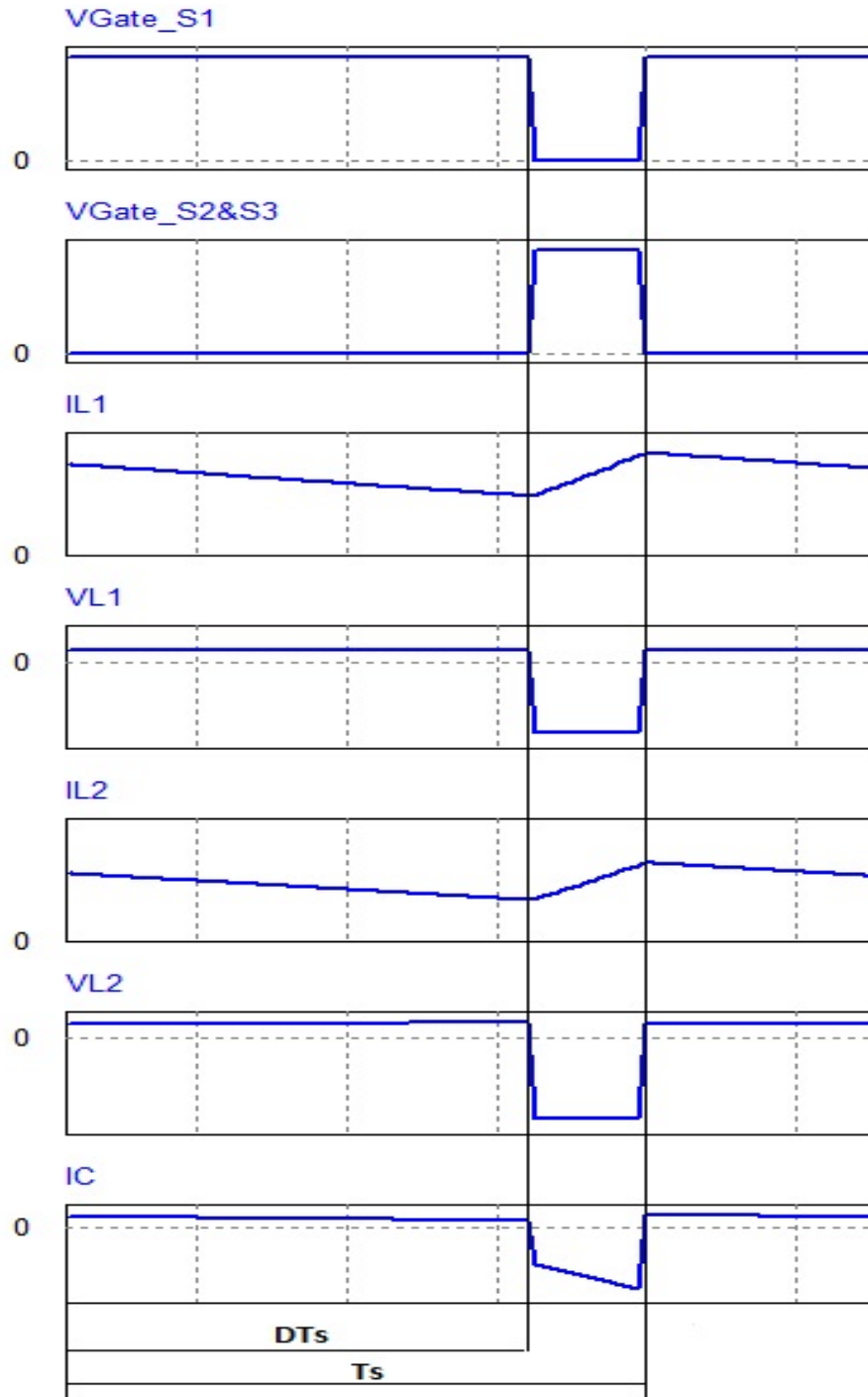
Fig.2.17. Waveforms of the main voltages and currents in Step-Down mode

The representations of the currents through L_1 and L_2, related to V_1 and V_2 voltages are shown in detail in Fig.2.18. Their mathematical forms and also the equations of the currents through the other components during t_{on} and t_{off} are presented (2.13)-(2.31)
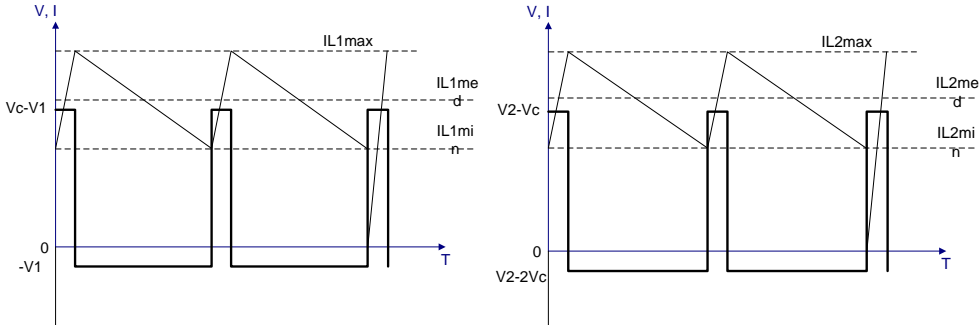
Fig.2.18. Waveforms of the currents through L_1 and L_2 Step-Down mode

The currents equations through the L_1 inductor during t_{on} are:

$$I_{L1}=I_{S1}-I_{L2} \qquad (t_{on}) \qquad\qquad (2.13)$$

$$V_1=-V_{L1} \qquad (t_{on}) \qquad\qquad (2.14)$$

$$I_{L1max}=I_{L1med}-\frac{V1 \cdot D \cdot T_s}{2 \cdot L1} \qquad\qquad (2.15)$$

$$I_{L1min}=I_{L1med+}\frac{V1 \cdot D \cdot T_s}{2 \cdot L1} \qquad\qquad (2.16)$$

The L_2 inductor and S_1 relations during t_{on} are:

$$I_{L2max}=I_{L2med-}\frac{(V2-2 \cdot Vc) \cdot D \cdot T_s}{2 \cdot L0} \qquad\qquad (2.17)$$

$$I_{L2max}=I_{L2med+}\frac{(V2-2 \cdot Vc) \cdot D \cdot T_s}{2 \cdot L0} \qquad\qquad (2.18)$$

$$I_{S1max}=I_{L1med}+I_{L2med}-\frac{V1 \cdot D \cdot T_s}{2 \cdot L1}-\frac{(V2-2 \cdot Vc) \cdot D \cdot T_s}{2 \cdot L0} \qquad\qquad (2.19)$$

$$I_{S1min}=I_{L1med}+I_{L2med}+\frac{V1 \cdot D \cdot T_s}{2 \cdot L1}+\frac{(V2-2 \cdot Vc) \cdot D \cdot T_s}{2 \cdot L0} \qquad\qquad (2.20)$$

The equations above are given during t_{on} ($D \cdot T$). During t_{off}($(1-D) \cdot T_s$), the equations can be also determined for L_1:

$$I_{L1}=2 \cdot I_{S1}-I_{L2} \qquad (t_{off}) \qquad\qquad (2.21)$$

$$V_1=V_C \qquad (t_{off}) \qquad\qquad (2.22)$$

$$I_{L1max}=I_{L1med+}\frac{(Vc-V1) \cdot (1-D) \cdot T_s}{2 \cdot L1} \qquad\qquad (2.23)$$

$$I_{L1min}= I_{L1med}-\frac{(Vc-V1)\cdot(1-D)\cdot T_s}{2\cdot L1} \qquad (2.24)$$

$$I_{L1max}=I_{L1med}+\frac{(Vc-V1)\cdot(1-D)\cdot T_s}{2\cdot L1} \qquad (2.25)$$

$$I_{L1min}= I_{L1med}-\frac{(Vc-V1)\cdot(1-D)\cdot T_s}{2\cdot L1} \qquad (2.26)$$

The currents for L_2 and the switch S_2 (which is the same with S_3) are:

$$I_{L2max}=I_{L2med}+\frac{(V2-Vc)\cdot(1-D)\cdot T_s}{2\cdot L2} \qquad (2.27)$$

$$I_{L2min}= I_{L2med}-\frac{(V2-Vc)\cdot(1-D)\cdot T_s}{2\cdot L2} \qquad (2.28)$$

$$I_{S2max}=\frac{IL1max+IL2max}{2} \qquad (2.29)$$

$$I_{S2max}=\frac{IL1med+IL2med}{2}+\frac{(Vc-V1)\cdot(1-D)\cdot T_s}{2\cdot L1}+\frac{(V2-Vc)\cdot(1-D)\cdot T_s}{2\cdot L2} \qquad (2.30)$$

$$I_{S2min}=\frac{IL1med+IL2med}{2}-\frac{(Vc-V1)\cdot(1-D)\cdot T_s}{2\cdot L1}-\frac{(V2-Vc)\cdot(1-D)\cdot T_s}{2\cdot L2} \qquad (2.31)$$

➤ **Boundary current mode analysis (BCM) of BHDC**

Discontinuous current mode (**DCM**) is by definition an operating mode of the converter when the currents through its inductors go to zero before the end of the switching period T_S. In other words, during the t_{off} interval, the current through an inductor goes to zero, before the end of the period T_S. When a converter operates this way, there arise serious problems related to its stability. In our case, during the DCM, the converter is unable to provide the required parameters. Between CCM and DCM there is a boundary conduction mode (**BCM**) when currents through the inductors go down to 0 at the end of t_{Off} and of course the end of T_S. The BCM analysis offers important details related to the behavior of the system. During this step there are established the equations and the limit values of the parameters over which the converter starts operating in DCM.

The proposed converter in step-down mode is intended to charge a battery stack. Starting from this hypothesis, the power of the converter can be considered lower than its nominal rated power when it operates this way (rechargeable batteries are usually charged with a current of about 10% of their full capacity). Thus, the DCM has to be treated more careful in order to observe the BHDC behavior at about 33% of its rated power, even if the converter is designed to operate in both directions at the rated nominal power.

Fig.2.19 shows the waveforms of the inductors currents in BCM. Their mathematical forms are also presented.
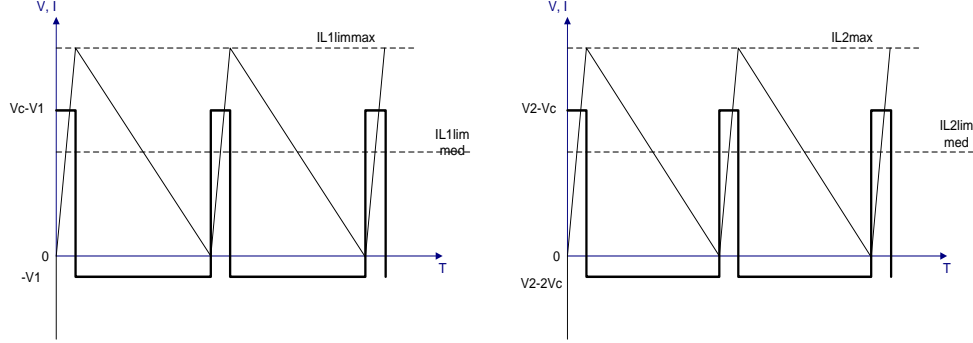
Fig.2.19 Limit current for BCM through L_1 and L_2

The equations of the currents in BCM are:

$$I_{L_{1limmax}} = \frac{V_1 \cdot D \cdot T_s}{L_1} \tag{2.32}$$

$$I_{L_{1limmed}} = \frac{I_{L_{1limmax}}}{2} = \frac{V_1 \cdot D \cdot T_s}{2 \cdot L_1} \tag{2.33}$$

$$I_{L_{2limmax}} = \frac{V_1 \cdot D \cdot T_s}{2 \cdot L_2} \tag{2.34}$$

$$I_{L_{2limmed}} = \frac{I_{L_{2limmax}}}{2} = \frac{V_1 \cdot D \cdot T_s}{2 \cdot L_2} \tag{2.35}$$

The equations above are written considering the t_{on} $(D \cdot T_s)$ period. During t_{off} $((1-D) \cdot T_s)$ the equations of the currents through the L_1 and L_2 and the $S_{2,3}$ switches are the following ones:

$$I_{L_{1limmax}} = \frac{V_2 \cdot D \cdot \frac{1-D}{1+D} \cdot T_s}{L_1} \tag{2.36}$$

$$I_{L_{1limmed}} = \frac{I_{L_{1limmax}}}{2} = \frac{V_2 \cdot D \cdot \frac{1-D}{1+D} \cdot T_s}{2 \cdot L_1} \tag{2.37}$$

$$I_{L_{2limmax}} = \frac{(V2-Vc) \cdot (1-D) \cdot T_s}{L2} \tag{2.38}$$

$$I_{L_{2limmed}} = \frac{(V2-Vc) \cdot (1-D) \cdot T_s}{2 \cdot L2} \tag{2.39}$$

$$I_{S2limmax} = \frac{(Vc-V1) \cdot (1-D) \cdot T_s}{2 \cdot L1} + \frac{(V2-Vc) \cdot (1-D) \cdot T_s}{2 \cdot L2} \tag{2.40}$$

$$I_{S2limmed} = -\frac{(Vc-V1) \cdot (1-D) \cdot T_s}{4 \cdot L1} - \frac{(V2-Vc) \cdot (1-D) \cdot T_s}{4 \cdot L2} \tag{2.41}$$

Taking into consideration the BCM equations, the minimum values of the duty cycle can be extracted in order to maintain the system in CCM:

$$I_{L_{1limmed}} + I_{L_{2limmed}} = \frac{V_2 \cdot D \cdot \frac{1-D}{1+D} \cdot T_s}{2 \cdot L_1} + \frac{(V2-Vc) \cdot (1-D) \cdot T_s}{2 \cdot L2} \tag{2.42}$$

Since $V_C = \frac{1}{1+D} V_2$, we can conclude that if:

$$D \leq 2 \cdot \frac{\text{IL1limmed} + \text{IL2limmed}}{V_2 \cdot \frac{1-D}{1+D} \cdot \text{Ts}} \cdot \frac{L1 + L2}{L1 \cdot L2} \ , \tag{2.43}$$

we can consider the converter working in CCM, else, if:

$$D > 2 \cdot \frac{\text{IL1limmed} + \text{IL2limmed}}{V_2 \cdot \frac{1-D}{1+D} \cdot \text{Ts}} \cdot \frac{L1 + L2}{L1 \cdot L2} \tag{2.44}$$

The converter starts operating in DCM. Other forms of the duty cycle can be obtained if we write them considering $V_1 = \frac{1-D}{1+D} \cdot V_2$. This way (2.43) becomes:

$$D \leq 2 \cdot \frac{\text{IL1med} + \text{IL2med}}{V1 \cdot \text{Ts}} \cdot \frac{L1 + L2}{L1 \cdot L2} \tag{2.45}$$

2.2.2. Analytical Study for step-up operation

> **Continuous current mode analysis (CCM) of BHDC**

The equivalent circuits of BHDC switching states operating in step-up mode, are presented in fig.2.20 a) and b).

a)

b)
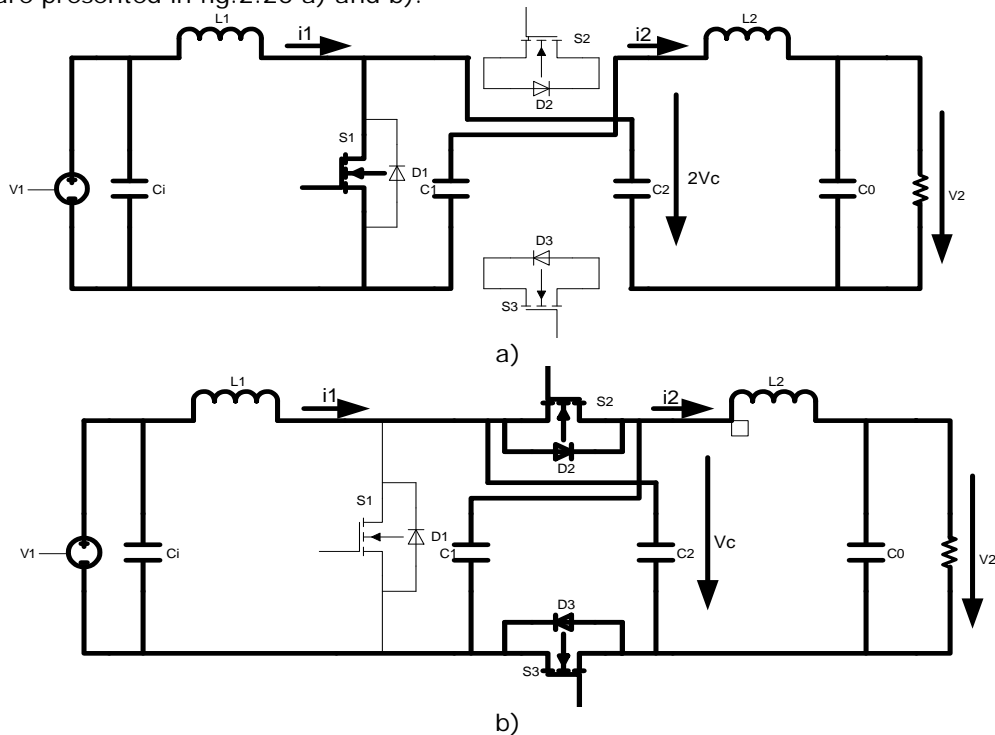
Fig.2.20. Equivalent circuit in step-up mode: a)t_{on}, b) t_{off};

If the converter is used in step-up mode the current flows from the battery stack to the microgrid high voltage DC bus. The same command signal is used to realize now a boost stage by switching the S_1 transistor. In the same time the two capacitors of the SCC are charged in parallel during t_{off} (for S_1), while during t_{on} the capacitors are discharged in series. The two transistors S_2 and S_3 can be switched in opposite to S1 to improve the converter efficiency or their command can be inhibited.

The analytical study of the BHDC operating in step-up mode begins considering the input and output voltages constant (C_i and C_0 are sufficiently large to assume a null voltage ripple), in order to obtain the equations of the circuit during a switching period:

$$[D \cdot V_1 + (1 - D) \cdot (V_1 - V_C)] = 0 \tag{2.46}$$

$$[D \cdot (2 \cdot V_C - V_2) + (1 - D) \cdot (V_C - V_2)] = 0 \tag{2.47}$$

Equalizing (2.46) with (2.47), the relation between the two voltages V1 and V2 is obtained in (2.48):

$$V_2 = \frac{1+D}{1-D} \cdot V_1 \tag{2.48}$$

In the equation above:

V_1 – is the input voltage;
V_2 – is the output voltage;
V_C – is the voltage drop across the capacitors C_1 and C_2;
 D – is the duty cycle $D = \frac{t_{on}}{T_S}$

The voltage through the capacitor cell and the duty cycle can be extracted from (2.46) and (2.47):

$$V_C = \frac{-V_1}{D-1} = \frac{V_1}{1-D} \tag{2.49}$$

$$D = \frac{V_2 - V_1}{V_2 + V_1} \tag{2.50}$$

The equation of duty cycle highlights the fact that it has the same value no matter in which operating mode the converter works. This is an advantage related to the switching command strategy, which simplifies more the BHDC control. The main waveforms of the voltages and currents through the circuit main components during t_{on} and t_{off}, with the BHDC working as a step-up converter, are presented in fig.2.21.
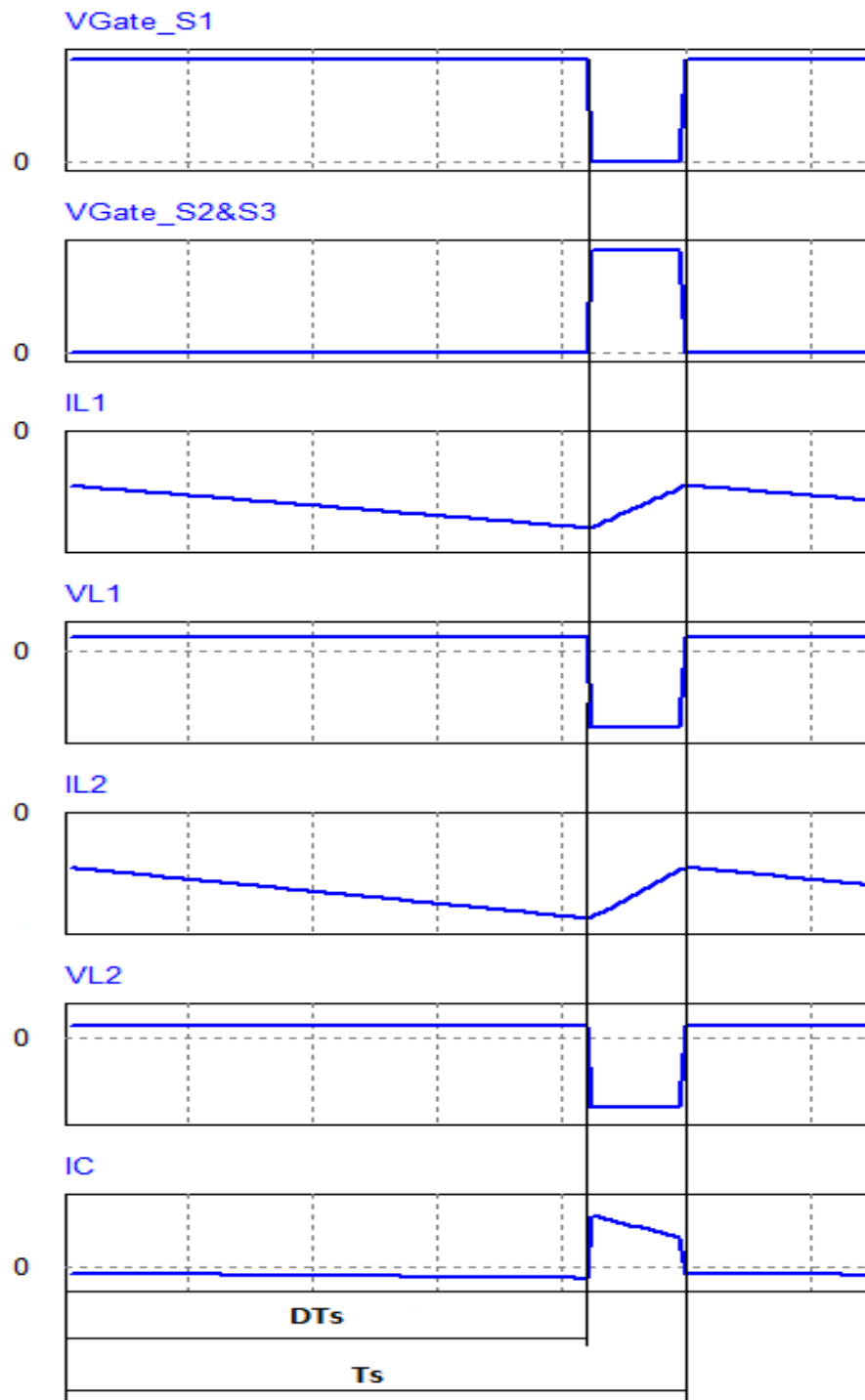
Fig.2.21. Waveforms of the main voltages and currents in step-up mode

The equations of the currents for this case are also studied for V_1, respectively V_2 constant.
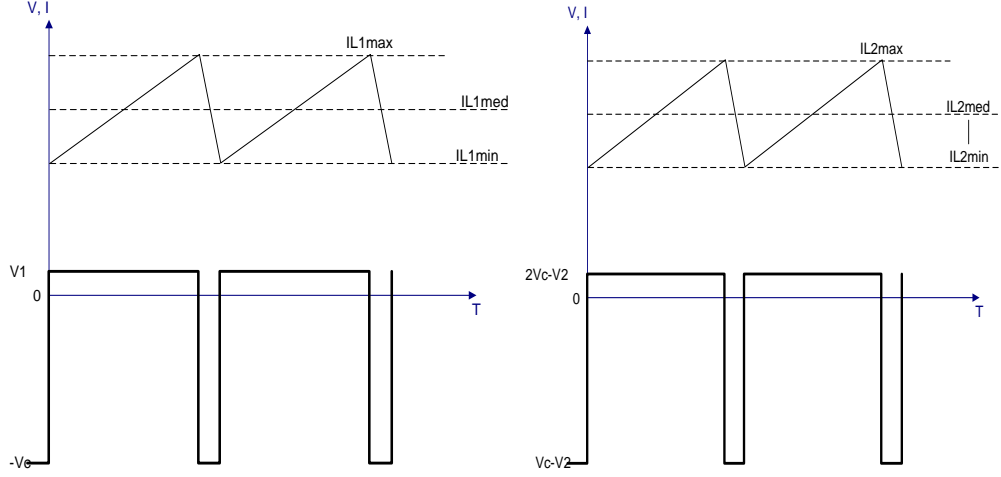
Fig.2.22. Waveforms of the currents through L_1 and L_2 Step-Up mode

The equations of the currents through L_1 inductor during t_{on} are:

$$I_{L1max}=I_{L1med}+\frac{V1 \cdot D \cdot Ts}{2 \cdot L1} \tag{2.51}$$

$$I_{L1min}=I_{L1med}-\frac{V1 \cdot D \cdot Ts}{2 \cdot L1} \tag{2.52}$$

The equations for the L_2 inductor and the S_1 switch are:

$$I_{L2max}=I_{L2med}+\frac{(2 \cdot Vc-V2) \cdot D \cdot Ts}{2 \cdot L0} \tag{2.53}$$

$$I_{L2max}=I_{L2med}-\frac{(2 \cdot Vc-V2) \cdot D \cdot Ts}{2 \cdot L0} \tag{2.54}$$

$$I_{S1max}=I_{L1med}+I_{L2med}+\frac{V1 \cdot D \cdot Ts}{2 \cdot L1}-\frac{(2 \cdot Vc-V2) \cdot D \cdot Ts}{2 \cdot L0} \tag{2.55}$$

$$I_{S1min}=I_{L1med}+I_{L2med}-\frac{V1 \cdot D \cdot Ts}{2 \cdot L1}+\frac{(2 \cdot Vc-V2) \cdot D \cdot Ts}{2 \cdot L0} \tag{2.56}$$

Based on the same principle, the equations of the currents are written for the t_{off} (T_s-t_{on}) period.

$$I_{L1max}=I_{L1med}+\frac{(V1-Vc) \cdot (1-D) \cdot T_s}{2 \cdot L1} \tag{2.57}$$

$$I_{L1min}=I_{L1med}-\frac{(V1-Vc) \cdot (1-D) \cdot T_s}{2 \cdot L1} \tag{2.58}$$

The currents for L_2 and the switch S_2 (or S_3) during t_{off} are:

$$I_{L2max}=I_{L2med}+\frac{(Vc-V2) \cdot (1-D) \cdot T_s}{2 \cdot L2} \tag{2.59}$$

$$I_{L2min}=I_{L2med}-\frac{(Vc-V2) \cdot (1-D) \cdot T_s}{2 \cdot L2} \tag{2.60}$$

$$I_{S2max} = \frac{IL1max + IL2max}{2} \tag{2.61}$$

$$I_{S2max} = \frac{IL1med + IL2med}{2} - \frac{(V1-Vc)\cdot(1-D)\cdot T_s}{2\cdot L1} - \frac{(Vc-V2)\cdot(1-D)\cdot T_s}{2\cdot L2} \tag{2.62}$$

$$I_{S2min} = \frac{IL1med + IL2med}{2} + \frac{(V1-Vc)\cdot(1-D)\cdot T_s}{2\cdot L1} + \frac{(Vc-V2)\cdot(1-D)\cdot T_s}{2\cdot L2} \tag{2.63}$$

➢ **Boundary current mode analysis (BCM) of BHDC**

Following the same principle, the determination of the limit current establishes the conditions when the converter starts operating in **DCM.** In Fig.2.23 are represented the limit currents through the inductors L_1 and L_2.
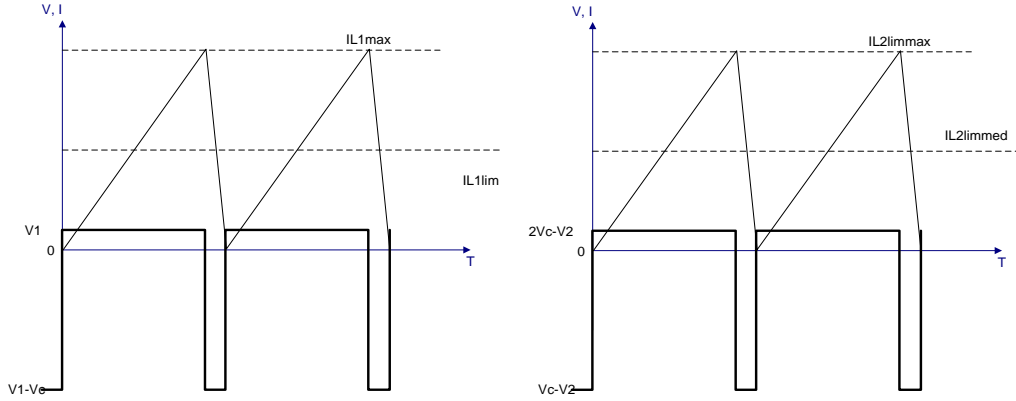
Fig.2.23. Limit currents for BCM through L_1 and L_2 in step-up mode

The limit currents are calculated considering the voltage V_1 constant in the equations bellow:

$$I_{L_{1max}} = \frac{V_1 \cdot D \cdot T_S}{L_1} \tag{2.64}$$

$$I_{L_{1lim}} = \frac{I_{L_{1max}}}{2} = \frac{V_1 \cdot D \cdot T_S}{2 \cdot L_1} \tag{2.65}$$

$$I_{L_{2max}} = \frac{D \cdot T_S \cdot (2 \cdot \frac{V_1}{1-D} - \frac{V_1 \cdot (1+D)}{1-D})}{L_2} \tag{2.66}$$

$$I_{L_{2lim}} = \frac{I_{L_{2max}}}{2} = \frac{V_1 \cdot D \cdot T_S}{2 \cdot L_2} \tag{2.67}$$

The equation that governs the operation of the converter in step-up mode and shows the relation between L_1 and L_1 inductors, the currents through them and the duty cycle is the following one:

$$I_{L_{1med}} + I_{L_{2med}} = \frac{V_1 \cdot D \cdot T_S}{L_1} + \frac{V_1 \cdot D \cdot T_S}{2 \cdot L_2} \tag{2.68}$$

This way the BCM equations for the duty cycle during t_{on} and t_{off} result:

$$D = 4 \cdot \frac{L1 \cdot L2}{L1+L2} \cdot \frac{I_{L_{1med}}}{V_1 \cdot D \cdot (1-D) \cdot T_s} \tag{2.69}$$

$$1 - D = 4 \cdot \frac{L1 \cdot L2}{L1+L2} \cdot \frac{(1-D) \cdot I_{L_{1med}}}{V_1 \cdot D \cdot (1+D) \cdot T_s} \tag{2.70}$$

The other components, which operation conditions lead to DCM, are the transistors S_2 and S_3 and their complementary diodes. During step-up mode, the currents that flow through them are close related to the currents through the inductors and duty cycle:

$$I_{S2min}=I_{S3min}=I_{Dmin}=I_{L1med}+I_{L2med}-\frac{(V1-Vc)\cdot(1-D)\cdot Ts}{2 \cdot L1}+\frac{(Vc-V2)\cdot(1-D)\cdot Ts}{2*L0} \tag{2.71}$$

The same equations, but related to V_1 and V_2 are:

$$I_{Dmin}=I_{L1med}+I_{L2med}-\frac{L1+L2}{L1 \cdot L2} \cdot \frac{V1 \cdot D \cdot Ts}{2} \tag{2.72}$$

$$I_{Dmin}=I_{L1med}+I_{L2med}-\frac{L1+L2}{L1 \cdot L2} \cdot \frac{V2 \cdot (1-D) \cdot D \cdot Ts}{2(1+D)} \tag{2.73}$$

Since the only variable parameter that appears in all the equations is the duty cycle, its value decides the transition of the converter in DCM.

If:
$$D \leq 2 \cdot \frac{IL1med+IL2med}{V1 \cdot Ts} \cdot \frac{L1+L2}{L1 \cdot L2} \tag{2.74}$$

the converter is working in CCM, else, if:

$$D > 2 \cdot \frac{IL1med+IL2med}{V1 \cdot Ts} \cdot \frac{L1+L2}{L1 \cdot L2} \tag{2.75}$$

it starts operating in DCM. The currents through the inductors are going to look like the ones in the fig.2.24.
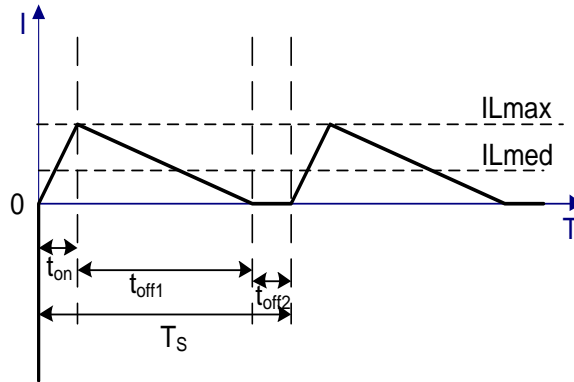
Fig.2.24. Currents waveforms for DCM through L_1 and L_2

where $T_s = t_{on} + t_{off1} + t_{off2}$

When operates as a step-up converter, a special treatment is required for the inductors dimensioning, especially because the values of the currents in the proposed application are higher and the stress over the circuit is significant.

2.3. Stability analysis

The robustness of power converters is given by their stability in various conditions, while the parameters of the components remain the same. The stability analysis shows the capability of the converter to operate properly beyond the nominal functioning regime. The stability analysis of the BHDC was realized using state space average models by defining the discrete time model and the operating phenomena of the circuit. The results are verified with the PWM Switch Model method. In the end, the results are to obtain compensation circuits which are applied and tested on the experimental prototype.

2.3.1. State-Space Averaging method

State-Space Averaging (**SSA**) was introduced in the literature about 40 years ago by Dr. Slobodan Cuk and documented since then. It is based on the mathematical analysis of the power converters highlighting the state variables in the circuits during the switching periods. The state-variables are associated usually with passive components like capacitors and inductors, elements that can store electrical energy in one way or another. This technique allows the linearization of a system around an operating point and implies the passing over the switching events with their corresponding ripples, considering the system output signal as a continuous one, with small variations. Neglecting the ripple, it offers the possibility to analyze the system equations as averaged and continuous functions. Thanks to SSA, any particular structure behavior can be described by its averaged equations. After the linearization around an operating point, these equations lead to the averaged small-signal model. This new model is useful to provide information regarding the AC response of the proposed topologies of converters and more than that, their stability can be analyzed and improved once the closed loop control and the compensation are designed.

The result of the small-signal response is the drawing of the Bode or Nyquist plots in snapshots, giving a stability evaluation of the studied system. Information about the impedance variations and the other components behavior during various operating conditions are also obtained. Another advantage of SSA is that the entire circuit is analyzed with no switching elements. This makes the simulation to be faster and permits the visualizations of long transient effects, checking if the output overshoot is close to the desired specifications. The disadvantage of this fact is the difficulty in observing the effects of parasitic characteristics like diodes forward voltage drops, or switching losses of semiconductors.

For the proposed converter, the stability analysis using SSA method is realized by reducing the circuit to each inductor and capacitor associated with the complementary power-poles. The power-poles represent bi-positional portions of the circuit and they refer mostly to the semiconductors during their on-off states and the related state variables that change their condition during switching.

The SSA method is presented in detail step by step highlighting the way it was applied on the stability analysis of the proposed converter. The corresponding models are presented during t_{on} and t_{off} for the converter operating as a step-down and a step-up converter connected to a voltage source and supplying a resistive load. The last averaged model is presented for the case when the converter is connected to two voltage sources on both sides.

2.3.1.1. SSA for step-down converter with resistive load

The first step of SSA method is to determine the state variables of our converter. In order to simplify the computation the circuit is analyzed exactly how it works during each operating mode, meaning that some of the existing switches are reduced to diodes because the complementary transistors in operation only double them. This fact is easier to understand after the presentation of the equivalent circuits, which highlights the state variables (fig.2.25):
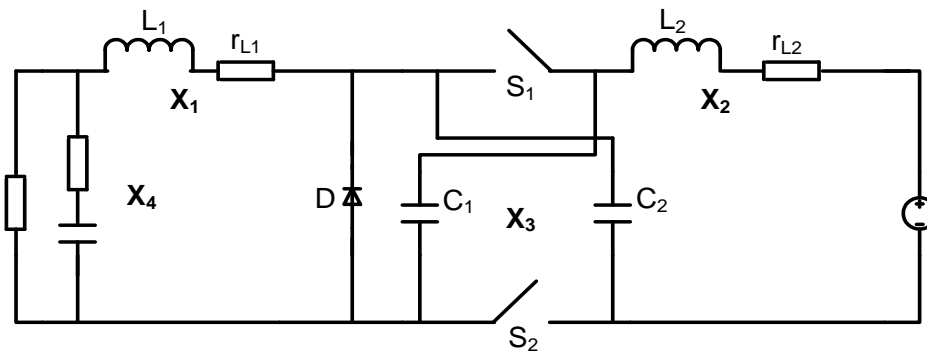
Fig.2.25. Highlighted State Variables for BHDC in step-down mode

The state variables x_1 and x_2 are the currents through L_1 and L_2 inductors. x_3 and x_4 are the voltages on the switching capacitor cell respectively the "output" capacitor. The simplified circuit is also shown separately during t_{on} and t_{off} in order to obtain the general state and output equations of the system, which have the following forms:

$$\dot{x} = Ax(t) + Bu(t) \tag{2.76}$$

$$y(t) = Cx(t) + Du(t) \tag{2.77}$$

In (2.76) and (2.77), $x(t)$ represents the state vector and contains all the states variables. In the same manner, $y(t)$ is called the output vector and it offers a way to obtain external waveforms as linear combinations of the state variables and input vectors. In other words:

$\dot{x} = \frac{dx}{dt}$ -time derivative of the state variable x;
A -state coefficient matrix;
u -source coefficient matrix;

B -source coefficient matrix;
C -output coefficient matrix;
D -output source coefficient matrix.

In fig.2.26 the equivalent circuit of BHDC is presented, highlighting the state variables during t_{on}, while operating in step-down mode. The equivalent series resistances for inductors and capacitors are added to the system, but only where their values affect the system behavior.
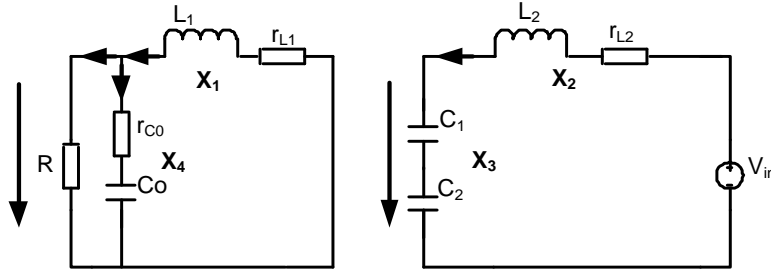
Fig.2.26. Equivalent circuit of BHDC during t_{on}

In this particular case, the input voltage source is V_{in} and it appears noted u_1 in the source coefficient vector. Since we do not have other sources in our circuit, the other elements are considered equal with zero. Considering the four state variables, a second order system of the proposed circuit is obtained from the characteristic equations of the circuit during all states of operation.

The simplified state equations neglecting dispensable terms during t_{on} derive from the equivalent circuits and are the following ones:

$$\dot{x}_1 = -\frac{r_{L1}+r_{C0}}{L_1}\cdot x_1 + 0\cdot x_2 + \frac{1}{L_1}\cdot x_3 - \frac{1}{L_1}\cdot x_4 \tag{2.78}$$

$$\dot{x}_2 = 0\cdot x_1 - \frac{r_{L2}}{L_2}\cdot x_2 - \frac{2}{L_2}\cdot x_3 + 0\cdot x_4 + \frac{1}{L_2}\cdot V_{in} \tag{2.79}$$

$$\dot{x}_3 = 0\cdot x_1 + \frac{1}{C_1}\cdot x_2 + 0\cdot x_3 + 0\cdot x_4 \tag{2.80}$$

$$\dot{x}_4 = \frac{1}{C_0}\cdot x_1 + 0\cdot x_2 + 0\cdot x_3 - \frac{1}{R_0\cdot C_0}\cdot x_4 \tag{2.81}$$

Using (2.78)-(2.81) the state and output equations matrix is obtained during t_{on}:

$$\begin{bmatrix} \dot{x}_1 \\ \dot{x}_2 \\ \dot{x}_3 \\ \dot{x}_4 \end{bmatrix} = \begin{bmatrix} -\frac{r_{L1}+r_{C0}}{L_1} & 0 & \frac{1}{L_1} & -\frac{1}{L_1} \\ 0 & -\frac{r_{L2}}{L_2} & -\frac{2}{L_2} & 0 \\ 0 & \frac{1}{C_1} & 0 & 0 \\ \frac{1}{C_0} & 0 & 0 & -\frac{1}{R_0\cdot C_0} \end{bmatrix} \cdot \begin{bmatrix} x_1 \\ x_2 \\ x_3 \\ x_4 \end{bmatrix} + \begin{bmatrix} 0 \\ \frac{1}{L_2} \\ 0 \\ 0 \end{bmatrix} \cdot V_{in} \tag{2.82}$$

The system during the on state is given by the equations $\dot{x}_1 = A_1 x + B_1 V_{in}$ and $v_{out} = C_1 x$. From (2.82) the A_1 and B_1 matrices are determined:

$$A_1 = \begin{bmatrix} -\frac{r_{L1}+r_{C0}}{L_1} & 0 & \frac{1}{L_1} & -\frac{1}{L_1} \\ 0 & -\frac{r_{L2}}{L_2} & -\frac{2}{L_2} & 0 \\ 0 & \frac{1}{C_1} & 0 & 0 \\ \frac{1}{C_0} & 0 & 0 & -\frac{1}{R_0 \cdot C_0} \end{bmatrix}; \quad B_1 = \begin{bmatrix} 0 \\ \frac{1}{L_2} \\ 0 \\ 0 \end{bmatrix}; \tag{2.83}$$

C_1 results in the following:

$$V_{out} = V_R = r_{L1} \cdot x_1 + 0 \cdot x_2 + 0 \cdot x_3 - 1 \cdot x_4; \text{ so:} \tag{2.84}$$

$$C_1 = [r_{L1} \quad 0 \quad 0 \quad -1] \tag{2.85}$$

The analysis of the state equations during t_{off} is obtained considering the following equivalent circuit during t_{off} following the same principle presented above:
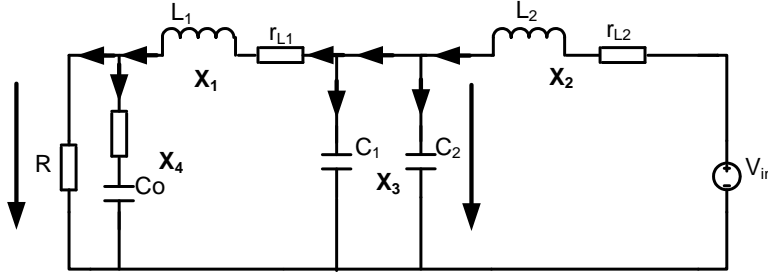
Fig.2.27. Equivalent circuit of BHDC during t_{off}

The state equations during t_{off} derive from the equivalent circuits and are the following ones:

$$\dot{x}_1 = -\frac{r_{L1}+r_{C0}}{L_1} \cdot x_1 + 0 \cdot x_2 + \frac{1}{L_1} \cdot x_3 - \frac{1}{L_1} \cdot x_4 \tag{2.86}$$

$$\dot{x}_2 = 0 \cdot x_1 - \frac{r_{L2}}{L_2} \cdot x_2 - \frac{1}{L_2} \cdot x_3 + 0 \cdot x_4 + \frac{1}{L_2} \cdot V_{in} \tag{2.87}$$

$$\dot{x}_3 = -\frac{1}{2 \cdot C_1} \cdot x_1 + \frac{1}{2 \cdot C_1} \cdot x_2 + 0 \cdot x_3 + 0 \cdot x_4 \tag{2.88}$$

$$\dot{x}_4 = \frac{1}{C_0} \cdot x_1 + 0 \cdot x_2 + 0 \cdot x_3 - \frac{1}{R_0 \cdot C_0} \cdot x_4 \tag{2.89}$$

Using (2.86)-(2.89) the state and output equations matrix is obtained during t_{off}:

$$\begin{bmatrix} \dot{x}_1 \\ \dot{x}_2 \\ \dot{x}_3 \\ \dot{x}_4 \end{bmatrix} = \begin{bmatrix} -\frac{r_{L1}+r_{C0}}{L_1} & 0 & \frac{1}{L_1} & -\frac{1}{L_1} \\ 0 & -\frac{r_{L2}}{L_2} & -\frac{1}{L_2} & 0 \\ -\frac{1}{2 \cdot C_1} & \frac{1}{2 \cdot C_1} & 0 & 0 \\ \frac{1}{C_0} & 0 & 0 & -\frac{1}{R_0 \cdot C_0} \end{bmatrix} \cdot \begin{bmatrix} x_1 \\ x_2 \\ x_3 \\ x_4 \end{bmatrix} + \begin{bmatrix} 0 \\ \frac{1}{L_2} \\ 0 \\ 0 \end{bmatrix} \cdot V_{in}; \tag{2.90}$$

Using (2.90), the A_2 and B_2 matrices are obtained corresponding to t_{off} this time. C_2 derives from (2.92).

$$A_2 = \begin{bmatrix} -\frac{r_{L1}+r_{C0}}{L_1} & 0 & \frac{1}{L_1} & -\frac{1}{L_1} \\ 0 & -\frac{r_{L2}}{L_2} & -\frac{1}{L_2} & 0 \\ -\frac{1}{2 \cdot C_1} & \frac{1}{2 \cdot C_1} & 0 & 0 \\ \frac{1}{C_0} & 0 & 0 & -\frac{1}{R_0 \cdot C_0} \end{bmatrix} ; \qquad B_2 = \begin{bmatrix} 0 \\ \frac{1}{L_2} \\ 0 \\ 0 \end{bmatrix} ; \qquad (2.91)$$

$$V_{out} = V_R = r_{L1} \cdot x_1 + 0 \cdot x_2 + 0 \cdot x_3 - 1 \cdot x_4 ; \qquad (2.92)$$

$$C_2 = C_1 = [r_{L1} \quad 0 \quad 0 \quad -1] \qquad (2.93)$$

The A_1, A_2, B_1, B_2, C_1 and C_2 final matrices, are weighted by the duty cycle D for t_{on} state and by (1-D) during t_{off} state, and the averaged equivalent system equations is obtained over one switching period. Because these equations are linear, the Laplace transfer functions of the system can be obtained and we can admit:

$$\dot{x} = Ax + BV_{in}; \qquad (2.94)$$

$$v_{out} = C\mathbf{x}; \qquad (2.95)$$

Where:

$$A = A_1 \cdot D + A_2 \cdot (1-D) \qquad (2.96)$$

$$B = B_1 \cdot D + B_2 \cdot (1-D) \qquad (2.97)$$

$$C = C_1 \cdot D + C_2 \cdot (1-D) \qquad (2.98)$$

The steady-state transfer function X_0 is obtained for $\dot{x} = 0$:

$$X_O = (-A^{-1}B)V_{in} \qquad (2.99)$$

For small variations $\tilde{d}$ of the duty cycle D, considering V_{in} constant, the averaged equivalent system for small variations over a switching period is:

$$\dot{\tilde{x}} = A\tilde{x} + \left[(A_1 - A_2)X_0 + (B_1 - B_2)V_{in} \right]\tilde{d} \qquad (2.100)$$

$$\tilde{v}_{out} = C\tilde{x} + \left[(C_1 - C_2)X_0 \right]\tilde{d} \qquad (2.101)$$

where $\tilde{x}$ and $\tilde{v}_{out}$ are the small variations of the state and respectively the output variables. The simplified state-space model of the inverter is obtained using the Matlab tools by introducing the matrices A_1, A_2, B_1, B_2, C_1 and C_2 and solving the equations (2.100) and (2.101) resulting the small signal transfer function of the system $\tilde{v}_{out}(s)/\tilde{d}(s)$.

The presented average model is practically used for steady state and for stability analysis using Bode or Nyquist diagrams. Since all its elements are determined, they are introduced in a m-function using Matlab. Because the symbolic form of the transfer functions raised many difficulties, the diagrams representing

the stability of the system were obtained using the real parameters of the proposed converter prototype. They are all listed in Table 2.1:

Table 2.1. BHDC prototype data (step-down)

Component	Value	Units	Specifications
V_{in}	400	V	Input voltage in step-down mode
L_2	1470	uH	L_2 inductance
r_{L2}	158	mΩ	ESR of L_2
$C_1 = C_2$	705	uF	Capacitance of the switching cap cell
L_1	200	uH	L_1 inductance
r_{L1}	4.5	mΩ	ESR of L_1
C_0	470	uF	Output filter capacitor
r_{C0}	75	mΩ	ESR of C_0
R	1	Ω	Resistive load
D	0.78	-	Duty Cycle

The Bode plots of the transfer functions are used for the system stability analysis. Each of the obtained plots corresponds to one of the four state variables small-signal transfer function and they determine the stability of the BHDC. Using the converter prototype data the following transfer function results:

$$\frac{\tilde{x}_1}{\tilde{d}} = \frac{1.031 \cdot 10^8 s^2 + 1.11 \cdot 10^{11} s - 2.305 \cdot 10^{14}}{s^4 + 2610 s^3 + 1.401 \cdot 10^7 s^2 + 6.799 \cdot 10^9 s + 1.766 \cdot 10^{13}} \qquad (2.102)$$

$$\frac{\tilde{x}_2}{\tilde{d}} = \frac{-1.892 \cdot 10^4 s^3 - 7.23 \cdot 10^7 s^2 - 2.935 \cdot 10^{11} s - 3.168 \cdot 10^{14}}{s^4 + 2610 s^3 + 1.401 \cdot 10^7 s^2 + 6.799 \cdot 10^9 s + 1.766 \cdot 10^{13}} \qquad (2.103)$$

$$\frac{\tilde{x}_3}{\tilde{d}} = \frac{2.061 \cdot 10^4 s^3 + 2.99 \cdot 10^7 s^2 + 1.815 \cdot 10^{11} s - 2.478 \cdot 10^{14}}{s^4 + 2610 s^3 + 1.401 \cdot 10^7 s^2 + 6.799 \cdot 10^9 s + 1.766 \cdot 10^{13}} \qquad (2.104)$$

$$\frac{\tilde{x}_4}{\tilde{d}} = \frac{-1419 s^3 - 5.422 \cdot 10^6 s^2 + 1.973 \cdot 10^{11} s - 2.54 \cdot 10^{14}}{s^4 + 2610 s^3 + 1.401 \cdot 10^7 s^2 + 6.799 \cdot 10^9 s + 1.766 \cdot 10^{13}} \qquad (2.105)$$

The system poles are $P_{1,2}$=-1164.7±3242.8i and $P_{3,4}$=-140.4±1211.5i. For each transfer function corresponding to a state variable, the system has 2 or 3 zeros. Fig.2.28 shows that the transfer function corresponding to $\tilde{x}_1/\tilde{d}$ is stable with a low oscillating behavior and a phase reserve of 90 degrees at the cutting frequency of ~3.5 kHz. The zeros corresponding to this transfer function are Z_1=-2127,7 and Z_2=1051. In fig.2.29 is shown the Bode plot corresponding to $\tilde{x}_2/\tilde{d}$. It has also a low oscillating behavior and a lack of phase reserve of at the cutting frequency of ~2 kHz. The transfer function has three zeros, $Z_{1,2}$=-1221.8±3264.5i and Z_3=-1378.6. These first two Bode plots indicate a stable operation for the inductor L_1 and an unstable operation for L_2.
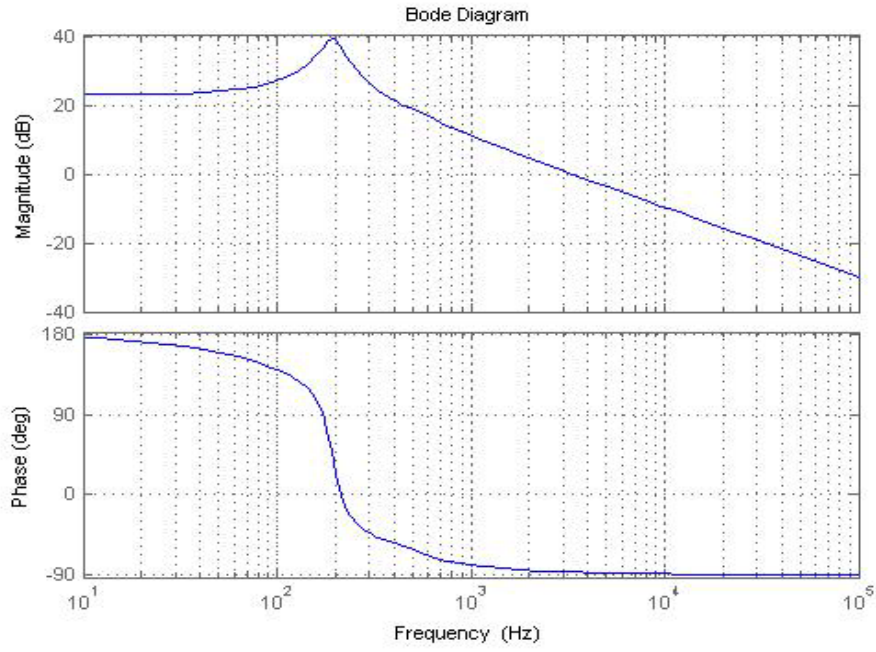
Fig.2.28. Bode plot for $\dfrac{\widetilde{x}_1}{\widetilde{d}}$ small signal transfer function
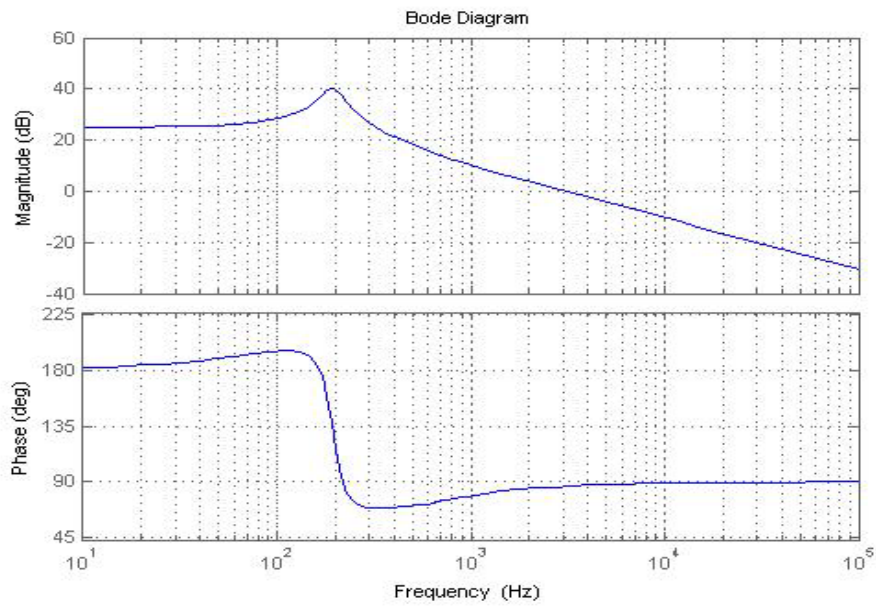
Fig.2.29. Bode plot for $\dfrac{\widetilde{x}_2}{\widetilde{d}}$ small signal transfer function

The Bode plot from fig.2.30 shows that the SCC operation is unstable. The cutting frequency is at ~1kHz but the small signal transfer function ac response does not have any phase reserve. The transfer function has three zeros, $Z_{1,2}$=-1251.3±3141.7i and Z_3=1051. Since the behavior of the SCC does not affect the output voltage and the currents through the "output" inductor L_1 can be controlled, the system stability is depends by the behavior of the output capacitor corresponding to x_4 state variable.
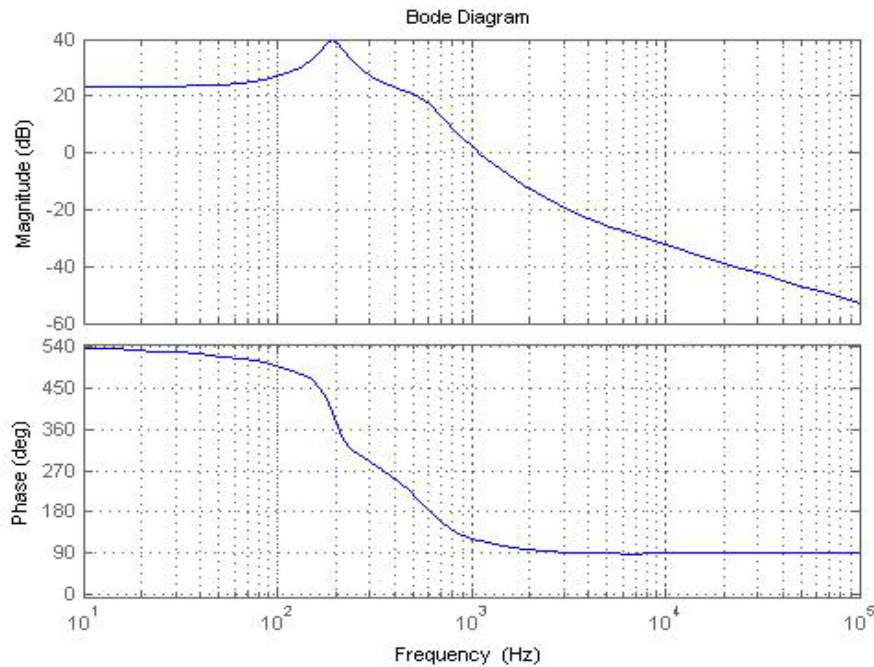
Fig.2.30. Bode plot for $\dfrac{\tilde{x}_3}{\tilde{d}}$ small signal transfer function

In fig.2.31 is presented the frequency response of the small-signal transfer function corresponding to the voltage on the output filter capacitor. The amplitude value shows a relative low oscillating response, but it does not raise any problems. The phase reserve is approximatively 25 degrees at a cutting frequency of ~1.7kHz. The transfer function (2.105) has three zeros, Z_1=-14368, Z_2=9188 and Z_3=1357. Since this ac response represents is related to the output of the system, we can conclude that the stability of the converter operating in step-down mode is confirmed.

As presented above not all the state variables small signal transfer functions have to be stable. The stability of a system is reflected mostly by the stable behavior of the state variables used by the control of the circuit and the ones that directly affects the system output.
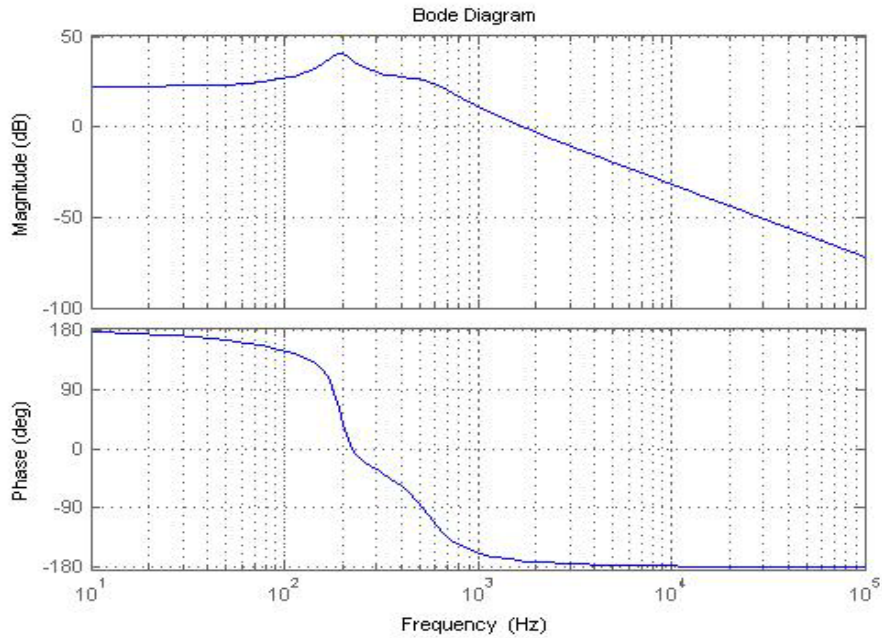
Fig.2.31. Bode plot for $\dfrac{\tilde{x}_4}{\tilde{d}}$ small signal transfer function

2.3.1.2. SSA for step-up converter with resistive load

In this subchapter, the stability of the system is analyzed considering the converter operating in step-up mode. Except the current sense, the differences between this circuit and the previous one is the input voltage source, which in this case is a 50 V DC one and the output filter capacitor which is placed in the opposite part just near the new load resistor. The new equivalent circuit is represented in fig.2.32:
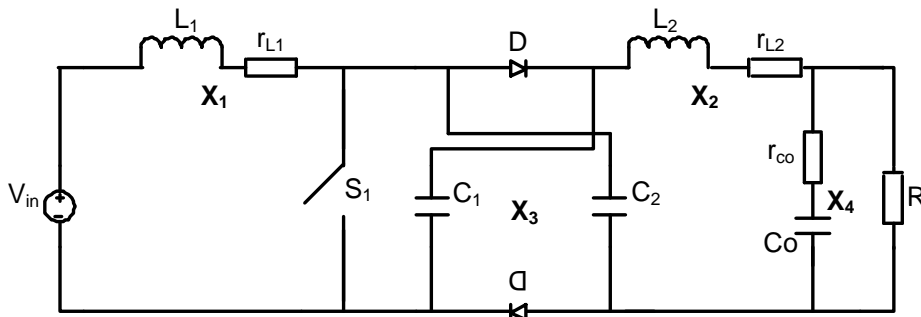
Fig.2.32. Highlighted State Variables for BHDC in step-up mode

Following the same procedure, the A_1, A_2, B_1, B_2, C_1 and C_2 matrices have to be obtained. The new equivalent circuits for step-up mode, for each switching time are presented in fig.2.33:
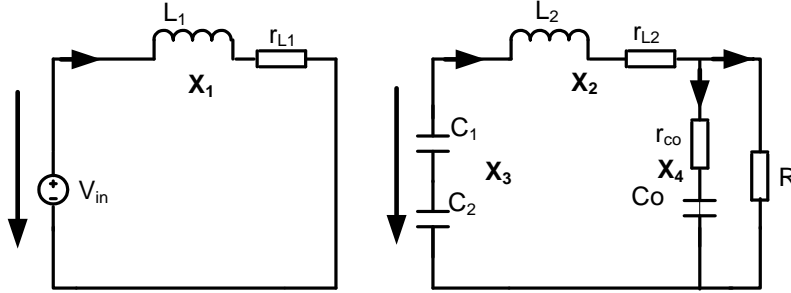
Fig.2.33. Equivalent circuit of BHDC during t_{on}

Considering the circuits from fig. 2.33 the following state equations results:

$$\dot{x}_1 = -\frac{r_{L1}}{L_1} \cdot x_1 + 0 \cdot x_2 + 0 \cdot x_3 + 0 \cdot x_4 + \frac{1}{L_1} \cdot V_{in} \tag{2.106}$$

$$\dot{x}_2 = 0 \cdot x_1 - \frac{r_{C0}+r_{L2}}{L_2} \cdot x_2 - \frac{2}{L_2} \cdot x_3 - \frac{1}{L_2} \cdot x_4 \tag{2.107}$$

$$\dot{x}_3 = 0 \cdot x_1 - \frac{1}{C_1} \cdot x_2 + 0 \cdot x_3 + 0 \cdot x_4 \tag{2.108}$$

$$\dot{x}_4 = 0 \cdot x_1 + \frac{1}{C_0} \cdot x_2 + 0 \cdot x_3 - \frac{1}{R_0 \cdot C_0} \cdot x_4 \tag{2.109}$$

Using (2.106)-(2.109) the state and output equations matrix is obtained during t_{on}:

$$\begin{bmatrix} \dot{x}_1 \\ \dot{x}_2 \\ \dot{x}_3 \\ \dot{x}_4 \end{bmatrix} = \begin{bmatrix} -\frac{r_{L1}}{L_1} & 0 & 0 & 0 \\ 0 & -\frac{r_{C0}+r_{L2}}{L_2} & -\frac{2}{L_2} & -\frac{1}{L_2} \\ 0 & -\frac{1}{C_1} & 0 & 0 \\ 0 & \frac{1}{C_0} & 0 & -\frac{1}{R_0 \cdot C_0} \end{bmatrix} \cdot \begin{bmatrix} x_1 \\ x_2 \\ x_3 \\ x_4 \end{bmatrix} + \begin{bmatrix} \frac{1}{L_1} \\ 0 \\ 0 \\ 0 \end{bmatrix} \cdot V_{in} \tag{2.110}$$

In (2.110) the A_1 and B_1 matrices are determined. C_1 derives from (2.112).

$$A_1 = \begin{bmatrix} -\frac{r_{L1}}{L_1} & 0 & 0 & 0 \\ 0 & -\frac{r_{C0}+r_{L2}}{L_2} & -\frac{2}{L_2} & -\frac{1}{L_2} \\ 0 & -\frac{1}{C_1} & 0 & 0 \\ 0 & \frac{1}{C_0} & 0 & -\frac{1}{R_0 \cdot C_0} \end{bmatrix}; \quad B_1 = \begin{bmatrix} \frac{1}{L_1} \\ 0 \\ 0 \\ 0 \end{bmatrix}; \tag{2.111}$$

$$V_{out} = V_R = 0 \cdot x_1 + r_{C0} \cdot x_2 + 0 \cdot x_3 - 1 \cdot x_4; \text{ so:} \tag{2.112}$$

$$C_1 = [0 \quad r_{C0} \quad 0 \quad -1] \tag{2.113}$$

The analysis of the state equations during t_{off} is obtained considering the equivalent circuit from fig.2.34 during t_{off} following the same principle:
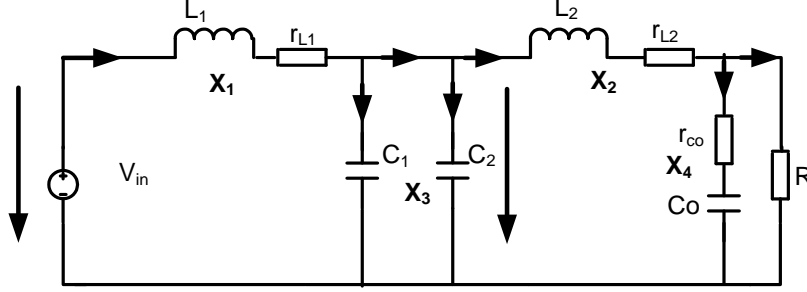
Fig.2.34. Equivalent circuit of BHDC during t_{off}

The state equations during t_{off} derive from the equivalent circuits and are the following ones:

$$\dot{x}_1 = -\frac{r_{L1}}{L_1} \cdot x_1 + 0 \cdot x_2 - \frac{1}{L_1} \cdot x_3 + 0 \cdot x_4 + \frac{1}{L_1} \cdot V_{in} \qquad (2.114)$$

$$\dot{x}_2 = 0 \cdot x_1 - \frac{r_{C0}+r_{L2}}{L_2} \cdot x_2 + \frac{1}{L_2} \cdot x_3 + \frac{1}{L_2} \cdot x_4 \qquad (2.115)$$

$$\dot{x}_3 = -\frac{1}{2 \cdot C_1} \cdot x_1 - \frac{1}{2 \cdot C_1} \cdot x_2 + 0 \cdot x_3 + 0 \cdot x_4 \qquad (2.116)$$

$$\dot{x}_4 = 0 \cdot x_1 + \frac{1}{C_0} \cdot x_2 + 0 \cdot x_3 - \frac{1}{R_0 \cdot C_0} \cdot x_4 \qquad (2.117)$$

Using (2.114)-(2.117) the state and output equations matrix is obtained during t_{off}:

$$\begin{bmatrix} \dot{x}_1 \\ \dot{x}_2 \\ \dot{x}_3 \\ \dot{x}_4 \end{bmatrix} = \begin{bmatrix} -\frac{r_{L1}}{L_1} & 0 & -\frac{1}{L_1} & 0 \\ 0 & -\frac{r_{C0}+r_{L2}}{L_2} & \frac{1}{L_2} & -\frac{1}{L_2} \\ \frac{1}{2 \cdot C_1} & -\frac{1}{2 \cdot C_1} & 0 & 0 \\ 0 & \frac{1}{C_0} & 0 & -\frac{1}{R_0 \cdot C_0} \end{bmatrix} \cdot \begin{bmatrix} x_1 \\ x_2 \\ x_3 \\ x_4 \end{bmatrix} + \begin{bmatrix} \frac{1}{L_1} \\ 0 \\ 0 \\ 0 \end{bmatrix} \cdot V_{in} ; \qquad (2.118)$$

Using (2.118), the A_2 and B_2 matrices are obtained corresponding to t_{off} this time. C_2 derives from (2.120).

$$A_2 = \begin{bmatrix} -\frac{r_{L1}}{L_1} & 0 & -\frac{1}{L_1} & 0 \\ 0 & -\frac{r_{C0}+r_{L2}}{L_2} & \frac{1}{L_2} & -\frac{1}{L_2} \\ \frac{1}{2 \cdot C_1} & -\frac{1}{2 \cdot C_1} & 0 & 0 \\ 0 & \frac{1}{C_0} & 0 & -\frac{1}{R_0 \cdot C_0} \end{bmatrix} ; \quad B_2 = \begin{bmatrix} \frac{1}{L_1} \\ 0 \\ 0 \\ 0 \end{bmatrix} ; \qquad (2.119)$$

$$V_{out} = V_R = 0 \cdot x_1 + r_{C0} \cdot x_2 + 0 \cdot x_3 - 1 \cdot x_4; \text{ so:} \qquad (2.120)$$

$$C_2 = C_1 = \begin{bmatrix} 0 & r_{C0} & 0 & -1 \end{bmatrix} \qquad (2.121)$$

The transfer functions for the state variables are also obtained using Matlab. Since all the needed elements are determined, they are introduced in a m-function using Matlab, in order to draw the corresponding Bode diagrams. The Bode diagrams for the stability analysis of the system were also obtained using the real parameters of the proposed converter prototype, but this time with the converter operating in step-up mode. All these parameters are listed in Table 2.2:

Table 2.2. BHDC prototype data (step-up)

Component	Value	Units	Specifications
V_{in}	50	V	Input voltage in step-down mode
L_2	1470	uH	L_2 inductance
r_{L2}	158	mΩ	ESR of L_2
$C_1 = C_2$	710	uF	Capacitance of the switching cap cell
L_1	200	uH	L_1 inductance
r_{L1}	4.5	mΩ	ESR of L_1
C_0	470	uF	Output filter capacitor
r_{C0}	75	mΩ	ESR of C_0
R	100	Ω	Resistive load
D	0.78	-	Duty Cycle

The Bode plots of the small signal transfer functions used for the system stability analysis correspond to one of the four state variables, determining the stability of the BHDC. Using Matlab and the converter prototype data, the following transfer function results:

$$\frac{\tilde{x}_1}{\tilde{d}} = \frac{1.133 \cdot 10^6 s^3 + 2.322 \cdot 10^8 s^2 + 3.595 \cdot 10^{12} s + 8.281 \cdot 10^{13}}{s^4 + 202.3 s^3 + 3.155 \cdot 10^6 s^2 + 1.304 \cdot 10^8 s + 2.497 \cdot 10^{11}} \tag{2.122}$$

$$\frac{\tilde{x}_2}{\tilde{d}} = \frac{1.542 \cdot 10^5 s^3 - 2.467 \cdot 10^7 s^2 + 2.392 \cdot 10^{11} s + 5.102 \cdot 10^{12}}{s^4 + 202.3 s^3 + 3.155 \cdot 10^6 s^2 + 1.304 \cdot 10^8 s + 2.497 \cdot 10^{11}} \tag{2.123}$$

$$\frac{\tilde{x}_3}{\tilde{d}} = \frac{-2.595 \cdot 10^4 s^3 - 2.307 \cdot 10^7 s^2 - 1.448 \cdot 10^{10} s + 2.555 \cdot 10^{14}}{s^4 + 202.3 s^3 + 3.155 \cdot 10^6 s^2 + 1.304 \cdot 10^8 s + 2.497 \cdot 10^{11}} \tag{2.124}$$

$$\frac{\tilde{x}_4}{\tilde{d}} = \frac{-1419 \cdot 10^4 s^3 + 3.261 \cdot 10^8 s^2 - 4.152 \cdot 10^{10} s + 5.106 \cdot 10^{14}}{s^4 + 202.3 s^3 + 3.155 \cdot 10^6 s^2 + 1.304 \cdot 10^8 s + 2.497 \cdot 10^{11}} \tag{2.125}$$

The system poles are $P_{1,2} = -82.1 \pm 1749.5i$ and $P_{3,4} = -19.1 \pm 2847i$. For each transfer function corresponding to a state variable, the system has 3 zeros.

Fig.2.35 shows that the transfer function (2.122) is unstable. The I_{L1} small signal transfer function is not stable because the cutting frequency is too far from the normal operation frequency, even if phase reserve appears to get fixed at

approximatively 90 degrees. The zeros corresponding to this transfer function are $Z_{1,2}$=-91±17777 and Z_3=-23.1.
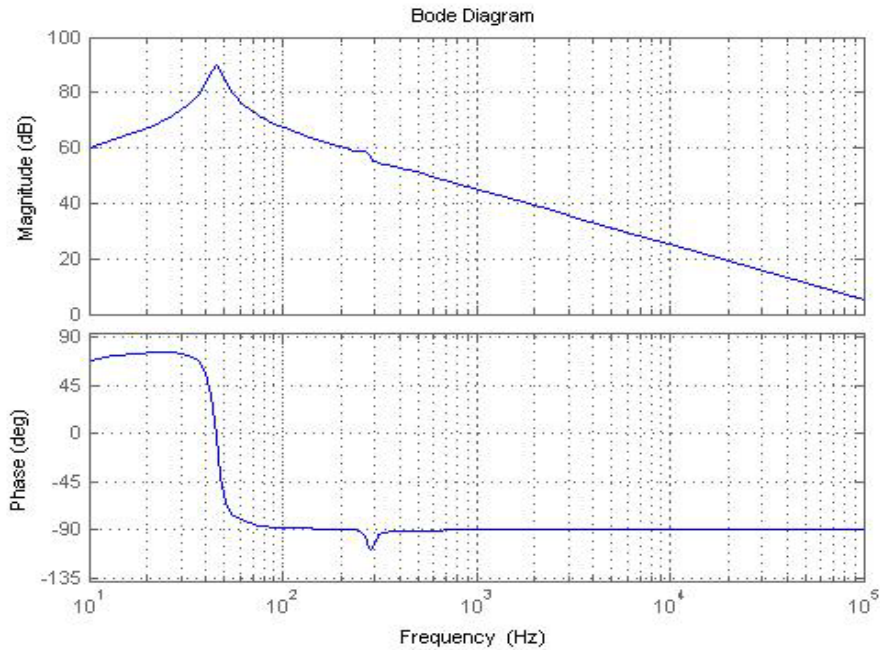
Fig.2.35. Bode plot for $\dfrac{\widetilde{x}_1}{\widetilde{d}}$ small signal transfer function

In fig.2.36 is shown the Bode plot corresponding to $\dfrac{\widetilde{x}_2}{\widetilde{d}}$. It shows a phase reserve of almost 90 degrees at a cutting frequency of 20 kHz. The transfer function has three zeros, $Z_{1,2}$=90.7±1244i and Z_3=-21.3. These two Bode plots presented in fig.2.35 and fig.2.36 indicate an unstable operation of the two inductors L_1 and L_2 because the cutting frequency is not reached and the AC response has an oscillating behavior.

Fig 2.37 shows a lack of stability for the SCC operation corresponding to $\dfrac{\widetilde{x}_3}{\widetilde{d}}$. At the cutting frequency of 4 kHz, the transfer function has no phase reserve and compensation should boost the phase with more than 90 degrees in order to get stable. The transfer function has three zero, $Z_{1,2}$=-1349.4±1903i and Z_3=1809.7.
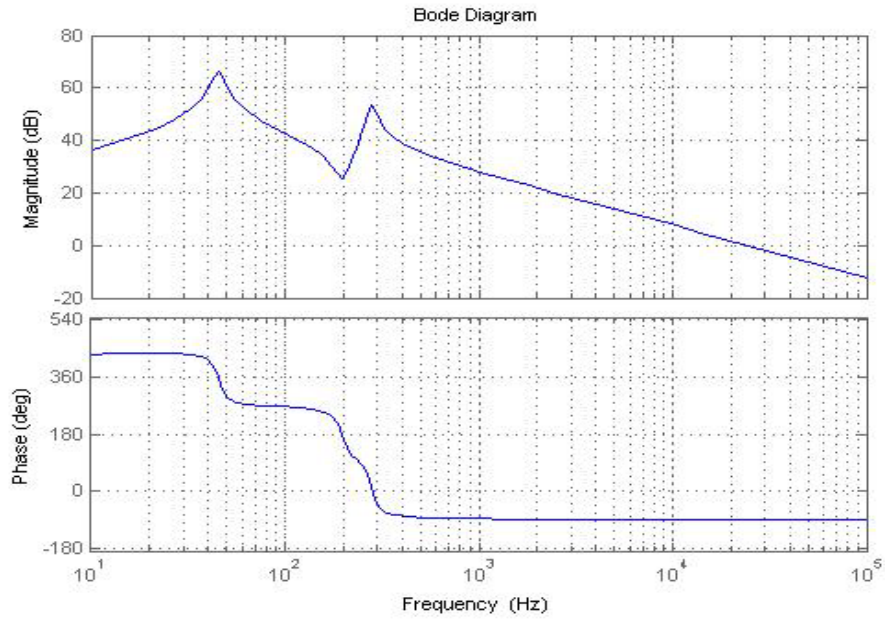
Fig.2.36. Bode plot for $\dfrac{\tilde{x}_2}{\tilde{d}}$ small signal transfer function
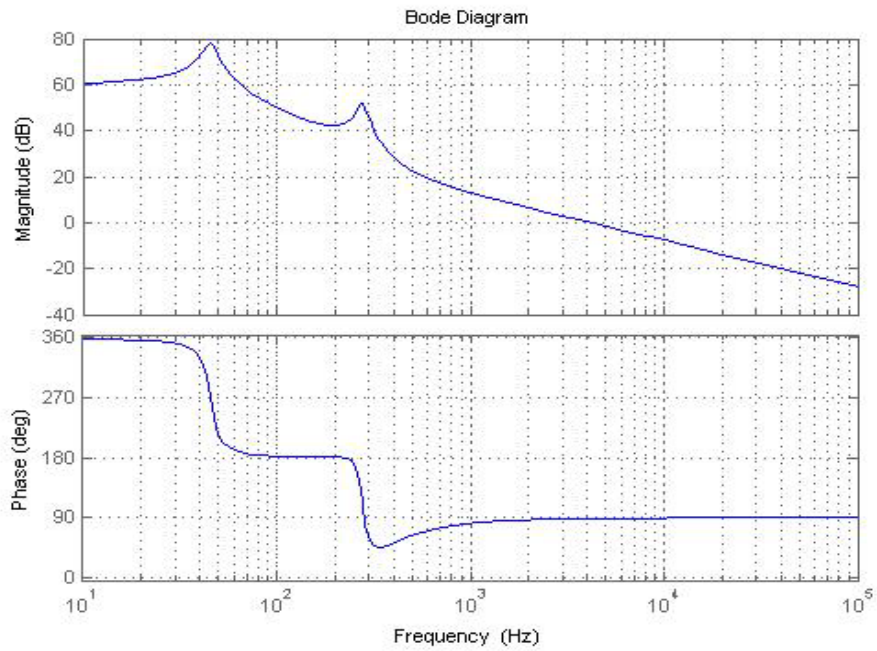
Fig.2.37. Bode plot for $\dfrac{\tilde{x}_3}{\tilde{d}}$ small signal transfer function

Fig.2.38 shows the frequency response of the transfer function corresponding to the output filter capacitor voltage. The amplitude is little bit higher but it does not raise any problems thinking to the fact that the phase reserve is approximatively 35 degrees at a cutting frequency of 3 kHz. The system output stability is good, so the BHDC operation can be considered stable in step-up mode. The transfer function has three zeros, $Z_1 = -28390$, $Z_{2,3} = 91 \pm 1244i$.
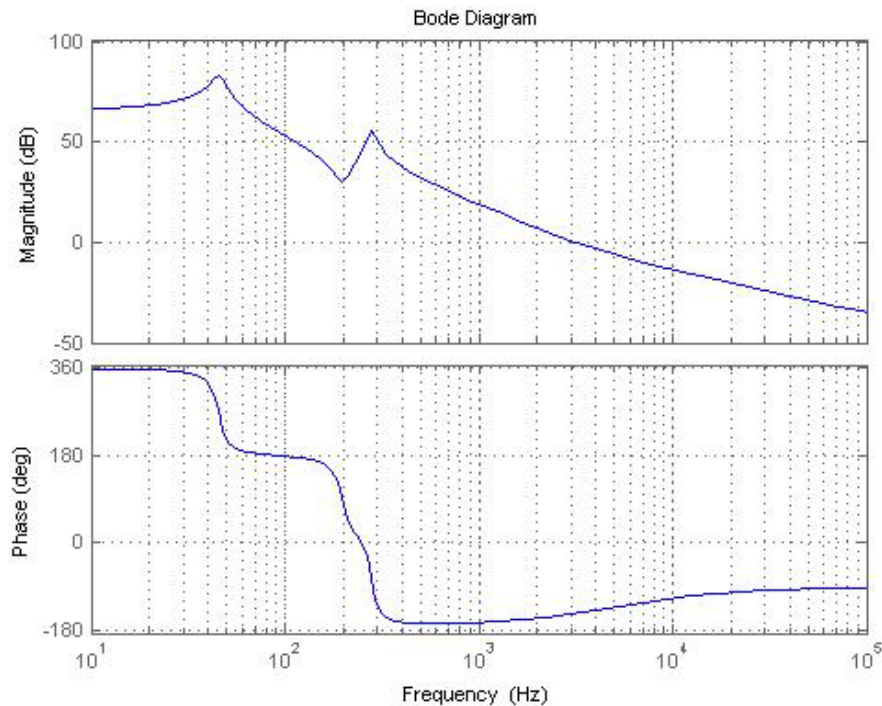
Fig.2.38. Bode plot for $\dfrac{\widetilde{x}_4}{\widetilde{d}}$ small signal transfer function

All the four Bode plots presented above proves that the proposed BHDC has a stable operation because of the confirmed stability for the output capacitor cell. In practice some problems could arise due to the instability of the small signal transfer function of L_1 due to the fact that the BHDC control monitors it.

2.3.1.3. SSA for bi-directional converter with two DC voltage sources

In this subchapter, the stability of the system is analyzed considering the converter operating in its default mode. Two DC voltage sources are connected at the opposite terminals. The differences between this circuit and the previous ones

are the existence of both voltage sources and because of them, the absence of any output filter capacitor. This simplification reduces the system state variables number from 4 to 3. The new equivalent circuit is represented in fig.2.39:
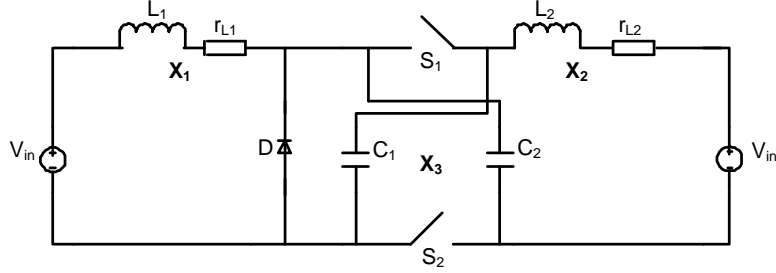
Fig.2.39. Highlighted State Variables for BHDC

The A_1, A_2, B_1, B_2, C_1 and C_2 matrices have to be obtained. Following the same procedure, the equivalent circuits for the proposed bi-directional converter are determined for each switching time. In fig.2.40, the equivalent circuit of BHDC during t_{on} is shown.
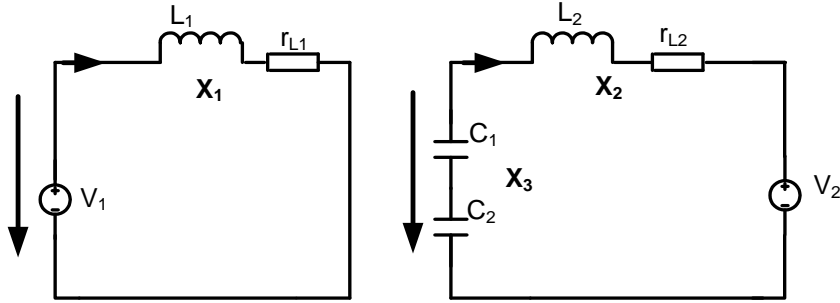
Fig.2.40. Equivalent circuit of BHDC during t_{on}

Considering the citcuits from fig. 2.40 the following state equations results:

$$\dot{x}_1 = -\frac{r_{L1}}{L_1} \cdot x_1 + 0 \cdot x_2 + 0 \cdot x_3 + \frac{1}{L_1} \cdot V_1 \tag{2.126}$$

$$\dot{x}_2 = 0 \cdot x_1 - \frac{2r_{C1} + r_{L2}}{L_2} \cdot x_2 + \frac{2}{L_2} \cdot x_3 - \frac{1}{L_2} \cdot V_2 \tag{2.127}$$

$$\dot{x}_3 = 0 \cdot x_1 - \frac{1}{C_1} \cdot x_2 + 0 \cdot x_3 \tag{2.128}$$

Using (2.126)-(2.128) the state and output equations matrix is obtained during t_{on}:

$$\begin{bmatrix} \dot{x}_1 \\ \dot{x}_2 \\ \dot{x}_3 \end{bmatrix} = \begin{bmatrix} -\frac{r_{L1}}{L_1} & 0 & 0 \\ 0 & -\frac{r_{C1} + r_{L2}}{L_2} & \frac{2}{L_2} \\ 0 & -\frac{1}{C_1} & 0 \end{bmatrix} \cdot \begin{bmatrix} x_1 \\ x_2 \\ x_3 \end{bmatrix} + \begin{bmatrix} \frac{1}{L_1} & 0 \\ 0 & -\frac{1}{L_2} \\ 0 & 0 \end{bmatrix} \cdot \begin{bmatrix} V_1 \\ V_2 \end{bmatrix} \tag{2.129}$$

From (2.129) the A_1 and B_1 matrices are determined:

$$A_1 = \begin{bmatrix} -\frac{r_{L1}}{L_1} & 0 & 0 \\ 0 & -\frac{r_{C1}+r_{L2}}{L_2} & \frac{2}{L_2} \\ 0 & -\frac{1}{C_1} & 0 \end{bmatrix}; \quad B_1 = \begin{bmatrix} \frac{1}{L_1} & 0 \\ 0 & -\frac{1}{L_2} \\ 0 & 0 \end{bmatrix}; \tag{2.130}$$

The C_1 matrix results from (2.131), depending by the settled direction of the current:

$$I_{out} = 1 \cdot x_1 + 0 \cdot x_2 + 0 \cdot x_3 \text{ or } I_{out} = 0 \cdot x_1 + 1 \cdot x_2 + 0 \cdot x_3 \text{ so:} \tag{2.131}$$

$$C_1 = \begin{bmatrix} 1 & 0 & 0 \end{bmatrix} \text{ or } C_1 = \begin{bmatrix} 0 & 1 & 0 \end{bmatrix} \tag{2.132}$$

The analysis of the state equations during t_{off} is realized considering the following equivalent circuit of BHDC from fig.2.41 during t_{off} following the same principle:
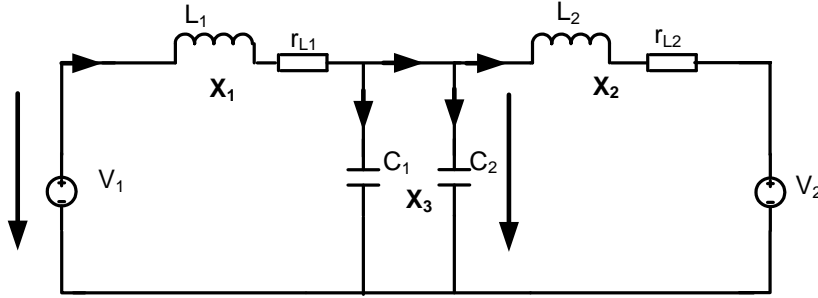
Fig.2.41. Equivalent circuit of BHDC during t_{off}

The state equations during t_{off} which derive from the equivalent circuits are the following ones:

$$\dot{x}_1 = -\frac{2r_{L1}+r_{C1}}{2L_1} \cdot x_1 + \frac{r_{C1}}{2L_1} \cdot x_2 - \frac{1}{L_1} \cdot x_3 + \frac{1}{L_1} \cdot V_1 \tag{2.133}$$

$$\dot{x}_2 = \frac{r_{C1}}{2L_2} \cdot x_1 - \frac{2r_{L2}+r_{C1}}{2L_2} \cdot x_2 + \frac{1}{L_2} \cdot x_3 - \frac{1}{L_2} \cdot V_2 \tag{2.134}$$

$$\dot{x}_3 = \frac{1}{2 \cdot C_1} \cdot x_1 - \frac{1}{2 \cdot C_1} \cdot x_2 + 0 \cdot x_3 \tag{2.135}$$

Using (2.133)-(2.135) the state and output equations matrix is obtained during t_{off}:

$$\begin{bmatrix} \dot{x}_1 \\ \dot{x}_2 \\ \dot{x}_3 \end{bmatrix} = \begin{bmatrix} -\frac{2r_{L1}+r_{C1}}{2L_1} & \frac{r_{C1}}{2L_1} & -\frac{1}{L_1} \\ \frac{r_{C1}}{2L_2} & -\frac{2r_{L2}+r_{C1}}{2L_2} & \frac{1}{L_2} \\ \frac{1}{2 \cdot C_1} & -\frac{1}{2 \cdot C_1} & 0 \end{bmatrix} \cdot \begin{bmatrix} x_1 \\ x_2 \\ x_3 \end{bmatrix} + \begin{bmatrix} \frac{1}{L_1} & 0 \\ 0 & -\frac{1}{L_2} \\ 0 & 0 \end{bmatrix} \cdot \begin{bmatrix} V_1 \\ V_2 \end{bmatrix} \tag{2.136}$$

From (2.136) the A_2 and B_2 matrices are determined, C_2 results from (2.138) depending by the settled direction of the current:

$$A_2 = \begin{bmatrix} -\dfrac{2r_{L_1}+r_{C_1}}{2L_1} & \dfrac{r_{C_1}}{2L_1} & -\dfrac{1}{L_1} \\ \dfrac{r_{C_1}}{2L_2} & -\dfrac{2r_{L_2}+r_{C_1}}{2L_2} & \dfrac{1}{L_2} \\ \dfrac{1}{2\cdot C_1} & -\dfrac{1}{2\cdot C_1} & 0 \end{bmatrix}; \quad B_2 = \begin{bmatrix} \dfrac{1}{L_1} & 0 \\ 0 & -\dfrac{1}{L_2} \\ 0 & 0 \end{bmatrix}; \tag{2.137}$$

$$I_{out} = 1 \cdot x_1 + 0 \cdot x_2 + 0 \cdot x_3 \text{ or } I_{out} = 0 \cdot x_1 + 1 \cdot x_2 + 0 \cdot x_3 \text{ so:} \tag{2.138}$$

$$C_2 = [1 \quad 0 \quad 0] \text{ or } C_2 = [0 \quad 1 \quad 0] \tag{2.139}$$

Once determined, the matrices corresponding to the bidirectional converter with two voltage sources are introduced in a m-function using Matlab, in order to obtain the Bode plots for the small signal transfer functions of the state variable. With the absence of the output filter capacitors, the frequency response of system depends by the considered direction of the current between the two voltage sources and the behavior of L_1 and L_2. The Bode plots that are needed for the stability analysis of the system were built using the real parameters of the proposed converter prototype. Because the converter operates bidirectional, a new list with parameters is given in Table 2.3:

Table 2.3. BHDC prototype data

Component	Value	Units	Specifications
V_1	50	V	Input voltage 1
V_2	400	V	Input voltage 2
L_2	1470	uH	L_2 inductance
r_{L2}	158	mΩ	Equivalent series resistance of L_2
I_{L1}	40 (-40)	A	The reference current through L_2
$C_1 = C_2$	705	uF	Capacitance of the switching cap cell
$r_{c1} = r_{c2}$	50	mΩ	ESR of the switching capacitor cell
L_1	200	uH	L_1 inductance
r_{L1}	4.5	mΩ	Equivalent series resistance of L_1
R	200-	Ω	Resistive load
D	0.78	-	Duty Cycle

The Bode plots of the small signal transfer functions are used for BHDC stability analysis. Using Matlab and the converter prototype data, the following equations result for the small signal transfer functions of the x_1, x_2 and x_3 state variable:

$$\frac{\tilde{x}_1}{\tilde{d}} = \frac{1.136 \cdot 10^6 s^2 + 1.909 \cdot 10^8 s + 1.938 \cdot 10^{12}}{s^3 + 214.3 s^2 + 1.696 \cdot 10^6 s + 9.357 \cdot 10^7} \tag{2.140}$$

$$\frac{\tilde{x}_2}{\tilde{d}} = \frac{1.546 \cdot 10^5 s^2 + 1.198 \cdot 10^7 s + 2.395 \cdot 10^{11}}{s^3 + 214.3 s^2 + 1.696 \cdot 10^6 s + 9.357 \cdot 10^7} \tag{2.141}$$

$$\frac{\widetilde{x}_3}{\widetilde{d}} = \frac{-1.775 \cdot 10^7 s + 1.456 \cdot 10^{10}}{s^3 + 214.3 s^2 + 1.696 \cdot 10^6 s + 9.357 \cdot 10^7}$$

(2.142)

The system poles are $P_{1,2}$=-79.4±11296.6i and P_3=-55.4. For each transfer function of a state variable representation, the corresponding zeros are listed.
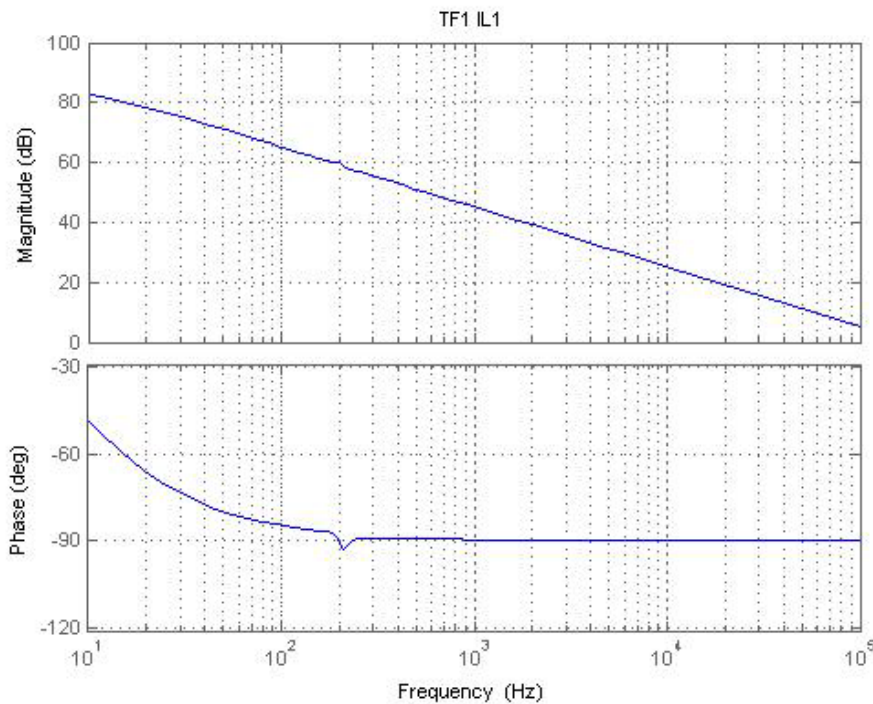
Fig.2.42. Bode plot for $\dfrac{\widetilde{x}_1}{\widetilde{d}}$ small signal transfer function

Fig.2.42 shows that the I_{L1} bevavior is unstable. It has a phase reserve of ~90 degrees, but the cutting frequency point is not reached in the range of normal operating frequency, so the response oscillates permanently. The zeros corresponding to this transfer function are $Z_{1,2}$=-84±1303.1i. Because this plot shows an oscillating response and the system works at 20 kHz, a compensation is needed to lower the amplitude and obtain a stable configuration.

In fig.2.43 is shown the Bode plot corresponding to $\dfrac{\widetilde{x}_2}{\widetilde{d}}$. It shows a phase reserve of almost 90 degrees at a cutting frequency of 23 kHz. The transfer function has two zeros, $Z_{1,2}$=-38.7±1244.1i. The two Bode plots presented in fig.2.42 and fig.2.43 indicate an unstable operation of the two inductors L_1 and L_2.
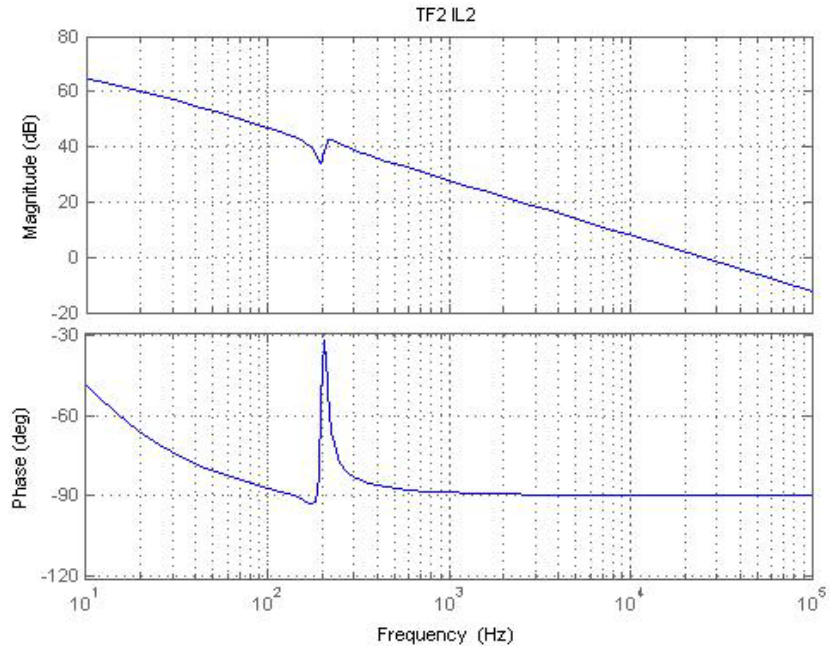
Fig.2.43. Bode plot for $\dfrac{\tilde{x}_2}{\tilde{d}}$ small signal transfer function
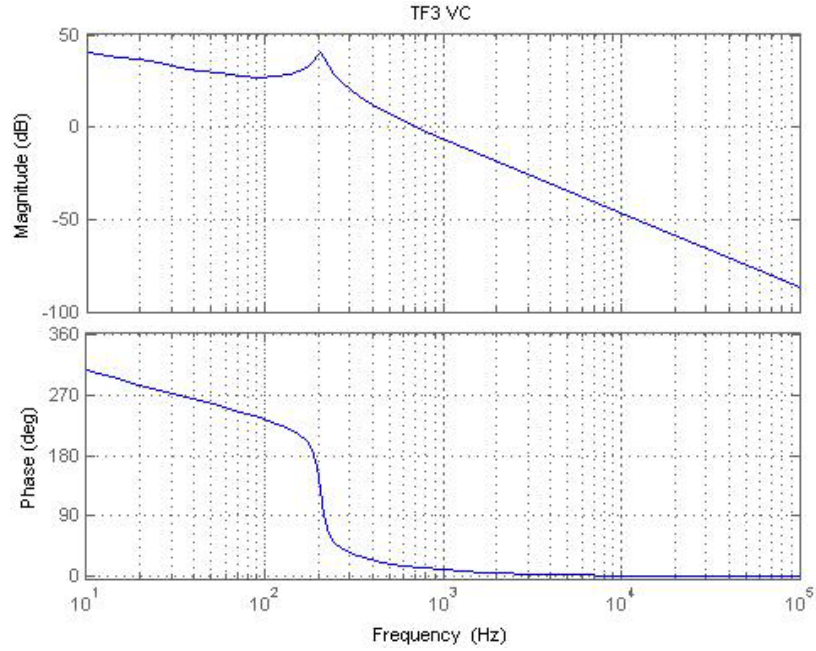
Fig.2.44. Bode plot for $\dfrac{\tilde{x}_3}{\tilde{d}}$ small signal transfer function

In fig.2.44 is shown that the SCC operation is unstable and oscillates. The transfer function has a zero $Z_1=820.5521$.

In the following, is presented the compensation of the system and the new Bode plots of the compensated transfer functions. This compensation is integrated in a simulation model and in BHDC prototype control.

The compensation is realized by adding new poles to the system transfer function. Its goal is to offer a stable behavior to the system operating between two voltage sources. For this, the current on the L_1 inductor determines the stability of the entire system.

In order to compensate the system and achieve a stable operation of the L_1 inductor, the initial transfer functions are multiplied with Hr (2.143), which represents the compensation function and it was determined based on the previous Bode plots analysis.

$$Hr = \frac{2150s + 4741000}{2.721s^2 + 0.0001929s + 0.0001929} \qquad (2.143)$$

The new compensated small signal transfer functions of the state variables obtained using Matlab are:

$$\frac{\tilde{x}_1}{\tilde{d}} = \frac{2.451s^3 + 5877s^2 + 5.226 \cdot 10^6 s + 9.227 \cdot 10^9}{2{,}721 \cdot 10^{-9} s^5 + 0.0001935s^4 + 0.04615s^3 + 327.5s^2 + 1.838 \cdot 10^4 s + 1.805 \cdot 10^4} \quad (2.144)$$

$$\frac{\tilde{x}_2}{\tilde{d}} = \frac{0.3308s^3 + 688.5s^2 + 4.228 \cdot 10^5 s + 1.131 \cdot 10^{10}}{2{,}721 \cdot 10^{-9} s^5 + 0.0001935s^4 + 0.04615s^3 + 327.5s^2 + 1.838 \cdot 10^4 s + 1.805 \cdot 10^4} \quad (2.145)$$

$$\frac{\tilde{x}_3}{\tilde{d}} = \frac{-0.05507s^3 - 168.2s^2 - 7.195 \cdot 10^4 s + 6.862 \cdot 10^7}{2{,}721 \cdot 10^{-9} s^5 + 0.0001935s^4 + 0.04615s^3 + 327.5s^2 + 1.838 \cdot 10^4 s + 1.805 \cdot 10^4} \quad (2.146)$$

In fig.2.45 is presented the Bode plot of the transfer function corresponding to I_{L1}, after compensation. The new poles of the compensated transfer function are: $P_1=-7088.6$, $P_2=-5.5$, $P_3=-0.1$. $P_{4,5}=-7.9\pm129.7i$. The new zeros of the transfer function are $Z_1=-2204.9$ and $Z_{1,2}=-96.4\pm1303.1i$. It can be observed that the frequency response of the inductor L_1 is stable, with low oscillations and a phase reserve of almost 70 degrees at the cutting frequency of 2 kHz. The stability analysis of the second inductor L_2 results from the Bode plot from fig.2.46. The new zeros of the transfer function in this case are $Z_1=-2204.9$ and $Z_{1,2}=61.9\pm1243.8i$ and the stability is also achieved, with lower response oscillations and phase reserve of more than 60degrees at a cutting frequency of ~500 Hz. The current through the circuit depends by the two inductors L_1 and L_2 because it is the only input variable for the system normal operation and it also set the direction of the energy flow. Once the stability of the related state variables is obtained through compensation, it means that the integration of this compensation in the real converter gives stability to the entire system.

For the result confirmation, the stability is analyzed using the PWM Switch Model procedure.
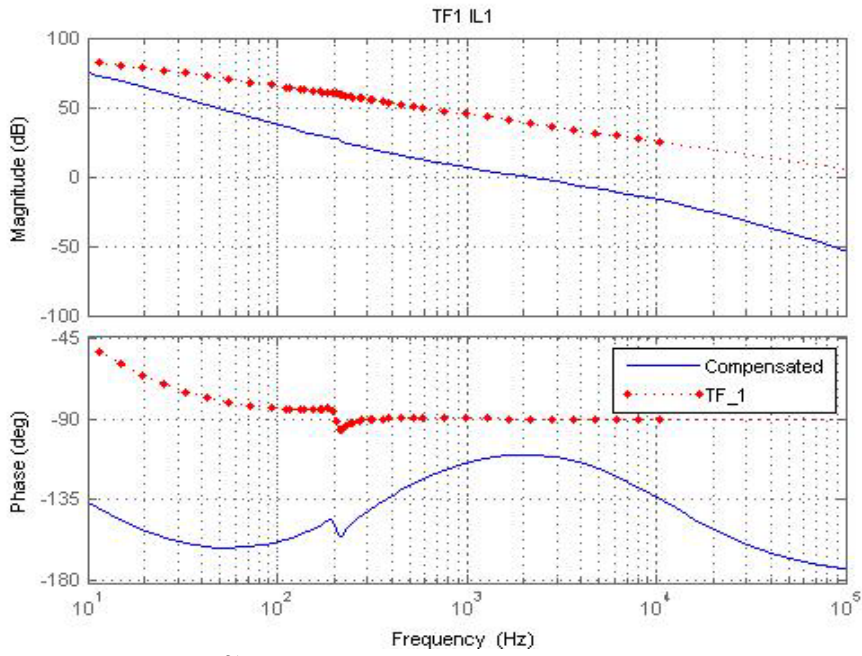
Fig.2.45. Bode plot for $\dfrac{\widetilde{x}_1}{\widetilde{d}}$ small signal transfer function with compensation (with blue)
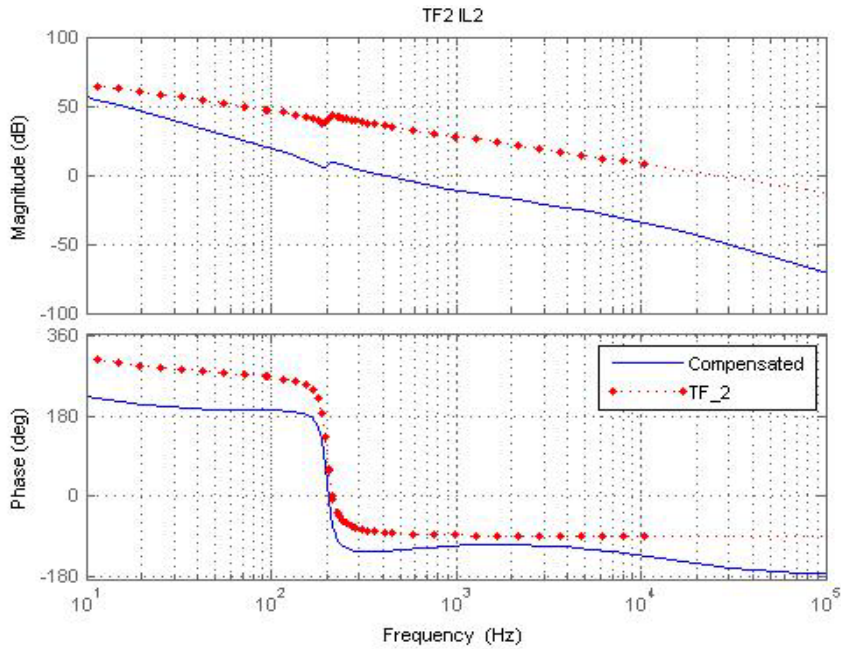
Fig.2.46. Bode plot for $\dfrac{\widetilde{x}_2}{\widetilde{d}}$ small signal transfer function with compensation

2.3.2. PWM Switch method

The SSA method can be considered a viable, but complicated way to derive small-signal models of power converters. The large number of state variables and the complex equations represent the main issues of this method. Many times, a part of these variables are neglected, but this also requires some experience in order to obtain useful results. In 1986 Dr. Vatche Vorperian from Virginia Polytechnic Institute, developed a new and more reliable concept of PWM Switch Model (**PWMSM**). The PWMSM has as starting point mainly the elements that introduce nonlinearities in systems, in this case, the diodes and the transistors. The solution is their substitution with a special three terminal model for the small signal analysis. A big advantage of this method is the fact that once realized, the small-signal model could be used for any existing topology without any average or linearization process. In fig.2.47 the PWMSM is presented with a single-pole double throw configuration for a better understanding of the PWM switch:
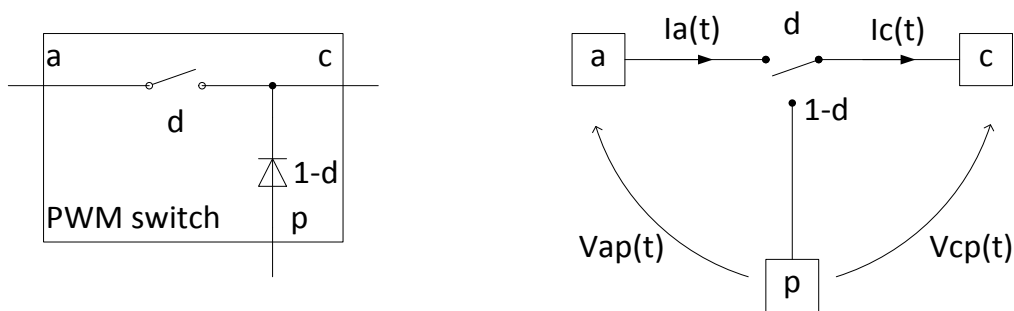
Fig.2.47. The PWM Switch model and a single-pole double-throw configuration

In fig.2.47, the PWMSM replaces a conventional power pole with a model that integrates a two states switch and a diode. The switch model terminals are the *active node* "**a**"- the switch terminal not connected to the diode- the *passive node* "**p**"- the diode terminal not connected to the switch- and the *common node* "**c**"- the junction between the diode and the power switch terminals. One of the most important advantages of PWMSM is that the new model works in both CCM and DCM operation. Still, in order to obtain correct results is essential to use the PWM switch model in a correct form adapted to the related circuit respecting the natural operation of the system.

The first step in applying the PWMSM is similar with the one we did in SSA and it consists in the identification of the PWM switch variables, average and perturbs them in order to obtain the small signal model.

The mediation of PWM switch variables starts with identifying the terminals of the PWM switch models, determining and averaging the related waveforms of the voltages and currents during one switching period. This procedure is the same with the one we use in calculating the average current through an inductor or the average voltage over a capacitor. If these models behavior is simulated, the

obtained waveforms of the currents and voltages over the switching components twist between zero and an averaged value during each switching period. For example, in fig.2.48 a typical current waveform during a switching period and the equivalent model is presented.
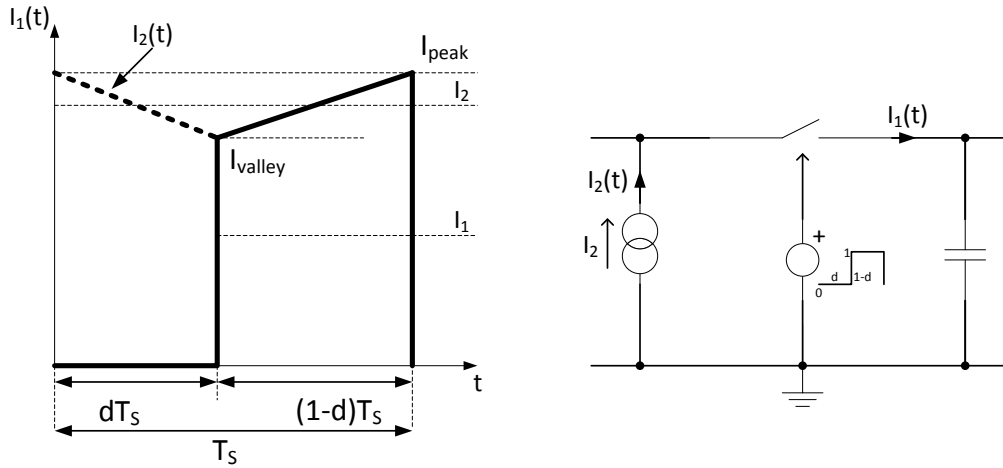
Fig.2.48. An usual current waveform and circuit that generates it

$I_2(t)$ represents the real waveform of the current through the circuit during T_s and it varies between I_{peak} and I_{valley}. During t_{on} ($d \cdot T_s$) the current through the transistor is zero because it is blocked. In this conditions we can consider a current $I_1(t)$ as a sampled version of $I_2(t)$ which is 0 during $d \cdot T_s$ and jumps to the averaged value of $I_2(t)$ during the entire period T_s.

$$I_2 = \frac{I_{peak} + I_{valley}}{2} \tag{2.147}$$

$$I_1 = \frac{1}{T_s} \cdot \int_0^{T_s} I_1(t)dt = (1-d) \cdot I_2 \tag{2.148}$$

In the same manner, the terminal voltages over the PWMSM are treated. Neglecting the position of the switch, $V_{ap}(t)$ value is always a DC level, that goes to the a and p terminals. On the other side, $V_{cp}(t)$ represent the output voltage of the PWMSM, depending by the duty cycle. The average value of V_{cp} is:

$$V_{cp} = \frac{1}{T_s} \cdot \int_0^{T_s} V_{cp}(t)dt = d \cdot V_{cp} \tag{2.149}$$

In the following subchapters, the stability analysis is realized considering the converter operation in step-down and step-up modes. The stability analysis using PWMSM ends with a comparison of the results obtained with SSA for the converter operating as an interface between two voltage sources.

2.3.2.1. PWMSM for step-down converter with resistive load

In this subchapter, the presentation of PWMSM method continues related to the proposed converter and how it was applied to our system when it operates in step-down mode. First, a new power stage equivalent circuit is presented in fig. 2.49, just as it was implemented in our design. This version of the circuit came as a solution during the prototype designing procedure and it created a more clear view of the corresponding PWMSM. The encircled arias are replaced with equivalent PWM switch models whose operation determines the same behavior of the circuit. The corresponding duty cycle is obtained differently in order to provide a much better steadiness of the system against perturbations and the detailed procedure is presented.
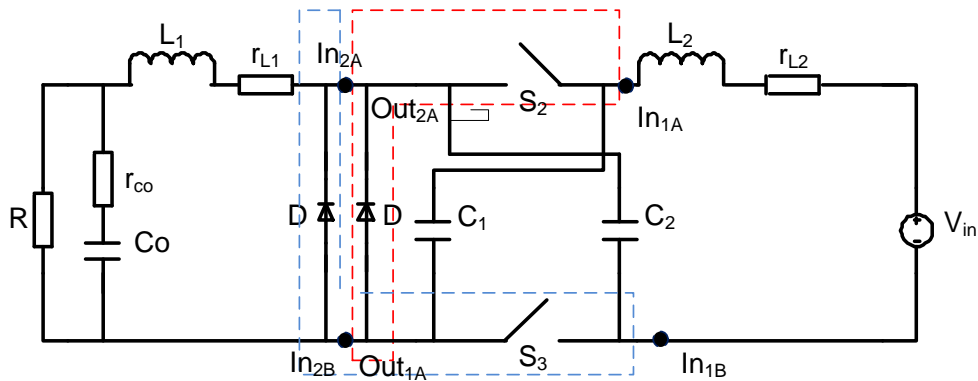
Fig.2.49. Step-down mode circuit highlighting switches disposition

In fig.2.50 is presented the replacement of the switching power poles to PWMSM, highlighting the current and voltage circuits. In step-down mode the related power poles of the converter contain the switches S_2 and S_3 combined with the additional antiparallel diode of the S_1 switch.
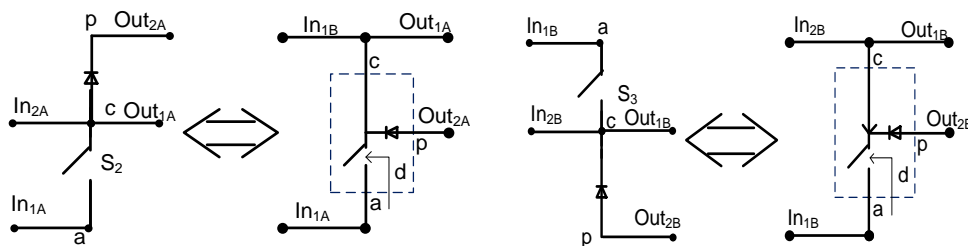
Fig.2.50. PWMSM of S_1 and S_2 switches

The equivalent circuit with PWMSM is presented in fig.2.51. It highlights the transformation of the step-down circuit, in an equivalent PWMSM circuit, by replacing the corresponding power poles with PWMSM.

Fig.2.51. Equivalent step-down circuit with PWMSM

TINA-TI software offers a special tool designed for the stability analysis of the electronic circuits with PWMSM. Similar to the Matlab results related to the Bode plots, the frequency response of the systems, obtained with TINA, indicate the stability of the related systems.

In fig.2.52 is presented the Tina TI model of the proposed circuit, operating in step-down mode with a resistive load. The PWMSMs are designed and they are placed in the circuit respecting the observations related to the currents and voltages. The rest of the components are modeled using the real parameters corresponding to the prototype data.

Fig.2.52. Simulation model of the circuit in step-down mode

The duty cycle apparently looks to be obtained with a close loop control. The value of the output voltage V_out is sent through a resistive divider to an operational amplifier and compared with a calculated reference voltage. It amplifies by 60 dB the difference between the chosen reference voltage V_ref and V_out. A LC filter is added to the obtained output featuring an extremely cutoff frequency, in order to get an open-loop control for the duty cycle when getting the AC response. During the bias point, the duty cycle is automatically computed according to the output voltage set point. The LoL inductor is shorcircuited and the CoL capacitor is open, so the duty cycle depends only by the output voltage set point given by R_3, R_4, and V_ref. This way, the modification of Vin or Rload as input conditions does not affect the system output V_out. During the AC analysis process, the LC filter will stop any AC excitation so the control circuit will act as an open loop control.

In fig.2.53 is presented the AC response related to the V_out (voltage on the output capacitor). Similar to the SSA method, it shows that it is stable, even if the phase reserve does not exceed 22-25 degrees.
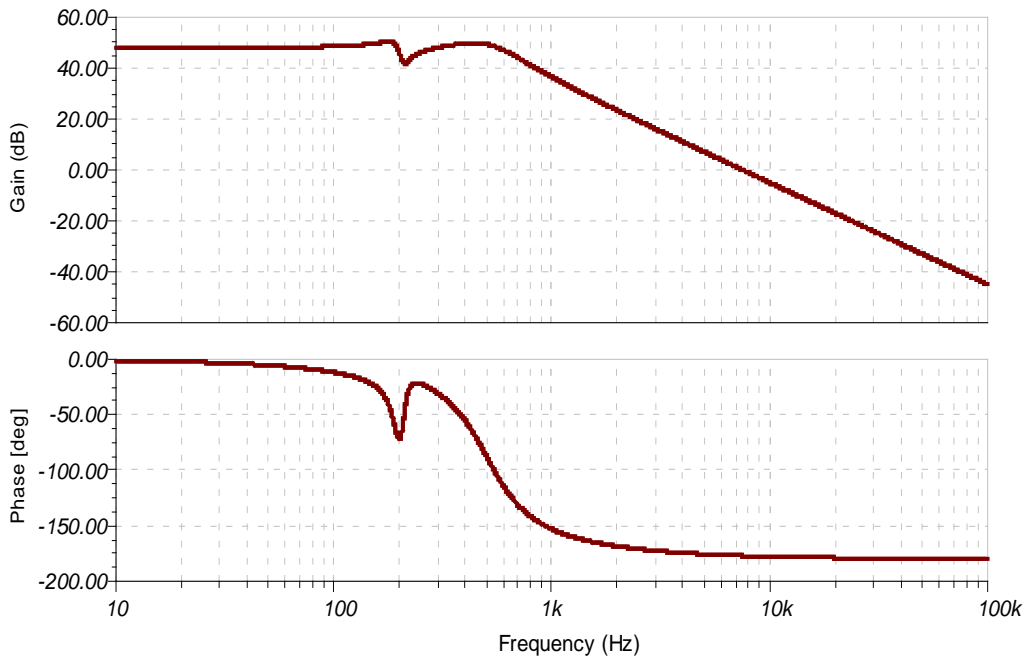
Fig.2.53. Bode plot for the V_out state variable

In fig.2.54 and fig.2.55 are presented the PWMSM AC responses corresponding to I_{L1}, respectively I_{L2} currents. Both Bode plots highlight a lack stability with the cutting frequency out of the operating frequency domain. Since the current on the L_1 inductor is high and used in the BHDC control, it would important to have a stable behavior for it. Also, the responses shapes are close to the ones obtained with the SSA method and the conclusion are similar.

In fig.2.56 is shown the PWMSM AC response for the voltage over the switching capacitor cell which is unstable, with no phase reserve at the cutting frequency.
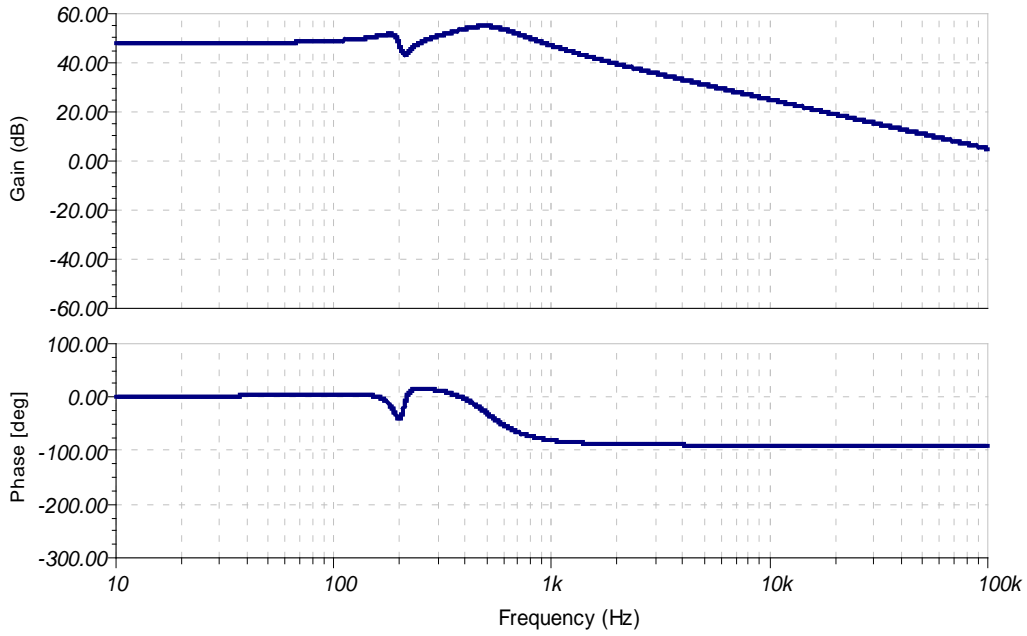
Fig.2.54. Bode plot for the AM1 (I_{L1}) state variable
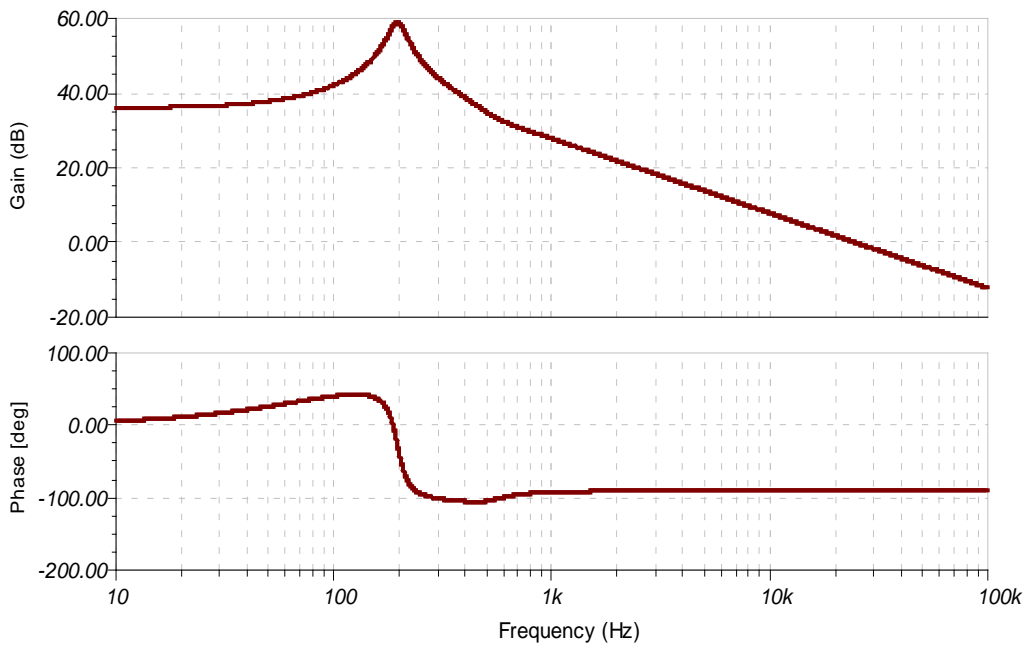
Fig.2.55. Bode plot for the AM2 (I_{L2}) state variable
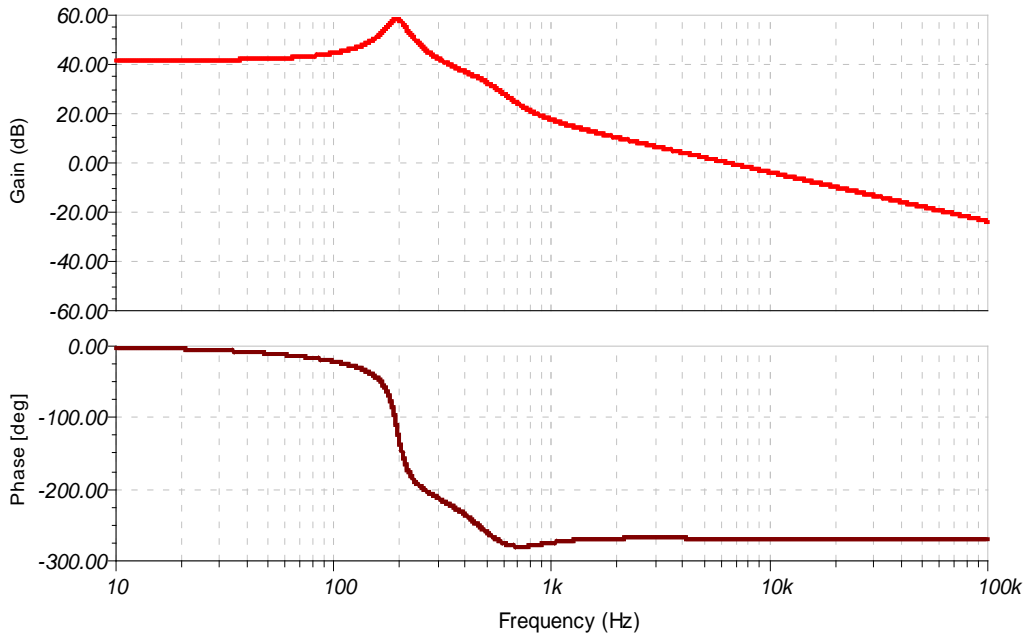
Fig.2.56. Bode plot for the V_C2 state variable

Comparing the stability analyses using SSA and PWMSM methods for the system operating in step-down mode, the results are similar.

2.3.2.2. PWMSM for step-up converter with resistive load

The PWMSM for step-up mode imposes a different equivalent circuit, because the switches operation is also different. The new equivalent circuit is shown in fig.2.57.
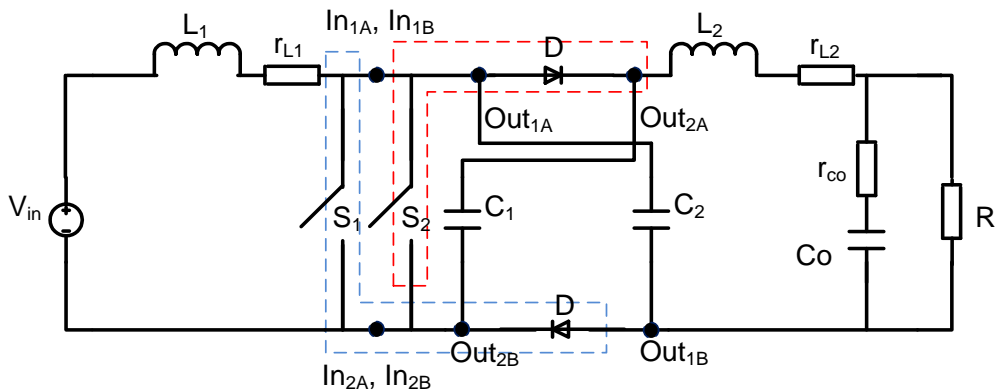
Fig.2.57. Step-up mode circuit highlighting switches disposition

According to the representation from fig.2.57, the PWMSM method analysis is adapted to the step-up operation mode of BHDC. In fig.2.58 are shown transformation and the connections of the PWM switch models in the circuit according to the inputs In_{1A}, In_{2A}, In_{1B}, In_{1B}, respective the outputs Out_{1A}, Out_{2A}, Out_{1B} and Out2B, corresponding to the current and voltage circuits, for the both power poles.
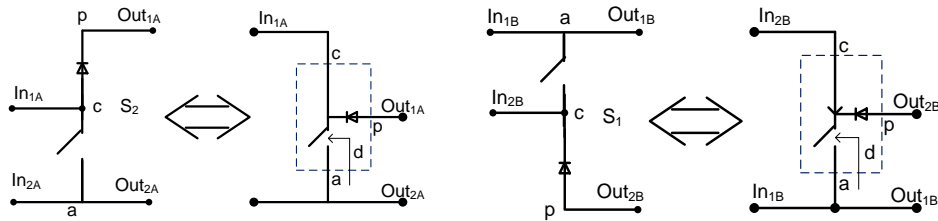
Fig.2.58. PWMSM of S_1 and S_2 switches

After the determination of the current and voltage circuits terminals, the new equivalent circuit with PWMSM for BHDC operating in step-up mode is designed and it is presented in fig.2.59.
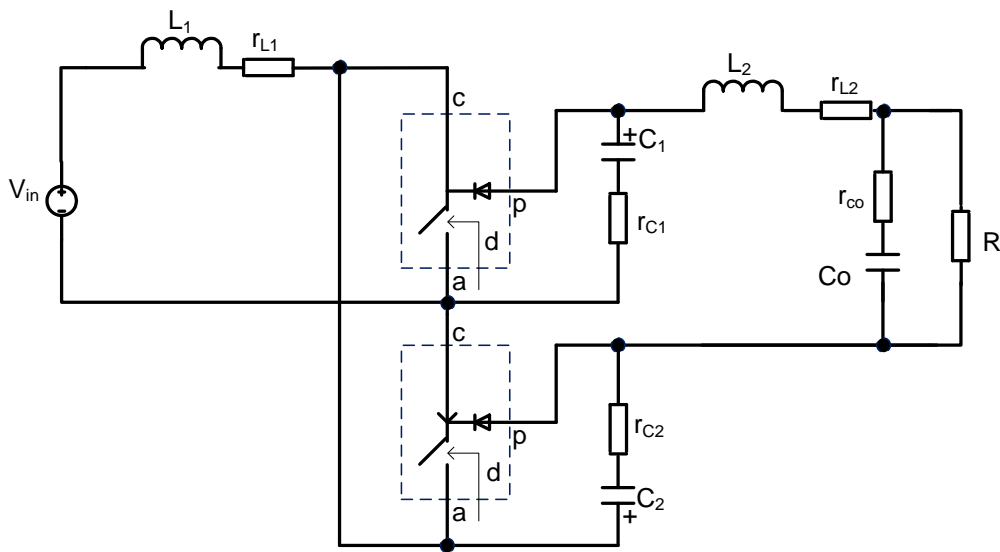
Fig.2.59. Equivalent step-up circuit with PWMSM

The proposed equivalent PWMSM circuit is digitally modeled using TINA TI software. Since this platform offers prebuilt models for the PWM switches modeled according to the presented theory, it is used to obtain the AC response for the main components of the BHDC. In fig. 2.60 is shown the simulation model of the circuit using PWMSM, considering the same specifications related to the open loop control given in the previous subchapter.
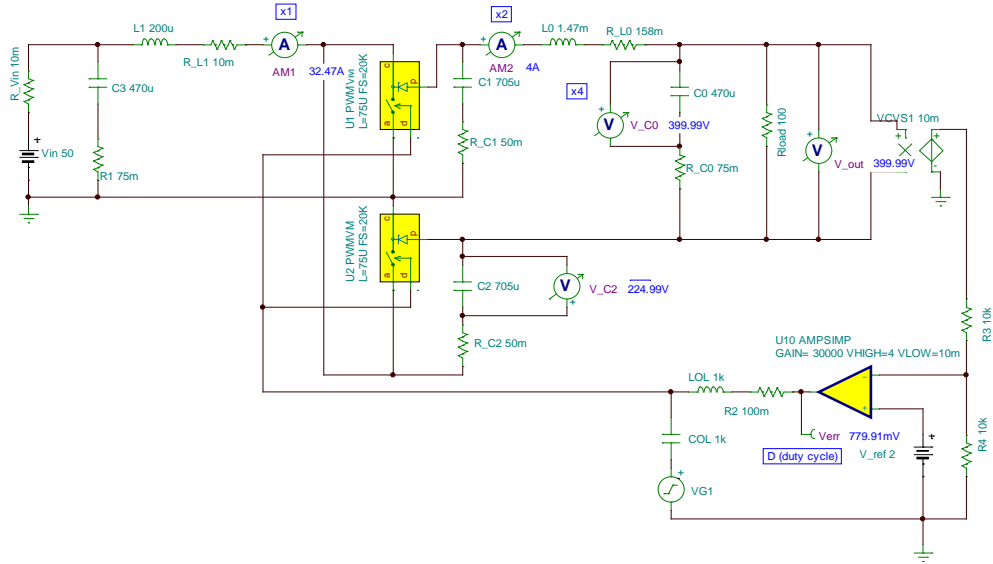
Fig.2.60. Simulation model of the circuit in step-up mode

In fig.2.61 is presented the Bode plot corresponding to the output voltage state variable of the system operating in step-up mode. Its behavior is stable with a low phase reserve at the cutting frequency.
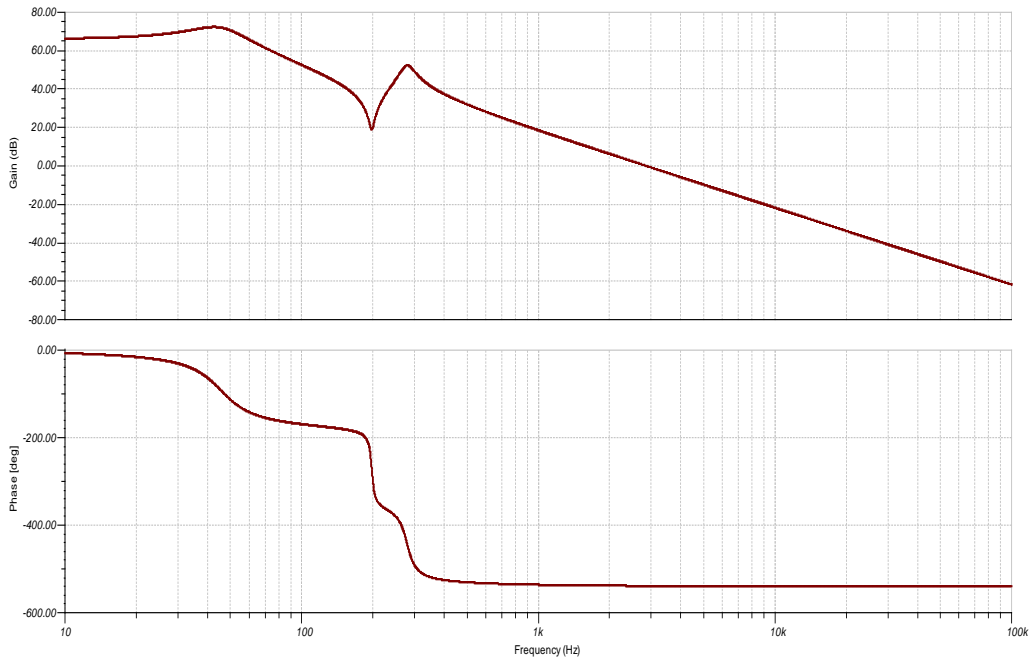
Fig.2.61. Bode plot for the V_out state variable
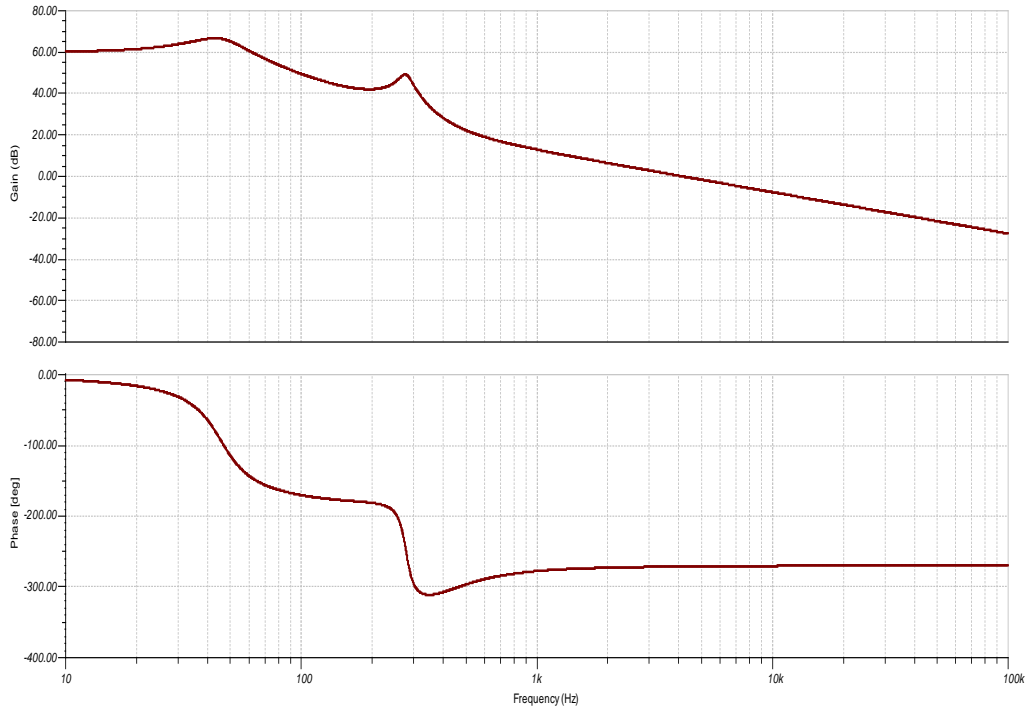
Fig.2.62. Bode plot for the V_C2 state variable
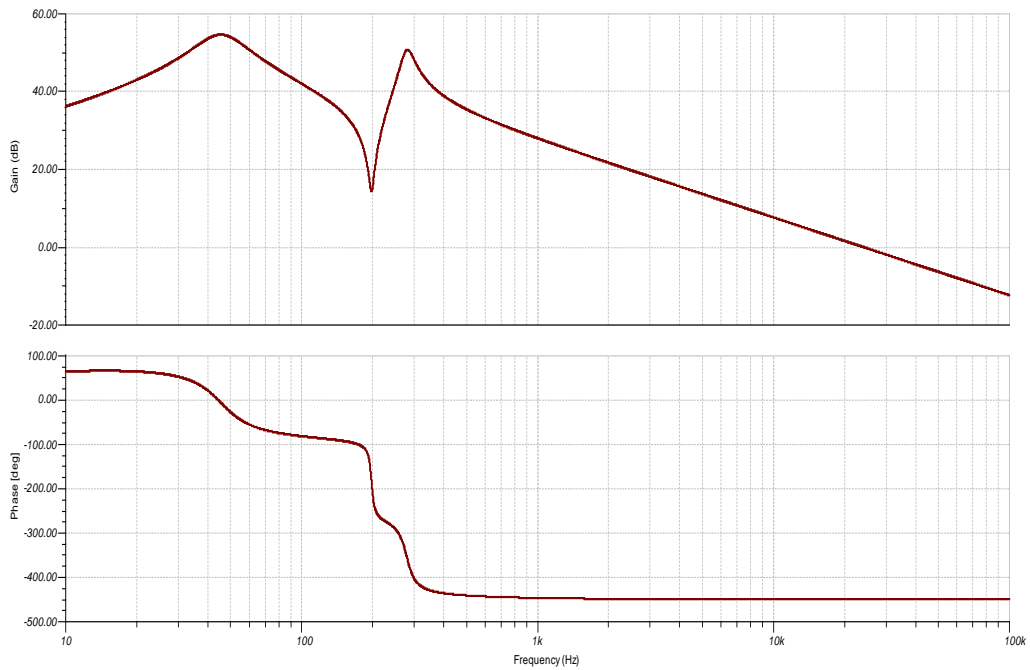
Fig.2.63. Bode plot for the AM2 (I_{L2}) state variable
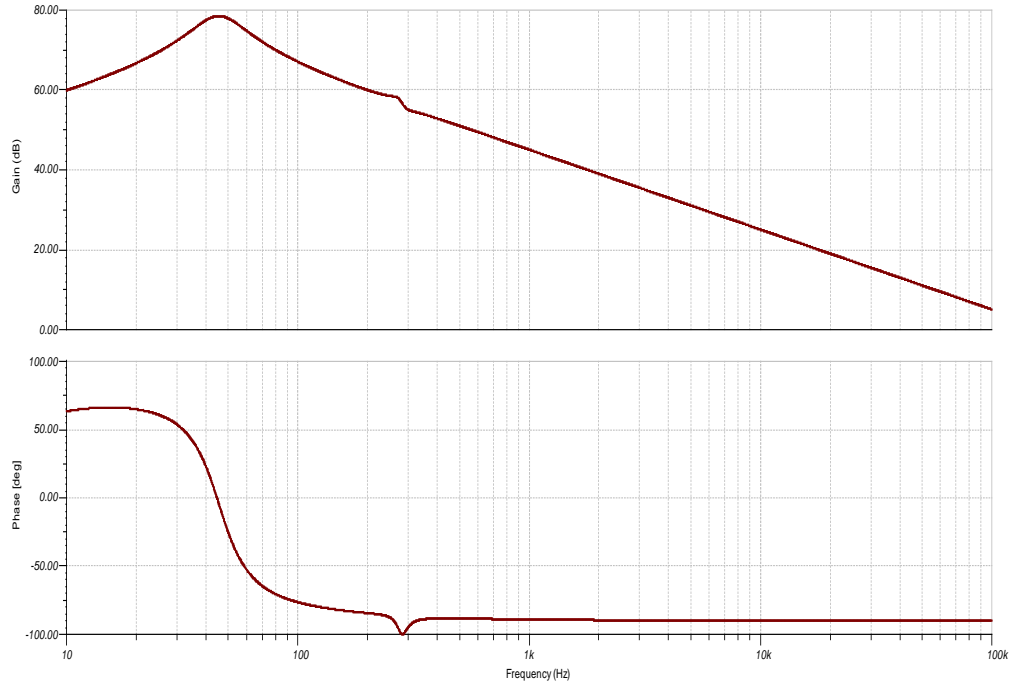
Fig.2.64. Bode plot for the AM1 (I_{L1}) state variable

The Bode plot from fig.2.62 shows that the PWMSM AC response for the switching capacitor cell is unstable. The result is similar with the one obtained with the SSA procedure and it does not affect the stability of the output voltage on the filter capacitor.

In fig.2.63 and fig.2.64 are shown the Bode plots for the currents through L_1, respectively L_2 inductors. Their behavior is unstable and the results confirm the ones obtained with SSA method.

In step-up operating mode, the BHDC offers the required output voltage and it has a stable behavior. Still, the control is based on the control of the currents through the L_1 and L_2 inductors and the voltage over the switching capacitor cell. The results of the stability analysis show that a compensation function may be needed in order to control the system.

2.3.2.3. PWMSM for bidirectional converter with two DC voltage sources

The analysis of the proposed converter with PWMSM in a two DC voltage sources configuration is realized using different models in TINA TI. The differences do not change the converter topology, they only set the direction of the energy flow by introducing a resistive load connected in parallel with the source on the side that receives energy. The PWMSM equivalent circuits are the same ones presented in step-down and step-up configurations with additional DC sources connected in parallel with the resistive loads.

Based on this hypothesis, stability information of the system are obtained twice depending by the direction of the current. In fig.2.65 is presented the PWMSM simulation model when the current flows from a 400 V DC source to a 50 V DC source and supplies a 2 kW resistive load.
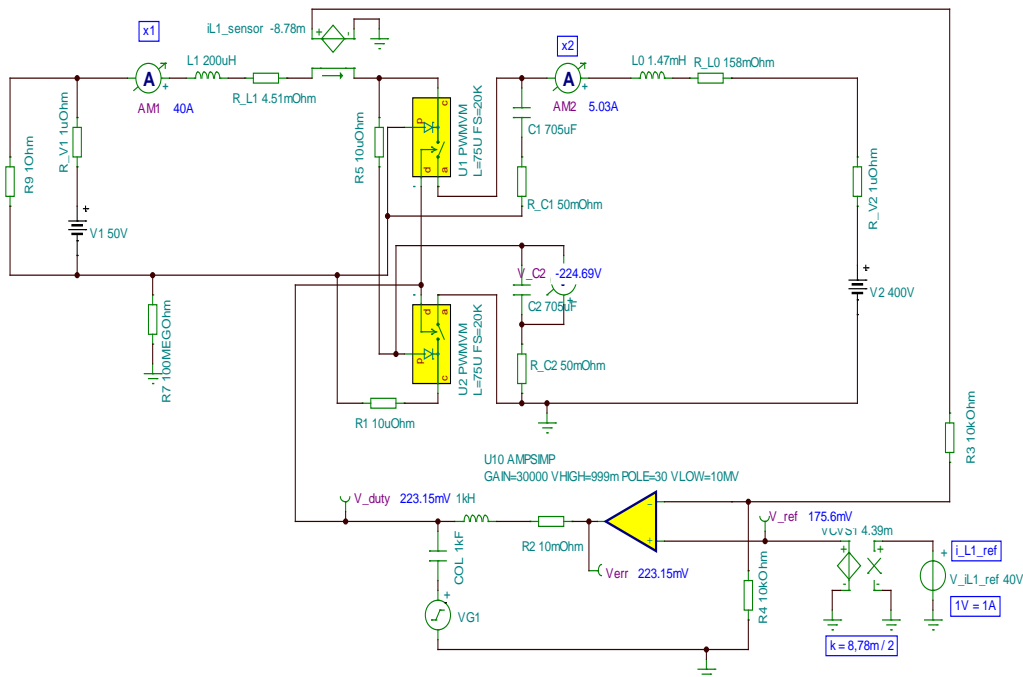
Fig.2.65. Dual voltage source PWMSM circuit in step-down mode

In the following, the AC response of the system is presented in comparison with the SSA, highlighting the main state variables, which are the currents through the L_1 and L_2 inductors and the voltage over the SCC. The AC responses for the currents are shown in fig.2.66 and fig.2.67. The results are almost similar with the ones obtained with the SSA method. For each state variable a comparison is made between the two methods. Operating as an interface between two voltage sources makes the stability of the state variables corresponding to the inductors currents mandatory. From the Bode plots, it can be seen that they have an unstable behavior and a compensation function has to be integrated in the system to improve the stability.

In fig.2.68 is presented the Bode plot corresponding to the voltage over the switching capacitor cell. With the results close to the ones obtained with SSA procedure, even if this state variable AC response is stable, it does not improve the overall BHDC stability.

The little differences between the Bode plots obtained with the SSA method and the ones obtained with the PWMSM method appear because of the both procedures particular features. Even so, the BHDC stability analysis with the two procedures has appropriate results and their similarities validate them.
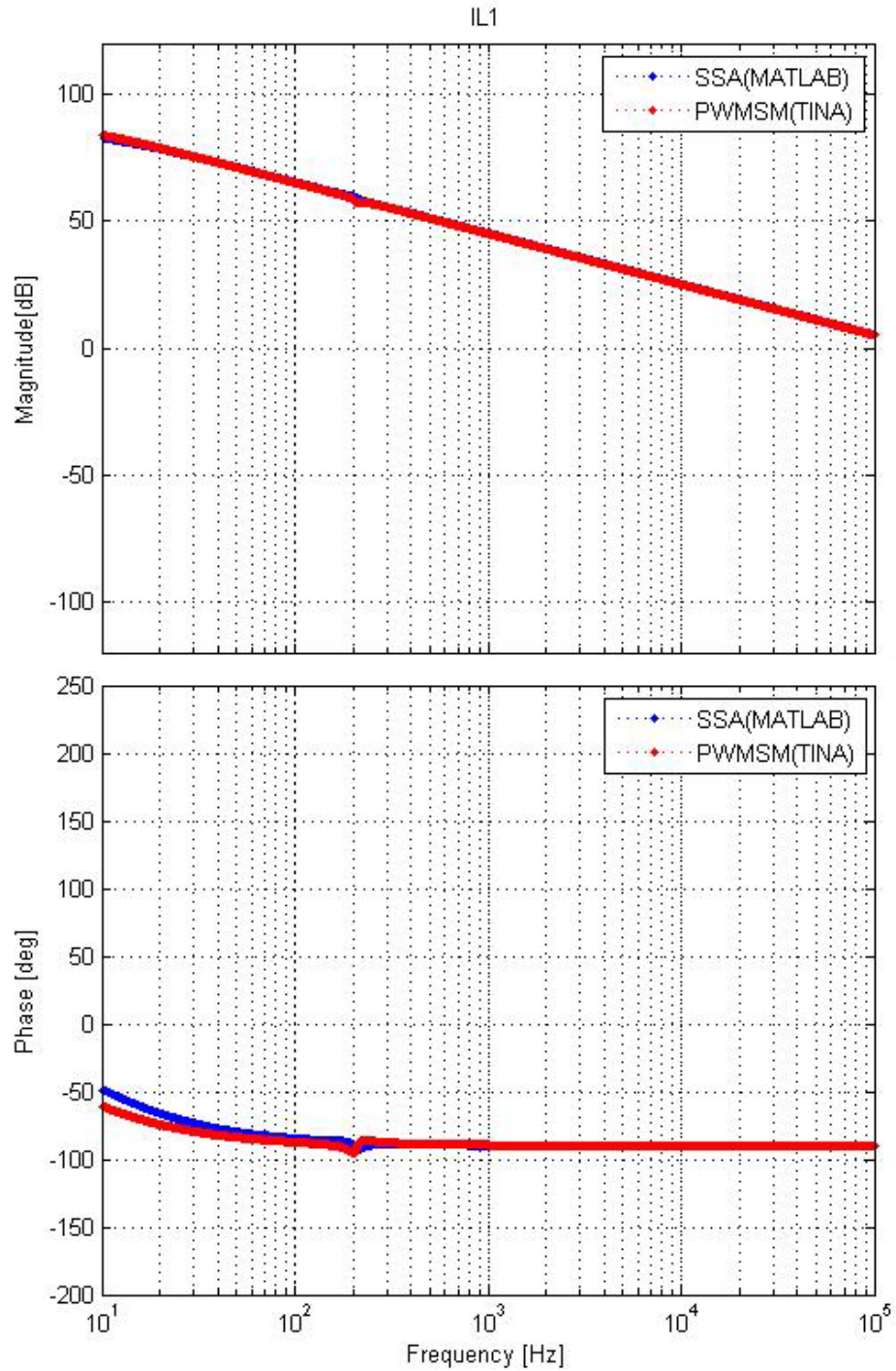
Fig.2.66. Bode plot for the IL_1 state variable
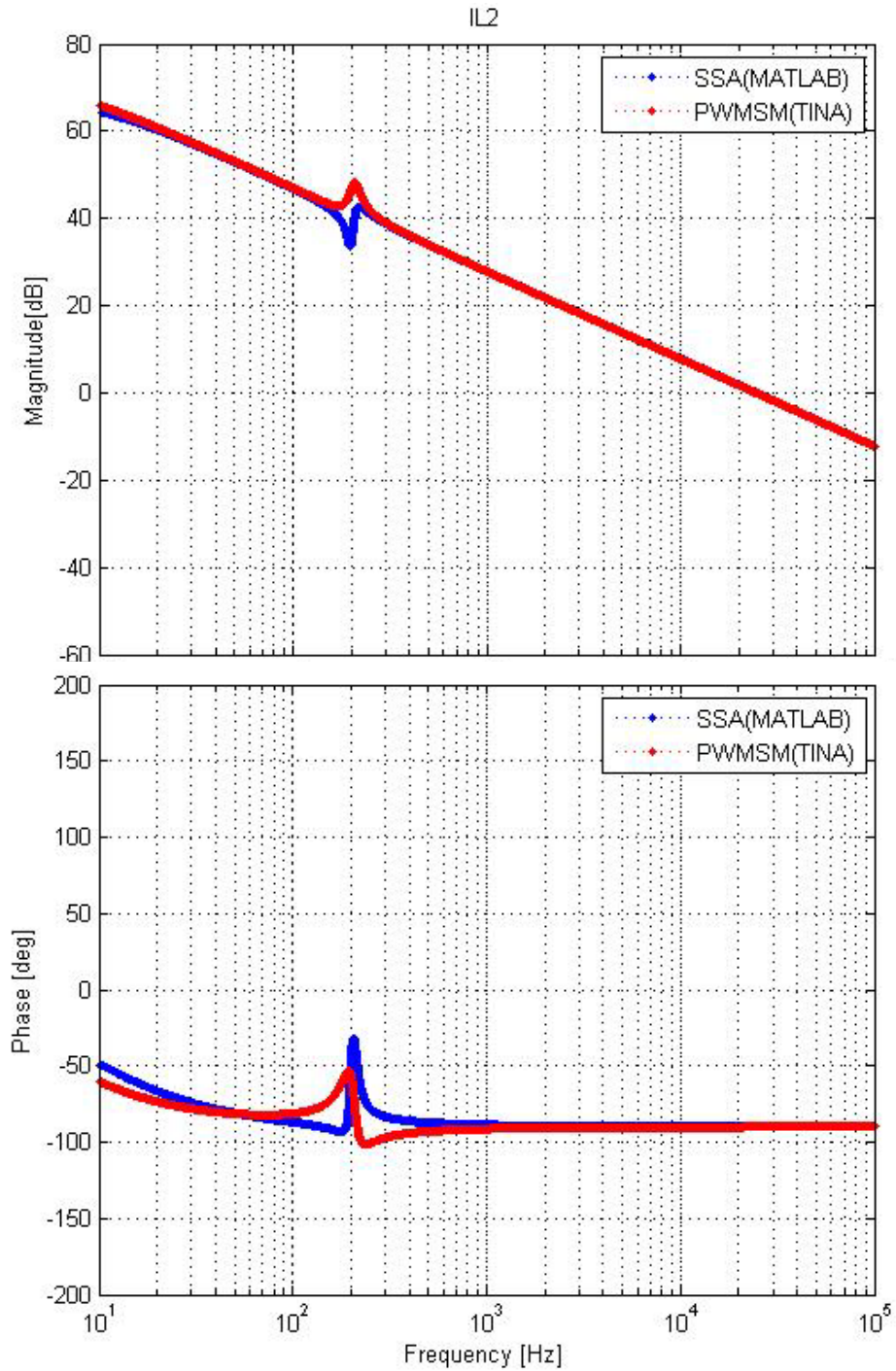
Fig.2.67. Bode plot for the IL_2 state variable
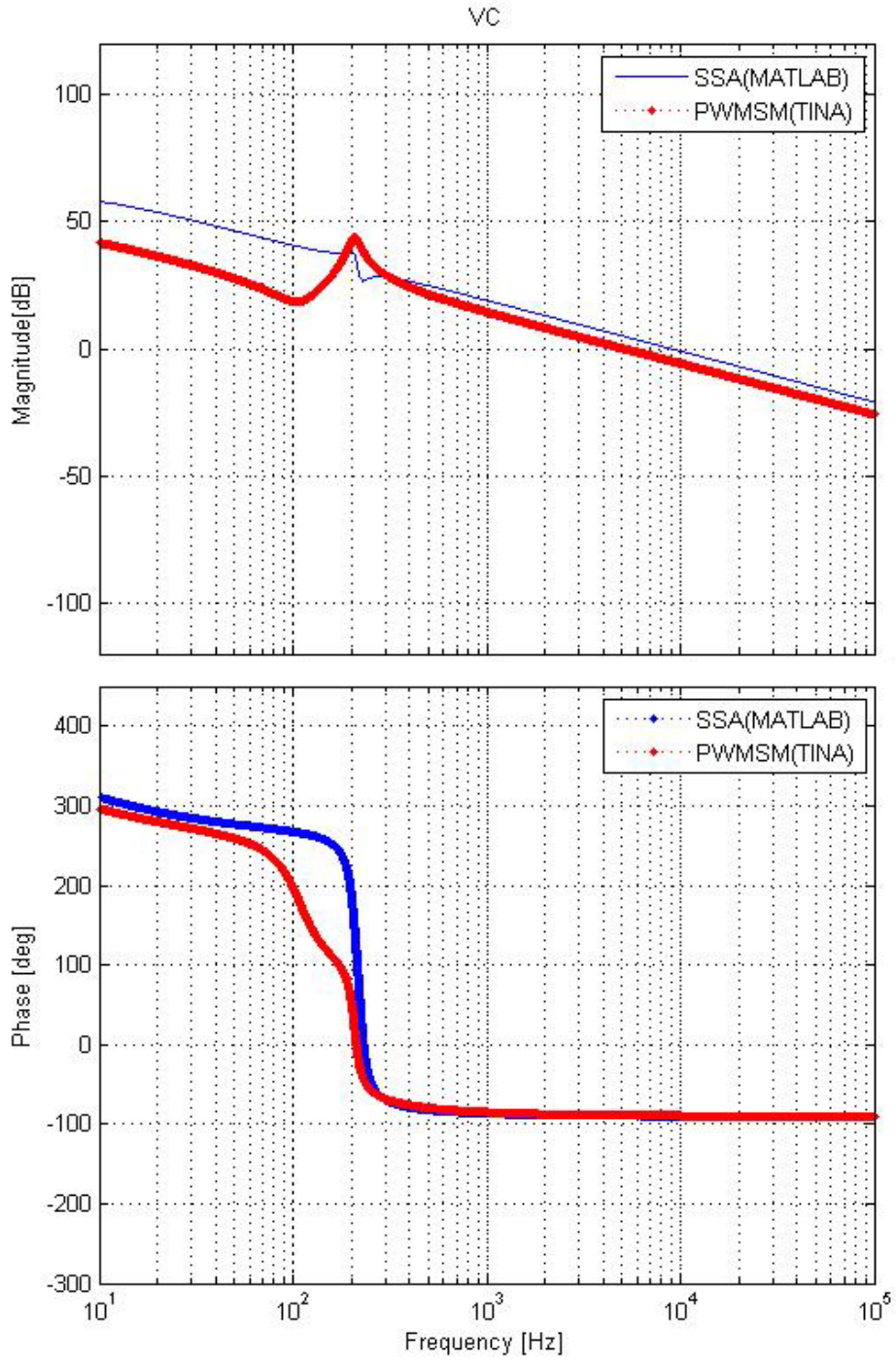
Fig.2.68. Bode plot for the V_C2 state variable

In fig.2.69 is presented the PWMSM simulation model when the current flows from a 50 V DC source to a 400 V DC source and supplies a 2 kW resistive load. The control of the system is based on the current through the L_1 inductor control, so its stability is mandatory. A new stability analysis of BHDC is realized using the corresponding energy flow direction and the following PWMSM equivalent circuit.
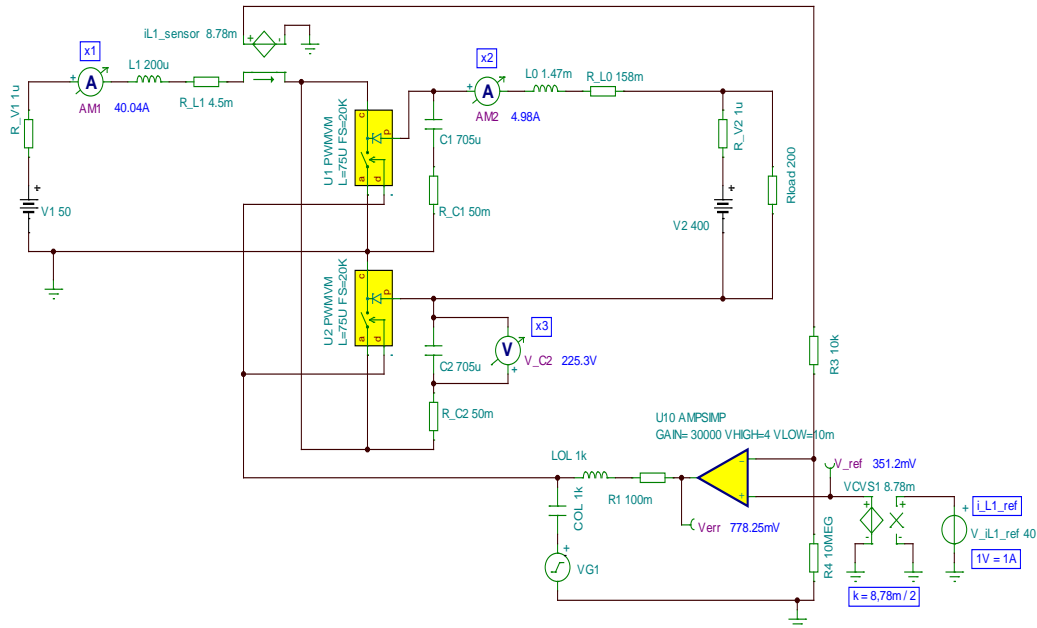
Fig.2.69. Dual voltage source PWMSM circuit in step-up mode

In the following the AC responses of the system state variable are presented in comparison with the ones obtained with the SSA method.

In fig.2.70 is presented the Bode plot corresponding to the current through the L_1 inductor. Since it shows an unstable behavior and the cutting frequency is far from the normal operation frequency, a compensation function is needed to obtain a proper cutting frequency.

In fig.2.71 is shown the Bode plot for the current through the L_2 inductor. The stability is close to be reached but the cutting frequency is very close to the normal operation frequency. Even if its behavior is better, it depends by the current through L_1 inductor. The BHDC control compensation will be realized considering the AC response of the I_{L1} state variable small signal transfer function.

 In fig.2.72 is presented the Bode plot for the voltage over the switching capacitor cell. Even if it is stable, it does not change the overall BHDC stability when the energy flow direction is from the lower voltage source to the higher voltage source.

The small differences between the Bode plots come from each method particularities. Regarding the phase response, it is cyclic for each 360 degrees so we can conclude that big similarities exist between the results obtained with SSA and with PWMSM. Because the system is unstable, a compensation function is introduced in the control system, in order to gain the needed stability of the BHDC.
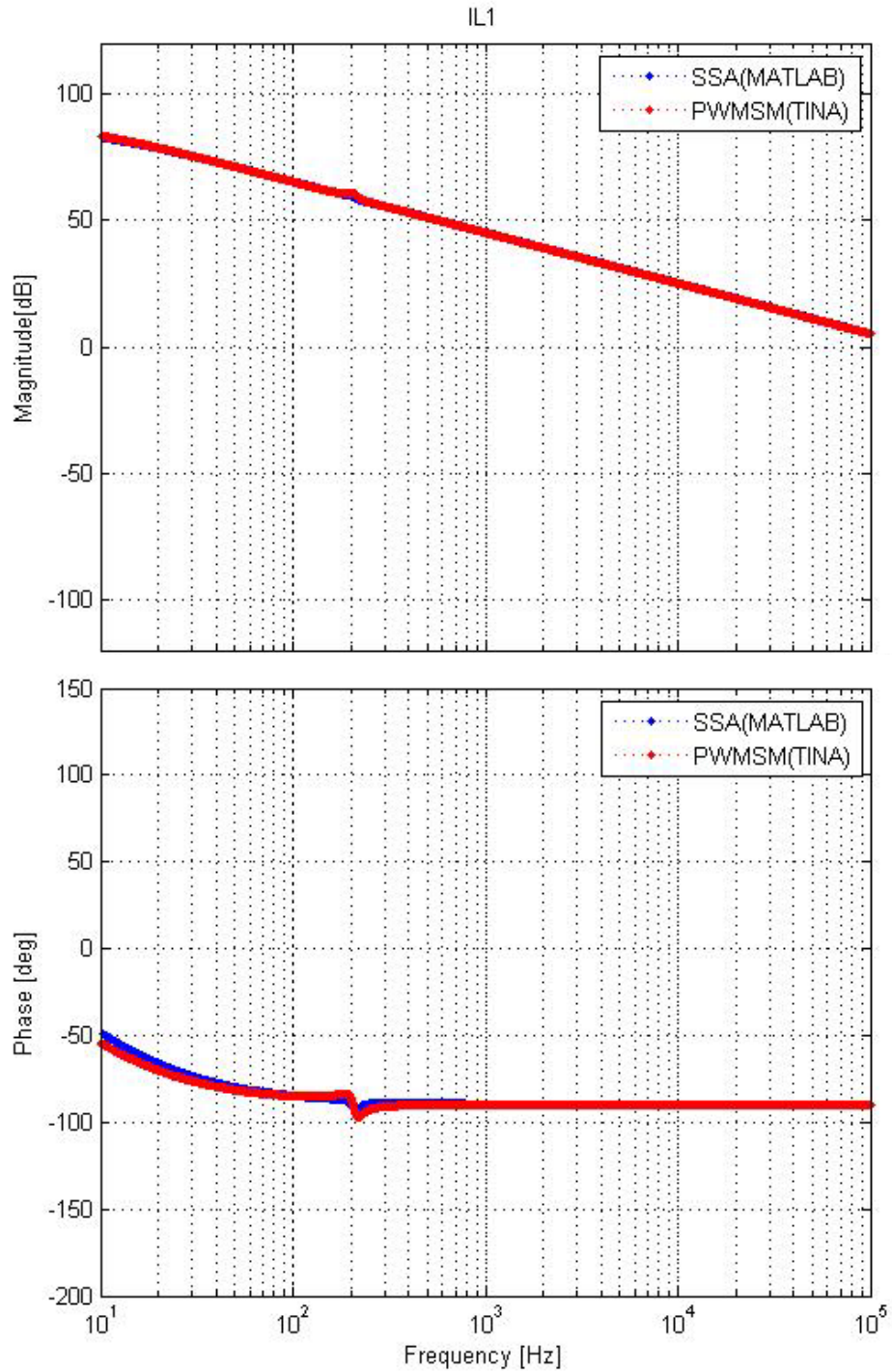
Fig.2.70. Bode plot for the IL_1 state variable
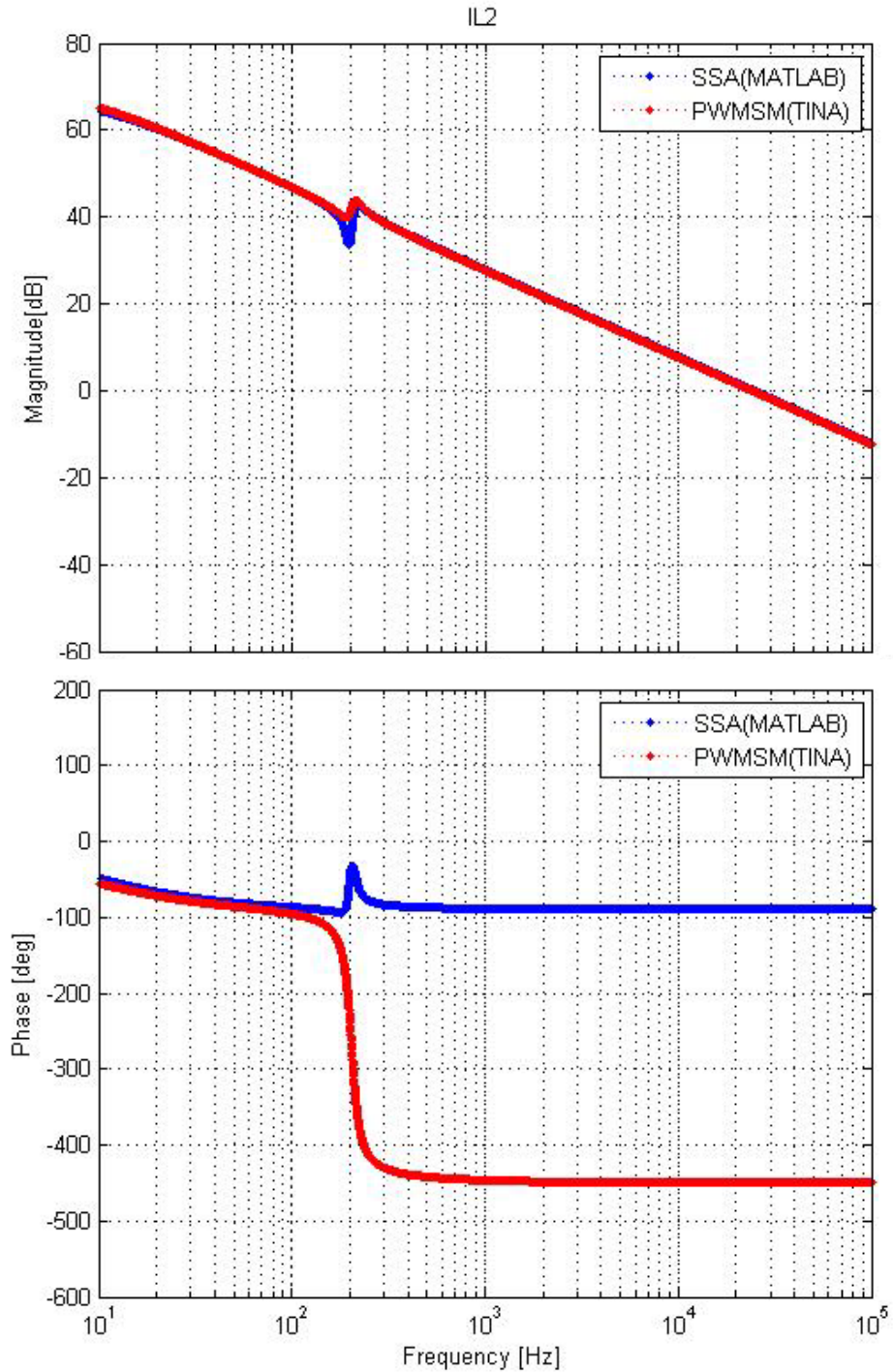
Fig.2.71. Bode plot for the IL_2 state variable
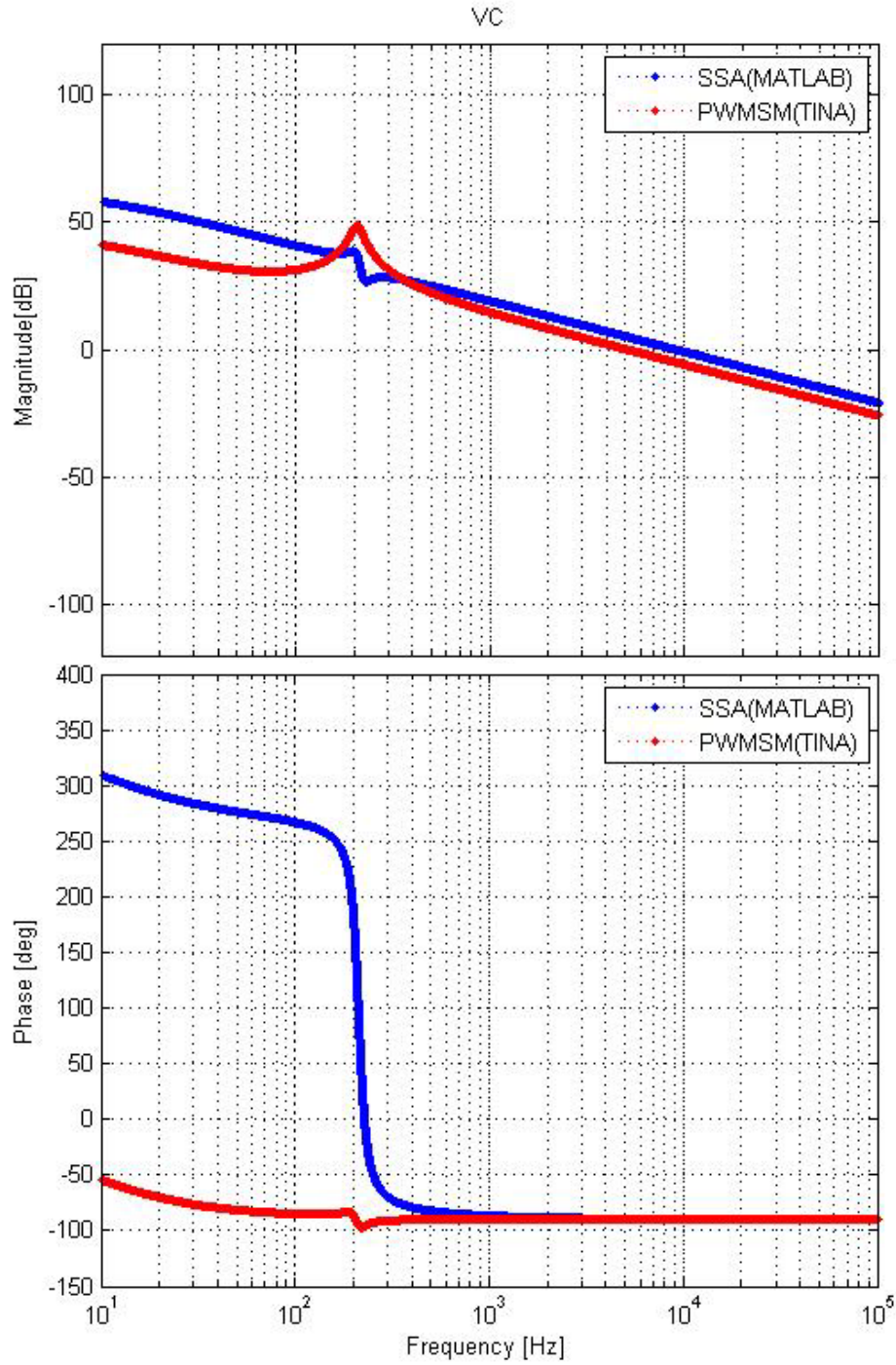
Fig.2.72. Bode plot for the VC state variable

2.3.3. Stability improvements tested with SSA and PWMSM

As shown in the previous subchapters, the proposed converter presents several problems regarding the system stability. In order to obtain a stable operation against various perturbations, the system has to be compensated. The stability improvement is seeking for larger phase reserves at the cutting frequencies for the main state variables. Only the normal operation with two voltage sources and bidirectional current flow is considered in this section for the stability analysis.

The compensation was realized in Matlab, by updating the SSA m-functions with the compensation function. The results are verified with PWMSM by adapting the simulation models. The current through the inductor L_1 needs more attention, due to its high value and the problems that may occur in the circuit if its operation gets out of control. The compensation made for the stability improvement is close related to I_{L1} state variable and it is highlighted in the resulted Bode plots.

The transfer function used in the stability analysis with SSA, is therefore adjusted with a compensation function Hr, in order to increase the phase reserve at a cutting frequency. In the same time, the magnitude is lowered for a faster response with low oscillations. The compensation function Hr was obtained in Matlab and it introduces an amplitude gain and a phase boost at the cutting frequency through an additional zero and two poles. The results were presented in section 2.3.2.3 and they are compared with the results obtained using PWMSM and the compensation is introduced in the simulation model, fig.2.73.
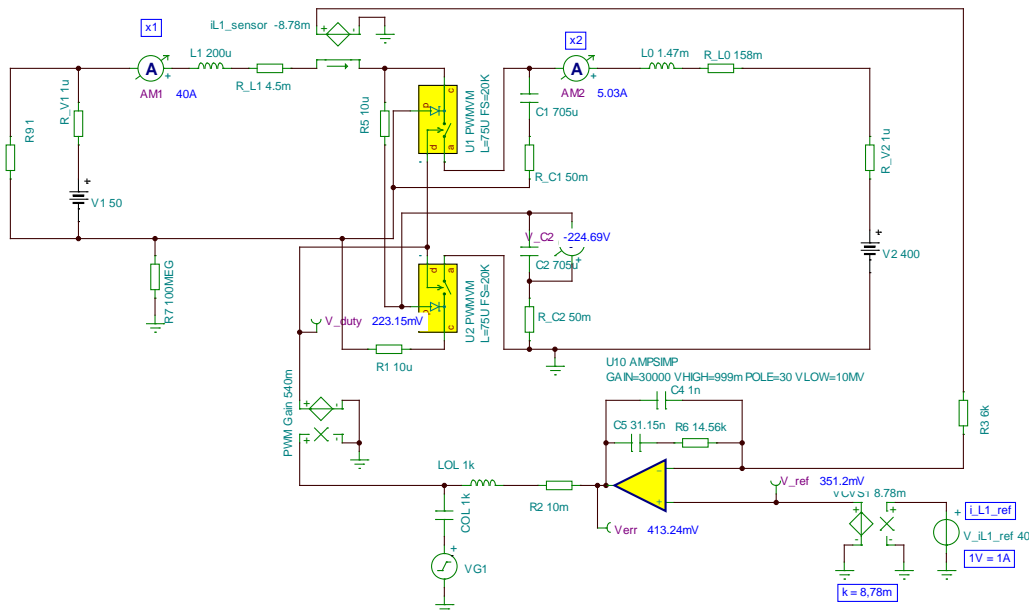
Fig.2.73. PWMSM circuit in step-down mode with compensation

The simulation model used for the AC response in Tina follows the results obtained with SSA. Practically, the same compensation function Hr is transformed in an operational circuit capable to increase the stability and get a desired phase boost at the crossover frequency. The compensation is realized through observation of the open loop Bode plot of the state variable which operation we want to stabilize. It consists of deriving a k factor, which indicates the necessary distances between the frequency positions of the poles and zeros that have to be brought by the compensation network. In fig.2.74.a, b and c is presented how this calculated k factor places the poles and zeros in order to obtain the desired crossover frequency as a geometric mean between these points.
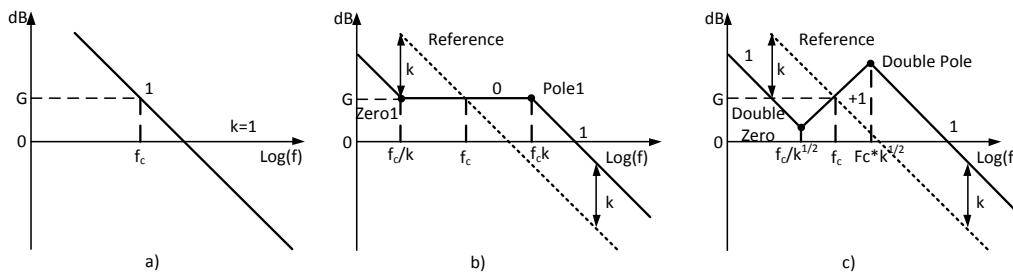
Fig.2.74.a), b), c)- The K factor action in obtaining the desired phase boost at the crossover frequency by adjusting the positions of poles and zeros

The compensation needed for our system is a compensation function that adds to the initial transfer function a pole and two zeros, in order to improve the AC response of the I_{L1}, in the purpose of a better control of the current through L_1. In fig.2.75. a *type 2* amplifier circuit is presented. It is used in our PWMSM and it represent the solution for a phase boost.
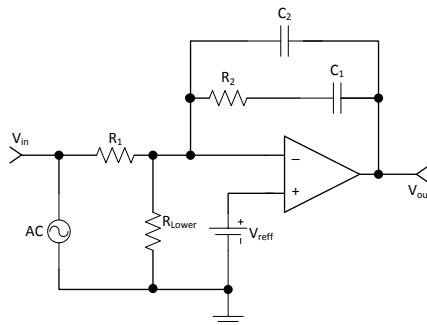
Fig.2.75. A type 2 amplifier for phase boost

In this circuit, the compensation function is obtained as a few lines of a Laplace equation (2.150):

$$Hr = \frac{1 + sR_2C_1}{sR_1(C_1 + C_2)(1 + sR_2 \frac{C_1C_2}{C_1 + C_2})}$$

(2.150)

In the fig.2.76 a comparison is presented between the SSA and PWMSM results, obtained with compensation.
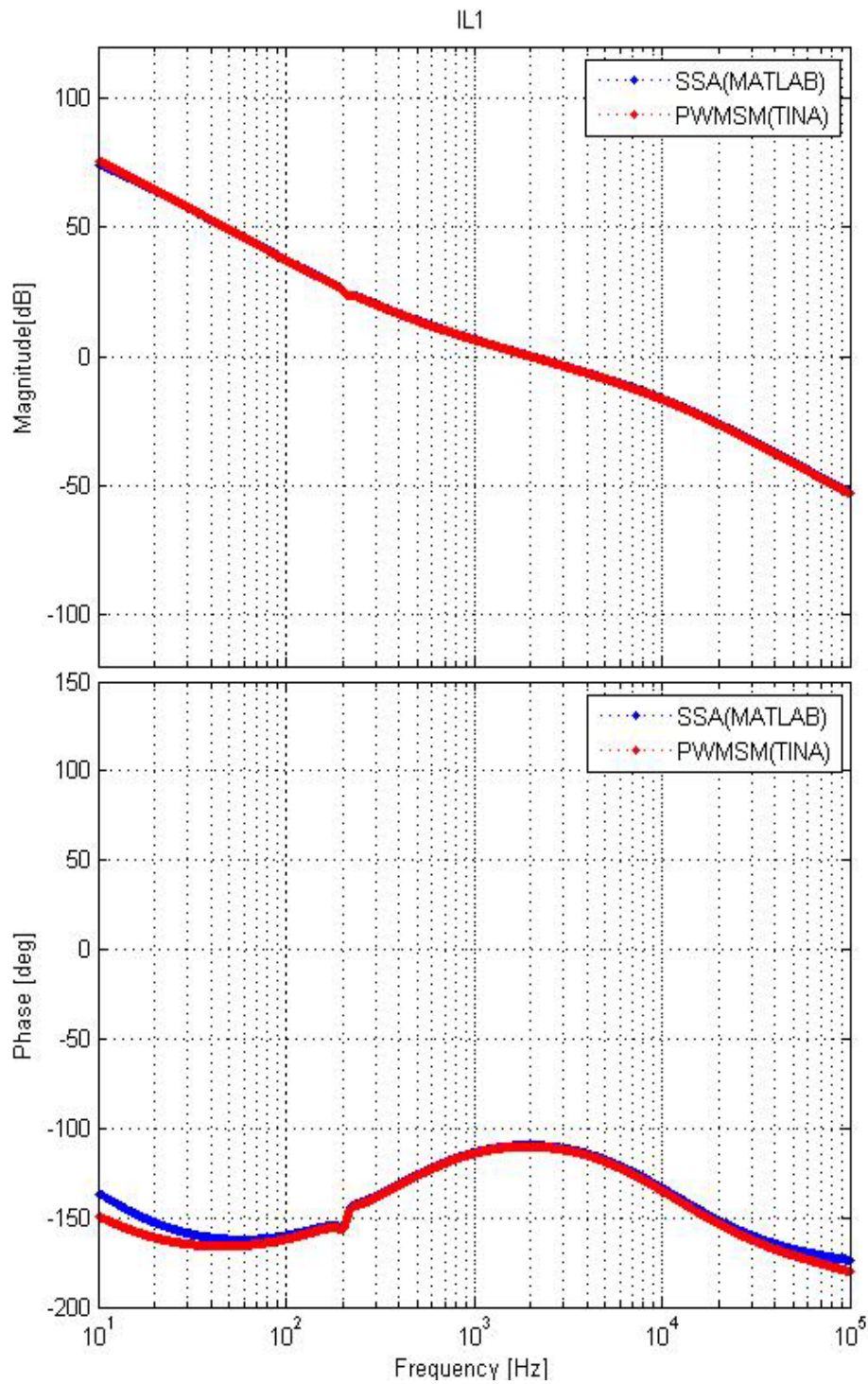
Fig.2.76. Bode plot for the IL_1 state variable with compensation

The compensation function lowers the cutting frequency down to 2kHz, which is very reasonable thinking to the fact that the normal operation frequency is 20kHz. The second advantage is related to the phase reserve which is boosted up to 70 degrees at the related cutting frequency.

In fig.2.77 the compensation circuit is introduced in the equivalent step-up PWMSM circuit of BHDC, operating as an interface between two voltage sources.
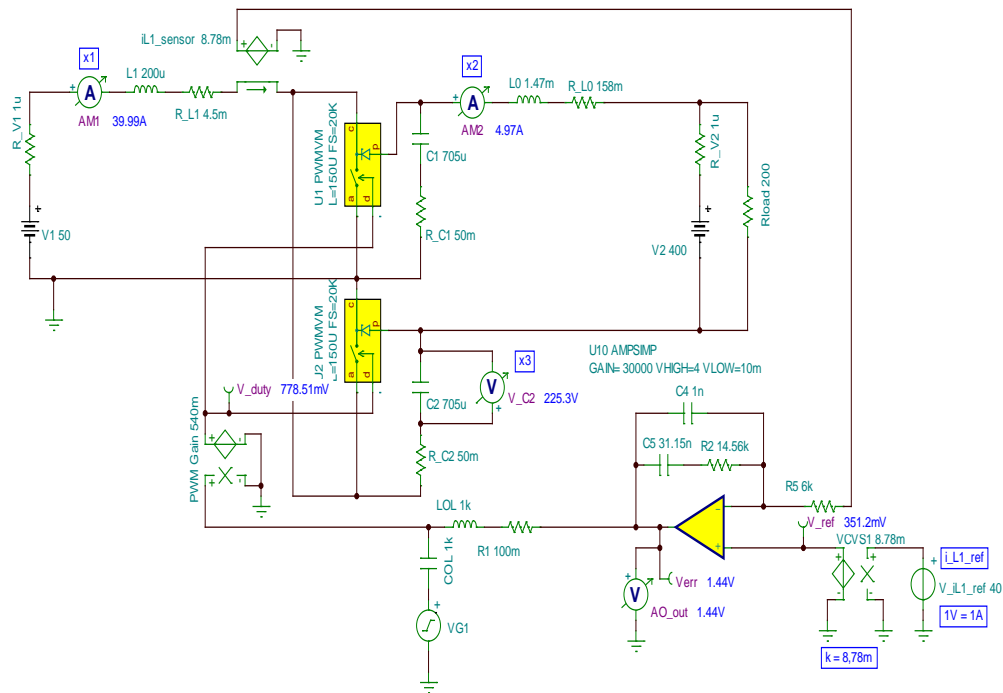
Fig.2.77. PWMSM circuit in step-up mode with compensation

In fig.2.78 are presented the Bode plots for the I_{L1} state variable with compensation. The results obtained with the PWMSM validate the ones obtained with the SSA method and they both confirm the compensation function effectiveness. The compensation circuit integrated in BHDC operating in this mode is lowering the cutting frequency down to 2 kHz and a phase reserve of 70 degrees is reached.

Due to the fact that the control is based on the monitoring of I_{L1}, its stability determines the stability of the entire system. In order to check and validate the stability analysis results, the PWMSM equivalent circuits are simulated in transient mode. This way is verified the capability of the BHDC PWMSM circuit to follow a reference waveform given for the current through L_1 inductor. The results are confirmed using a simulation model realized in Psim with real models for the semiconductors.
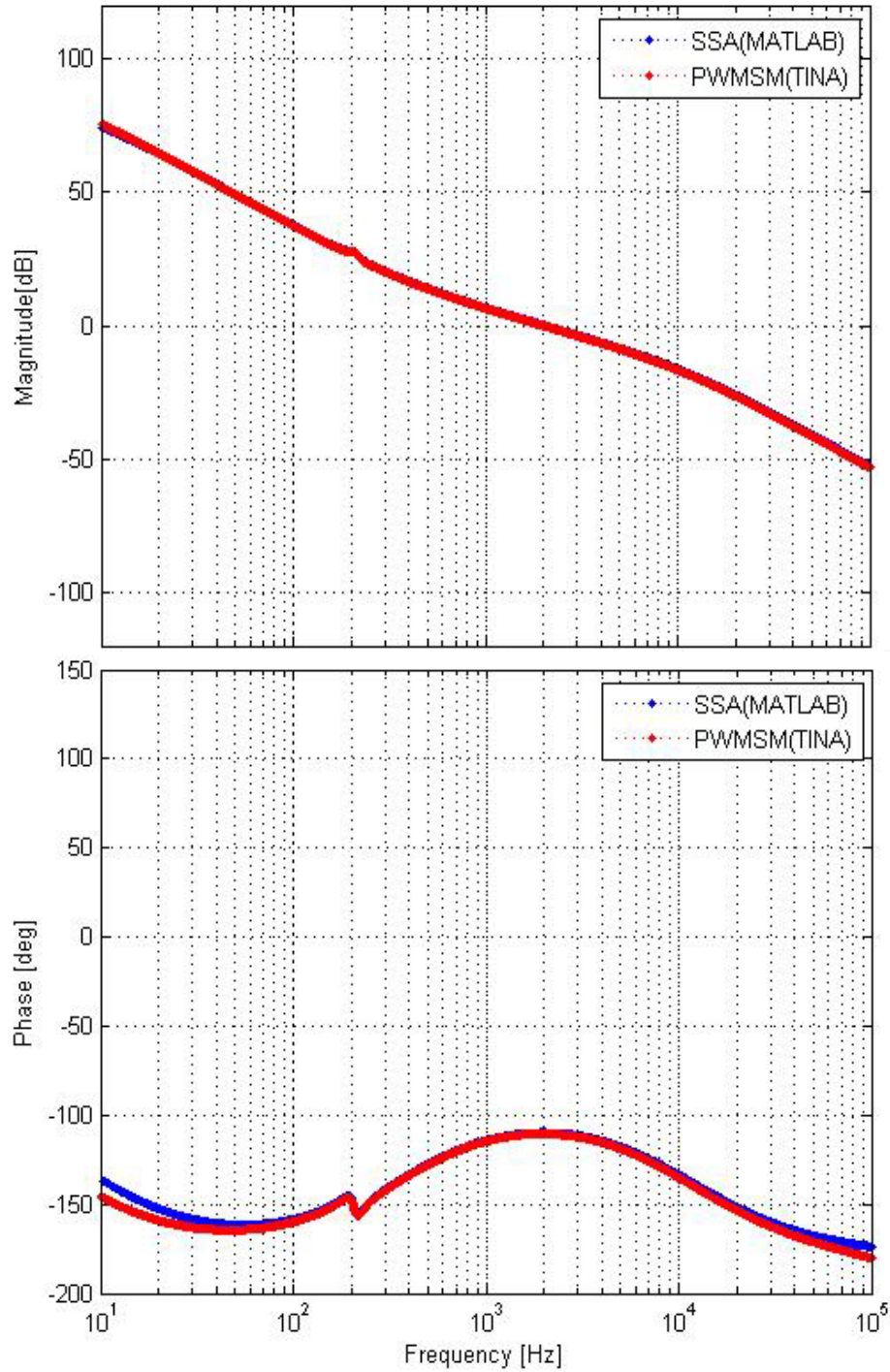
Fig.2.78. Bode plot for the IL_1 state variable with compensation

2.4. Digital simulations

The information regarding the proposed bidirectional DC-DC converter obtained after the analytical study, the stability and compensation analysis are used at the prototyping procedure. Before this, all the results are verified through simulation using the PWMSM with compensation in transient mode and with a step signal reference for I_{L1}, in order to verify how fast the BHDC can operate at different values of the current and how high are the oscillations. A second validation is made with the same compensation circuit, but this time applied to a spice model of BHDC realized in PSIM with real models for the semiconductors.

2.4.1. Digital simulations of BHDC in step-down mode

In fig. 2.79 is presented the simulation model of BHDC using PWMSM during a transient process. It is used to obtain the waveforms for the currents through L_1 and L_2 inductors.
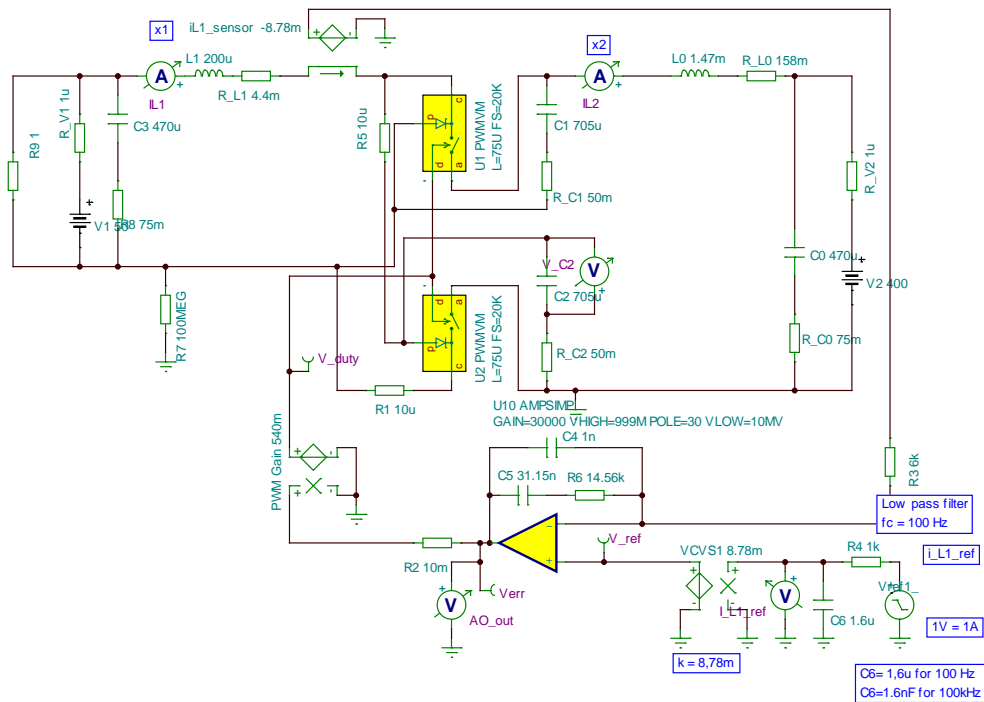
Fig.2.79. PWMSM simulation circuit in transient step-down mode

In fig.2.80 are presented the waveforms for the currents I_{L1} and I_{L2} for a step signal reference at different values passed through a 100 Hz filter. The results show that the proposed converter is able to follow a given reference signal.
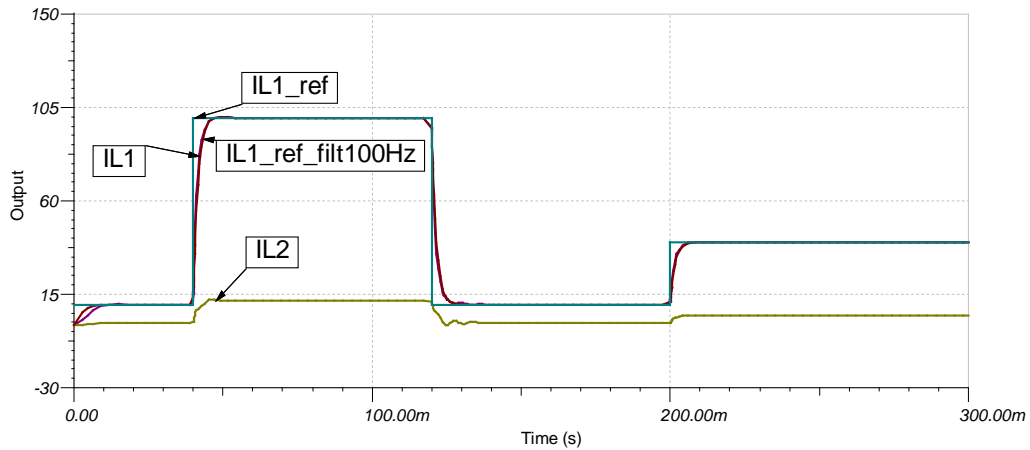
Fig.2.80. I_{L1} Reference signals with 100 Hz filter and I_{L1} and I_{L2} PWMSM simulation waveforms

In fig.2.81 the same waveforms are represented using a 100 kHz filter for the reference signal. Adding this filter, forces the converter to operate following a more severe reference signal.
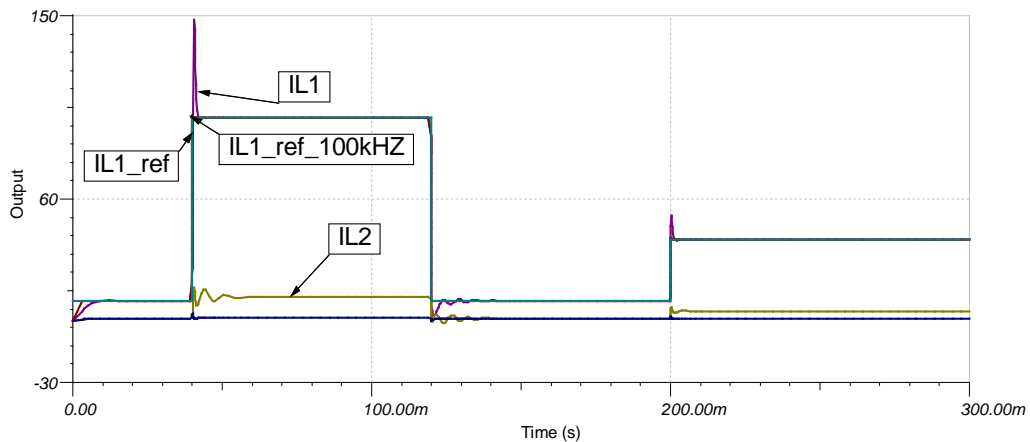
Fig.2.81. I_{L1} Reference signals with 100 kHz filter and I_{L1} and I_{L2} PWMSM simulation waveforms

The BHDC is simulated in the following using Psim software in order to observe the operation using real models for the semiconductors. The simulations are realized using the same compensation circuit used in TINA for the PWMSM. The reference signal is also identical, so the results comparison will be used for the digital validation of the proposed circuit working as an interface between two DC buses when the energy flows from the upper voltage source to the lower voltage source, injecting a maximum power of 5 kW. The Psim simulation circuit is presented in fig.2.82.
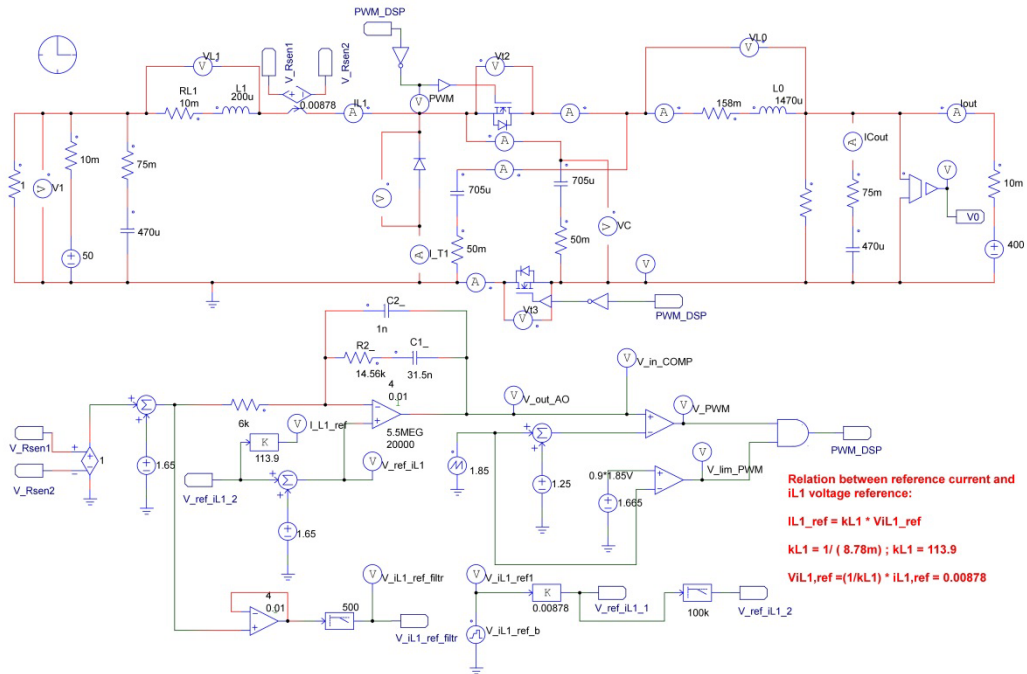
Fig.2.82. PSIM simulation circuit in transient step-down mode

In fig.2.83 and 2.84 are presented the simulation results obtained using Psim. Despite the variations of the waveforms introduced by the semiconductors models, which are normal since no mediation is done, it can be seen that the waveforms are similar with the ones obtained previously using PWMSM.
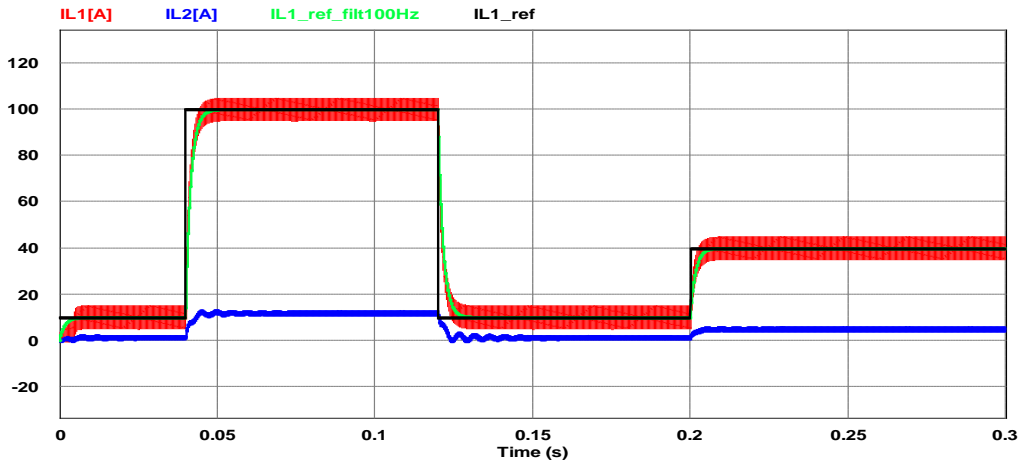
Fig.2.83. I_{L1} Reference signals with 100 Hz filter and I_{L1} and I_{L2} PSIM simulation waveforms
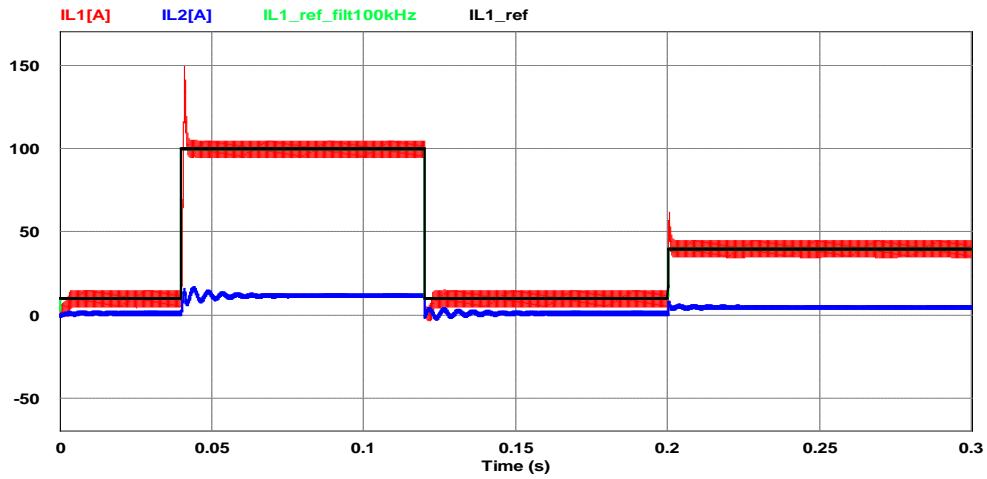
Fig.2.84. I_{L1} Reference signals with 100 kHz filter and I_{L1} and I_{L2} PSIM simulation waveforms

2.4.2. Digital simulations of BHDC in step-up mode

The PWMSM step-up simulation circuit is run in transient mode in order to obtain the I_{L1} and I_{L2} currents through the inductors when the energy flows from the lower energy source to the upper one. The step reference signal for the I_{L1} current used in the simulation is passed through a 100 Hz and a 100 kHz filter using the simulation circuit from fig.2.85.
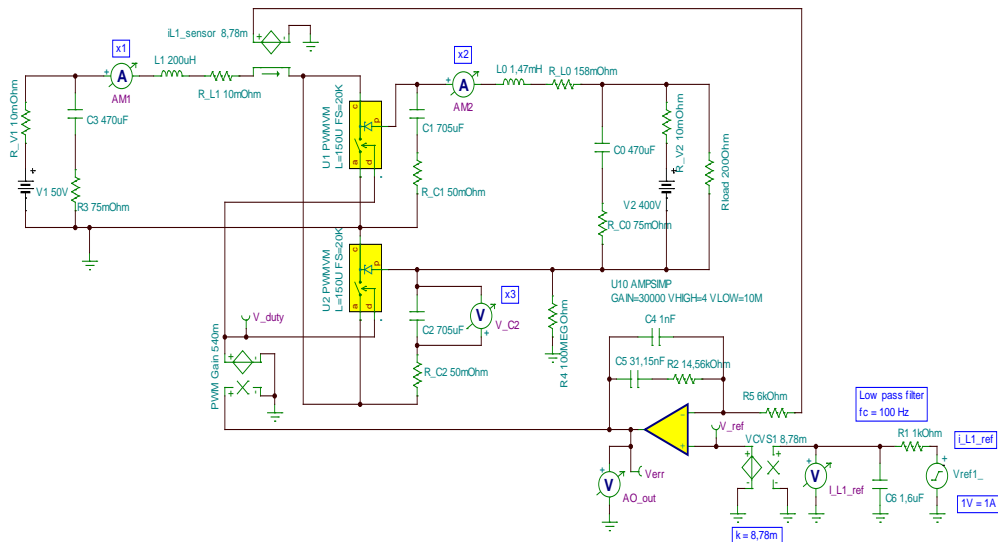
Fig.2.85. PWMSM simulation circuit in transient step-up mode

The waveforms obtained with the PWMSM simulation model are presented in fig.2.86 using a first order low-pass filter at with the cutting frequency at 100 Hz and in fig.2.87 using the same filter but with the cutting frequency at 100 kHz.
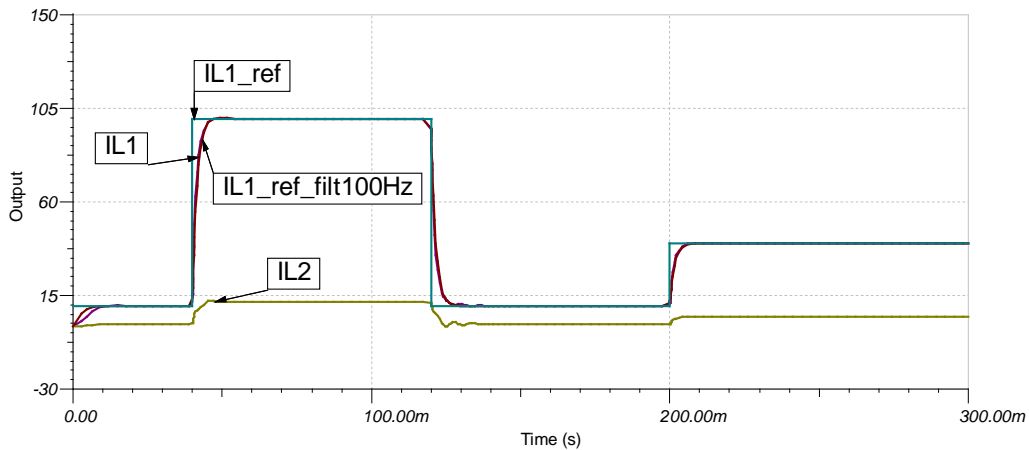
Fig.2.86. I_{L1} Reference signals with 100 Hz filter and I_{L1} and I_{L2} PWMSM simulation waveforms
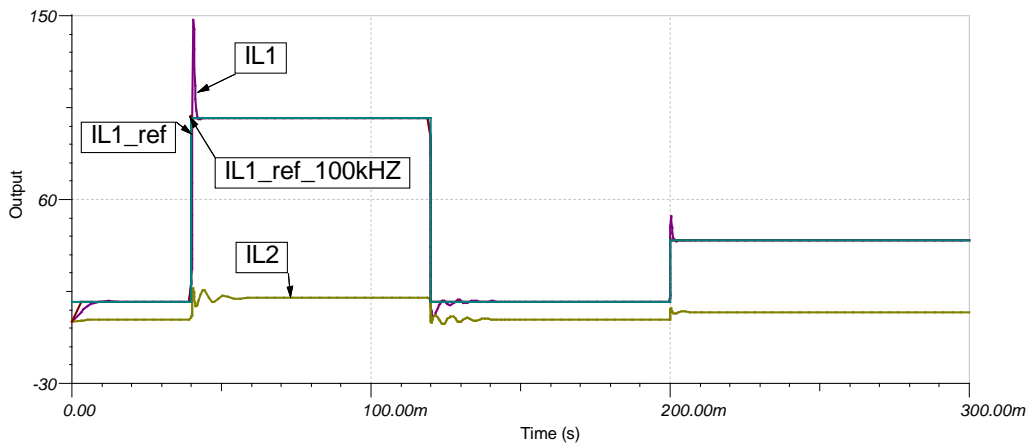
Fig.2.87. I_{L1} Reference signals with 100 kHz filter and I_{L1} and I_{L2} PWMSM simulation waveforms

The BHDC is simulated in the following operating in step-up mode using Psim. The simulations are realized using the same compensation circuit used in TINA for the PWMSM. The reference signal is identical, so the results comparison will be used for the digital validation of the proposed circuit working as an interface between two DC buses when the energy flows from the lower voltage source to the upper voltage source, injecting a maximum power of 5 kW. The Psim simulation circuit is presented in fig.2.88.
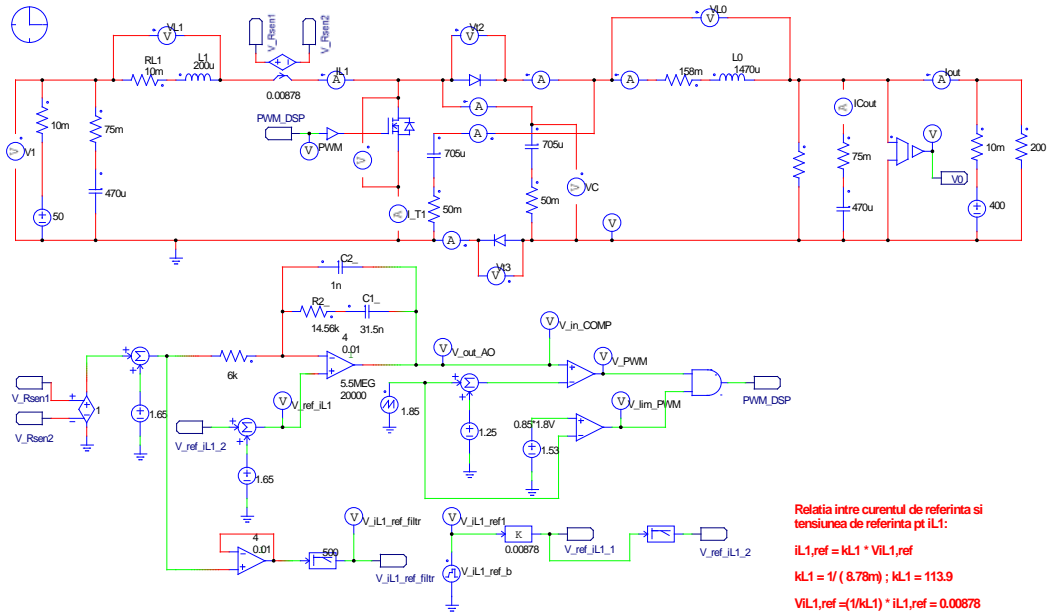
Fig.2.88. Psim simulation circuit in transient step-up mode

The simulation waveforms of the above circuit are presented in fig.2.89 and fig.2.90. The waveform shapes follows the ones obtained using the PWMSM and validate once again the good operation of the converter.
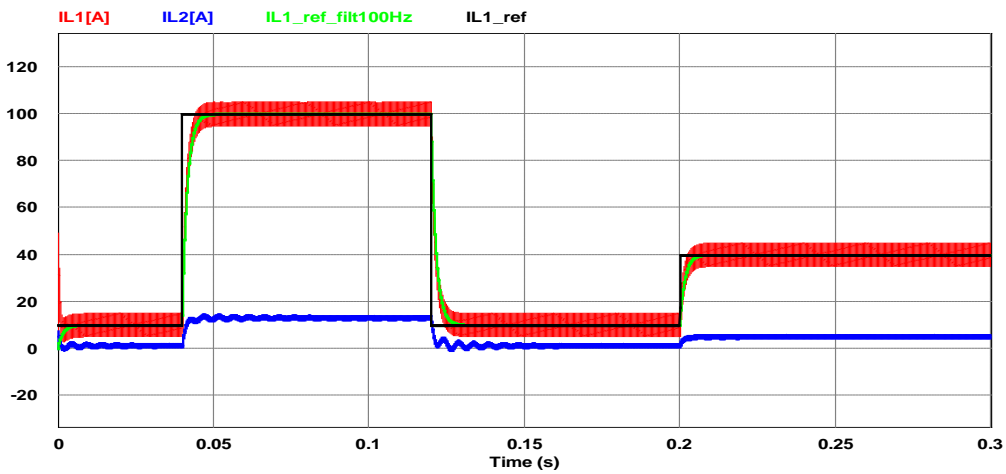
Fig.2.89. I_{L1} Reference signals with 100 Hz filter and I_{L1} and I_{L2} PSIM simulation waveforms
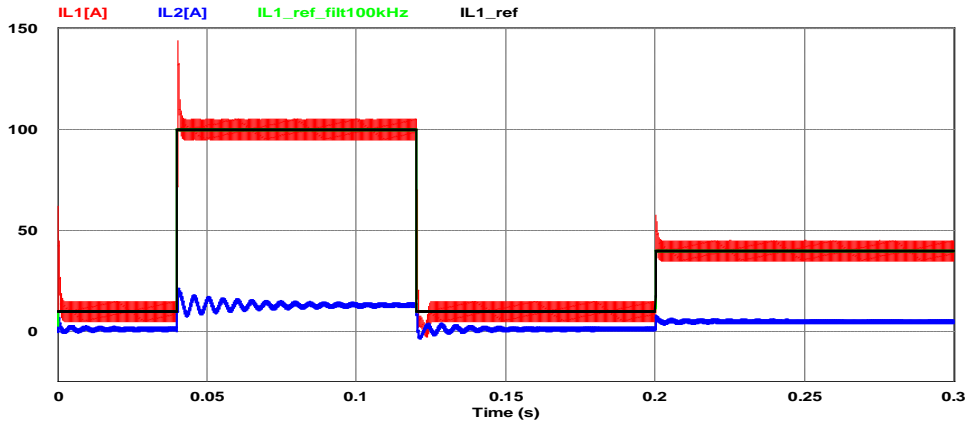
Fig.2.90. I_{L1} Reference signals with 100 kHz filter and I_{L1} and I_{L2} PSIM simulation waveforms

2.4.3. Digital simulations of BHDC

The presented simulation results show that BHDC can operate smoothly in both step-down and step-up mode, following rough reference inputs. The next simulation model presented in fig.2.91 shows the last BHDC configuration with the switching control circuit and protections, exactly how they are built in the prototype.
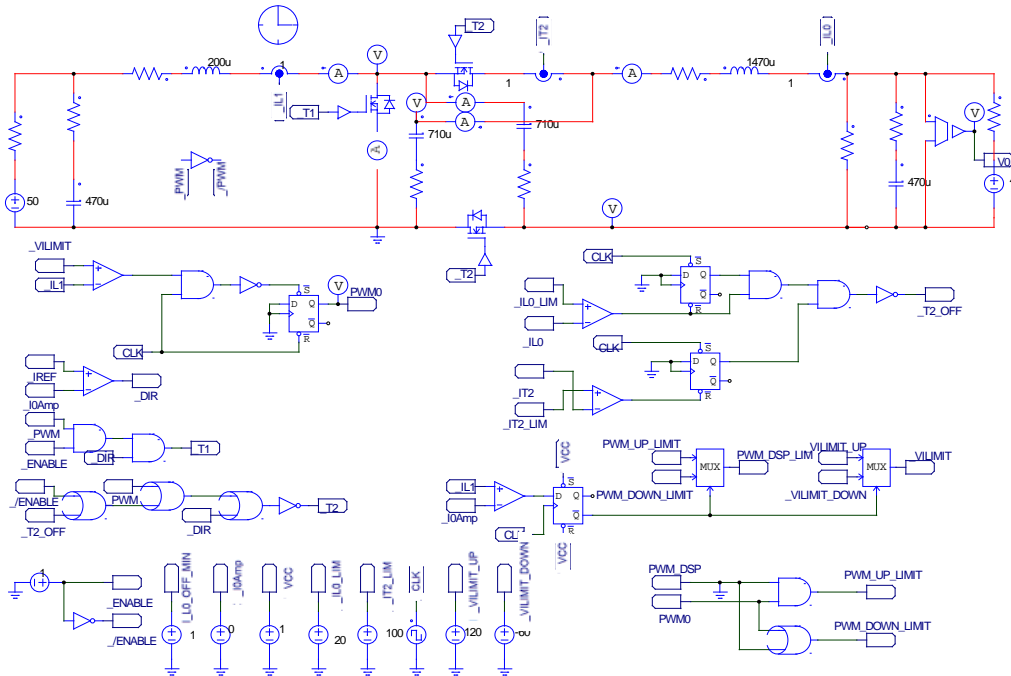
Fig.2.91. BHDC simulation circuit

In fig.2.92 is presented the switching control circuit with the compensation function additional circuit integrated.

Fig.2.92. BHDC switching control and compensation circuit

The presented simulation models are used to obtain all the needed waveforms in order to validate the normal operation of the proposed BHDC. All the existing limitations are physically integrated in the experimental prototype. Their goal is to protect the components and the grid every time a malfunction is detected. Several current and voltage sensors are used for determination of the parameters on different circuit meshes. Based on the experimental prototype constraints, all the information received from the sensors are compared with some maximum values compatible with the physical components.

In fig.2.93 are presented the simulation waveforms of the currents through the L_1 and L_2 inductors during several reversals of the current at different values. The BHDC control is based on the I_{L1} monitoring and the waveforms validate the proposed control because it follows with very low oscillations a reference waveform during fast reversals of the energy flow at relative high currents. The I_{L2} current has higher oscillations but for a short time. The waveforms of the currents through the S_1, S_2 and S_3 semiconductors highlight the good operation of the semiconductors. Because these currents do not reach harmful levels confirm that the proposed control circuit is working well. In conclusion, the current flow reversal is realized by BHDC in a smooth mode and the current change its direction in an effective manner with a very low stress for the semiconductors and the other passive components.

Fig.2.93. BHDC current waveforms for I_{L1} following the reference, I_{L2}, I_{S1} and I_{S2_3}

2.5. Experimental prototype and results

The positive results of the simulations led to the start of the prototype design. The design of the power stage circuit is presented in the following. Comparisons are made between the prototype experimental results and the results obtained from simulations of the full power stage and switching control circuit model.

2.5.1. Experimental prototype design

The power stage circuit of BHDC is presented in fig.2.94. The connectors J_1 and J_2 serve for the L_1 coupling and J_5 and J_6 serve for L_2. The BHDC capacitors have a modular configuration and they are presented separately. The filter capacitors C_i and C_o are connected between VP50 and GND_50, respectively VP400 and GND_400. The switching cell capacitor C_1 is connected between VC1 and GND_400 respectively C_2 between VC2 and GND_50.
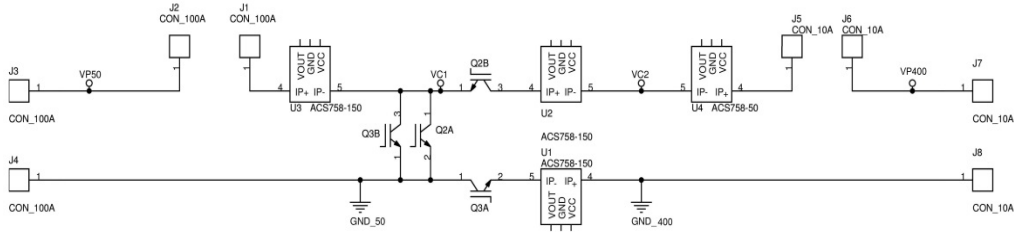
Fig.2.94. Power stage circuit schematic

➢ **Capacitors C_1, C_2, C_i, C_0 dimensioning:**

Considering $C=C_1=C_2$, during t_{off} the capacitors are discharged in series from the input voltage and during t_{on} they are charged in parallel. Assuming a voltage ripple of y percent from the maximum voltage, results:

$$\Delta V_C = [y]\% \cdot V_{2,max} \qquad (2.151)$$

From the expression of currents through these capacitors during t_{on} the rated current through the switching cell capacitors is obtained in (2.152 and 2.153), the capacitor's capacity is obtained in (2.154):

$$i_C = C \cdot \frac{\Delta V_C}{\Delta t} \qquad (2.152)$$

$$i_C = \frac{1}{2} \cdot (I_1 - I_2) \qquad (2.153)$$

$$C = I_C \cdot \frac{\Delta t}{\Delta V_C} \qquad (2.154)$$

For C_0 it is also imposed a voltage ripple of y percent from the maximum output voltage through the capacitor:

$$\Delta V_{C_o} = [y]\% \cdot V_{2,max} \tag{2.155}$$

Considering (2.156), (2.157) and (2.158), the capacitance of C_0 is obtained in (2.159) and C_i in (2.160) :

$$\Delta V_2 = \frac{\Delta Q}{C_0} \tag{2.156}$$

$$\Delta Q = \frac{\frac{\Delta I_{L_2} \cdot T_S}{2}}{2} \tag{2.157}$$

$$\Delta V_2 = \frac{\Delta Q}{C_0} = \frac{1}{C_0} \cdot 2 \cdot \frac{T_s}{2} \cdot \frac{\Delta I_{L_2}}{2} \tag{2.158}$$

$$C_0 = \frac{T_S}{2} \cdot \frac{\Delta I_{L_2}}{\Delta V_{C_0}} \tag{2.159}$$

Assuming the same hypotheses, the expression of C_i is written in (3.182):

$$C_i = \frac{T_S}{2} \cdot \frac{\Delta I_{L_1}}{\Delta V_{C_i}} \tag{2.160}$$

Based on the above equations and calculations considering a 1% ripple of the voltages, the following capacitors configurations were chosen:

$$C_i - 4\text{X}470 \text{ uF}/400 \text{ V} + 10\text{X}470 \text{ nF} + 4\text{X}470 \text{ nF} \approx 470 \text{ uF};$$

$$C_0 - 4\text{X}470 \text{ uF}/400 \text{ V} + 10\text{X}470 \text{ nF} \approx 470 \text{ uF};$$

$$C_1 = C_2 - 6\text{X}470 \text{ uF}/400 \text{ V} + 6\text{X}470\text{nF} \approx 705 \text{ uF};$$

The capacitors C_i, C_1, C_2 and C_0 configurations are presented in fig.2.95-2.97.
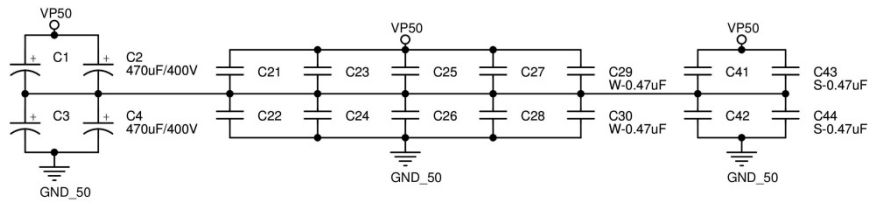
Fig.2.95. C_i capacitor circuit structure
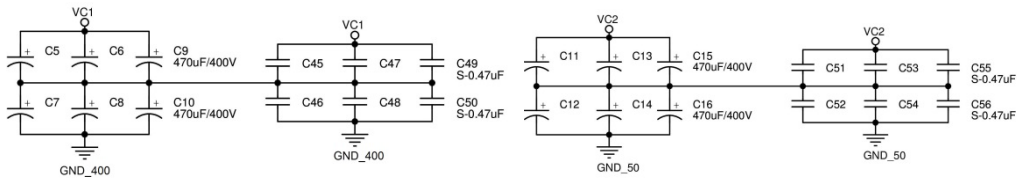
Fig.2.96. C_1 and C_2 capacitor circuit structures
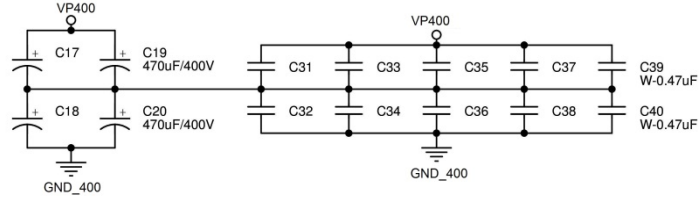
Fig.2.97. C_0 capacitor circuit structure

> **The inductor L1 dimensioning:**

The value of the input current is equal with the mean value of the current through the input inductor, L1:

$$I_1 = I_{L_{1,med}} \tag{2.161}$$

The input current is calculated using the following equation taking into consideration, the maximum input power and the input voltage:

$$I_{1,max} = \frac{P_{1,max}}{V_{1,min}} \tag{2.162}$$

$$I_{1,min} = \frac{P_{1,max}}{V_{1,max}} \tag{2.163}$$

During t_{off} the voltage drop across the input inductor can be calculated with the following equation:

$$V_{L_1} = V_1 - V_C = V_1 - \frac{V_1}{1-D} = V_1 \cdot \frac{D}{D+1} \tag{2.164}$$

We impose the inductor current ripple equal to x percent of the maximum input current:

$$\Delta I_{L_1} = [x]\% \cdot I_{1,max} = [x]\% \cdot \frac{P_{1,max}}{V_{1,min}} \tag{2.165}$$

The maximum and minimum values of the current through the input inductor have the following expressions:

$$I_{L_{1,max}} = I_{L_{1,med}} + \frac{\Delta I_{L_1}}{2} \tag{2.166}$$

$$I_{L_{1,min}} = I_{L_{1,med}} - \frac{\Delta I_{L_1}}{2} \tag{2.167}$$

Considering that $\Delta t = D \cdot T_s$ and (2.168), the value of the input inductance is obtained in (2.169) and (2.170):

$$V_{L_1} = L \cdot \frac{\Delta I_{L_1}}{\Delta t} \tag{2.168}$$

$$L_1 = \frac{V_{L_1}}{\Delta I_{L_1}} \cdot \Delta t \tag{2.169}$$

$$L_1 = \frac{V_1 \cdot D}{\Delta I_{L_1} \cdot (1+D)} \cdot \Delta t \tag{2.170}$$

Based on the considerations above and a x=10% ripple for the I_{L1} current, the resulted inductance of L_1 was chosen 200 uH at a maximum current of 120 A. Since no prebuilt inductors were found with these parameters, the inductor was manufactured. Following a dimensioning procedure found in [2.37] and a dedicated inductor design tool software offered by Metglas.Inc for validation, the inductor was realized using an AMCC400 Metglas Alloy core with a 2.4mm air gap and 22 turns of 16mm2 wired copper.

➢ **The inductor L_2 dimensioning:**

The value of the output current is equal with the mean value of the current through the output inductor, L_2:

$$I_2 = I_{L_{2,med}} \tag{2.171}$$

The output current is calculated using the following equation taking into consideration the maximum output power and the output voltage:

$$I_2 = \frac{P_{2,max}}{V_2} \tag{2.172}$$

During t_{off} the voltage drop across the output inductor can be calculated with the following equation:

$$V_{L_2} = 2 \cdot V_C - V_2 = \frac{2 \cdot V_2}{1+D} - V_2 = V_2 \cdot \frac{1-D}{1+D} \tag{2.173}$$

An inductor current ripple equal to x percent of the maximum output current is imposed:

$$\Delta I_{L_2} = [x]\% \cdot I_{2,max} = [x]\% \cdot \frac{P_{2,max}}{V_{2,max}} \tag{2.174}$$

The maximum and minimum values of the current through the output inductor have the following expressions:

$$I_{L_{2,max}} = I_{L_{2,med}} + \frac{\Delta I_{L_2}}{2} \tag{2.175}$$

$$I_{L_{2,min}} = I_{L_{2,med}} - \frac{\Delta I_{L_2}}{2} \tag{2.176}$$

Considering that $\Delta t = D \cdot T_s$ and (2.178), the value of the input inductance is obtained in (2.179) and (2.180):

$$V_{L_2} = L \cdot \frac{\Delta I_{L_2}}{\Delta t} \tag{2.178}$$

$$L_2 = \frac{V_{L_2}}{\Delta I_2} \cdot \Delta t \tag{2.179}$$

$$L_2 = \frac{V_2 \cdot (1-D)}{\Delta I_{L_2} \cdot (1+D)} \cdot \Delta t \tag{2.180}$$

Based on the considerations above and a x=20% ripple for the I_{L1} current, the resulted inductance of L_2 was chosen 1470uH.

$$L_2 - 1X1000uH/11A + 1X470uH/16A \approx 1470uH;$$

> ➤ **The S$_1$, S$_2$ and S$_3$ switches:**

The transistors S$_1$, S$_2$ and S$_3$ are planned to support voltages up to 600 V and currents up to 120 A, at an operating frequency of 20 kHz. In order to avoid any breakdown, beside protection circuit, the switches have to support a maximum VCE of 1200 V and a current of 150 A (for S$_1$) considering the frequency and thermal constraints. For the proposed prototype, two Semikron IGBT modules (SKM75GB123) are used. Their internal configuration is shown in fig. 2.98. Since these modules have two transistors per package and the maximum current is 75 A, based on their configuration and the BHDC parameters, the S$_1$ transistor is realized by two transistors from two modules, connected in parallel, offering this way a double maximum current (150 A). The other two switches from each module are used as S$_2$ and S$_3$.
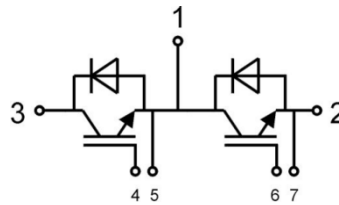
Fig. 2.98. IGBT module – internal schematic

Because VCEsat voltage decreases with the increase of temperature and the temperature of the transistors increase when the handle high currents at high frequencies, the chosen switches were analyzed to see if they can handle a 100 A current at a frequency of 20 kHz, when switching at 600 V. Using the equation (2.181) (provided in Advanced Power Technology's application notes [2.36]), the maximum switching frequency of SKM75GB123 can be determined by limiting the maximum dissipated power.

$$f_{max} = \frac{\frac{T_J - T_C}{R_{\theta JC}} - V_{CE} \times I_C \times D}{E_{ON} + E_{OFF}} \tag{2.181}$$

Having a thermal resistance (RθJC) of 0.27 K/W, a maximum junction temperature (TJ) of 125 °C, at a duty cycle of 0.875 (corresponding to the input and output voltages), the maximum frequency has a value of approximately 19 kHz. Since the heat sink used for the prototype is a passive one and the operating frequency is 20 kHz, the prototype will be tested at maximum a value of 50 A for the I$_{L1}$ current.

The dimensioned components used for the power stage circuit and the current sensors are listed in Table.2.4.

Table.2.4. List of BHDC components

Components	Value	Configuration	Additional Details
L1 inductor	211uH	1X211uH inductor	The inductor was dimensioned and realized using 2 AMCC400 U cores and 22 turns of copper wire of 16mm^2
L2 inductor	1470mH	1x1000mH+ 1x470mH inductors	The inductor was realized connecting 2 ferrite based inductors connected in series
Ci capacitor	470uF	4X470uF+ 12x0.47uF	2 series connected groups of 2 electrolytic caps connected in parallel with 6 polyester caps
C0 capacitor	470uF	4X470uF+ 10x0.47uF	2 series connected groups of 2 electrolytic caps connected in parallel with 5 polyester caps
C1-C2 capacitors	705uF	12X470uF+ 12X0.47uF capacitors	Each capacitor of the capacitor cell contain 2 groups connected in series of 3 electrolytic caps connected in parallel with 3 polyester caps
S1,S2,S2	2xSKM75GB123 D IGBT modules	4XIGBT of 1200V and 75A	S1 is realized with 2 IGBTs of each module connected in parallel. The other 2 remaining IGBTs are used independently for S2 and S3 switches
IL1, IS1, IS2	3xACS758-150	150 A current sensors	IL1- current sensor for L_1 IS2- current sensor for S_2 IS3- current sensor for S_3
IL2	1xACS758-50	50 A current sensor	IL2- current sensor for L_2

2.5.2. Experimental prototype and results

In this section digital simulations and experimental results of BHDC will be presented.

Using the components listed in Table 2.4 the BHDC prototype was realized and it is presented in fig.2.99.
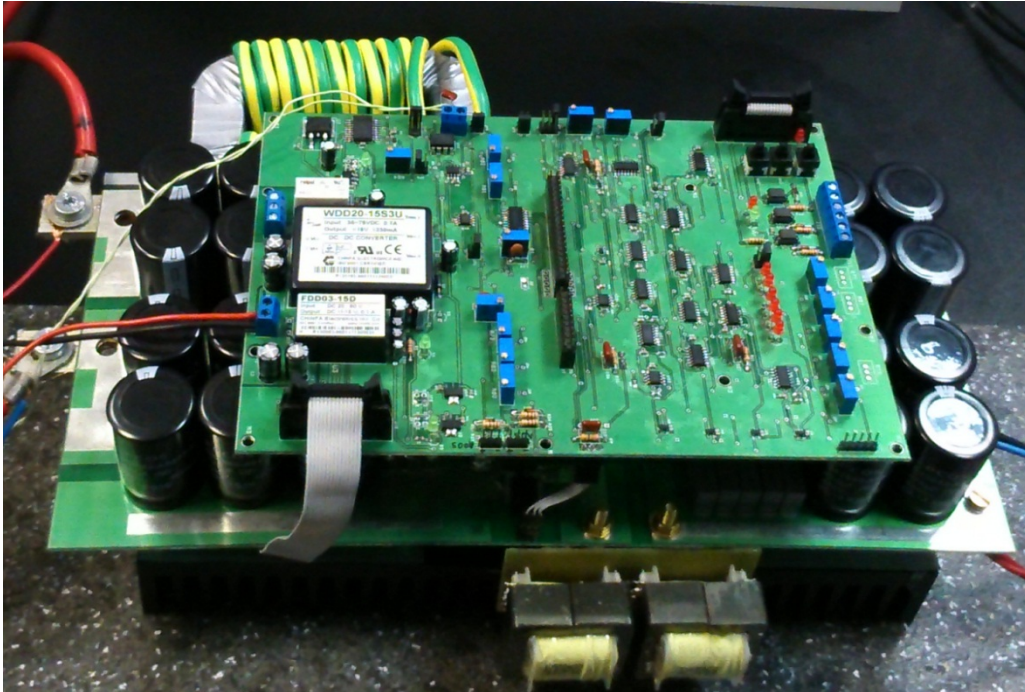
Fig. 2.99. BHDC prototype

The prototype is connected to a 100 Ah battery stack at 48 V to the lower voltage side and to a 2 kW, 0-400 V voltage controlled power supply source on the high voltage side. The battery stack can be charged and discharged so no additional loads are needed. On the other side, in parallel with the DC voltage source is connected a programmable 2 kW resistive load in order to test the current injection in both ways. This way the proposed BHDC can be tested in a similar operation corresponding to a microgrid application. Due to the equipment limitations, the experimental tests are realized at a maximum power of 2 kW.

In fig.2.100 are presented the waveforms of the currents through L_1 and L_2 inductors. With a reference signal that forces the converter to operate in both ways at different values of the current. Using the Psim digital model of the converter, the simulation and experimental waveforms are given for the same reference waveform given for I_{L1}. We can see that both I_{L1} and I_{L2} follow the reference signal. The experimental waveforms are smoother because of the acquisition system. Since the test duration is 5 seconds, the oscilloscope automatically averages the acquired data in order to reduce the number and dimension of points. Except this difference, the prototype operates well and it follows the reference in harder conditions than the intended application.
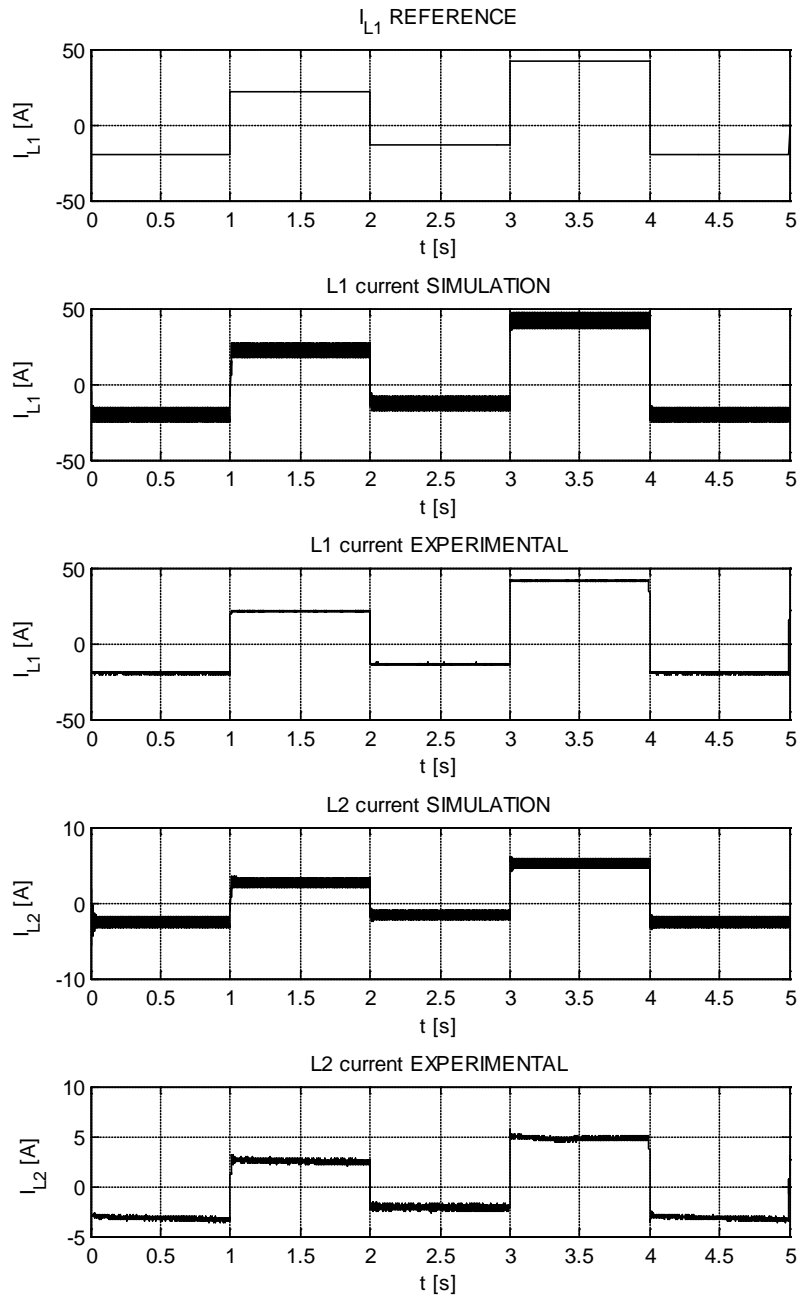
Fig.2.100. Comparison of simulation and experimental results for
IL_1 and I_{L2} currents following a reference signal

In fig.2.101 is shown a comparison between the I_{L1} and I_{L2} current waveforms obtain numerically and experimental. The similarity between them shows that the proposed converter has a good operation in step-up mode.

I_{L1} Current SIMULATION

I_{L1} Current EXPERIMENTAL

I_{L2} Current SIMULATION

I_{L2} Current EXPERIMENTAL
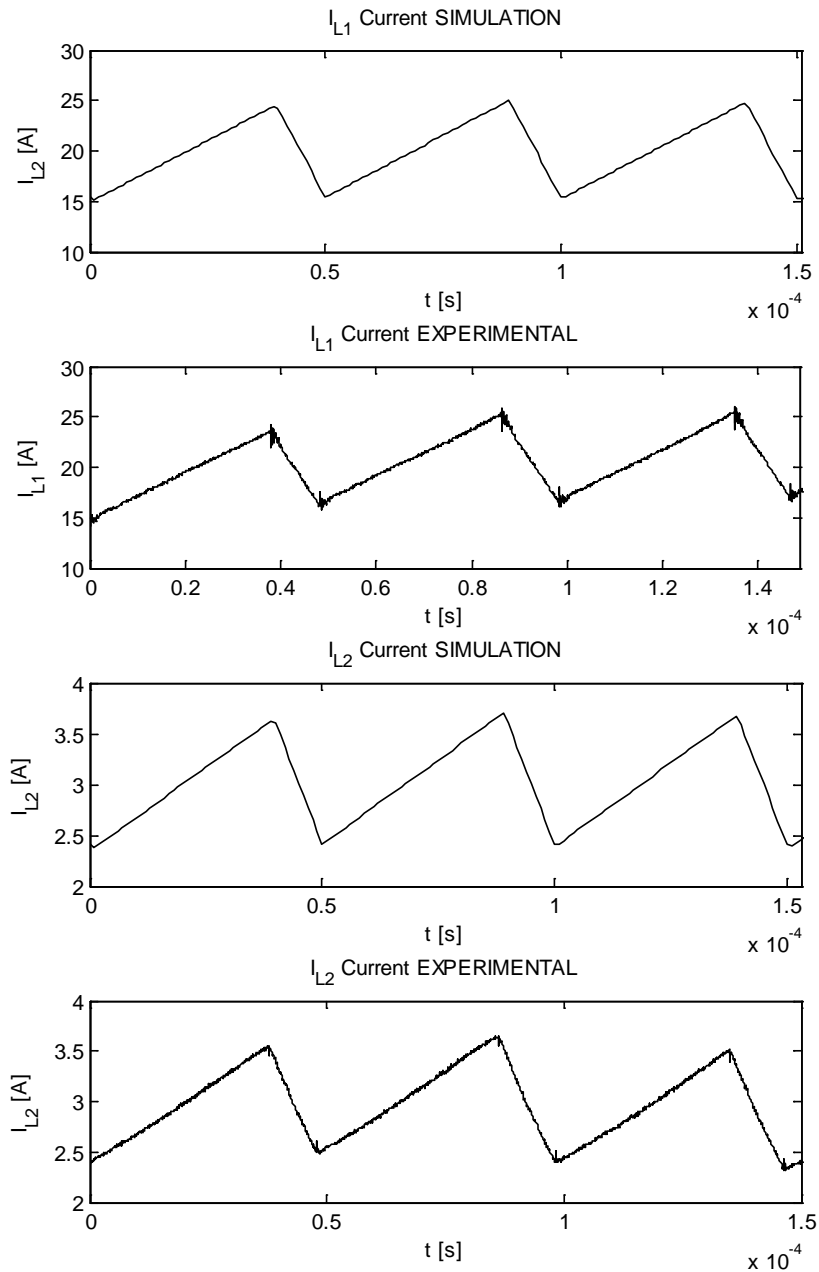
Fig.2.101. Comparison of simulation and experimental results for

IL_1 and I_{L2} currents operating in step-up mode

In fig.2.102 is shown a comparison between the IL1 and IL2 current waveforms obtain numerically and experimental. The similarity between them shows that the proposed converter has a good operation in step-down mode.
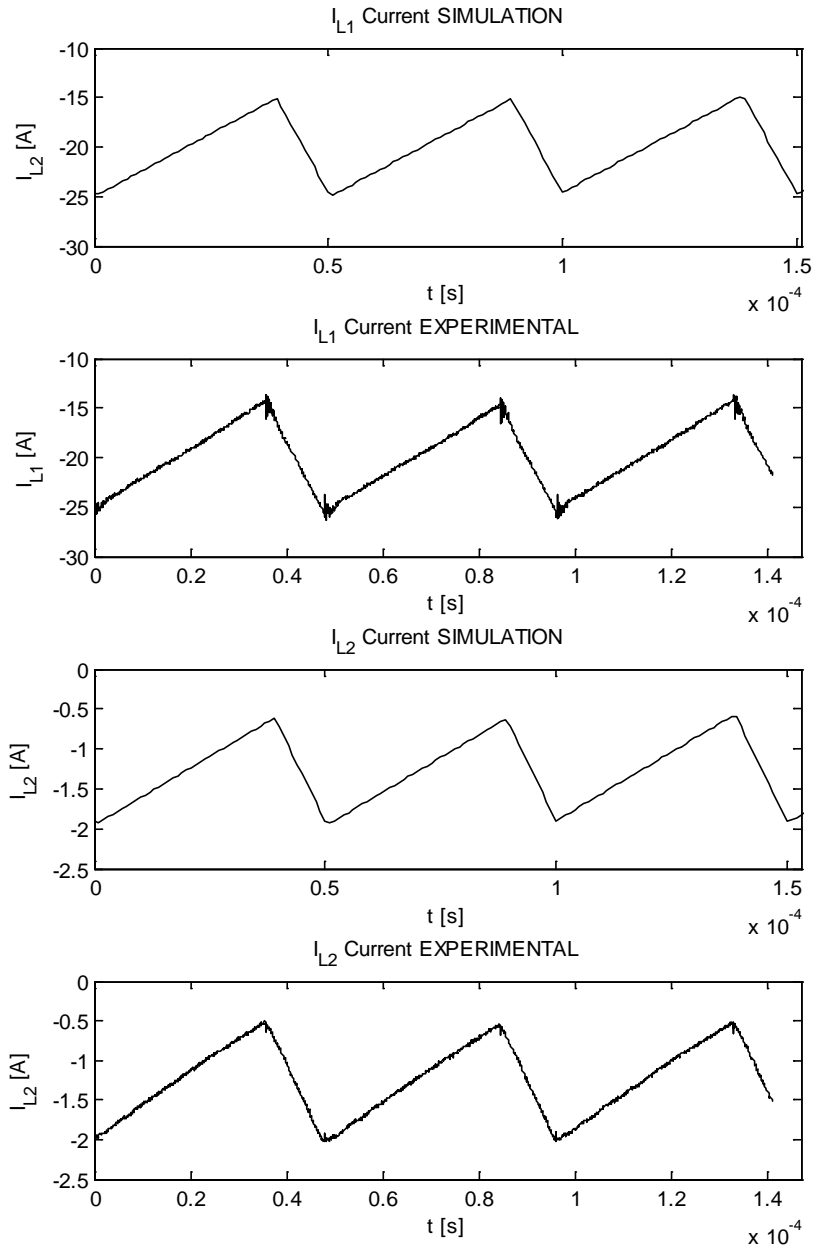
Fig.2.102. Comparison of simulation and experimental results for

IL_1 and I_{L2} currents operating in step-down mode

In fig.2.103 is shown a comparison between the S_1 and S_{2_3} PWM control signals, with waveforms obtained numerically and experimental. The similarity between them shows that the switching signals are identical, the prototype operation is stable and the simulation results are validated.
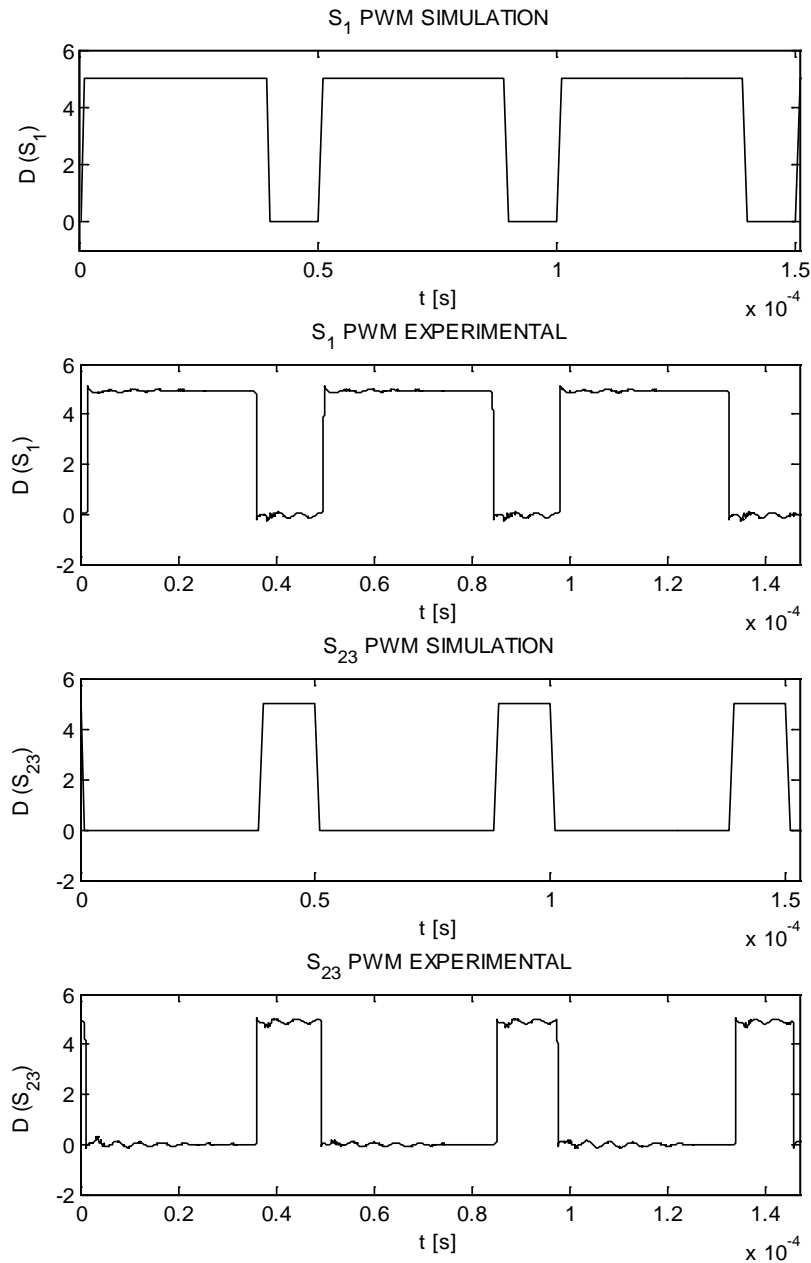
Fig.2.103. Comparison of simulation and experimental results for

PWM signals for S_1 and S_{2_3}

The above simulation and experimental waveforms show a good behavior of the BHDC. The waveforms obtained during the spice simulation are experimentally confirmed being almost identical.

2.6. Conclusion

In this chapter is presented a bidirectional DC-DC converter with large conversion ratio.

It starts with an introduction designed to present a general overview of the main topologies of bidirectional DC-DC converters used in microgrids applications. They were selected from literature because of their relative simple and robust structures make them appropriate for renewable energy applications.

The presented BHDC was found in literature as a simple topology but it was never studied in detail. Considering this, the originality of this research comes from the fact that for a first time a full analytical study was realized in this chapter in order to establish the operation principles and the equations of the currents and voltages for the main components. As a result of this analytical study, there were obtained important information about the topology constraints and capabilities which were used in the prototyping procedure of the power stage circuit and for the switching control circuit. After a preliminary design, a stability analysis was made for the BHDC. Its main goal was to verify the behavior of each component during the operation in all the possible modes. Using the SSA method, the stability was verified for the converter working in step-up/step-down mode with simple resistive loads and one voltage source connected once a time. It was also verified with two voltage sources connected. The SSA results were verified with the PWMSM method. The stability results were identical and they all shown an instability of the system when it operates as an interface between two DC busses. Because of this, a compensation function was needed and it was integrated in the BHDC circuit especially to improve the stability of the current through the L_1 inductor, which is used as input for the control. Using a compensation function that introduces new poles and zeros in the original transfer functions and based on the Bode plots obtained before, the new AC responses of the main components became stable. After SSA validation, the compensation function was integrated in a compensation circuit. The circuit was tested with PWMSM regarding the stability and using a spice simulation model to verify the operation. The simulation waveforms confirmed the good behavior of the proposed BHDC and allowed the design of a prototype. The resulted prototype follows the information collected in the previous sections, including the compensation function. Design considerations, simulation and experimental results are presented.

The BHDC prototype is functional, stable and it is integrated in a emulator of the intended application. The tests confirm its stability during harsh conditions.

References

[2.1]   Di Han; Noppakunkajorn, J.; Sarlioglu, B., "Efficiency comparison of SiC and Si-based bidirectional DC-DC converters," Transportation Electrification Conference and Expo (ITEC), 2013 IEEE , vol., no., pp.1,7, 16-19 June 2013.

[2.2]   Samosir, A.S.; Yatim, A.H.M., "Implementation of Dynamic Evolution Control of Bidirectional DC–DC Converter for Interfacing Ultracapacitor Energy Storage to Fuel-Cell System", IEEE Transactions on Industrial Electronics, vol.57, no.10, pp.3468,3473, Oct. 2010.

[2.3]   Hyun-Lark Do, "Nonisolated Bidirectional Zero-Voltage-Switching DC–DC Converter", IEEE Transactions on Power Electronics, vol.26, no.9, pp.2563,2569, Sept. 2011.

[2.4]   Krishnamachari, B.; Czarkowski, D., "Bidirectional buck-boost converter with variable output voltage", 1998. ISCAS '98. Proceedings of the 1998 IEEE International Symposium on Circuits and Systems , vol.6, no., pp.446,449 vol.6, 31 May-3 Jun 1998.

[2.5]   M. K. Kazimierczuk, *Pulse-Width Modulated DC-DC Power Converters*, John Wiley & Sons, 2008.

[2.6]   Sunkara, S.; Kondrath, N., "Design and PSpice simulation of synchronous bidirectional PWM DC-DC buck-boost converter operating in CCM," India Conference (INDICON), 2013 Annual IEEE , vol., no., pp.1,6, 13-15 Dec. 2013.

[2.7]   Himmelstoss, F.A.; Ecker, M.E., "Analyses of a bidirectional DC-DC half-bridge converter with zero voltage switching", ISSCS 2005. International Symposium on Signals, Circuits and Systems, vol.2, no., pp.449,452 Vol. 2, 14-15 July 2005.

[2.8]   Pahlevaninezhad, M.; Das, P.; Drobnik, J.; Jain, P.K.; Bakhshai, A., "A Novel ZVZCS Full-Bridge DC/DC Converter Used for Electric Vehicles,", IEEE Transactions on Power Electronics, vol.27, no.6, pp.2752,2769, June 2012.

[2.9]   Shu-Wei Kuo; Yu-Kang Lo; Huang-Jen Chiu; Shih-Jen Cheng; Chung-Yi Lin; Yang, C.S., "A high-performance bidirectional DC-DC converter for DC micro-grid system application," Power Electronics Conference (IPEC-Hiroshima 2014 - ECCE-ASIA), 2014 International , vol., no., pp.3185,3189, 18-21 May 2014.

[2.10] Rodriguez, M.; Lamar, D.G.; de Azpeitia, M.A.; Prieto, R.; Sebastian, J., "A Novel Adaptive Synchronous Rectification System for Low Output Voltage Isolated Converters", IEEE Transactions on Industrial Electronics, vol.58, no.8, pp.3511,3520, Aug. 2011.

[2.11] Kuei-Hsiang Chao; Chun-Hao Huang, "Bidirectional DC-DC soft-switching converter for stand-alone photovoltaic power generation systems," Power Electronics, IET , vol.7, no.6, pp.1557,1565, June 2014.

[2.12] Lin, C.-C.; Yang Lung-Sheng; Wu, G.W., "Study of a non-isolated bidirectional DC-DC converter," Power Electronics, IET , vol.6, no.1, pp.30,37, Jan. 2013.

[2.13] Khan, F.H.; Tolbert, L.M.; Webb, W.E., "Hybrid Electric Vehicle Power Management Solutions Based on Isolated and Nonisolated Configurations of Multilevel Modular Capacitor-Clamped Converter", IEEE Transactions on Industrial Electronics, vol.56, no.8, pp.3079,3095, Aug. 2009.

[2.14] Ardi, H.; Reza Ahrabi, R.; Najafi Ravadanegh, S., "Non-isolated bidirectional DC–DC converter analysis and implementation," Power Electronics, IET , vol.7, no.12, pp.3033,3044, 12 2014.

[2.15] L. Czarnecki, D. Gutzeit, D. Schekulin, and A. Winter, "„Coolcept" - eine neue PV-Wechselrichter-Topologie für sehr hohe Wirkungsgrade," 2010, pp 1-6.

[2.16] Guran, E., "High efficiency power converters for renewable sources of energy" IEEE 8th International Symposium on Applied Computational Intelligence and Informatics (SACI), 2013, vol., no., pp.381,386, 23-25 May 2013.

[2.17] Inoue, S.; Akagi, H., "A Bidirectional Isolated DC–DC Converter as a Core Circuit of the Next-Generation Medium-Voltage Power Conversion System", IEEE Transactions on Power Electronics, vol.22, no.2, pp.535,542, March 2007.

[2.18] Inoue, S.; Akagi, H., "A Bidirectional DC–DC Converter for an Energy Storage System With Galvanic Isolation", IEEE Transactions on Power Electronics, vol.22, no.6, pp.2299,2306, Nov. 2007.

[2.19] Xiaodong Li; Bhat, A.K.S., "Analysis and Design of High-Frequency Isolated Dual-Bridge Series Resonant DC/DC Converter", IEEE Transactions on Power Electronics, vol.25, no.4, pp.850,862, April 2010.

[2.20] Tsai-Fu Wu; Yung-Chu Chen; Jeng-Gung Yang; Chia-Ling Kuo, "Isolated Bidirectional Full-Bridge DC–DC Converter With a Flyback Snubber", IEEE Transactions on Power Electronics, vol.25, no.7, pp.1915,1922, July 2010.

[2.21] Haifeng Fan; Hui Li, "High-Frequency Transformer Isolated Bidirectional DC–DC Converter Modules With High Efficiency Over Wide Load Range for 20 kVA Solid-State Transformer", IEEE Transactions on Power Electronics, vol.26, no.12, pp.3599,3608, Dec. 2011.

[2.22] Ortiz, G.; Biela, J.; Bortis, D.; Kolar, J.W., "1 Megawatt, 20 kHz, isolated, bidirectional 12kV to 1.2kV DC-DC converter for renewable energy applications," Power Electronics Conference (IPEC), 2010 International , vol., no., pp.3212,3219, 21-24 June 2010.

[2.23] Inoue, S.; Akagi, H., "A Bi-Directional DC/DC Converter for an Energy Storage System," Applied Power Electronics Conference, APEC 2007 - Twenty Second Annual IEEE , vol., no., pp.761,767, Feb. 25 2007-March 1 2007.

[2.24] Chongming Qiao; Smedley, K.M., "An isolated full bridge boost converter with active soft switching," Power Electronics Specialists Conference, 2001. PESC. 2001 IEEE 32nd Annual , vol.2, no., pp.896,903 vol.2, 2001.

[2.25] Kashif, M., "Bidirectional flyback DC-DC converter for hybrid electric vehicle: Utility, working and PSPICE computer model," Microelectronics and Electronics (PrimeAsia), 2012 Asia Pacific Conference on Postgraduate Research in , vol., no., pp.61,66, 5-7 Dec. 2012.

[2.26] Fanghua Zhang; Lan Xiao; Yangguang Yan, "Bi-directional forward-flyback DC-DC converter," Power Electronics Specialists Conference, 2004. PESC 04. 2004 IEEE 35th Annual , vol.5, no., pp.4058,4061 Vol.5, 20-25 June 2004.

[2.27] Watson, R.; Lee, F.C.; Hua, G.C., "Utilization of an active-clamp circuit to achieve soft switching in flyback converters", IEEE Transactions on Power Electronics, vol.11, no.1, pp.162,169, Jan 1996.

[2.28] Zhu, L., "A novel soft-commutating isolated boost full-bridge ZVS-PWM DC-DC converter for bidirectional high power applications," Power Electronics

Specialists Conference, 2004. PESC 04. 2004 IEEE 35th Annual , vol.3, no., pp.2141,2146 Vol.3, 20-25 June 2004.

[2.29] Kunrong Wang; Lee, F.C.; Lai, J., "Operation principles of bi-directional full-bridge DC/DC converter with unified soft-switching scheme and soft-starting capability," Applied Power Electronics Conference and Exposition, 2000. APEC 2000. Fifteenth Annual IEEE , vol.1, no., pp.111,118 vol.1, 2000.

[2.30] Yu Du; Lukic, S.; Jacobson, B.; Huang, A., "Review of high power isolated bi-directional DC-DC converters for PHEV/EV DC charging infrastructure," Energy Conversion Congress and Exposition (ECCE), 2011 IEEE , vol., no., pp.553,560, 17-22 Sept. 2011.

[2.31] Jacobson, B.; DiPerna, R., "Series resonant converter with clamped tank capacitor voltage," Applied Power Electronics Conference and Exposition, 1990. APEC '90, Conference Proceedings 1990., Fifth Annual , vol., no., pp.137,146, 11-16 March 1990.

[2.32] Jacobson, B.; DiPerna, R., "Design of a series resonant converter with clamped capacitor voltage and anti-cross-conduction inductors," Applied Power Electronics Conference and Exposition, 1998. APEC '98. Conference Proceedings 1998., Thirteenth Annual , vol.2, no., pp.829,833 vol.2, 15-19 Feb 1998.

[2.33] Ho, T.T.J.; Verghese, George C.; Osawa, C.; Jacobson, B.S.; Kato, T., "Dynamic modeling, simulation and control of a series resonant converter with clamped capacitor voltage," Power Electronics Specialists Conference, PESC '94 Record., 25th Annual IEEE , vol., no., pp.1289,1296 vol.2, 20-25 Jun 1994.

[2.34] Yu Du; Xiao Bian; Lukic, S.; Jacobson, B.S.; Huang, A.Q., "A novel wide voltage range bi-directional series resonant converter with clamped capacitor voltage," Industrial Electronics, 2009. IECON '09. 35th Annual Conference of IEEE , vol., no., pp.82,87, 3-5 Nov. 2009.

[2.35] Cornea, O.; Guran, E.; Muntean, N.; Hulea, D., "Bi-directional hybrid DC-DC converter with large conversion ratio for microgrid DC busses interface," International Symposium on Power Electronics, Electrical Drives, Automation and Motion (SPEEDAM), 2014, vol., no., pp.695,700, 18-20 June 2014.

[2.36] J. Dodge, J. Hess, "IGBT Tutorial", Application Note APT0201, Rev. B, July 1, 2012.

[2.37] Col. Wm. T. McLyman "Transformer and Inductor Design Handbook", Third Edition", pp 348-533, 2004.

3. FLYBACK BIDIRECTIONAL DC-AC POWER CONVERTER

The following subchapters are related to high efficiency inverters used in renewable applications. They are described in terms of operation, underlining the advantages and disadvantages that make them more or less appropriate for specific applications. Every topology was simulated using Psim software. The resulted efficiencies were above 95%, up to 99%. The efficiency was obtained using digital models for transistors that integrate the real parameters of the semiconductors. The parameters used for the switch models were chosen considering the last generation of high efficiency SiC semiconductors. They are capable to manage big amounts of energy with very low losses helping this way the converters to be able to reach high efficiencies. In conclusion, the new technologies of semiconductors have advanced the transformerless topologies to reach high efficiencies, overtaking somehow the traditional converters with transformer [3.1]. With a proper control and using high performance semiconductors, the actual transformerless converters can achieve efficiencies over 99% for some specific conditions [3.2]. Still, there are many applications where a galvanic isolation is mandatory and the well-known transformer is needed, especially when the systems include photovoltaic modules. In order to obtain lower losses, all the specific applications work at high frequency and many times the HF transformer uses all its particular features in order to convert the energy and transfer it from one side to another more efficient. Many existent topologies realize the energy conversion in one stage using HF transformers with split secondary windings in order to get the isolation and a specific conversion of the energy, or in two stages using the transformer only for galvanic isolation and use additional electronic circuits for the rest [3.3].

The Push-Pull, Forward and Flyback DC converters are integrated in many inverters topologies and their efficiencies depend on the number of semiconductors, the switching frequency and the way the transformer is used. On the other hand, the conversion of energy requires the mandatory use of passive components and this supports the use of the transformers, especially because of their inductive additional features [3.4-3.8].

Mostly used in relative low power DC applications, Flyback converters are also used in different topologies of inverters. The actual configurations are designed to realize the alternating current in many ways. Most topologies completely separate its features during the functioning states. On the DC side, a boost stage is preferred, obtaining this way the necessary energy that has to be transferred. This is made by using the primary winding as the needed inductor for step-up. After this step, specific circuits are used to manage the current flow, in order to obtain the AC character. Another preferred way is to alternate the current using a boost stage on the DC side and split secondary winding which is followed by a circuit that directs and manages the current flow and acts as an inverter. Respecting these facts, it have been developed many topologies that are currently available on market [3.9-3.11]. The control strategies are multiple, but all of them are based on the management of the current flow and the transferred energy. Because of this, only close loop control can be used [3.12-3.13]

3.1. High Efficiency DC-AC Converters

➢ **Heric H5 Converter**

This converter has one of the simplest topology and it is in the same time a very efficient one (Fig.3.1). It has only five intelligently controlled transistors and by being transformerless, its efficiency is increased with about 3%. For the efficiency improvement, the fifth switch (S5) was introduced in the traditional H-Bridge circuit. Its goal is to make the connection to the grid more efficient by eliminating the parasitical leakage currents. It also plays an important role in simplifying the command of the other four switches by using unipolar control strategy, resulting in decreased switching losses for two transistors.

Related to the transistors and diodes, it is preferred to be chosen by having the same parameters, because it is very important to obtain the voltage symmetrically distributed through the high frequency switched elements [3.14].
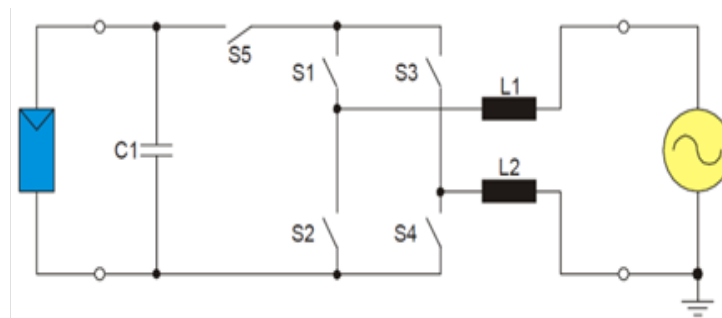
Fig.3.1.   Heric H5 Converter

The rated efficiency for Heric H5 Converter is over 96%. This value can be considered high enough to make it a competitive converter. An advantage is given by the S_5 switch, which allows the switches S1-S4 of the inverter to be switched using an unipolar strategy control, that lowers the switching losses for two of the switches. The other two switches are PWM controlled and their losses depend by the transistors performances.

With a relative high efficiency and a simple circuit, the biggest disadvantage of this converter is related to the fact that the energy source has to offer a high DC voltage at the inverter input. The filter capacitors and the inductors have to be larger and sometimes over dimensioned in order to obtain a stable operation. Still, because of the simplicity, its price makes this converter competitive. More than that, these characteristics make it very adaptive for UPS Applications. These kinds of systems are available on the market. Most of them are readapted for the new tasks or even recycled and reconfigured using new generation of semiconductors. In related papers about this converter, the rated efficiency can be increased up to 98% if some special transistors are used [3.15].

➢ **Coolcept Converter**

„Coolcept" converter topology is presented in fig.3.2 and it comes with an innovative circuit design able to reach high efficiencies. In present, this topology is integrated in StecaGrid inverters, which are designed and well sold for renewable energy applications. The „Coolcept" converter topology is based on a single-stage transformerless switching concept that uses proven standard components to implement symmetric step-down converters with downstream pole-reversing circuits. More than that, it is a multi-level topology and because of the intelligent control, it can do all these tasks mainly with two of the all six transistors [3.16].
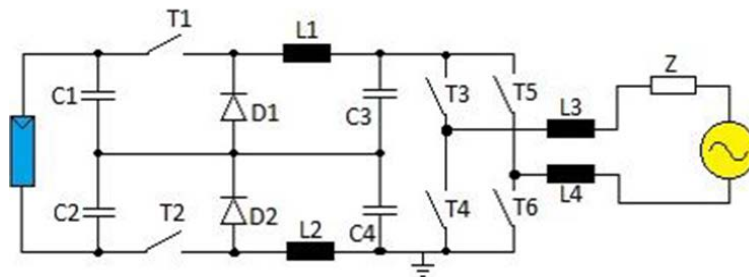
Fig.3.2. "Coocept" Converter

"Coolcept" converter, through its hybrid Buck stage on the DC Bus can operate on three levels. The related efficiencies are over 98% for special conditions and high efficiency semiconductors. Its complexity is not so high and the most important, the losses are highly decreased by the number of transistors and the low frequency of the inverter. Previously, at its beginning, this topology was realized using IGBTs as switching elements, the most adequate technology available at that time. After a while, the development of MOSFETs has marked the existence of this topology, especially because of the improvements related to high frequency and less dependence by temperature. Nowadays, the SiC technology, which develops continuously, places this converter among the most effective structures [3.2].

Based on its operation, this topology may be considered one of the latest generations of high efficiency converters. For a better understanding of its operation is useful to split the system in two parts, the first part which acts as a two sided Buck converter and the second part which is a traditional inverter that works at very low frequency. It has to be mentioned that unlike the traditional Buck output the resulted shape of the output waveform is a rectified sinusoid, built on three levels. The inverter is the well-known traditional H Bridge with four transistors whose task is to let parts of the current to go through and alternate its sign. However, this time it doesn't create the sinusoid by its own and only opens the opposite transistors of the two arms. This way a complete sinusoid with the frequency of 50 or 60 [Hz] is created by splitting the Buck output, letting one half of the sinusoid the way it is and inverting the other one.

Using high quality semiconductors, this converter efficiency may be increased up to 99.2% at specific loads and parameters. These results are reported in papers and are the effect of the high performance transistors and the low number of components used for this topology [3.2]. This is remarkable thinking to the fact that this converter offers the possibility of using lower filters because of its multi-

level operation mode. More than that, it can adapt itself to the renewable energy sources, acting like a Buck converter and offering the possibility of getting the maximum power point.

It has to be mentioned that the circuit design of the StecaGrid 3000 and StecaGrid 3600, already available on the market, provides very high efficiencies for grid feeding inverters rated up to 20 kW. They are rated at 3 kW and 3.6 kW and can achieve a peak efficiency of 98.6% [3.16].

➤ Cascade Boost-Switched-Capacitor Converter

In fig.3.3 a Cascade Boost-Switched-Capacitor Converter is presented. The efficiency of this converter is high due to the low number of transistors, the type of commutation and control. Two structures, a switched-capacitor based boost converter and a two-level inverter, are connected in cascade. The DC multilevel output voltage which consists of series of positive halves of a sinusoid becomes the input voltage of the classical inverter, resulting in an alternating waveform for the inverter output voltage. Because the multilevel waveform is meant to be close to a sinusoid its harmonics can be reduced using multiple stages for the switched-capacitor converter. The output filter which is very important for single stage converters, have lower dimensions, resulting in a smaller size of the entire converter. Usually, both stages switch at a high frequency, but in this case, only the DC stage operates at high frequency, opposite to the inverter [3.17].
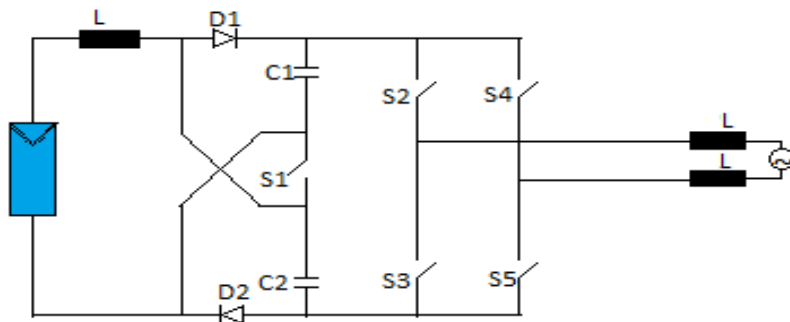
Fig.3.3. Cascade Boost-Switched-Capacitor Converter

For a better understanding, this converter also can be split in two: the DC part, respectively the inverting part. The DC part is a larger step-up ratio converter. Two identical capacitors are connected through the diodes to the output of a boost converter and this makes its step-up ratio to be much larger compared with the conventional boost converter. The explanation is that the capacitors are charged in parallel and discharged in series through the on-off transition of the main S1. The circuit is simple and has some significant features of extended output voltage, less input current ripple and a lower output voltage ripple compared to the conventional boost converters.

The second part is a traditional one phase inverter. Considering this we can admit that the efficiency may be increased by using a more efficient topology for the inverter, but the main purpose of presenting this concept is that there are specific applications which can successfully use its particular features. The most relevant applications are the photo-voltaic ones, when the output voltage of the panels is under 50 volts [3.17][3.18].

With a rated efficiency over 96%, the goal of this topology is to obtain multilevel inverters using a cascade of a boost-switched-capacitor converters, which offers a larger step-up ratio and attached to it is a traditional full-bridge inverter. This circuit contains fewer elements than the other existent solutions for inverters with five-level output waveform. The multilevel output waveform can be improved, by simply adding more switched-capacitor circuits. Adding more cascaded switched capacitors offers the possibility of adding more levels to the output, lowering the parameters of the filters and the rating values of the semiconductors. Because a switched-capacitor circuit can reach any voltage ratio, it allows boosting of the input voltage to high values, but being much unregulated is hard to get a high efficiency. That's why the boost stage of this converter has a secondary purpose to avoid diode-reverse recovery problems, operating at a relative low duty cycle.

The presented converter may be considered an integrated cascade interconnection of two power stages. Having a simple and robust circuit, it offers the possibility to obtain high voltage ratios with a transformerless configuration, the Cascade Boost-Switched-Capacitor Converter offers a good overall efficiency [3.19][3.20].

➢ 5 Level Converter

This topology is illustrated in fig.3.4 and it is a single-phase multilevel converter that can decrease the harmonic components of the output voltage and load current.
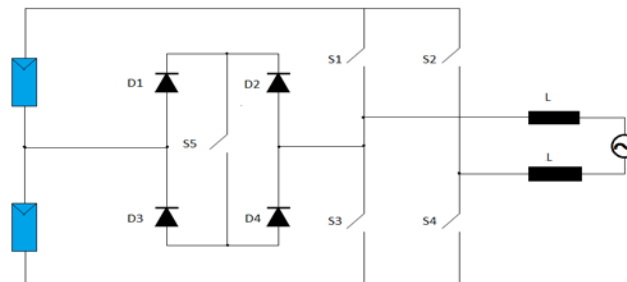
Fig.3.4. 5 Level Converter

One switching element and four diodes are added to the conventional full bridge inverter. This additional module is connected between the middle points of the two sources and the two arms of inverter. With a proper switching control of the fifth transistor (S5), it generates a half level of the DC total supply voltage, and by alternating its sign, 5 levels of the final voltage are obtained (-Vin, -Vin/2, 0, Vin/2 and Vin). Just like the topologies presented before, the efficiency of this converter is mainly influenced by the switches performance. All transistors work at high frequency and it is very important to have very efficient diodes too. The rated efficiency of this converter, using high performance semiconductors, is approximately 98% [3.21][3.22].

The power stage circuit of the 5 Level Converter has several advantages for the use as a single-phase, stand-alone photovoltaic system. One of these advantages is that this converter can be adapted to work with an additional DC-DC converter, influenced by the input source and power. Depending on the application where it is used, the 5 Level Converter can be configured differently. For example if

it is used as a motor drive, it does not require an output filter, because high order harmonics are effectively filtered directly by the reactance of the motor load; therefore, it can produce a high quality output alternative voltage and current with good harmonic characteristics. Also, it reduces stresses on power switching devices and the result is a lower Radio Frequency noise and Electromagnetic Interference. Also, this converter provides fewer Electromagnetic Compatibility problems, since multilevel inverters operate with a relative low switching frequency and voltage switching is done for lower voltage levels [3.23].

In the same time this converter offers good results when it is used in unconventional energy applications. With a carefully designed control and proper filters, it can make the transfer of energy from the power sources to the grid with lower losses and parasitical distortions. With a maximum of about 98%, the efficiency of this converter is a major reason for it to be used in lots of renewable energy applications.

➢ Soft Switching Converter

This is another inverter topology whose number of switches is low enough to obtain lower switching and conduction losses. More than that, because of the way this converter works, the losses are even lower. At first sight, the converter which is illustrated in fig.3.5 looks like an incomplete "Coolcept" design. Actually it has the advantage of a lower number of elements.
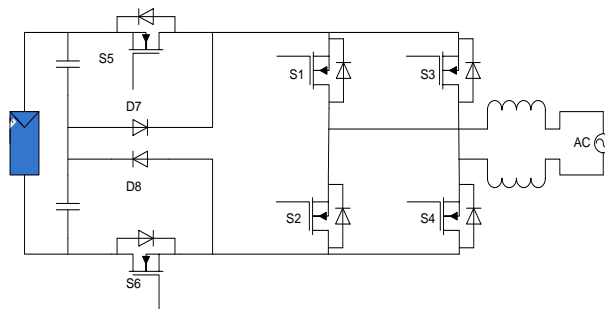
Fig.3.5. Soft switching Converter

The rated efficiency for this converter is over 98 % in special conditions. This makes this converter desirable in low power applications and smart grids, especially when the incoming energy is from a photovoltaic module. Also, by the way it works this converter pushes up the quality of the semiconductors to be so high, in order to decrease the conduction losses for the inverter and the switching losses, for the DC converter [3.24].

This topology does not generate any common-mode voltage, provides a high efficiency and its operating mode is almost independent by the power factor. The average efficiency is about 96% for input voltages between 350 V and 800 V. As a conclusion, this is another topology that can be considered a convenient power-conversion stage for transformerless PV systems connected to the grid. Any improvement of its semiconductor, despite their higher price, has good repercussions for its efficiency and this will pay off later for the initial price of the converter [3.25].

3.2. Bidirectional Flyback Inverter

In this chapter is presented a single-phase voltage source inverter with a high frequency flyback bidirectional dc-dc converter, as a previous stage, and a full-bridge inverter. The flyback converter generates a rectified sinusoidal voltage waveform across the output capacitor. The full bridge transistors switch two times in one AC period transforming the output capacitor voltage in an AC waveform. The converter offers galvanic insulation between input and output. The flyback transformer gives a possible high conversion voltage ratio. An analytic study is made and the proposed converter. The system stability is analyzed using the SSA procedure and a controller is proposed. Digital simulations validate the control stability, a proper operation of the inverter and a low THD value of the output voltage.

➢ Analytical Study

The following converter is a hybrid bidirectional flyback DC-AC (**HBFAC**) topology, which realizes the conversion of energy with a low number of components. An analytical study is presented in order to understand how the energy flows through the converter and why it has a permanent bidirectional characteristic. It also help to determine the equations and parameters of the currents and voltages of the active and passive components. A non-isolated DC-AC converter found in literature inspired this inverter [3.26]. It contains a buck-boost DC-DC bidirectional conversion stage and a full-bridge power inverter. The DC-DC conversion stage is replaced with a flyback converter with a bi-directional power flow, in order to have galvanic insulation and a possible high voltage conversion ratio. This modification led to two new novel topologies. The first one has a lower number of semiconductors, it uses a split capacitor cell and operates at a double value of the output voltage. Neglecting the higher voltage, a major disadvantage of this topology is the imbalance of the energy stored in the split capacitor cell during the AC conversion. It causes a high voltage THD which depends by the output load size. The power stage circuit for this first topology is shown in fig.3.6 [3.27].
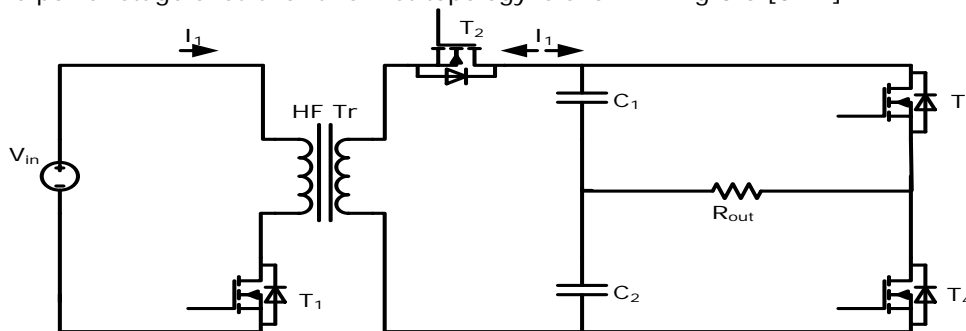
Fig.3.6. HBFAC with split capacitor

The second proposed topology solves these disadvantages by using a full bridge inverter in the final conversion stage and it is presented in detail along this

chapter. With a H-bridge inverter operating at 50Hz and using high efficiency semiconductors, the two additional transistors do not represent a major disadvantage since the THD factor becomes very low. In fig.3.7 is presented the power stage circuit of the proposed HBFAC. The left side of it is a lower voltage source able to sustain high current needs, where the energy is being normally supplied by or stored in battery stacks. The right side of the inverter can be connected directly to AC loads or even to grid.
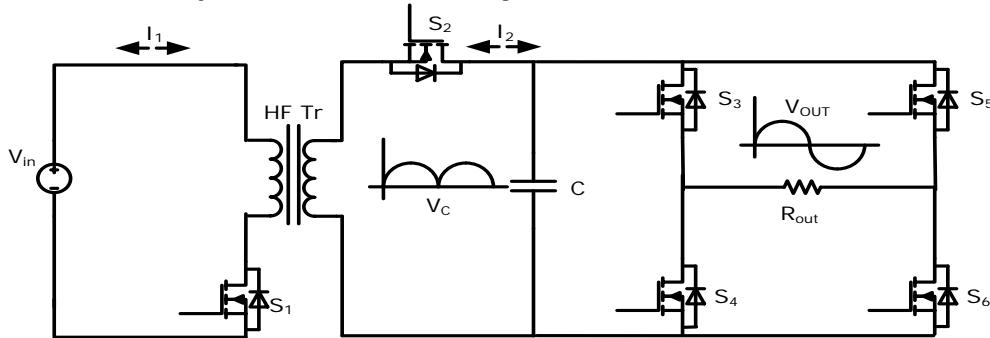
Fig.3.7. Proposed HBFAC power stage circuit

For a better understanding of HBFAC operation, in fig.3.8.1 a), b), c) and d) are presented the possible states during switching. The conversion process starts with a DC-DC conversion stage that is realized using a conventional flyback converter on the left side by switching at high frequency the transistors S_1 and S_2. Instead of a constant value of the voltage on the filter capacitor C, the flyback converter output is an irregular voltage with the waveform of a rectified sinusoid. During this process are used two features of the flyback converter. First is related to the galvanic isolation and the possibility of high ratio conversion given by the flyback transformer and second is related to the bidirectional characteristic that is used constantly during operation when the filter capacitor charging and discharging process is controlled in order to obtain the needed waveform of the voltage and the energy flows in both ways. The conventional flyback converter becomes bidirectional only by adding a complementary transistor to the diode from the secondary circuit. The H-bridge added to the filter capacitor has the simple role of inverting the rectified sinusoidal voltage and obtain this way AC voltage. A major advantage comes out during this process because of the low frequency at which the inverter works. The shape of the voltage that comes at its input is already processed and the four transistors S_3-S_6 which at switch 50 (60) Hz. In terms of efficiency, using new generation semiconductors and a flyback transformer with low losses, the proposed HBFAC performances depends only by its construction. The relative high power circulated through the flyback transformer raises switching problems for the semiconductors S_1 and S_2, because of the voltage peaks that appear due to the leakage inductance of the transformer, which cannot be eliminated and this requires the snubbers existence. Being involved large amounts of energy, only non-dissipative snubbers can be used. Because of this, there are two possible solutions that can be used. One of them implies a resonant circuit able to recirculate the energy back to the main circuit and the second one is an additional circuit able to collect that energy and use it for different purposes.
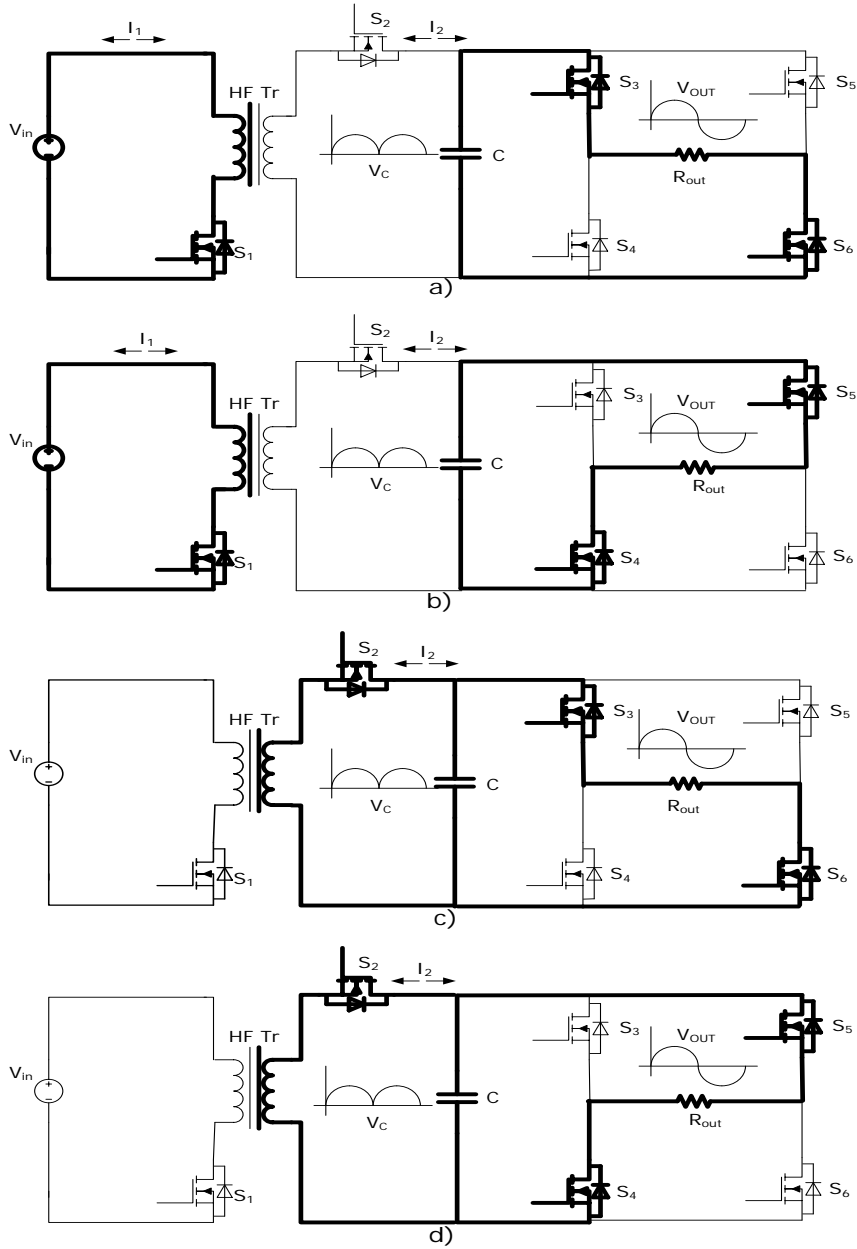
Fig.3.8. The HBFAC the operating states:

a) and c) t_{on} and t_{off} for S_1 during positive alternance;

b) and d) t_{on} and t_{off} for S_1 during negative alternance

(S_1 and S_2 control signals are complementary)

If V_{peak} is considered the amplitude of the output voltage v_{out}, then the equation that gives the relation between them is:

$$V_{out} = V_{peak} \cdot \sin(\omega t) \tag{3.1}$$

Going backward, the prescribed voltage that is required on the filter capacitor is:

$$V^*_C = |\ V_{peak} \cdot \sin(\omega t)| \tag{3.2}$$

Considering V_{in} the input DC voltage, then the value of the voltage across the capacitor v_C is given by (3.3):

$$v_C = \frac{k \cdot D}{1-D} \cdot V_{in} \tag{3.3}$$

In (3.3) D is the duty cycle for S_1 and **$k = N_2/N_1$** represents the transformer ratio. A complementary duty cycle 1-D is used for S_2.

The particularity of flyback transformer which applies to the entire converter is the fact that it does not carry current in primary and secondary circuits simultaneously during the semiconductors switching and this is why its operation is more like two magnetically coupled inductors. Because of this, the primary winding is considered as a first inductor with the inductance L_1, respectively the voltage over it, V_1; and the secondary winding is a second inductor with its own inductance, L_2 and voltage, V_2. Since the converter is bidirectional and it has a similar operation in each way. Considering that the energy flows from V_{in} to the filter capacitor the following relations can be written, when **S_1 is active**:

$$V_1 = V_{in} \tag{3.4}$$

$$V_2 = V_{in} \cdot k \tag{3.5}$$

$$V_{in} = L_1 \cdot \frac{di_1}{dt} \tag{3.6}$$

The energy stored in L_1 during this transition is given in (3.7) and due to the law of conservation of energy it is important to determine maximum I_1 current at the end of the conduction period.

$$V_{in} = L_1 \cdot \frac{I_1^2}{2} \tag{3.7}$$

In the secondary circuit since S_2 is inactive and the complementary diode is also reversed biased, the voltage V_{S2} over them is:

$$V_{S2} = V_C + V_{in} \cdot K \tag{3.8}$$

When S_1 is turned off and **S_2 become active**, the current I_2 through the secondary circuit becomes:

$$I_2 = \frac{I_1}{k} \tag{3.9}$$

$$V_C = -\ L_2 \cdot \frac{di_2}{dt} \tag{3.10}$$

$$V_1 = \frac{V_C}{k} \tag{3.11}$$

$$V_2 = V_C \tag{3.12}$$

When S_1 is inactive and the complementary diode is reversed biased, the voltage V_{S1} over them is:

$$V_{S1} = V_{in} + \frac{V_C}{k} \tag{3.13}$$

In fig.3.9 are presented the waveforms of currents through L_1 and L_2 and voltages over them when at the output of the flyback converter is connected a resistive load and supplied with constant voltage.
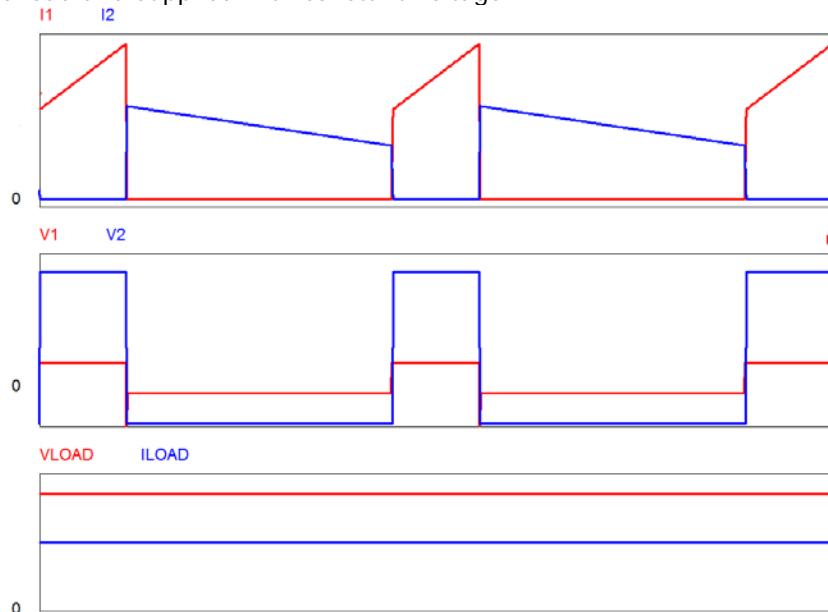
Fig.3.9. Flyback circuit waveforms in CCM and constant output voltage

The relations between the currents through the circuits are:

$$I_1 - I_0 = \frac{V_{in}}{L_1} \cdot DT_s \tag{3.14}$$

The mean voltage across the transformer windings are:

$$V_{in} \cdot D = \frac{V_C}{k} \cdot (1-D) \tag{3.15}$$

Because the reference voltage given for the DC link capacitor is a rectified sinusoidal, the duty cycle does not have a constant value and the controller permanently change it between a low value corresponding to the zero crossing time intervals and a high value corresponding to the time intervals when V_C is close to V_{peak}.

Combining the DC operation with the expected operation of the flyback inverter, the currents and voltages through the circuits depends by a close loop controller that establishes continuously the value of D and the direction flow of the energy through the transformer.

3.3. Stability analysis

The robustness and feasibility of proposed HBFAC is given by its stability in various conditions, while the parameters of the components remain the same. The stability analysis of the proposed DC-AC converter was realized using state-space average models by defining the discrete time model considering an unfavorable operating point, obtained from spice simulations.

For HBFAC, the stability analysis using SSA method is realized by reducing the circuit to a flyback DC converter considering the aspects discussed in section 2.3. Because the H-bridge does not need any additional control loops and it only inverts the already shaped DC voltage, it can be neglected in the stability analysis while the entire attention is focused on the voltage over the DC link capacitor. The SSA method is presented in detail step by step highlighting the way it was applied on the stability analysis of the proposed HBFAC.

The corresponding models are presented during t_{on} and t_{off} for the flyback converter acting as a step-up converter connected to a voltage source and supplying a resistive load. The state variables are identified and based on the considered simplifications, the equivalent circuit results in fig.3.10. The L_1 and L_2 inductances of the flyback transformer are treated together, because they are magnetically coupled and the transformation ratio k offers a direct relation between them. This simplifies more the stability analysis by reducing the state variables at only two.
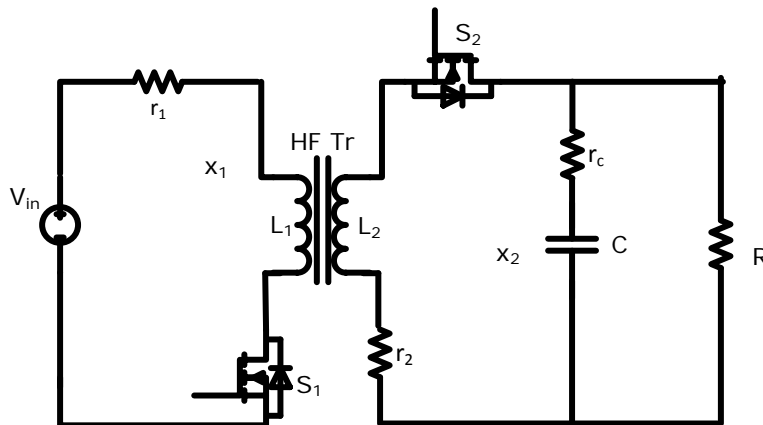
Fig.3.10. Highlighted State Variables for HBFAC

The state variables in the equivalent simplified circuit are x_1, which corresponds to the current through the magnetization inductance L of the flyback transformer and x_2, which is the voltage over the capacitor C.

During t_{on} the equivalent circuit is presented in fig.3.11. Based on it the state and output equations are written.
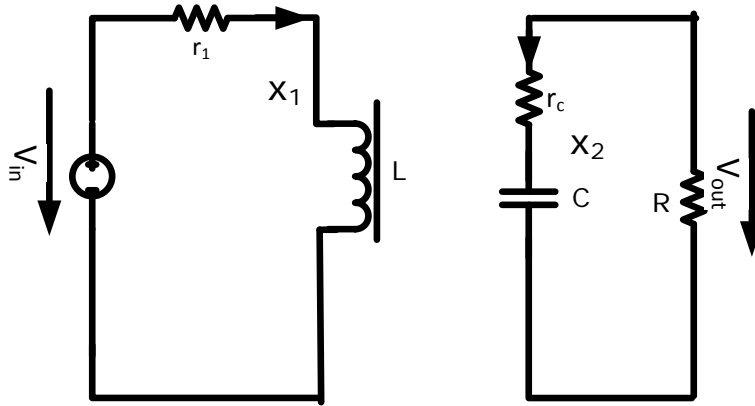
Fig.3.11. Equivalent circuit of BHDC during t_{on}

The simplified state equations during t_{on} derive from the equivalent circuit and are the following ones:

$$\dot{x}_1 = -\frac{r_1}{L} \cdot x_1 + 0 \cdot x_2 + \frac{1}{L} \cdot V_{in} \tag{3.16}$$

$$\dot{x}_2 = 0 \cdot x_1 - \frac{1}{RC} \cdot x_2 \tag{3.17}$$

Using (3.16) and (3.17) the state and output equations matrix is obtained during t_{on}:

$$\begin{bmatrix} \dot{x}_1 \\ \dot{x}_2 \end{bmatrix} = \begin{bmatrix} -\frac{r_1}{L} & 0 \\ 0 & -\frac{1}{RC} \end{bmatrix} \cdot \begin{bmatrix} x_1 \\ x_2 \end{bmatrix} + \begin{bmatrix} \frac{1}{L} \\ 0 \end{bmatrix} \cdot V_{in} \tag{3.18}$$

The system during the on state is given by the equations $\dot{x}_1 = A_1 x + B_1 V_{in}$ and $v_{out} = C_1 x$. From (3.18) the A_1 and B_1 matrices are determined:

$$A_1 = \begin{bmatrix} -\frac{r_1}{L} & 0 \\ 0 & -\frac{1}{RC} \end{bmatrix}; \quad B_1 = \begin{bmatrix} \frac{1}{L} \\ 0 \end{bmatrix} ; \tag{3.19}$$

C_1 results in the following:

$$V_{out} = V_C = 0 \cdot x_1 + 1 \cdot x_2 \quad \text{so:} \tag{3.20}$$

$$C_1 = \begin{bmatrix} 0 & 1 \end{bmatrix} \tag{3.21}$$
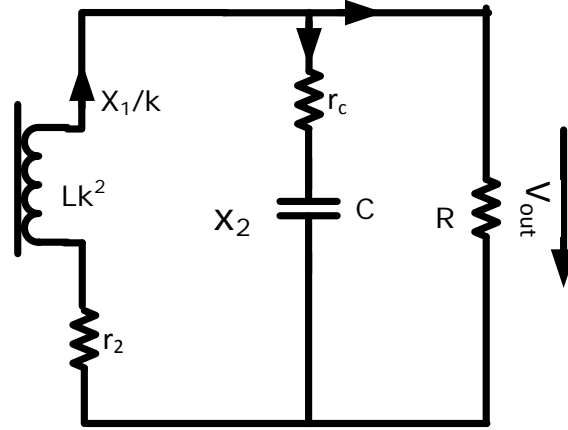
Fig.3.12. Equivalent circuit of BHDC during t_{off}

The simplified state equations during t_{off} derive from the equivalent circuit and are the following ones:

$$\dot{x}_1 = -\frac{r_2+r_c}{k^2 L} \cdot x_1 - \frac{1}{kL} \cdot x_2 \qquad (3.22)$$

$$\dot{x}_2 = \frac{1}{kC} \cdot x_1 - \frac{1}{RC} \cdot x_2 \qquad (3.23)$$

Using (3.22) and (3.23) the state and output equations matrix is obtained during t_{on}:

$$\begin{bmatrix} \dot{x}_1 \\ \dot{x}_2 \end{bmatrix} = \begin{bmatrix} -\frac{r_2+r_c}{k^2 L} & -\frac{1}{kL} \\ \frac{1}{kC} & -\frac{1}{RC} \end{bmatrix} \cdot \begin{bmatrix} x_1 \\ x_2 \end{bmatrix} + \begin{bmatrix} 0 \\ 0 \end{bmatrix} \cdot V_{in} \qquad (3.24)$$

The system during t_{on} state is given by the equations $\dot{x}_1 = A_1 x + B_1 V_{in}$ and $v_{out} = C_1 x$. From (3.24) the A_1 and B_1 matrices are determined:

$$A_1 = \begin{bmatrix} -\frac{r_2+r_c}{k^2 L} & -\frac{1}{kL} \\ \frac{1}{kC} & -\frac{1}{RC} \end{bmatrix}; \quad B_1 = \begin{bmatrix} 0 \\ 0 \end{bmatrix}; \qquad (3.25)$$

C_1 results in the following:

$$V_{out} = V_C = 0 \cdot x_1 + 1 \cdot x_2 \quad \text{so:} \qquad (3.26)$$

$$C_1 = [0 \quad 1] \qquad (3.27)$$

Considering $\tilde{d}$ as small variations of the duty cycle ratio D and V_{in} constant, the averaged equivalent system for small variations over a switching period is:

$$\dot{\tilde{x}} = A\tilde{x} + \left[(A_1 - A_2)X_0 + (B_1 - B_2)V_{in} \right]\tilde{d} \qquad (3.28)$$

$$\tilde{v}_{out} = C\tilde{x} + \left[(C_1 - C_2)X_0\right]\tilde{d} \tag{3.29}$$

In (3.28) and (3.29) $\dot{\tilde{x}}$ and $\tilde{v}_{out}$ are the small variations of the state and respectively the output variables. Using these relations, the simplified state-space model of the inverter is given in (3.30):

$$\begin{bmatrix} \dot{\tilde{x}}_1 \\ \dot{\tilde{x}}_2 \end{bmatrix} = \begin{bmatrix} -\dfrac{r_1}{L}D & -\dfrac{1-D}{kL} \\ \dfrac{1-D}{kC} & -\dfrac{1}{RC} \end{bmatrix} \cdot \begin{bmatrix} x_1 \\ x_2 \end{bmatrix} + \left[\begin{bmatrix} -\dfrac{r_1}{L} & \dfrac{1}{kL} \\ -\dfrac{1}{kC} & 0 \end{bmatrix} \cdot \begin{bmatrix} I_L \\ V_C \end{bmatrix} + \begin{bmatrix} \dfrac{1}{L} \\ 0 \end{bmatrix} \cdot V_{in} \right] \tilde{d} \tag{3.30}$$

Using Matlab tools, the related transfer function $\dfrac{\tilde{v}_{out}\,(s)}{\tilde{d}\,(s)}$ is obtained from (3.28) and (3.29).

The above average model is used to obtain the Bode plots for steady state and for stability analysis. Because the symbolic form of the transfer functions raised many difficulties, the diagrams representing the stability of the system were built using the real parameters of the proposed HBFAC. The prototype data is listed in Table 3.1:

Table 3.1. HBFAC prototype data

Component	Value	Units	Specifications
V_{in}	50	V	Input voltage in step-down mode
L	20	uH	Primary winding inductance of the flyback transformer
L_{lk}	1.6	uH	Leakage inductance of the flyback transformer
r_1	4.5	mΩ	Primary winding resistance of the flyback transformer
C	100	uF	Filter capacitor
r_C	10	mΩ	ESR of C
R_{load}	50	Ω	Resistive load
k	5		Flyback transformer conversion ratio

The Bode plots of the small signal transfer functions are used for the system stability analysis. Each of the obtained plots corresponds to one of the four state variables, determining the stability of the BHDC. Using the converter prototype data the following transfer function results:

$$\frac{\tilde{x}_1}{\tilde{d}} = \frac{3.991 \cdot 10^6 s + 1.097 \cdot 10^9}{s^2 + 359.4s + 7.844 \cdot 10^6} \tag{3.31}$$

$$\frac{\tilde{x}_2}{\tilde{d}} = \frac{-4.281 \cdot 10^4 s + 4.982 \cdot 10^9}{s^2 + 359.4s + 7.844 \cdot 10^6} \tag{3.32}$$

The system poles are $P_{1,2}$=-179.7±2975i. For (3.31) there is a negative zero Z_1=-274.8563 and for (3.32) the corresponding zero is Z_2=116390. The corresponding Bode plots for the small-signal transfer functions of the state variables are presented in fig.3.13 and fig.3.14.

The following Bode plot shows that the $\dfrac{\tilde{x}_1}{\tilde{d}}$ small signal transfer function is unstable and the practically the flyback transformer cannot support various perturbations and maintain a proper operation. The cutting frequency point is far from the normal operation point frequency. Still, the attention is focused on the operation of the output capacitor filter whose characteristics determine the good operation of the HBFAC. In fig.3.14 it can be seen that the related Bode plot shows that the $\dfrac{\tilde{x}_2}{\tilde{d}}$ small signal transfer function is also unstable. This results involves the necessity of the transfer functions for a compensation, which will be integrated in the HBFAC controller.
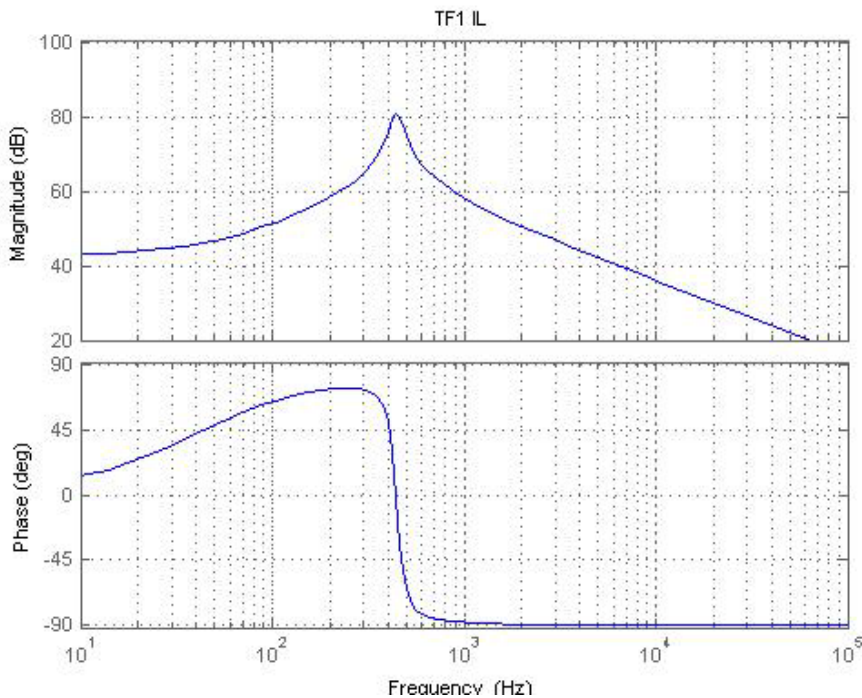
Fig.3.13. Bode plot for $\dfrac{\tilde{x}_1}{\tilde{d}}$ small signal transfer function
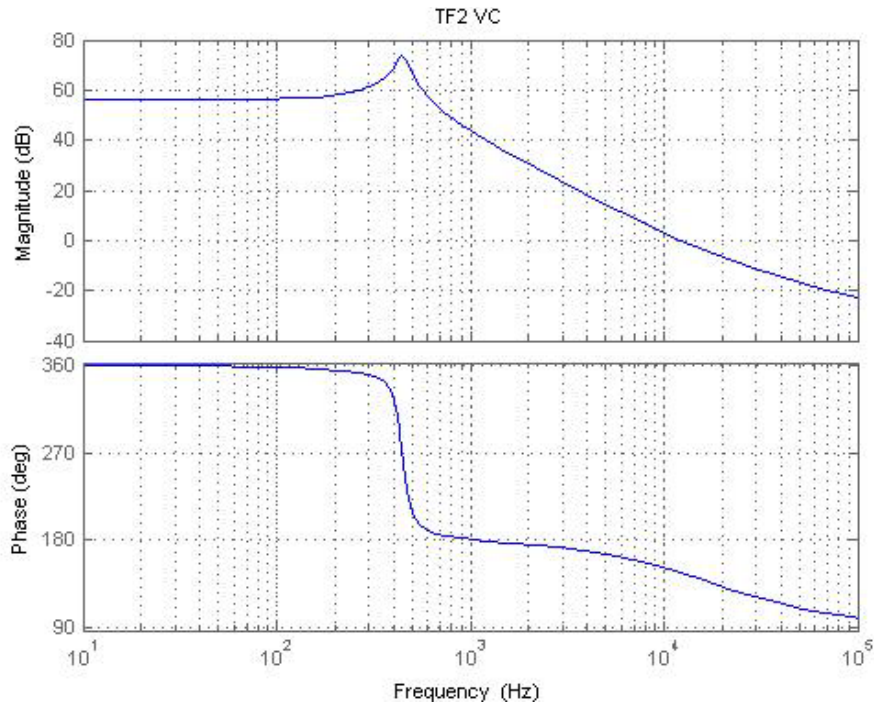
Fig.3.14. Bode plot for $\dfrac{\tilde{x}_2}{\tilde{d}}$ small signal transfer function

For the compensation, a controller with a pole-zero is used for the phase boost of the ac response on the output capacitor filter, which is presented in fig.3.14. The compensation transfer function is:

$$H(s) = \frac{0.1s + 500}{s + 25000} \tag{3.33}$$

With ω_{zero}=5000 rad/s (~795 Hz) being several times lower than $\omega_{pole=}$25000 (~3.98 kHz), the phase is boosted on that interval and the cutting frequency is lowered to a more appropriate value. The Bode plots for the system transfer functions, including the compensation, are presented in fig.3.15 and fig 3.16. In fig.3.16 a phase margin at 219 (-141) degrees is obtained at a cutting frequency of 2.7 kHz. This results show that the compensated system has a phase reserve of 39 degrees at the cutting frequency, corresponding to good system stability. The proposed compensation function is going to be integrated in the simulation models and in the experimental prototype.
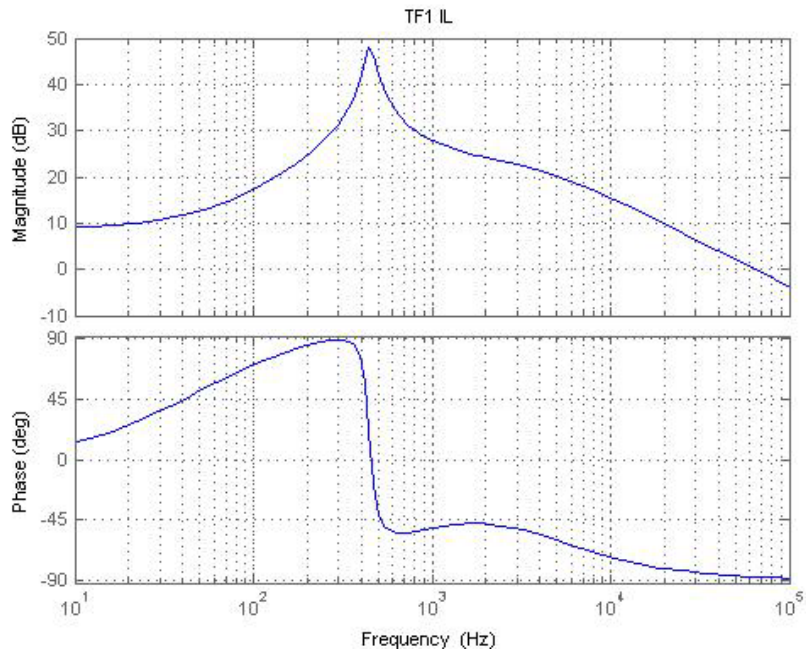
Fig.3.15. Bode plot for $\dfrac{\tilde{x}_1}{\tilde{d}}$ small signal transfer function with compensation
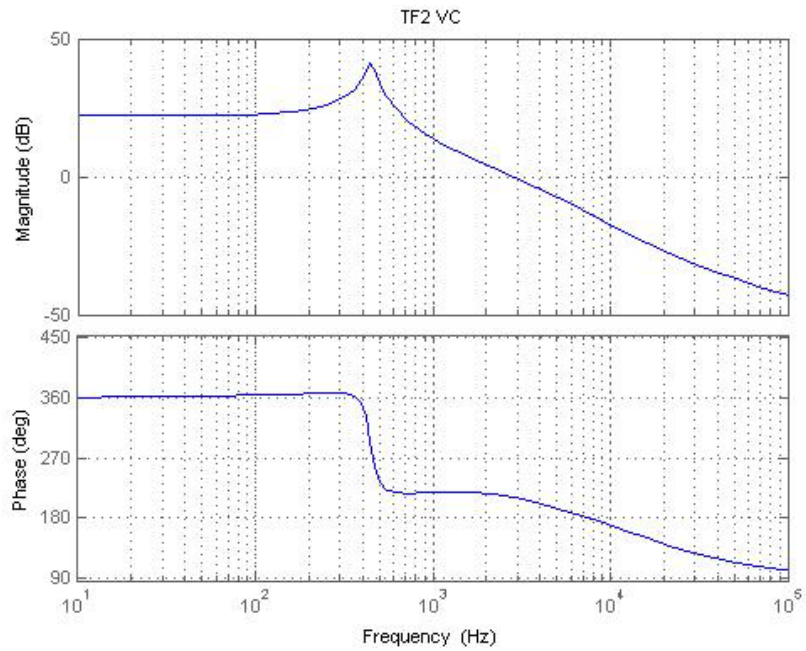
Fig.3.16. Bode plot for $\dfrac{\tilde{x}_1}{\tilde{d}}$ small signal transfer function with compensation

3.4. Digital simulations

The information regarding the proposed bidirectional DC-AC converter after the analytical study and the compensation analysis are used for the simulation and the prototyping procedure. Using the compensation transfer function and a proper control that integrate a rectified sinusoidal signal as reference for the voltage over the DC link capacitor, a spice model of HBFAC was realized in PSIM.

In fig.3.17 is presented the spice model of the proposed HBFAC.
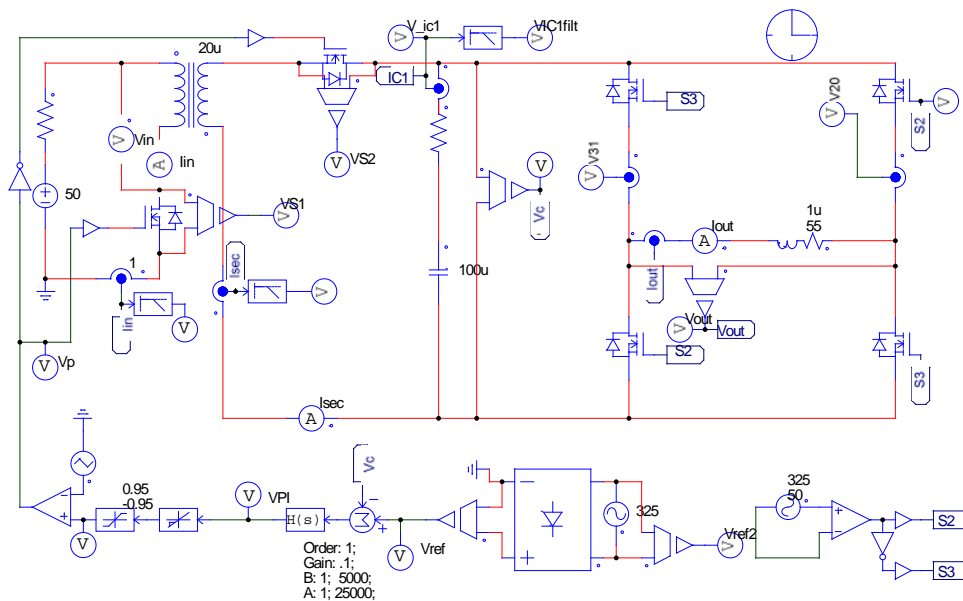
Fig.3.17. HBFAC simulation circuit

The upper side of the simulation model represents the power stage circuit. The high frequency flyback transformer used in simulation, is modeled using the real parameters. Since the snubber circuits are not selected yet, they do not appear in simulation. Additional resistances appear in the model in order to reproduce the real components.

On the bottom side of the simulation model, the control circuit is presented. While the H-bridge is controlled using a sinusoidal zero crossing detector, the flyback converter on the left side contain the rectified sinusoidal reference signal and the compensation function H(s).

In fig.3.18 are presented the simulation results. They confirm the well operation of the proposed HBFAC and the compensation function efficacy.
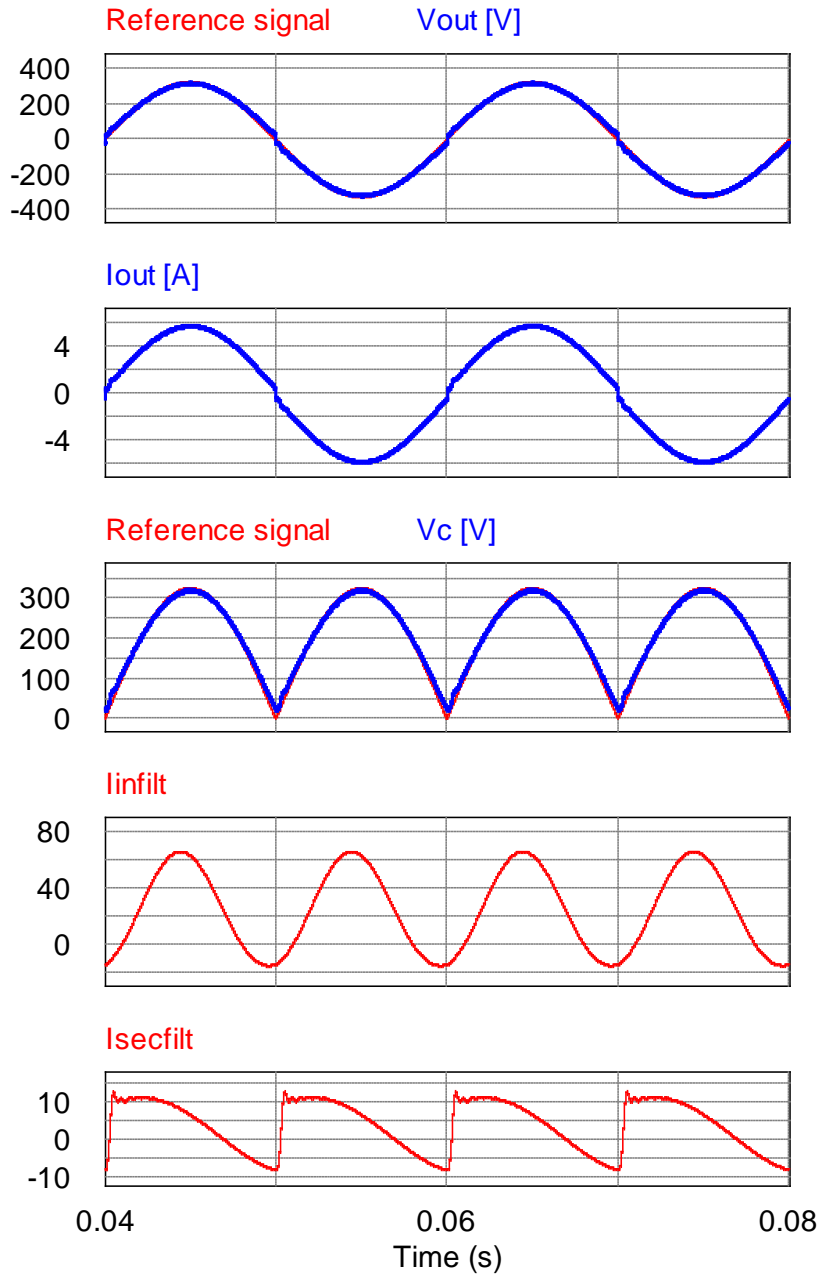
Fig.3.18. HBFAC simulation waveforms of the output voltage and current, the voltage and current over the DC link capacitor, following the reference waveforms and the filtered currents through the primary and secondary circuit.

The simulation waveforms show that the proposed HBFAC has a good operation. The filtered waveforms of the currents through the primary and secondary circuit highlights the bidirectional feature of the converter, considering the operating mode when the energy flows only from a 50V DC voltage source to a 230V AC resistive load. Since the voltage over the DC link capacitor represent the main variable that have to be controlled, the waveforms show that using a proper controller that integrates the mentioned compensation function, the system is able to follow the reference signal and the voltage over the capacitor is similar with a rectified sinusoidal voltage.

In order to test the compensation function and the capability of the HBFAC to operate in different conditions, the simulation model response was obtained using a variable resistive load. In fig.3.19 are shown the voltage and current waveforms considering a resistive load of 220, 165, 110 and 55 Ohms.
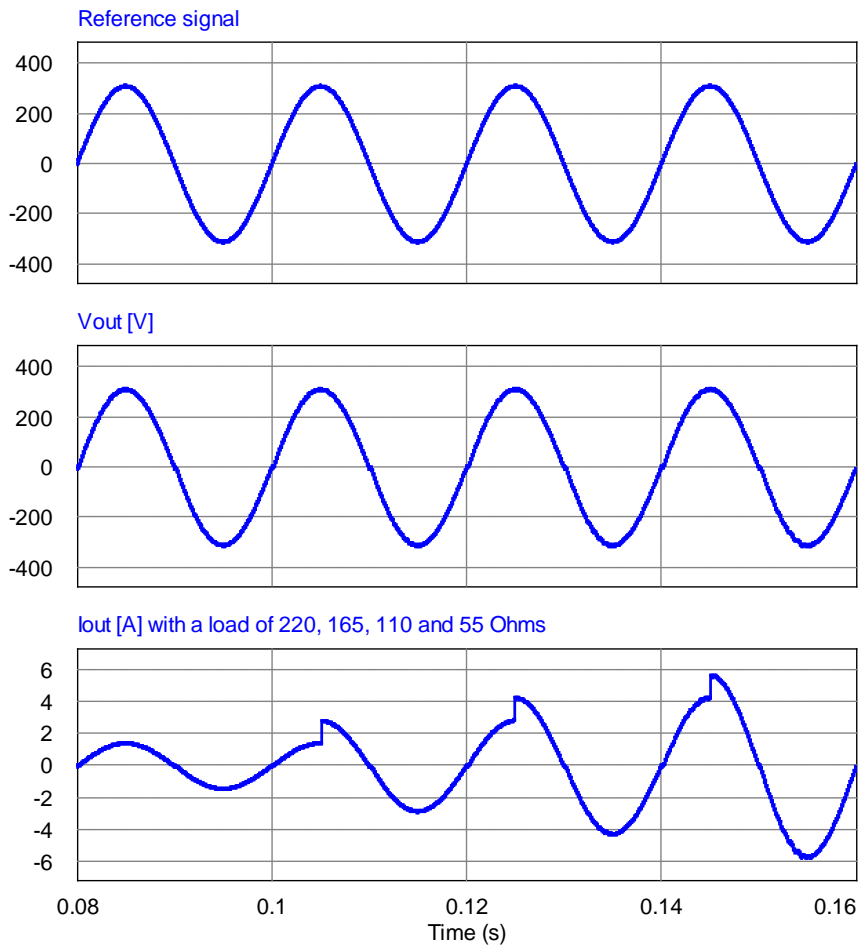
Fig.3.19. HBFAC simulation waveforms of the output voltage and current with a variable resistive load of 220, 165, 110 and 55 Ohms

The output voltage and current present a low THD factor and they highlight that the proposed HBFAC is operational. With additional resonant snubbers, protection and limitation circuits the above simulation model is going to be the basis of an experimental prototype.

3.5. Experimental prototype design

With positive results during the analytical and stability studies, confirmed afterwards through simulation, a prototyping procedure was initiated. In the beginning of this chapter, two quite similar topologies were proposed. Since there are not so many differences, a configurable circuit was conceived.

The power stage circuit of HBFAC is presented in fig.3.20. The connectors TS1, TP2, TS1 and TS2 are used for the flyback transformer primary and secondary windings connection to the circuit. Since the currents through these windings are used for the system control, two current sensors IS1 and IS2 are added. The connectors V+50 and V-50 are designed for the lower voltage source connection to the circuit. On the other side, the connectors V230ACF and V230AC represent the output of the converter when the h-bridge is used. In the second configuration, only a half of the h-bridge is used and the output is given by the V230ACF and a midpoint V230ACm, between 2 identical capacitor cells connected between VCCap2 and VCC650 connectors.
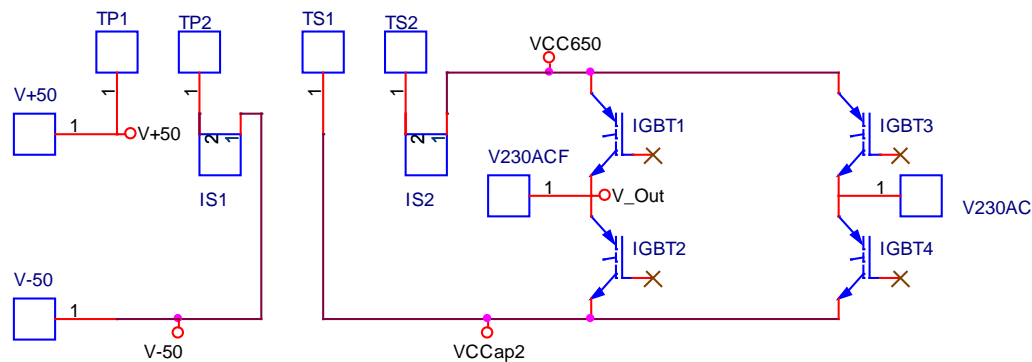
Fig.3.20. Power stage circuit schematic

Three capacitors cells are designed for this configurations. Between V+50 and V-50 is connected the first filter capacitor cell Ci on the lower voltage source side. The two remaining capacitors cells C_1 and C_2 are connected between VCC650 and VCCCap2. They have a configurable design and they can be connected in series, parallel or only one at the time. In fig.3.21 are presented the capacitor cells circuits.
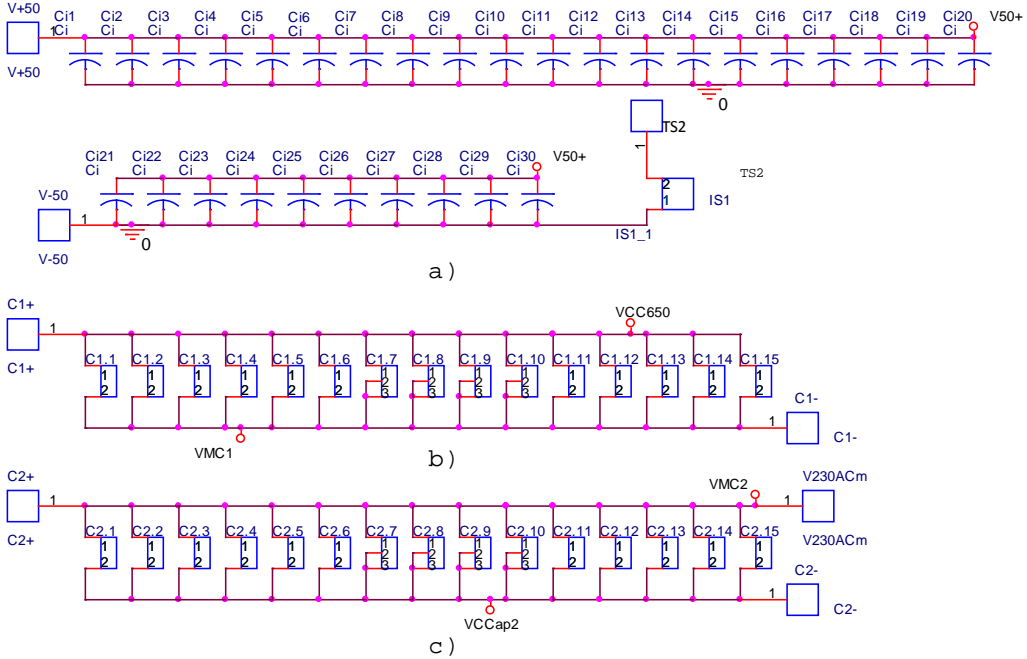
Fig.3.21. Capacitor circuit structure C_i(a), C_1(b) and C_2(c)

The Ci input filter capacitor is intended to be used as voltage buffer only for the voltage source protection. Its value of approximatively 2000 uF was chosen high enough to protect the battery stack from any voltage peaks that that can appear during experimental test.

The flyback transformer was based on the fact that the currents through its windings are not constant and a low magnetic inertia is needed for a fast reversal of the energy flow. (3.34) gives the maximum energy transferred by the transformer and a first relation between the rated power and the primary winding inductance is given in (3.35)

$$E = \frac{L \cdot I^2}{2} \qquad (3.34)$$

$$P \approx \frac{(V_{in} \cdot D \cdot T_s)^2}{2 \cdot T_s \cdot L_p} \qquad (3.34)$$

Since the duty cycle is permanently changing during a switching period all the determined values for the inductances had a minimum and a maximum value. A spice simulation model was used to verify these values and was chosen as the final solution a 20uH value, for the primary winding inductance. The transformer was designed and physically realized experimentally in the laboratory, using high quality Metgas U cores following [3.28] and a dedicated Core Calculator software offered by Metglas.Inc. In Table 3.1 are listed the dimensioned components of the HBFAC.

Table.3.1. List of HBFAC components

Components	Value	Configuration	Additional Details
Primary winding L1 inductor	20uH	6 turns of 6mm^2 copper conductor	The flyback transformer was designed and realized using 2 AMCC100 U cores, 6 turns of 6mm^2 copper wire of for the primary winding, 30 turns of 1.5 mm^2 for the secondary winding and 1.2mm air gap between U cores
Secondary winding L2 inductor	700uH	30 turns of 1.5mm^2 copper conductor	
Ci capacitor	2000uF	20X100uF + 10x2.2uF	2 parallel connected groups of 20 electrolytic caps connected also in parallel with 10 polyester caps
C1-C2 capacitor cells	50uF	20X5uF + 10X0.47uF capacitors	Each capacitor of the capacitor cell contain 2 groups connected in parallel of 6 up to 10 large polyester caps connected in parallel with 5 up to 9 small polyester caps
S1,S2	2xSKM200GB125D IGBT modules	2XIGBT of 1200V and 150A	S1 is realized using 1 IGBT from one module. S2 uses 1 IGBT from the second module
IS1	LA100-P	100 A current sensor	IS1- current sensor for L_1
IS2	LA50P	50 A current sensor	IS2- current sensor for L_2

3.6. Conclusion

In this chapter is presented a bidirectional hybrid DC-AC converter with galvanic isolation and a low number of components.

This chapter starts with an introduction presenting a general overview of high efficiency topologies of DC-AC converters used in microgrids applications. They were found in literature and most of them are actually integrated in renewable energy applications

In this chapter, two novel topologies of bidirectional flyback inverters are proposed. Only one topology of HBFAC is presented in detail. An analytical study is realized in order to establish the operation principles and constraints, based on the current and voltages equations. After a preliminary design procedure a parametrized circuits of the HBFAC is obtained. In order to verify its operation behavior a stability analysis is made using the state-space average procedure and the results show

that the system is unstable. A compensation function was designed based on the Bode plots obtained for the transfer functions of the main components. After its effectiveness was verified, it was integrated in a spice simulation model. The Bode plots for the compensated transfer functions shown that the system became stable and the simulation waveforms confirmed the good behavior of the proposed HBFAC. This allowed the design of a prototype which follows the information collected in the previous sections, including the compensation function. Design considerations and simulation results are presented.

References

[3.1]   Guran, E., "High efficiency power converters for renewable sources of energy," Applied Computational Intelligence and Informatics (SACI), 2013 IEEE 8th International Symposium on , vol., no., pp.381,386, 23-25 May 2013;

[3.2]   L. Czarnecki, D. Gutzeit, D. Schekulin, and A. Winter, "Coolcept"-eine neue PV-Wechselrichter-Topologie für sehr hohe Wirkungsgrade, " 2010, pp 1-6.

[3.3]   S. B. Kjaer, J. K. Pedersen and F. Blaabjerg, "A review of singlephase grid-connected inverter for photovoltaic modules," IEEE Trans. on Industry Applications, Vol. 41, No. 5, pp. 1292-1306, Sep/Oct. 2005.

[3.4]   Holmes, D.G.; Atmur, P.; Beckett, C.C.; Bull, M.P.; Kong, W.Y.; Luo, W.J.; Ng, D.K.C.; Sachchithananthan, N.; Su, P.W.; Ware, D.P.; Wrzos, P., "An Innovative, Efficient Current-Fed Push-Pull Grid Connectable Inverter for Distributed Generation Systems," Power Electronics Specialists Conference, 2006. PESC '06. 37th IEEE , vol., no., pp.1,7, 18-22 June 2006;

[3.5]   Glaser, J.S.; Rivas, J.M., "A 500 W push-pull dc-dc power converter with a 30 MHz switching frequency," Applied Power Electronics Conference and Exposition (APEC), 2010 Twenty-Fifth Annual IEEE , vol., no., pp.654,661, 21-25 Feb. 2010;

[3.6]   Li Zhang; Lanlan Feng; Yan Xing; Xudong Ma, "A single-stage forward inverter with high frequency isolation for grid-connected application," Industrial Electronics, 2009. IECON '09. 35th Annual Conference of IEEE , vol., no., pp.4537,4542, 3-5 Nov. 2009;

[3.7]   [8] Lin Sun; Yongchun Liang; Chunying Gong; Yangguang Yan, "Research on Single-Stage Flyback Inverter," Power Electronics Specialists Conference, 2005. PESC '05. IEEE 36th , vol., no., pp.849,854, 16-16 June 2005

[3.8]   Kyritsis, A. Ch; Tatakis, E.C.; Papanikolaou, N.P., "Optimum Design of the Current-Source Flyback Inverter for Decentralized Grid-Connected Photovoltaic Systems," Energy Conversion, IEEE Transactions on , vol.23, no.1, pp.281,293, March 2008;

[3.9]   Wuhua Li; Lingli Fan; Yi Zhao; Xiangning He; Dewei Xu; Bin Wu, "High-Step-Up and High-Efficiency Fuel-Cell Power-Generation System With Active-Clamp Flyback—Forward Converter," Industrial Electronics, IEEE Transactions on , vol.59, no.1, pp.599,610, Jan. 2012;

[3.10]   Alian Chen; Shao Daming; Du Chunshui; Chenghui Zhang, "High-frequency DC link flyback single phase inverter for grid-connected photovoltaic system," Power Electronics for Distributed Generation Systems (PEDG), 2010 2nd IEEE International Symposium on , vol., no., pp.364,367, 16-18 June 2010;

[3.11]   Tamyurek, B.; Kirimer, B., "An interleaved flyback inverter for residential photovoltaic applications," Power Electronics and Applications (EPE), 2013 15th European Conference on , vol., no., pp.1,10, 2-6 Sept. 2013;

[3.12]   GongChunying; Sun Lin; Liang Yongchun; Wang Huizhen; Yan Yangguang, "Research on the Control Strategies of Single-Stage Flyback Inverter,"

Power Electronics Specialists Conference, 2006. PESC '06. 37th IEEE , vol., no., pp.1,5, 18-22 June 2006

[3.13] Zhang, Yue; He, Xiao-Fei; Zhang, Zhiliang; Liu, Yan-Fei, "A hybrid control method for photovoltaic grid-connected interleaved flyback micro-inverter to achieve high efficiency in wide load range," Applied Power Electronics Conference and Exposition (APEC), 2013 Twenty-Eighth Annual IEEE , vol., no., pp.751,756, 17-21 March 2013;

[3.14] Matthais Victor, Frank Greizer, Sven Bremicker, and Uwe Hubler, "United States Patent No: US 7,411,802 B2," Dec.8, 2008.

[3.15] B. Burger and D. Kranzer, "Extreme high efficiency PV-power converters," 2009, pp. 1-13.

[3.16] Steca Elektronik GmbH, "StecaGrid 3000 and StecaGrid 3600 Brochure," 2011.

[3.17] B. Axelrod, Y. Berkovich, and A. Ioinovici, "A cascade boost-switched-capacitor-converter - two level inverter with an optimized multilevel output waveform," Circuits and Systems I: Regular Papers, IEEE Transactions on, vol. 52, no. 12, pp. 2763-2770, Dec.2005.

[3.18] O. Abutbul, A. Gherlitz, Y. Berkovich, and A. Ioinovici, "Step-up switching-mode converter with high voltage gain using a switched-capacitor circuit," Circuits and Systems I: Fundamental Theory and Applications, IEEE Transactions on, vol. 50, no. 8, pp. 1098-1102, Aug.2003.

[3.19] H. Nomura, K. Fujiwara, and M. Yoshida, "A New DC-DC Converter Circuit with Larger Step-up/down Ratio," 2006, pp. 1-7.

[3.20] B. Axelrod, Y. Berkovich, and A. Ioinovici, "Switched-Capacitor/Switched-Inductor Structures for Getting Transformerless Hybrid DC–DC PWM Converters", IEEE Transactions on Circuits and Systems I: Regular Papers, vol. 55, no. 2, pp. 687-696, Mar.2008.

[3.21] P. Sung-Jun, K. Feel-Soon, H. L. Man, and U. Cheul, "A new single-phase five-level PWM inverter employing a deadbeat control scheme," Power Electronics, IEEE Transactions on, vol. 18, no. 3, pp. 831-843, May2003.

[3.22] N. S. Choi, J. G. Cho, and G. H. Cho, "A general circuit topology of multilevel inverter," 1991, pp. 96-103.

[3.23] R. Anand and A. Nazar Ali, "A Single phase Five level Inverter for Grid Connected Photovoltaic System by employing PID Controller," 2011.

[3.24] R.González, E.Gubia and J. López, "Transformerless Single-Phase Multilevel-Based Photovoltaic Inverter", IEEE Transactions on Industrial Electronics, vol. 55, no.7, pp.2694-2702, July 2008.

[3.25] [16] R.González and J. López, "Transformerless Inverter for Single- Phase Photovoltaic Systems", IEEE Transactions on Power Electronics, vol. 22, no.2, pp.693-697, March 2007.

[3.26] A.M. Salamah, S.J. Finney, B.W. Williams, "Single-Phase Voltage Source Inverter With a Bidirectional Buck–Boost Stage for Harmonic Injection and Distributed Generation", IEEE Transactions on Power Electronics, vol.24, no.2, pp.376,387, Feb. 2009.

[3.27] E. Guran, O. Cornea, N. Muntean, "Novel Topology Flyback Inverter for a Microgrid System", 6th International Workshop on Soft Computing Applications SOFA2014, JULY 2014;

[3.28] Col. Wm. T. McLyman "Transformer and Inductor Design Handbook", Third Edition", pp 348-533, 2004.

4. EXPERIMENTAL SETUP

4.1. Introduction

In the previous chapters, two novel topologies are presented. They are intended to be integrated in smart microgrids applications considering their particular features like bidirectionality, low number of components and simple control. The microgrid applications are nowadays very popular, mostly because of the continuous increase of the energy need while the conventional energy sources represent a real problem on relative long term (25-35 years).

This thesis presents two solutions for a microgrid application that is under construction. The two proposed topologies can be found in fig.4.1 which is sketch of the intended microgrid.
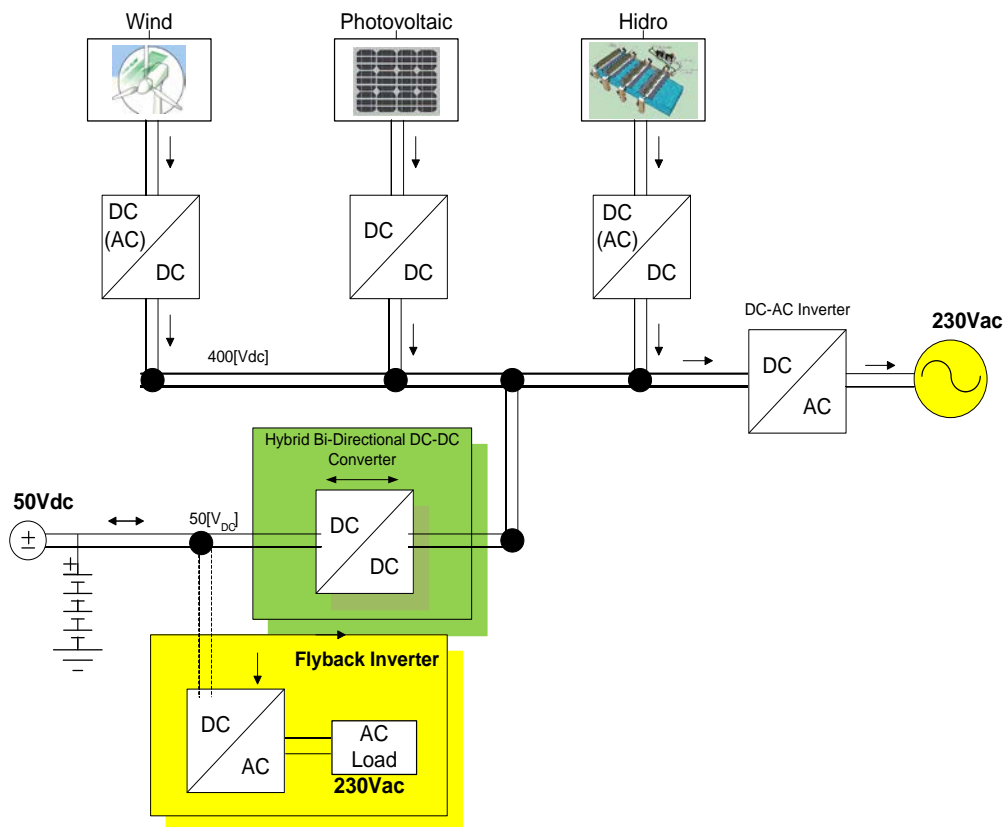
Fig.4.1. A microgrid application that integrates the two proposed topologies

The presented microgrid has two DC busses. The first one is a high DC voltage bus that collects energy from three different renewable energy sources at a value of 400 V. It is connected through an inverter to AC loads or even to the grid in order to inject energy and interfaced to a secondary bus of 50V. The interface between the two busses is realized using the proposed bidirectional DC-DC converter. The 50V bus is connected to a battery stack and through the BHDC, the power flow is realized in both directions, up to the 400V bus and the AC loads.

The proposed Flyback inverter appears in the microgrid sketch, but it has a particular purpose. It is intended to supply with energy directly from the storage system special loads and equipment. It operates like an UPS, but it receives the input energy from the battery stack [4.1].

4.2. BHDC Experimental Setup

In this subchapter are presented the experimental test conditions and equipment. In fig.4.2 is shown the configuration of the setup during the experimental tests.
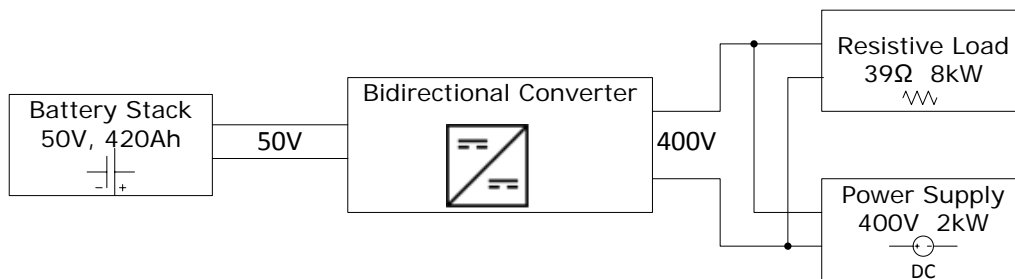
Fig.4.2. Experimental setup structure for BHDC

The experimental tests were realized complying with the design specifications and with the equipment limitations. The proposed BHDC is intended to be used in up to 5 kW applications. The circuit passive components were designed and dimensioned to operate at the rated power. But the SKM75GB123 IGBT modules were chosen by economic criteria. Since their configuration and parameters match with the proposed application requirements but at a lower rated power, these semiconductors were used. The limitation introduced by them is related to the maximum current through the two IGBTs connected in parallel, which is less than 95 A at a 20 kHz frequency.

The rest of the equipment will be presented in detail from the lower voltage side to the higher voltage side. Currently, the BHDC was integrated in the intended microgrid and it realize the interface between the lower voltage DC bus which corresponds to a 50 V and 420 Ah gel battery stack shown in fig.4.3 and a 400 V and 2 kW power source which emulates the second DC bus. This battery stack [4.2, 4.3] can provide a high current capacity of over 400 Ah when it is used as a power supply. During its charging, the current that can be injected is about 10% of its capacity. Because of this, the BHDC can be tested at a maximum power of 2 kW, in order to protect the batteries.

Fig.4.3. A 50 V, 400 Ah battery stack emulating a storage system

The BHDC prototype is presented in fig.4.4 during operation. An electronic signal generator is used for the reference input signal of the converter. Based on the reference waveforms and values, the converter automatically establishes the duty cycles, switching strategy and the energy flow direction. Since the converter is connected directly to two voltage sources, no data was acquired regarding the input/output voltages. The current waveforms through the L_1 and L_2 inductors were obtained using current probes directly on their connections to the circuit. The PWM switching pulses were collected from the transistor gates. In the presented image, the 50 V power cables come through cable ladders from the battery stack, and the higher voltage side of the converter is connected directly to the 400 V, 2 kW Regatron TopCon Quadro Power Supply [4.4] in parallel with a resistive load of 39 Ω, 8 kW [4.5, 4.6]. During its operation, in this configuration the converter can transfer energy in each direction. It was tested at a maximum power of 2.5 kW with good results.
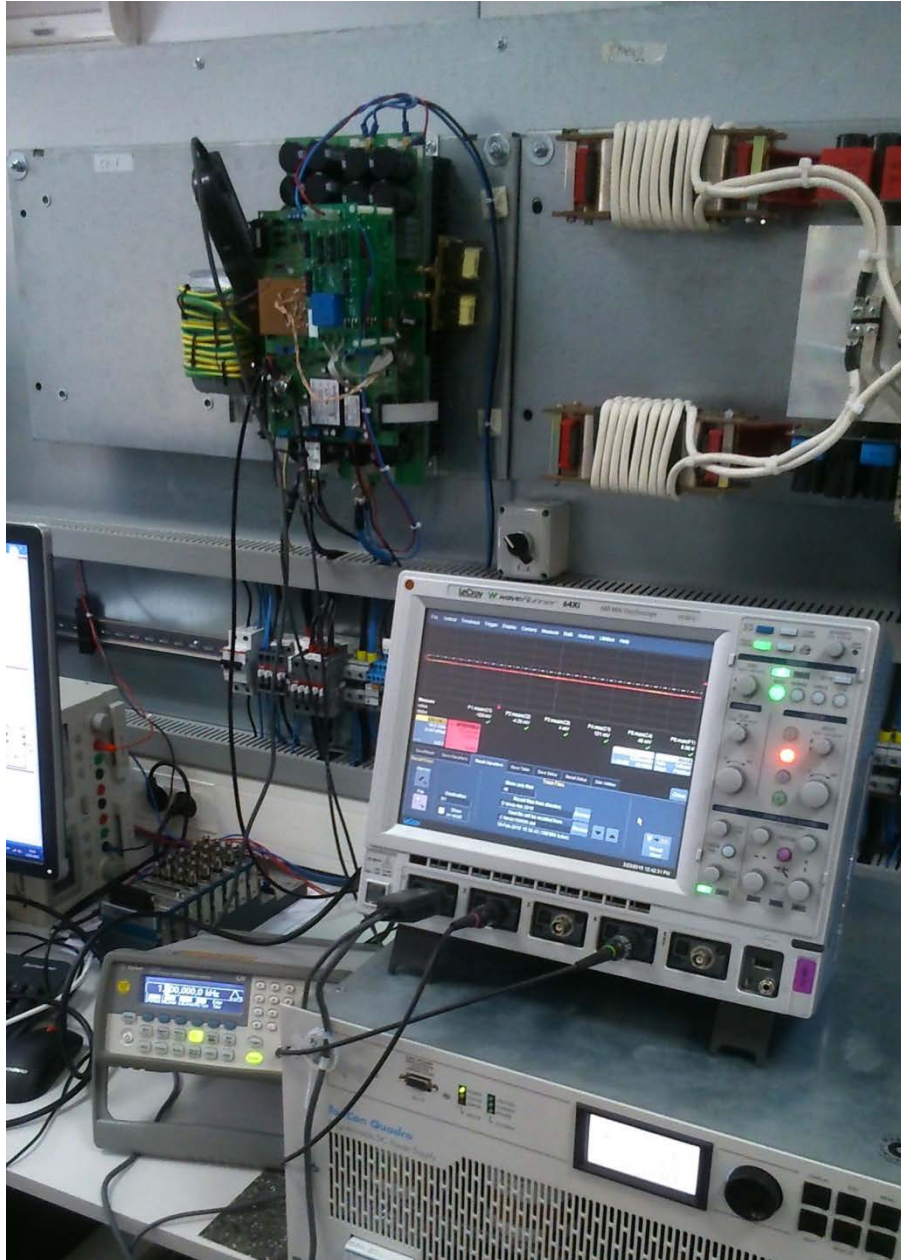
Fig.4.4. BHDC Prototype during operation

In fig.4.5 is presented the 400 V power supply unit and the resistive load that emulates the 400 V DC bus. Due to the power supply constraints (2 KW), the system cannot be tested at a higher power.

a)

b)

Fig.4.5. a) 39 Ω, 8 kW resistive load; b) 400 V DC 2KW Regatron TopCon Quadro Power Supply

Regatron power supplyes are ususally used for:

- Simulation and substitution of real DC sources like:
    - Batteries
    - PVs
    - Fuel cell stacks
- Supply of:
    - Burn-in- and test-systems
    - Plasma loads e.g. surface technology
    - Radar modulators (klystron, magnetron)
    - Highly dynamic DC applications
    - Pulse laser
    - Demagnetizing and degaussing systems

Regatron TopCon Quadro Power Supply main output specifications:
- Output ratings:
- Output power range .... 0 – 10 [kW]
- Output voltage range .... 0 – 400 [Vdc]
- Output current range .... 0 – 31 [A]
- Internal resistance range .... 0 – 1000 [mΩ]
- Operating modes
- Voltage regulation (CV) .... 0 – 100 % [Umax]
- Current regulation (CC) .... 0 – 100 % [Imax]
- Power regulation (CP) .... 5 – 100 % [Pmax]

4.3. Conclusion

In this chapter are presented the experimental setup used to obtain the prototype experimental results.

The structure of the intended microgrid application where the two proposed converters are going to be integrated is presented.

Starting with a schematic of how the BHDC is used as an interface between a battery stack and higher DC voltage source, the main components of the experimental setup are presented.

The high power rechargeable batteries are shown as a lower voltage source. They are able to supply energy and collect energy through the BHDC, assuring this was the possibility of a bidirectional power flow.

On the other side, the 400 V DC source is connected in parallel with a resistive load in order to obtain the same bidirectional power flow during the experimental tests.

With the BHDC prototype connected to the presented sources, experimental results are collected. Because of the equipment constraints, the experiments are realized at a lower power, but the results validate the good operation of the converter.

References

[4.1]   Cornea, O.; Guran, E.; Muntean, N.; Hulea, D., "Bi-directional hybrid DC-DC converter with large conversion ratio for microgrid DC busses interface," International Symposium on Power Electronics, Electrical Drives, Automation and Motion (SPEEDAM) 2014, , vol., no., pp.695,700, 18-20 June 2014;
[4.2]   MOLL   Batteries   Available: http://www.moll-batterien.de/produkte/solar_en.html;
[4.3]   MOLL   Batterien   Available: http://www.moll-baterii.ro/bateriile-moll-cu-tehnologia-efb-startstop;
[4.4]   REGATRON   Available: http://www.regatron.com/en/products-topcon/topcon-quadro-tc-p

[4.5]   http://www.italohm.com/lang_en/products/pdf/ROPPE_EN.pdf;
[4.6]   OFEL Elettromeccanica, Available:
          http://www.agftechnology.com/products/ofel_prod.html

5. CONCLUSION AND CONTRIBUTIONS

5.1. Conclusion

This thesis is a power electronics research with references to bidirectional DC-DC and galvanic isolated DC-AC converters. These topologies are close related to the microgrid applications and the presented converters are intended to be used in a microgrid system.

This study starts with a general overview regarding smart grids. Its goal is to present the main components of these systems and underline their special features. On the other hand are presented the limitations, weaknesses and the elements constraints.

After the microgrid concept is understood, the attention is focused on the converters that these systems usually integrate. These converters with high efficiencies have a simple control, a low number of components and because of their bidirectional features they can be used as interfaces between the DC-DC or DC-AC busses of a microgrid.

The first analyzed topology is a bidirectional hybrid DC-DC converter able to convert energy with a large voltage ratio without using a transformer and with a low number of components. A full analytical study is realized in order to establish the operation principles and limitations of the BHDC. The voltages and currents equations are written for the main components.

Using the real prototype information, a stability analysis is made using the state-space average method and the PWM switch model method. The results of both stability analyses are presented and compared, determining this way the stability of the state variables whose operation determines the proper operation of BHDC. The results are used to obtain a compensation function that improves the converter stability and which is integrated in a spice simulation model in order to verify its efficacy.

A spice simulation model is designed in Psim. It matches the experimental setup design and integrates in addition to the control loop the compensation function obtained during the stability analysis. The main waveforms of the currents and voltages confirm the good behavior of the proposed BHDC. They validate the theoretical considerations and allow the experimental tests directly on the prototype.

The experimental results are obtained in tough conditions during fast reversals of the current at different values. The currents and voltages waveforms show that the proposed BHDC operates in good conditions, with fast responses to the reference signal and low oscillations. These tests confirm its stability during harsh conditions.

The second proposed converter is a bidirectional flyback inverter. An analytical study is realized highlighting its operating principles and limitations.

After a prototyping procedure, the real components parameters are used in a stability analysis using the state-space average procedure. The results are

analyzed and the AC response of the main state variables, which determine the proper operation of the entire system, is assessed. Since its behavior is not stable, a compensation function was obtained and integrated into the system, in order to improve its stability.

The compensation function and the design considerations are used to create a simulation model in Psim. During simulations, the waveforms of the currents and voltages showed a good operation of the proposed flyback inverter and a low THD factor.

The simulation and experimental results confirm the robustness of the two proposed converters and qualify them to be used on large scale in microgrids applications due to their special features.

5.2. Contribution

The author contributions to this thesis can be summarized as follows:

➢ A general overview of smart microgrids was made, highlighting their main features and components;
➢ A hybrid bidirectional DC-DC converter was analytically studied, designed and validated through digital simulation;
➢ A stability analysis was made using two different procedures. The results were analyzed, compared and the results were used to design a compensation function needed to improve the stability requirements;
➢ A prototype was built and the theoretical considerations were validated;
➢ A general overview of high efficiency DC-AC topologies used in microgrid applications was made and they were tested through simulation;
➢ An analytical study and design were made for a proposed flyback inverter.
➢ A stability analysis was made for the proposed flyback inverter. The results were analyzed and used to obtain a compensation function, the stability performances were improved;
➢ The theoretical considerations were validated through simulations.
➢ Five papers in international conferences were written.

5.3. Future Work

The thesis subject includes the two proposed converters and it is close related to the main microgrid application presented in chapter 4. All the future work will be focused on the complete development of it:

➢ The BHDC will be tested at 5KW operating between the two 50V and 400V DC busses and particular efficiency determinations will be made;
➢ The HBFAC prototype will be realized including resonant snubbers. It will be tested unidirectional and bidirectional, integrated in the microgrid application. Efficiency determinations will be made.
➢ The proposed converters will be exploited in different microgrid scenarios and applications.

Author papers related to the thesis

- Guran, E., "High efficiency power converters for renewable sources of energy," IEEE 8th International Symposium on Applied Computational Intelligence and Informatics (SACI2013), pp.381,386, 23-25 May 2013;
- Cornea, O.; Guran, E.; Muntean, N.; Hulea, D., "Bi-directional hybrid DC-DC converter with large conversion ratio for microgrid DC busses interface", International Symposium on Power Electronics, Electrical Drives, Automation and Motion 2014 (SPEEDAM2014), pp.695,700, 18-20 June 2014;
- Guran, E.; Cornea, O.; Muntean, N.; „Novel Topology Flyback Inverter for a Microgrid System", 6th International Workshop on Soft Computing Applications (SOFA2014), 24-26 July 2014;
- Andreescu, G.D.; Cornea,O.; Muntean,N.;Guran,E.; „Bidirectional Flyback Inverter with Low Output Voltage THD", IEEE 10th International Symposium on Applied Computational Intelligence and Informatics (SACI2015), 21-23 May 2015 (accepted paper).

europass

Curriculum vitae

PERSONAL INFORMATION	**Emil Guran**

📍 10, Burebista, 300678 Timisoara (Romania)

📱 (+40) 720 351 981

✉ emil.guran@upt.ro

Sex Male | Date of birth 8 Dec 1985 | Nationality Romanian

WORK EXPERIENCE

Aug 2012–Present — **Research Assistant**

"Politehnica University of Timisoara, Faculty of Electrical and Power Engineering, Romania, Timisoara (Romania)

Project name: "Hybrid Renewable Energy Conversion in an Integrated Low Power Microgrid", PN-II-PT-PCCA-2011-3.2-1519

- Bibliographical research;
- Scientific reports;
- Simulation and experimental tests;
- experimental prototyping
- Research dissemination.

Renewable energies sector

Sep 2011–Feb 2014 — **Teaching Assistant**

"Politehnica University of Timisoara", Faculty of Electrical and Power Engineering, Timisoara (Romania)

- labs preparation before classes;
- teaching activities regarding PLCs and Power Electronics;
- students evaluations.

Aug 2009–Present — **Team Leader**

SC.MCCARTHY HOLTHUS.SRL, Timisoara (Romania)

- digital databases updates;
- team management;
- high responsibilities regarding work quality and effectiveness;
- Activity reports, meetings, manuals and procedures.

EDUCATION AND TRAINING

Oct 2011–Present — **PhD Student in Electrical Engineering Department**

Politehnica University of Timisoara, Timisoara (Romania)

- Research on smart microgrids;
- Study of power converters for renewable energy applications;

Oct 2009–Jul 2011 — **Master Degree in Electrical Engineering**

Politehnica University from Timisoara, Timisoara (Romania)

- PLCs, FEM Analyses, Power Electronics

Sep 2005–Jul 2009	**Electrical Engineer Degree**

Politehnica University of Timisoara, Timisoara (Romania)

Power Electronics, Electrical Drives, Automotive Electronics and Systems, Computer Science.
Computer skills acquired: Psim, Matlab, Labview, Catia

Sep 2001–Jun 2005	**Baccalaureate Degree, Average Programmer Certificate**

Colegiul Tehnic Domnul Tudor, Drobeta Turnu Severin (Romania)

PERSONAL SKILLS

Mother tongue(s) Romanian

Other language(s)

UNDERSTANDING		SPEAKING		WRITING
Listening	Reading	Spoken interaction	Spoken production	
English				
C1	C1	B2	B2	B2
French				
B1	B2	A2	A2	A2

Levels: A1 and A2: Basic user - B1 and B2: Independent user - C1 and C2: Proficient user
Common European Framework of Reference for Languages

Communication skills
- Good communication and public speaking skills gained from the participation at scientific symposiums and from the teaching assistant activity.

Organisational / managerial skills
- leadership skills(I currently lead a team of 7 members);
- team working skills acquired during the las 6 years work;
- management skills gained during the leadership experience.

Job-related skills
- Power Electronics, Electrical design and control, HMIs, PLC's, Virtual Instrumentation, Testing skills

Computer skills Matlab, Psim, Labview, TiNA, PLC's, FEMM, Microsoft Office (including Visio), Orcad.

Other skills Open-minded for creative and difficult tasks, sociable, punctual, ambitious.

Driving licence B

ADDITIONAL INFORMATION

Publications
- Guran, E., "High efficiency power converters for renewable sources of energy," Applied Computational Intelligence and Informatics (SACI), 2013 IEEE 8th International Symposium on , vol., no., pp.381,386, 23-25 May 2013;
- Cornea, O.; Guran, E.; Muntean, N.; Hulea, D., "Bi-directional hybrid DC-DC converter with large conversion ratio for microgrid DC busses interface", Electrical Drives, Automation and Motion (SPEEDAM), 2014 International Symposium on Power Electronics, vol., no., pp.695,700, 18-20 June 2014;
- Guran,E.; Frigura-Iliasa,F.M.; Frigura-Iliasa,M; "Power Quality Monitoring Software and Hardware

BUPT

for a Romanian Power Station", The 10th International Conference on Digital Technologies (DT2014), 9-11 July 2014;

- Guran, E.; Cornea, O.; Muntean, N.; „Novel Topology Flyback Inverter for a Microgrid System", 6th International Workshop on Soft Computing Applications (SOFA2014); 24-26 July 2014;

- Andreescu, G.D.; Cornea,O.; Muntean,N.;Guran,E.; „Bidirectional Flyback Inverter with Low Output Voltage THD", IEEE 10th International Symposium on Applied Computational Intelligence and Informatics (SACI), 21-23 May 2015.